Galactic Archaeology with the oldest stars in the Milky Way

Anke Arentsen
Leibniz-Institut für Astrophysik Potsdam (AIP)

Kumulative dissertation

zur Erlangung des akademischen Grades
doctor rerum naturalium (Dr. rer. nat.)
in der Wissenschaftsdisziplin Astrophysik

Eingereicht an der Mathematisch-Naturwissenschaftlichen Fakultät
Institut für Physik und Astronomie
der Universität Potsdam
und
das Leibniz-Institut für Astrophysik Potsdam (AIP)

Potsdam, 16.09.2020

Betreuer: Dr. Else Starkenburg/Prof. Dr. Matthias Steinmetz
1. Gutachter: Dr. Else Starkenburg
Leibniz-Institut für Astrophysik Potsdam
2. Gutachter: Prof. Dr. Matthias Steinmetz
Leibniz-Institut für Astrophysik Potsdam/Universität Potsdam
3. Gutachter: Prof. Dr. Norbert Christlieb
Zentrum für Astronomie der Universität Heidelberg/Landessternwarte

Published online on the
Publication Server of the University of Potsdam:
https://doi.org/10.25932/publishup-47602
https://nbn-resolving.org/urn:nbn:de:kobv:517-opus4-476022

"... it is difficult to resist the impression that the evolution of the stellar universe proceeds at a slow majestic pace ..."

— Sir A. S. Eddington
(The internal constitution of the stars, 1920)

Contents

Summary

The first stars in the Universe were born out of gas consisting of only the three lightest elements (hydrogen, helium and lithium) – no heaver elements ("metals") were yet present. Metals were produced in subsequent generations of stars, which have chemically enriched the Universe over time. Low-mass stars that formed in the early Universe are therefore expected to be poor in metals. Some of these stars became members of the Milky Way system over the course of their lives, where we can currently observe them in detail. Metal-poor stars are extremely useful probes to learn about the First Stars and the conditions in the early Universe, and they are also important tools for Galactic Archaeology – the study of the formation and evolution of the Milky Way.

Many of the stars with metallicities less than 1% of that of the Sun ([Fe/H] < -2.0) have unexpectedly high abundances of carbon. The fraction of such carbon-enhanced metal-poor (CEMP) stars increases for stars with even lower metallicities. This indicates that there may be an important connection between the CEMP stars and the First Stars. There are two main types of CEMP stars – those that formed as the result of an interaction with a binary companion where material rich in carbon and s-process elements was transferred to the star we see today (CEMP-s stars), and those that are not enhanced in *s*-process elements (CEMP-no stars). The latter are expected to represent the gas out of which they formed, and are typically the most useful for studying the First Stars.

Chapter 2 of this thesis describes the investigation of the binary properties of CEMP-no stars. A difference is found between two groups of CEMP-no stars: the more carbon-rich CEMP-no stars appear to be in binary systems more often (47^{+15}_{-14}%) than the rest of the CEMP-no stars (18^{+14}_{-9}%). This could indicate that binary mass-transfer also plays a role in the formation of (some of the) CEMP-no stars, whereas their abundance patterns are usually assumed to directly reflect the gas out of which they formed. This formation scenario had been proposed previously for the hyper metal-poor star HE 0107−5240, although there was no evidence for a companion – until our work confirmed that its velocity is indeed (slowly) varying. Being in a binary system does not necessarily mean a star has undergone mass-transfer, but it cannot be ruled out and therefore care should be taken in the interpretation of the abundance patterns of these stars.

The discovery of new metal-poor stars often relies on the use of low or medium resolution spectroscopic observations. Such observations are feasible for large numbers of stars and contain a wealth of information. The spectra are typically analysed by comparison with model spectra. These models can be empirical or synthetic, each with their own (dis)advantages. In Chapter 3 of this thesis, a uniform set of stellar atmospheric parameters is presented for the recent empirical X-shooter Spectral Library (XSL) covering a large wavelength range from 3000 Å to 24 800 Å in medium resolution. A data-driven method was used to derive the

effective temperature $T_{\rm eff}$, the surface gravity $\log g$, and the metallicity [Fe/H] with high precision, for 764 spectra of 616 XSL stars with widely varying properties (2900 $< T_{\rm eff} <$ 38 000 K, $0 < \log g < 5.7$, $-2.5 <$ [Fe/H] $< +1.0$ with a handful of stars at very low metallicities, down to [Fe/H] $= -3.7$). XSL will also be a useful tool for the improvement of synthetic models.

The search for metal-poor stars is usually focussed on the Galactic halo – this is on average the most metal-poor component of the Milky Way and can be targeted without too many complications. Relatively large samples of extremely metal-poor halo stars can be found in the literature; these provide us with important clues about the First Stars and can be used to investigate the early build-up of our Galaxy. Simulations of Milky Way-type galaxies, however, show that many of the oldest metal-poor stars are expected to be located in the central regions – in their bulges. The origin of the Galactic bulge has been discussed extensively in recent years. The current generally accepted picture is that most of it formed from an instability in the Galactic disk at an early time, with little room for a "classical", pressure-supported component. The overwhelming majority of stars in the bulge are relatively metal-rich. This population has been the most-studied, and the properties of the more metal-poor stars in the inner Galaxy are largely unknown. Extremely efficient selection methods are required to build large samples of metal-poor stars in this region with high extinction, severe crowding, large numbers of foreground stars and high average metallicity.

The final three thesis chapters are dedicated to the search for and the study of metal-poor stars in the inner Galaxy. They present results from the *Pristine* Inner Galaxy Survey (PIGS), which uses metallicity-sensitive narrow-band *CaHK* photometry to preselect candidate metal-poor stars in the bulge. The survey is presented in Chapter 5, which describes the photometric observations, the photometric target selection, the spectroscopic follow-up observations, the analysis of the low/medium-resolution spectra, and the performance of the survey. PIGS currently consists of ~ 250 deg^2 *CaHK* photometry and spectroscopic follow-up for ~ 8000 stars. The spectra have been analysed with two independent methods; one using a very similar approach as for XSL, and one with synthetic models. The latter method provides metallicities down to [Fe/H] $= -4.0$ and an estimate of the carbon abundance [C/Fe]. The spectroscopic follow-up efforts have resulted in a sample of ~ 1300 confirmed stars with [Fe/H] < -2.0, which is the largest known sample of very metal-poor stars in the inner Galaxy. The PIGS success rates are unprecedented, with 90% of the best photometric candidates having a spectroscopic [Fe/H] < -2.0, as have 75%/60% (lower/higher extinction) of a larger, less strictly selected sample.

The spectroscopic PIGS sample not only contains very metal-poor stars, but also thousands of stars with [Fe/H] < -1.0. PIGS stars of all metallicities have been used in Chapter 4 to study the kinematical properties of the metal-poor inner Galaxy. General bulge studies (which contain mainly metal-rich stars) have shown that the stars in the bulge rotate cylindrically around the Galactic centre – the signature of a bar. The PIGS results show for the first time that, for metal-poor stars, the rotation around the Galactic centre decreases as a function of metallicity. The very metal-poor stars ([Fe/H] < -2.0) do not appear to rotate at all. Additionally, the velocity dispersion steeply increases with decreasing metallicity, extending the trend seen at

higher metallicity. These observations are signatures of kinematical processes that have formed the inner Galaxy. They provide constraints on formation models of the Milky Way and its inner regions.

The final Chapter 6 of the thesis combines the inner Galaxy with the topic of the first chapter: CEMP stars. A previous survey of metal-poor inner Galaxy stars found only one out of 33 metal-poor stars to be carbon-enhanced. Immediately, the question arises if this striking difference in CEMP fraction between the inner Galaxy and the halo could be real, or the result of either selection effects or small number statistics. The large number of very metal-poor stars in PIGS with [C/Fe] estimates from the low/medium resolution spectroscopy allows re-investigation of this question. The chapter presents a sample of 66 new CEMP stars in the inner Galaxy – a giant leap forward as only two such stars have been reported in the literature so far. The fraction of CEMP-no stars in PIGS appears to be similar to the Galactic halo, although it is on the low side. The fraction of CEMP-s stars, however, is much lower. This could indicate differences in the binary properties of metal-poor stars between the halo and the inner Galaxy, but might also be the result of biases in the photometric selection. The CEMP stars (or the lack thereof) in the inner Galaxy will provide unique clues about the formation of this old Galactic component.

Each chapter contributes in a unique way to the study of "Galactic Archaeology with the oldest stars in the Milky Way". The future for this field is bright, with ongoing and upcoming surveys contributing a huge amount of new information. The combination of dynamical and chemical information for unprecedentedly large samples of metal-poor stars will provide new insights into the earliest stages of the formation of our Galaxy. At the same time, the revolutionary increase in the number of the most metal-poor stars studied in detail will greatly inform constraints on the properties of the First Stars.

Zusammenfassung

In einer dunklen Nacht kann man tausende Sterne sehen. All diese Sterne befinden sich innerhalb der Milchstraße, unsere Heimatgalaxie. Nicht alle Sterne sind gleich, sie können zum Beispiel unterschiedliche Größen, Massen, Temperaturen und Alter haben. Die schwereren Sterne leben (aus astronomischer Sicht) nicht lange, nur wenige Millionen Jahren, aber Sterne kleiner als die Sonne können mehr als zehn Milliarden Jahren alt werden. Kleine Sterne die ganz am Anfang des Universums entstanden sind leuchten immer noch. Diese uralten Sterne sind sehr hilfreich um mehr über das frühe Universum, die erste Sterne und die Geschichte der Milchstraße zu erfahren. Aber wie erkennt man uralte Sterne? Anhand ihrer chemischen Fingerabdrücke! Am Anfang des Universums gab es nur zwei chemische Elemente: Wasserstoff und Helium (und ein klein bisschen Lithium). Alle schwereren Elementen wie zum Beispiel Kohlenstoff, Kalzium und Eisen sind erst später innerhalb von Sternen und in Sternexplosionen entstanden. Je mehr Sternen geboren werden, sich entwickeln und explodieren, desto mehr chemische Elemente gibt es im Universum. Sterne die später entstehen werden mit einer größeren Menge an schweren Elementen, beziehungsweise einer größeren Metallizität, geboren. Im Bereich der Astronomie der sich „Galaktische Archäologie" nennt benutzt man Sterne mit unterschiedlichen Metallizitäten um die Geschichte der Milchstraße zu erforschen. In dieser Doktorarbeit liegt der Fokus auf den metallarmen Sterne, da man erwartet dass diese Sterne am ältesten sind und uns deswegen viel über die frühe Geschichte erzählen können.

Bis heute haben wir noch keinen metallfreien Stern entdeckt, aber die metallärmsten Sterne geben uns wichtige Einblicke in das Leben und Sterben der ersten Sterne. Viele von diesen ältesten, metallärmsten Sternen haben unerwartet viel Kohlenstoff im Vergleich zu zum Beispiel Eisen. Diese kohlenstoffreichen, metallarmen Sterne (CEMP Sterne) erzählen uns etwas über die allerersten Sterne im Universum: sie haben relativ viel Kohlenstoff produziert. Wenn wir uns die genauen chemischen Fingerabdrücke von CEMP Sterne angucken, erzählen sie uns noch viel mehr. Aber unsere Interpretation hängt von der Annahme ab, dass der chemische Fingerabdruck sich während des Lebens eines Sternes nicht geändert hat. In dieser Dissertation werden neue Daten präsentiert die zeigen dass diese Annahme vielleicht zu einfach ist: viele extrem metallarme CEMP Sterne befinden sich in Doppelsternsystemen. Interaktion zwischen zwei Sternen in einem Doppelsternsystem könnte die Oberfläche von CEMP Sternen verschmutzt haben. Zwar wurden die meisten CEMP Sterne höchstwahrscheinlich nicht verschmutzt, aber wir sollten vorsichtig sein mit unserer Interpretation.

Die CEMP Sterne und andere metallarme Sterne sind auch wichtig für unser Verständnis der frühen Geschichte der Milchstraße. Die meisten Forscher, die metallarme Sterne studieren, suchen diese Sterne im Halo der Milchstraße: einer riesigen, diffuse Komponente die ungefähr 1% der Sterne in unserer Galaxie enthält.

Modelle sagen aber vorher dass die *ältesten* metallarmen Sterne sich im Zentrum der Milchstraße befinden (im „Bulge"). Das Zentrum ist leider, wegen großer Mengen Staub zwischen uns und dem Zentrum und einer überwältigenden Mehrheit an metallreichen Sternen, schwierig zu beobachten. Diese Dissertation präsentiert Ergebnisse des „Pristine Inner Galaxy Survey" (PIGS), einer neuen Himmelsdurchmusterung, die die ältesten Sterne im Bulge der Milchstraße sucht (und findet). PIGS benutzt Bilder mit einer Farbe, die für die Metallizität der Sterne empfindlich ist, und kann deswegen sehr effektiv die metallarmen Sterne aus Millionen anderer Sterne auswählen. Von interessanten Kandidaten wurden Spektren aufgenommen und mit zwei unabhängigen Methoden analysiert. Mit dieser Strategie hat PIGS die bislang größte Anzahl an metallarmen Sternen in der inneren Galaxie entdeckt. Ein neues Ergebnis aus den PIGS Daten ist, dass die metallärmeren Sterne langsamer um das Galaktische Zentrum drehen als die metallreichen Sterne, und dass sie mehr willkürliche Bewegung zeigen. Eine zweite wichtige Leistung von PIGS ist die Entdeckung von dutzenden CEMP Sternen in der innere Galaxie, wo vorher nur zwei bekannt waren.

Die neuen Ergebnisse aus dieser Dissertation helfen uns die ersten Sterne und die Geschichte der Milchstraße besser zu verstehen. Laufende und neue Himmelsdurchmusterungen in den nächsten Jahren werden uns noch viel mehr Informationen geben: es ist eine aufregende Zeit für die Galaktische Archäologie.

1 Introduction

> *"In our world," said Eustace, "a star is a huge ball of flaming gas." – "Even in your world, my son, that is not what a star is, but only what it is made of."*
>
> **— C.S. Lewis**
> (in his book The Voyage of the Dawn Treader)

In the beginning of our Universe, none of the chemical elements that we know today existed. The first, and most abundant, element hydrogen (H) began to appear about 10^{-6} seconds after the Big Bang in the form of protons. After a few minutes, the Universe had cooled down enough for protons and neutrons to combine with each other to form the second element: helium. These two elements currently make up roughly 99% of all baryonic matter. Cecilia Payne was the first to suggest that the Sun and other stars consist mainly of hydrogen and helium, contrary to the common picture at the time that stars reflected the composition of the Earth (Payne, 1925). Besides some additional traces of lithium, all elements heavier than hydrogen and helium ("metals" in astronomer language) did not form in the same way right after the Big Bang, as the temperature and density dropped too quickly with the Universe's expansion. The metals were formed later through nuclear fusion in the cores of stars (first suggested by Eddington 1920) and through neutron bombardments of pre-existing heavier elements. These processes have continued to further chemically enrich the Universe since its beginning. This allows us to use the chemical richness (or "metallicity") of stars as a relative time stamp for their birth, assuming their atmospheric composition has not changed significantly over their lifetime (which appears to be a valid assumption for the largest part of the life of most stars). Stars with low metallicities are generally expected to have formed earlier than stars with high metallicities. Low-mass stars can get very old, which means that we can use stars of different metallicities to reconstruct the long history of our home galaxy the Milky Way: this is the goal of Galactic archaeology.

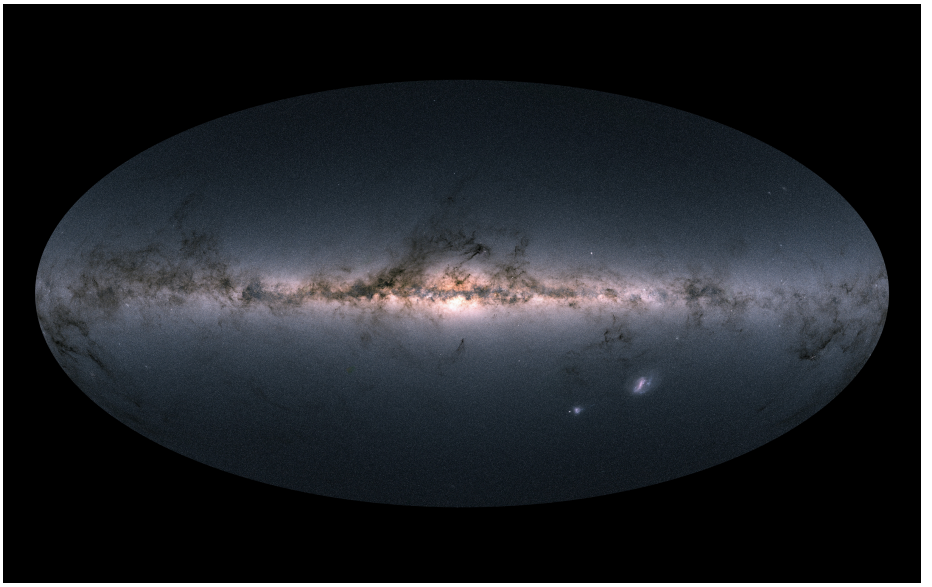

Figure 1.1 — All-sky view of the Milky Way from the *Gaia* satellite (credit: ESA/Gaia/DPAC, CC BY-SA 3.0 IGO).

The Milky Way

The Milky Way (or simply "the Galaxy" with a capital G) is a spiral galaxy containing a few hundred billion stars, our Sun being one of them. About 99% of the stars in the Milky Way are located in a large flat disc or in the inner regions of the Galaxy (Bland-Hawthorn & Gerhard, 2016), these stars show common rotation around the Galactic centre. The remaining 1% of the stars are located in the spheroidal Galactic halo, showing a wide variety of orbital properties that are not aligned with the disc, without significant rotation. An image of the Milky Way from our local perspective within the Galactic disc is shown in Figure 1.1.

That there are (at least) two groups of stars with different velocities in the neighbourhood of the Sun was recognised by Oort (1926), he noted that they seemed to have different properties: the luminous O and B stars had lower velocities and the stars that looked similar to globular cluster stars had higher velocities. This was re-iterated by Baade (1944) who described what seemed to be two types of stars in the Andromeda galaxy (he called them type I and II), with similar photometric properties to the two groups Oort found for the Milky Way. With our current more complete understanding of the Hertzsprung-Russell diagram, stellar evolution and stellar spectroscopy, we now know that Baade's type II stars, those with higher velocities, are generally older and more metal-poor than Baade's type I stars, and that they are part of the Galactic halo. The type I stars appear to be younger, they are moving at a roughly common velocity and are located in the Galactic disc.

What is the origin of these two components, and why is there a difference in stellar ages? The current picture of galaxy formation is a hierarchical one: first

Table 1.1 — Nomenclature for metal-poor stars (Beers & Christlieb, 2005).

[Fe/H]	Term	Acronym
$> +0.5$	Super metal-rich	SMR
~ 0.0	Solar	–
< -1.0	Metal-poor	MP
< -2.0	Very metal-poor	VMP
< -3.0	Extremely metal-poor	EMP
< -4.0	Ultra metal-poor	UMP
< -5.0	Hyper metal-poor	HMP
< -6.0	Mega metal-poor	MMP

smaller systems form, then these galaxies containing dark matter, gas and stars merge with each other to build larger, gas-rich systems. The gas settles into a disc due to friction, whereas the accreted stars do not necessarily form a disc and can have all kinds of orbital properties. New stars start to form in the gas disc, and simultaneously the galaxy keeps accreting more and more smaller galaxies. The stars that were accreted over the history of the Milky Way now form the Galactic stellar halo (although there is accumulating evidence that a significant fraction of the halo actually originates from the kicked-up early disc, e.g. Di Matteo et al. 2019; Belokurov et al. 2019). There is an age and metallicity difference between the halo and the disc because the disc keeps forming stars, whereas the smaller systems that were accreted and now form the halo stopped forming stars at some point when they lost their gas in the past. The oldest, metal-poor stars in the Milky Way are expected to currently reside in the Galactic halo, and in the central regions of the Galaxy: in the Galactic bulge (Diemand et al., 2005; Tumlinson, 2010; Starkenburg et al., 2017a). However, unexpectedly, they are also found in the disc (Sestito et al., 2019), which challenges our understanding of early Galactic evolution.

Metal-poor stars

Since metal-poor stars are typically old and they retain their kinematical and chemical information, studying them allows us to learn about the early history of the Milky Way. It is additionally possible to indirectly learn about the First Stars, by studying the most metal-poor stars we can find in close detail. A recent review on using metal-poor stars for Galactic archaeology (or "near-field cosmology") has been published by Frebel & Norris (2015).

Metal-poor stars come in different flavours, and they are summarised with the commonly-used nomenclature in Table 1.1. The [Fe/H] is used as a metallicity indicator, although it actually represents the iron abundance relative to hydrogen compared to the Sun. The convention to write relative abundances for elements X and Y is as follows: $[\mathrm{X/Y}] = \log(N_\mathrm{X}/N_\mathrm{Y})_* - \log(N_\mathrm{X}/N_\mathrm{Y})_\odot$, where the asterisk subscript refers to the considered star, and N is the number density of each element. Iron is commonly used as an indication of the metallicity, because it scales well with the overall metallicity and its abundance is relatively easy to determine since there

are many iron lines in stellar spectra. The adopted metallicity scale is logarithmic, meaning that a VMP star with [Fe/H] = −2.0 has 1% of the solar metallicity.

What the concept of a "metal-poor" star means depends on the astronomy sub-community and the Galactic environment(s) they study. In Galactic bulge studies, stars with [Fe/H] < −0.5 are considered metal-poor, and sometimes even all stars with sub-solar metallicities ([Fe/H] < 0.0). These stars form the tail of the bulge metallicity distribution function, which peaks at metallicities larger than −0.5. The Galactic halo is much more metal-poor on average, and those studying the halo might consider stars with [Fe/H] < −2.0 metal-poor, because these stars form the low-metallicity tail of the halo. But those interested in using low-metallicity stars for learning about the First Stars typically care about the extremely, ultra, hyper and mega metal-poor stars ([Fe/H] < −3.0). In this thesis, each of these concepts of metal-poor has its place in the different chapters. Chapter 2 studies the binarity properties of a sample of the most metal-poor stars known, Chapter 4 uses a sample of [Fe/H] < −1.0 stars in the Galactic bulge to study the kinematics, Chapter 5 presents the details of this sample and includes a focus on the stars with [Fe/H] < −2.0. These stars at [Fe/H] < −2.0 are discussed in further detail in Chapter 6, where their carbon abundances are investigated.

In this Introduction, I will first discuss the importance of extremely metal-poor stars in the quest for learning about the First Stars. Then I will describe what can be learned about the Milky Way from various kinds of metal-poor stars, after which I will explore what can be learned about the Galactic bulge. Finally I will describe the use of low/medium-resolution spectroscopy in these endeavours. Each section will provide relevant background information for the study of Galactic archaeology with the oldest stars in the Milky Way – the topic of this thesis.

1.1 What can we learn from metal-poor stars about the First Stars?

The very First Stars in the Universe must have been metal-free when they were born a few hundred million years after the Big Bang (Bromm, 2013), since Big Bang nucleosynthesis only produced hydrogen, helium and trace amounts of lithium. The expectation is that these First Stars were very massive, because without metals or dust, only massive clouds of gas can cool enough to start forming stars. Hydrogen and helium have only limited cooling capabilities, but metals are good at cooling gas clouds. The electrons in metal atoms can be easily excited by collisions with other atoms in dense gas regions, and they can radiate away that energy through emitting photons. This cools the gas to lower temperatures, allowing smaller, denser gas clouds with smaller Jeans masses to form, resulting in the formation of smaller stars.

The estimated mass range of the First Stars in the literature has varied significantly over time, where their masses were thought to be higher in earlier years (typically $\gtrsim 100\ M_{\odot}$, see the review from Bromm & Larson 2004) and lower nowadays with more modern simulations ($10 - 100\ M_{\odot}$, see the more recent review from Bromm 2013). None of these stars are low-mass enough to survive until today –

they would have already ended their lives. Recently, simulations are showing that low-mass stars ($< 1 M_{\odot}$) could form in the accretion discs of massive First Stars, but it is unclear whether these are eventually accreted by the massive star or whether they could survive (e.g. Greif et al., 2012; Hirano & Bromm, 2017). Additionally, the results depend on modelling assumptions.

No metal-free star has been observed at this time, although there have been significant efforts searching for the most metal-poor stars in the Milky Way (see e.g. Beers & Christlieb, 2005; Da Costa et al., 2019; Starkenburg et al., 2017b). This lack of metal-free stars in the current surveys puts an upper limit on the number of these stars still present in the Milky Way, if any. Magg et al. (2019) use a simple analytical model to estimate that if there had been any First Star survivors, we should expect to have already found one in the existing surveys. Upcoming large surveys with for example the 4MOST and WEAVE multi-object spectroscopic facilities (de Jong et al., 2019; Dalton et al., 2018) will put even stronger constraints on this number.

1.1.1 Using observations to set constraints on the First Stars

Besides using theoretical predictions and computer simulations to understand the First Stars, we can learn about them from observations of the most metal-poor stars. The supernovae of the First Stars introduced heavy elements into the interstellar medium, which mixed with the pristine gas resulting in slightly metal-enhanced gas clouds. Extremely metal-poor stars likely formed in gas clouds which were enriched by only one First Star, or a small number of First Stars. Assuming that the atmospheric chemical composition of the metal-poor stars has not changed over the course of their lifetime, their chemical abundance patterns reflect the early enrichment of the gas out of which they formed.

Theoretical yields for the supernovae of the First Stars predict variations in the expected abundance patterns of second generation stars, which in each case depends on the properties of the First Star; its mass, its rotation speed, and the explosion energy of its supernova. Frebel & Norris (2015) present an overview of different key elemental ratios that can help distinguish between different properties of the First Stars, for example [C/Fe], [C/N], [Na, Mg, Al/Fe], [α/Fe][1], [Ca/Fe] and [Zn/Fe] (Umeda & Nomoto, 2003; Meynet et al., 2006; Woosley & Weaver, 1995; Heger & Woosley, 2002; Umeda & Nomoto, 2002). Measuring a range of different elemental abundances in second generation stars can therefore teach us about the properties of the First Stars. To get detailed abundance patterns for metal-poor stars, high-resolution, high signal-to-noise spectroscopic observations are necessary. In extremely metal-poor stars, metal lines are typically very weak and excellent data quality is required to be able to make robust line-strength measurements.

The most iron-poor star observed to date has an upper limit on the measurement for iron of [Fe/H] < -7.3 (less than ten millionth of the iron abundance of the Sun), and the only elements measured in this star are lithium, carbon, oxygen, magnesium and calcium (Keller et al., 2014; Nordlander et al., 2017). What is striking about this star is its extremely high carbon abundance: it has 3% of the carbon

[1] α elements are those that can be made out of a multiple of helium-4 nuclei. Elements typically included in [α/Fe] are Mg, Si, Ca and Ti.

abundance of the Sun, which is huge compared to the tiny amount of iron. Most "normal" stars at higher metallicity have [C/Fe] ~ 0, but this star has [C/Fe] > +5.4. And it is not the only one of its kind – of the fourteen known stars with [Fe/H] < −4.5, eleven stars have [C/Fe] $\gtrsim$ +3.0.

A high fraction of carbon-enhanced metal-poor (CEMP) stars is also seen among very and extremely metal-poor stars, which was recognised by Beers et al. (1992) about 30 years ago. Taking [C/Fe] > +1.0 as the CEMP criterium (first defined by Beers & Christlieb, 2005), a CEMP fraction of 27% for very metal-poor stars, 38% for extremely metal-poor stars and 69% for ultra metal-poor stars has been reported by Placco et al. (2014). Of the CEMP stars with [Fe/H] > −3.0, about half appears to be the result of mass-transfer from a former asymptotic giant branch (AGB) binary companion, based on their over-abundance of *s*-process elements[2] and their radial velocity variations (Preston & Sneden, 2001; Lucatello et al., 2005; Starkenburg et al., 2014; Hansen et al., 2016b; Abate et al., 2015). These stars are called CEMP-*s* stars. For the other half of [Fe/H] > −3.0 CEMP stars and almost all of the extremely metal-poor CEMP stars, the large carbon abundance appears to be intrinsic. They do not show the typical *s*-process signature related to mass-transfer, and appear to be mainly single stars (Norris et al., 2013a; Starkenburg et al., 2014; Hansen et al., 2016b). These are the CEMP-no stars. They are a strong indication that some process in the early Universe was functioning differently from today, creating large over-abundances of carbon.

1.1.2 Models of CEMP star origins

There are various potential explanations for the existence of the CEMP-no stars. Second generation stars (which the CEMP-no stars likely are) formed out of pristine gas enriched by the First Stars, so the large carbon over-abundances appear to be telling us about processes in the First Stars and their deaths. Models of normal massive-star supernovae cannot reproduce the abundance patterns of the most metal-poor stars, especially the carbon abundance but also other elemental ratios (e.g. Mg, Al, Zn) (Nomoto et al., 2013).

Mixing-and-fallback supernovae

Umeda & Nomoto (2003, 2005) presented new supernova models for zero/low-metallicity stars with "faint" explosions, which were able to produce a large carbon-to-iron ratio. Faint supernovae do not have enough energy to expel all the stellar material outside of the stellar core, but only remove the outer layers in the explosion while the rest of the material falls back and forms a black hole. The production of elements in massive stars is layered, where the heavier elements are made deeper inside the star. Such a faint explosion would therefore result in the lighter elements (like C, N, O) being expelled while the more massive elements (like Mg, Fe) barely escape, causing the [C/Fe] in the next generation of stars to be high. The CNO elements are produced in the helium-burning layer, when hydrogen is mixed into

[2] *s*-process elements are created in the slow neutron-capture process. AGB stars have a strong production of *s*-process elements at the end of their life.

this layer. Some additional mixing is necessary to expel enough of the heavier elements formed in deep layers (like Zn, Co, Ti), which have been observed in the most metal-poor stars.

These "mixing-and-fallback" supernovae models have been successful in reproducing the abundance patterns of CEMP-no stars and extremely metal-poor stars in general (e.g. Tominaga et al., 2014). A constraint on the masses of the First Stars coming out of abundance pattern fitting with these models is that they were likely not extremely massive: the best-fitting models typically have $\lesssim 40 M_{\odot}$ (Ishigaki et al., 2018).

Spinstars

Another model which successfully reproduces the large carbon abundances among the most metal-poor stars is that of the rapidly rotating massive stars ("spinstars"), first suggested by Meynet et al. (2006). Stars generally lose mass through stellar winds (especially when they rotate quickly), but metal-poor stars do not lose much mass because there are no metals in the atmosphere for the radiation to act upon and the outer layers do not get pushed away. Thus, they do not lose much angular momentum either and they can rotate quickly for most of their lives. This rotation affects the internal mixing inside the star. Additionally, the mixing is extra strong in extremely metal-poor stars due to stronger angular velocity gradients inside the star. In the helium-burning phase of the spinstar, efficient mixing of hydrogen down into the helium-burning layer allows the synthesis of large amounts of CNO. When these elements are dredged up to the surface, the star can start to lose much of its mass through episodes of strong winds because the CNO elements increase the opacity of the outer layers and the radiation can push them away. These strong, carbon-rich winds enrich the surrounding interstellar medium, and if clumps form of wind-material mixed with pristine gas, this is where future CEMP stars can be born (Meynet et al., 2010). A requirement is that there is no supernova event at the end of the life of the massive star that destroys those clumps; either a black hole should form without any supernova, or an anisotropic supernova explosion could happen which leaves some of the clumps to survive. It might also be that if a supernova occurs, further enrichment of some of the clumps happens with other elements – the spinstar scenario can be combined with the mixing-and-fallback scenario above.

1.1.3 3D/NLTE effects on the carbon abundance

A word of caution was published recently by Amarsi et al. (2019) and Norris & Yong (2019) about the fraction of CEMP stars among the most metal-poor stars. Some assumptions made in the analysis of stellar spectra are simplified, which may produce biased results that can be particularly significant in the derivation of the carbon abundance. To quantify the measurement of spectral features, the observed metal lines or molecular bands need to be compared to synthetic spectra. These synthetic spectra are produced from model stellar atmospheres, which are usually created under the assumption that stars are symmetric and can be approximately

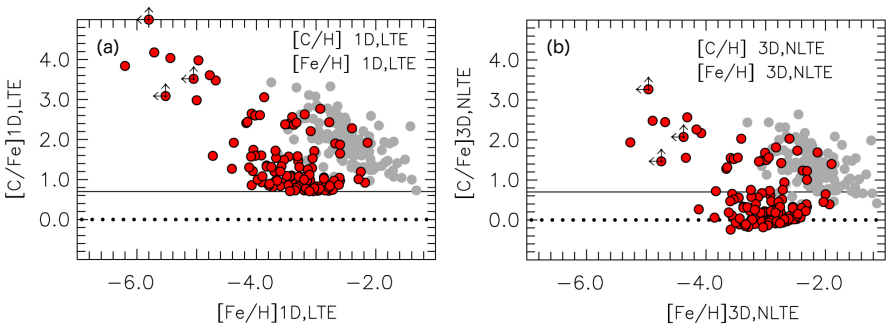

Figure 1.2 — Metallicity versus carbon abundance for a sample of CEMP stars, figure adapted from Norris & Yong (2019). CEMP-*s* stars are shown in grey, CEMP-no stars in red. The Aoki et al. (2007) CEMP criterion at [C/Fe] = +0.7 is indicated with the solid line, and the dotted line is at the Solar ratio. Panel (a) presents the abundances in 1D/LTE, panel (b) includes corrections for 3D and non-LTE effects.

described hydrostatically using one dimension (the radius), and that they are in local thermodynamic equilibrium (LTE). Such 1D/LTE models are relatively successful at producing the correct line-strengths of neutral or ionised atoms (although non-LTE corrections can be significant, especially in metal-poor stars). For molecular features like those of carbon, however, differences between 1D/LTE models and time-dependent 3D models including non-LTE effects can be large (for a review on departure from LTE and 1D, see Asplund, 2005).

The molecular CH features are typically used for the derivation of carbon in metal-poor stars since they are strong and present in most optical spectra, but they are significantly affected by 3D/non-LTE effects. Amarsi et al. (2019) re-analyse a number of high-resolution spectra and determine [C/Fe] from C I lines, and find that even with a 1D/LTE analysis the carbon abundance for three CEMP-no turn-off stars is much lower than their previous literature values. Including 3D and non-LTE effects in their analysis, the total difference with the literature is 0.8-1.0 dex, which places these stars between [C/Fe] = +0.1 and +0.3 – far outside the CEMP category. They also find that the general trend of increasing [C/Fe] with decreasing [Fe/H] almost disappears when adopting the 3D/non-LTE values for their 39 analysed stars between $-3.5 <$ [Fe/H] < -1.0.

Such three-dimensional calculations are extremely expensive, and (currently) cannot be done for all CEMP stars. Norris & Yong (2019) instead extrapolated 3D/non-LTE corrections derived for a number of stars in previous works and apply them to a large sample of CEMP stars collected by Yoon et al. (2016). Their results are summarised in the [Fe/H]–[C/Fe] diagrams in Figure 1.2, where the left-hand side shows the reported literature values and the right-hand side the 3D/non-LTE corrected values. The red circles indicate the CEMP-no stars, the grey circles the CEMP-*s* stars (assumed to be the result of mass-transfer from a former AGB binary companion), and the solid line indicates [C/Fe] = +0.7 (the CEMP criterion of Aoki et al. 2007). It is clear that many of the CEMP-no stars move outside the CEMP

region after the 3D/non-LTE corrections. Most of the ultra metal-poor stars with [Fe/H] < -4.0, however, are still clearly carbon-enhanced.

The implications of these preliminary 3D/non-LTE results, on for example First Star supernova-yield fitting and early chemical evolution, have not yet been fully explored. The ultra metal-poor carbon-enhanced stars are an indication that processes which produce large amounts of carbon are still necessary, but if the 3D/non-LTE effects are truly as large as in Figure 1.2, the prevalence of CEMP-no stars above [Fe/H] > -4.0 is unclear.

1.1.4 Contribution of this thesis to the field

There are still many open questions regarding CEMP stars, and their relation to the First Stars. The results presented in Chapter 2 contribute to the discussion in the literature and revive the question whether all of the currently claimed intrinsic CEMP-no stars were really born with their large carbon abundance, or whether some of them could have been influenced by binary mass-transfer from a former AGB companion. It reports that CEMP-no stars with very high [C/Fe] (which likely remain carbon-enhanced even after 3D/non-LTE corrections) appear to have a larger binary fraction than the other, less carbon-rich, CEMP-no stars (which might not be carbon-enhanced at all, according to the discussion above). Although being in a binary system does not mean a star has undergone mass-transfer, the possibility cannot be excluded. One important discovery is that the hyper metal-poor carbon-rich star HE 0107−5240 is in a binary system – this is currently the lowest metallicity binary star known, and there is a possibility that its abundance pattern was influenced by a companion star. The paper constituting Chapter 2 has been cited regularly since its publication, which is an indication of the importance of the results.

Additionally, in Chapter 6, the first ever sample of tens of CEMP stars in the inner Galaxy is presented, twenty of which are likely CEMP-no stars. Only one CEMP-no star was known in this region of the Milky Way previously, and there were suggestions that the carbon-enhanced fraction of metal-poor stars is lower in the inner Galaxy than in the Galactic halo (Howes et al., 2015, 2016). The preliminary results from the *Pristine* Inner Galaxy Survey presented in Chapter 6 suggest that the CEMP-no fraction could be compatible with the halo, but the fraction of CEMP-s stars is significantly lower. The latter is possibly a selection effect of the survey. The new CEMP-no stars are very interesting targets for high-resolution spectroscopic follow-up, as they likely contain clues about the First Stars in the inner Galaxy building blocks.

1.2 Galactic archaeology with pristine stars

Metal-poor stars cannot only provide a wealth of information about the First Stars, they are also extremely useful probes of (early) Galactic evolution. The metallicity of stars is not perfectly correlated with age because it also depends on the environment where the star formed. However, because stellar ages are difficult to

determine (especially for large numbers of stars), the metallicity is the best available representative. We want to know how the Milky Way formed, and the oldest/metal-poor stars can provide insights into the earliest times. The combination of the kinematics and the chemistry of metal-poor stars is a powerful tool for near-field cosmology/Galactic archaeology, as reviewed by Freeman & Bland-Hawthorn (2002) and Frebel & Norris (2015).

1.2.1 How to find metal-poor stars

If one would pick a random star in a field towards the Galactic halo, it will most likely not be extremely metal-poor: Youakim et al. (2017) estimate that only 1 out of 800 stars in a magnitude range of $14 < V < 18$ would have [Fe/H] < -3.0. To build large samples of the most metal-poor stars for doing Galactic archaeology, a more efficient method compared to randomly selecting stars should therefore be employed. One possibility is to make a kinematic selection of halo stars, which are likely more metal-poor than disc stars. This method resulted in the discovery of the first extremely metal-poor star (G 64-12, Carney & Peterson, 1981), however, the yields of such surveys were small.

The first large samples of very metal-poor stars came from objective-prism methods. The HK survey was the main source of very metal-poor stars for many years (Beers et al., 1985, 1992), using very low resolution prism spectra to identify stars with weak Ca II H & K lines (by eye!) which were then followed up with higher resolution spectroscopy. The strength of the Ca H&K lines is expected to scale with the iron abundance of a star, in general. A similar technique was used in the Hamburg/ESO (HES) survey (but automated), which yielded many more very and extremely metal-poor stars because it went two magnitudes deeper than the HK survey and because it covered the entire Southern sky (Christlieb et al., 2008). Several of the most iron-poor stars to date were found through HES, for example the famous HE 0107–5240 (Christlieb et al., 2002) and HE 1327–2326 (Frebel et al., 2005) which both have [Fe/H] < -5.0 and [C/Fe] $> +3.5$.

Alternative sources of the most metal-poor stars are very large spectroscopic surveys, which will have some of these stars "by accident". The Sloan Digital Sky Survey (SDSS) has been a rich source, allowing for the discovery of the first carbon-normal ultra metal-poor star by Caffau et al. (2011) and several hyper metal-poor stars (Aguado et al., 2018, 2019). Not only did the aforementioned surveys result in the discovery of some of the most metal-poor stars, they also produce large samples of stars with [Fe/H] < -2.0 which are very useful for Galactic archaeology. For example, Li et al. (2018) recently published a sample of several thousand very metal-poor stars identified in the Large Sky Area Multi-Object Fibre Spectroscopic Telescope (LAMOST) survey.

1.2.2 Photometric surveys

In recent years, the preselection of metal-poor stars based on narrow-band photometry in the Ca H&K region (combined with broad-band photometry) has become very successful. The SkyMapper survey of the Southern hemisphere includes

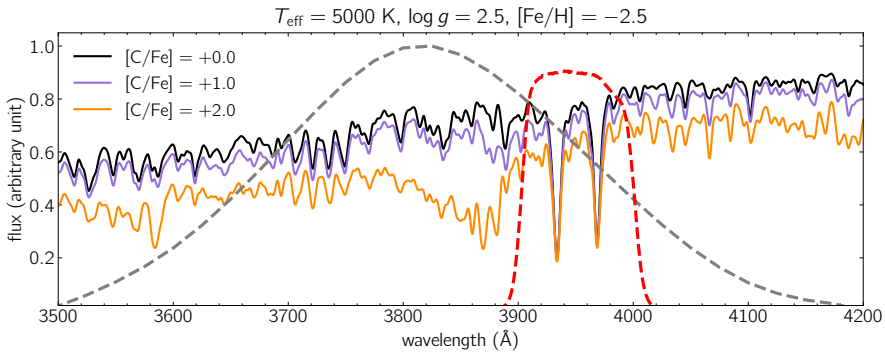

Figure 1.3 — Synthetic spectra of a carbon-normal and two carbon-enhanced very metal-poor giant stars, with the Pristine *CaHK* filter (red) and SkyMapper v filter (grey) over-plotted. [C/N] is assumed to be −0.5, [C/O] +0.5, more details are discussed in Chapter 6.

observations in the v-filter, a narrow-band filter that is sensitive to metallicity due to presence of the strong Ca H&K lines in its short wavelength coverage (Wolf et al., 2018). Because the strength of the Ca H&K lines is also highly dependent on the temperature of a star, the narrow-band photometry should be combined with broad-band photometry for an estimate of the temperature. Using this technique, the SkyMapper team has found the two most iron-poor stars to date with [Fe/H] < −7.3 and [Fe/H] = −6.2 (Keller et al., 2014; Nordlander et al., 2019), and ∼ 2500 very metal-poor stars (Da Costa et al., 2019). The SkyMapper photometry is also powerful either by itself or combined with *Gaia* astrometric and/or radial velocity information (see e.g. Casagrande et al., 2019; Sahlholdt et al., 2019, who use the photometry to produce stellar parameters for millions of stars, or use them to study the origin of the Galactic halo).

The source of metal-poor stars that plays a central role in this thesis is the Northern hemisphere *Pristine* survey (Starkenburg et al., 2017b) at the Canada-France-Hawaii Telescope (CFHT). *Pristine* employs a similar technique to the SkyMapper survey, but with an even narrower filter centred on the Ca H&K lines. It does not have its own broad-band photometry, therefore is matched to existing surveys like SDSS or *Gaia*. The coverage of both narrow-band filters is shown in Figure 1.3. The large feature between 3800 − 3900 Å is the result of the CN molecule: this likely causes the SkyMapper selection to be biased against carbon-rich stars in some temperature and metallicity ranges (Da Costa et al., 2019). The expectation was that because the *Pristine* filter does not include this band, it is not biased against carbon-rich stars. However, the continuum is affected and there are still some CH lines that fall within the *CaHK* range. Additionally, the broad-band photometry with which the *Pristine* photometry is combined is affected by carbon features as well. The first investigation of the carbon-sensitivity of the *CaHK* filter is discussed in Chapter 6; it is very relevant for the determination of CEMP fractions.

Some highlights of the *Pristine* survey, many of which the author of this thesis has contributed to, are discussed in the next sub-section. While the focus of this

section is on results from the *Pristine* survey, several other recent works in the (currently booming) field of Galactic archaeology are also briefly described.

1.2.3 Recent metal-poor Milky Way results

For the past five years the *Pristine* survey has been gathering CFHT MegaCam *CaHK* photometry in the Northern hemisphere, building up to the current main survey footprint of > 5000 deg^2 (which is still growing). Low/medium-resolution spectroscopic follow-up of promising candidates has been ongoing for most of these years, resulting in a sample of ~ 700 confirmed new VMP stars and ~ 100 confirmed new EMP stars (Aguado et al., 2019). Youakim et al. (2017) used the spectroscopic follow-up to estimate success rates of the photometric selection, which was updated with a larger sample in Aguado et al. (2019) to a success rate of 56% for stars with [Fe/H] < −2.5 and 23% for stars with [Fe/H] < −3.0. The SkyMapper survey published similar success rates (Da Costa et al., 2019). These success rates for preselecting the most metal-poor stars are unprecedented in the literature.

The Galactic halo

Youakim et al. (2020) used the spectroscopic *Pristine* sample to re-calibrate the photometric metallicities to investigate the metal-poor tail of the metallicity distribution function (MDF) of the Galactic halo. The MDF of the halo tells us something about its formation – the assumption is that most of the halo formed hierarchically from smaller systems (building blocks), and information about what kind of building blocks were involved is contained in the halo metallicity distribution. Small systems are typically more metal-poor, whereas larger building blocks contributed more metal-rich stars to the halo. With the second data release (DR2) of *Gaia* (Gaia Collaboration et al., 2016, 2018) it has become clear that a large fraction of the halo appears to be the remainder from one large building block, which has been given the name *Gaia*-Enceladus or the *Gaia*-Sausage (Helmi et al., 2018; Belokurov et al., 2018), and another large fraction of the halo might be the result of either the kicked-up Galactic disc or a relatively metal-rich in-situ halo population (Di Matteo et al., 2019; Gallart et al., 2019; Belokurov et al., 2019; Sahlholdt et al., 2019).

The very metal-poor tail of the MDF (the result of smaller building blocks) has not been very well studied. Previously published MDFs are typically based on spectroscopic samples, which are limited in size and are plagued by selection effects (Schörck et al., 2009; Allende Prieto et al., 2014). Using the *Pristine* photometric metallicities, Youakim et al. (2020) were able to use many more stars with a less complicated selection function to study the metal-poor tail of the halo MDF. They concluded that there may be more very metal-poor stars in the halo than expected previously, and that if globular clusters follow the same metallicity distribution as the halo, the lack of globular clusters with [Fe/H] < −2.5 has a physical reason and is not just due to small number statistics.

Kinematics of very metal-poor stars

With the advent of the *Gaia* DR2 astrometric data, it has become possible to investigate the orbital properties of many individual stars. For the most metal-poor stars, the expectation was that they would all be on "typical" halo orbits – relatively radial orbits with more or less random orbital inclinations with respect to the Galactic plane, without a preference for direction of rotation around the Galactic centre. This fits the scenario where these stars were accreted as part of the smallest dwarf galaxies at early epochs. Sestito et al. (2019) derived orbits for the 42 known stars with [Fe/H] < -4.0, using *Gaia* DR2 astrometry and photometry combined with radial velocities from the literature. They find that roughly a quarter of these stars do not follow the expectation of typical halo orbits; instead, they all orbit in the same direction as the Galactic disc (prograde) and stay within only 3 kpc of the Galactic plane.

Repeating the analysis for a much larger sample of very metal-poor stars from the *Pristine* and LAMOST surveys, Sestito et al. (2020) find that $\sim$ 30% of the [Fe/H] < -2.5 stars that are currently within 3 kpc from the Galactic plane stay within that plane throughout their (usually prograde) orbit. There are different possible scenarios that could explain these observations. It could be that these VMP stars came into the Milky Way inside small building blocks which deposited their stars close to the plane, and in time, the orbits of these stars became more disc-like due to dynamical effects. It is also possible that they were part of the bigger building blocks that formed the early disc of the Milky Way, or that they formed inside the disc. In any case, the orbital properties of the most metal-poor stars currently challenge our understanding of the assembly and evolution of the Milky Way.

The combination of kinematics and chemistry for very metal-poor stars is a very powerful tool for Galactic archaeology. Venn et al. (2020) derive abundances from high-resolution spectroscopy for a sample of bright stars selected as part of the *Pristine* survey, and analyse their orbits. Some of the very metal-poor stars show unusual kinematic properties given their chemical composition, for example having disc-like kinematics or orbits that take them deep into the Galactic bulge. They also identified a number of metal-poor stars consistent with the *Gaia*-Enceladus/Sausage accretion event, which aids the investigation of the early chemical evolution inside this large Milky Way halo building block.

Other recent chemo-dynamical studies have hinted at the fact that there may be an additional large merger event contributing to the Galactic halo dubbed the Sequoia, which is more metal-poor than the *Gaia*-Enceladus/Sausage event (Mackereth et al., 2019; Matsuno et al., 2019; Myeong et al., 2019). The Sequoia stars have a large retrograde motion, and are distinct in their α-abundances, indicating they came from a different progenitor. However, the numbers of stars (especially at the very metal-poor end) used in these analyses are small, and larger spectroscopic samples of metal-poor stars are necessary for a better characterisation.

Metal-poor stars in the Galactic bulge

Most studies of very metal-poor stars have mainly focused on the Galactic halo, for good reasons. It is on average the most metal-poor component of the Milky Way,

and it can be targeted relatively easily by selecting regions in the sky avoiding the Galactic plane. It is however not the only location of metal-poor stars; simulations predict that some of the oldest metal-poor stars are currently located in the area of the Galactic bulge. The SkyMapper EMBLA survey has targeted the bulge, and uncovered a handful of extremely metal-poor stars in that region (Howes et al., 2015, 2016). Some of their stars have very tight orbits that stay within the Galactic bulge, which is an indication that these are likely some of the oldest stars known.

1.2.4 Contribution of this thesis to the field

All published large samples of very metal-poor stars are mainly in the (local) halo of the Milky Way. However, the halo has its highest density towards the centre and the metal-poor stars there are likely to be older/accreted earlier on; it is therefore crucial to look for VMP stars in the inner Galaxy. This is a challenging undertaking due to the high density of (mainly metal-rich) stars, the large dust extinction and the disc foreground. If an efficient selection method for finding the most metal-poor stars in the halo is necessary, it is even more so the case in the Galactic bulge.

With such good success rates in the halo, the *Pristine* selection using *CaHK* photometry is a promising method for finding large samples of VMP stars in the inner Galaxy. This thesis contains the description and results of the successful *Pristine* Inner Galaxy Survey (PIGS). The survey strategy and the photometric and spectroscopic observations and analysis are described in Chapter 5. It also presents the largest sample of VMP stars in the inner Galaxy to date ($\sim$ 1300 stars), and shows that PIGS has an unprecedented selection efficiency of VMP stars in the bulge region. A closer investigation of this sample of new VMP stars will reveal insights into the early build-up of the inner Galaxy.

An investigation of the first sample of inner Galaxy CEMP stars from PIGS is discussed in Chapter 6 (as summarised earlier in the Introduction), which includes the first investigation of possible biases against carbon-rich stars in the *Pristine* selection. The kinematics of metal-poor inner Galaxy stars is the topic of Chapter 4, which will be summarised and put into context in the next section of the Introduction.

1.3 The Galactic bulge

As alluded to in the previous section, the Galactic bulge is a privileged location to look for metal-poor stars. In this section we therefore discuss this Galactic component in more detail. In the image of the Milky Way in Figure 1.1, the bulge clearly protrudes out of the disc in the centre of the Galaxy. Baade (1946) pointed out that most stars in this region seem to be of type II and that they are distinct from stars in other regions of the Milky Way disc. The Galactic bulge stars appear to be older than the disc, and more similar in age to halo stars (e.g. Ortolani et al. 1995). The origin of the bulge has been a topic of discussion for decades, where multiple formation scenarios have been proposed. The bulge could be made up of accreted stars and be like a more concentrated version of the halo (or simply

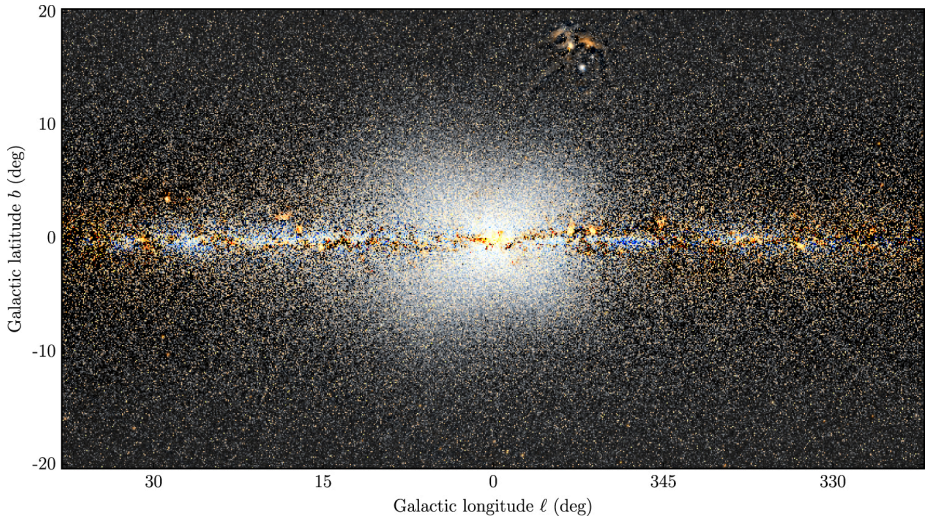

Figure 1.4 — WISE photometry from the $W1$ and $W2$ bands in Galactic coordinates towards the bulge. In this image, the median of each row of the image has been subtracted for contrast. Image from Ness & Lang (2016).

the extension of the halo); it could have formed very early on as the result of the collapse of a large gas cloud (or multiple collapse events) in the centre of the Milky Way; or it could have formed from the disc which is currently vertically extended in the centre due to dynamical processes. The first two scenarios are related to "classical" bulges, which are more spheroidal in shape, whereas the latter can be described as a "pseudo"-bulge, or a "boxy/peanut (B/P)"-shaped bulge. Pseudo-bulges and classical bulges differ from each other in their structure, the kinematics of their stars, and in the chemical properties of their stellar populations. Both types of bulges have been observed in external galaxies, but the difficulty with our own bulge is that we observe it from our obstructed view point from within the Galactic disc. There have been many Galactic bulge studies in the past ~30 years which have produced a significant amount of data, and combined with theoretical models, we are finally able to determine which of the different formation models is supported better. A recent review on the Galactic bulge can be found in Barbuy et al. (2018), and some of the key points are summarised here.

1.3.1 Evidence for a pseudo-bulge in the Milky Way

Important evidence that the Galactic bulge is not spheroidal in shape came from photometry and star counts towards the inner Galaxy. COBE photometry showed clear evidence that there was a difference in size and brightness of the bulge between positive and negative Galactic longitudes (Weiland et al., 1994), and using standard candle red clump (RC) stars Stanek et al. (1994) showed that the bulge stars at positive longitude are closer to us than those at negative longitudes. Later studies using RC star counts found that the brightness of RC stars has two peaks along the

minor axis of the bulge, which has been interpreted as two populations of RC stars at different distances, indicative of an X-shape in the bulge (e.g. Nataf et al., 2010; McWilliam & Zoccali, 2010). Photometry from WISE reveals both the asymmetry and the X-shape structure in the bulge, see Figure 1.4 (Ness & Lang, 2016). Each of these observations points to the Milky Way having a strong pseudo-bulge.

Additional evidence for a non-classical bulge comes from large spectroscopic surveys, using radial velocities for thousands of stars to trace their kinematics. For example, the Bulge Radial Velocity Assay of red giants (BRAVA, Howard et al., 2008; Kunder et al., 2012) and the Abundances and Radial velocity Galactic Origins Survey of RC stars (ARGOS, Ness et al., 2013b) found that the bulge is a cylindrically rotating system: stars up to a latitude of 10 degrees rotate with the same velocity around the Galactic centre, independent of latitude. Additionally, the velocity dispersion increases strongly with decreasing latitude. These observations are consistent with the bulge of the Milky Way originating from the Galactic disc, being currently shaped like a puffed-up, boxy bar. Modelling of the BRAVA data by Shen et al. (2010) shows that the observed kinematics can be reproduced well by pure bar models, and that there is little room for a massive classical bulge component because those models have too high velocity dispersions.

There were some observations pointing towards a possible classical origin of (part of) the bulge, for example an observed metallicity gradient with Galactic latitude where the outer regions are more metal-poor (e.g. Zoccali et al., 2008). Such a gradient is expected in a classical bulge, but seemed inconsistent with a scenario where the bulge solely resulted from vertical heating of a bar. However, recent models of bulge formation find that it is also possible to reproduce the apparent metallicity gradient in a pure-disc origin of the bulge, if the velocity dispersion of the disc at the time of bar formation varied with metallicity (Di Matteo, 2016; Debattista et al., 2017; Fragkoudi et al., 2018).

There are some who have questioned the X-shape-interpretation of the double red clump, arguing that a double red clump could also be the signature of two populations of red clump stars with different helium abundances (Lee et al., 2015, 2018). Globular clusters are known to show double red clumps for this reason, and such a dual population in the bulge could be the result of the disruption of many globular clusters. Their model proposes a classical bulge (mainly made of disrupted globular clusters) with two red chemically different clump populations, on top of a bar. However, Sanders et al. (2019) have recently shown that the two red clumps have different kinematical signatures in their *Gaia* DR2 proper motions – this would not be expected if it is a population effect, but does fit with the interpretation of two red clumps at different distances.

The general consensus today appears to be that the Galactic bulge is almost purely a pseudo-bulge, originating from an instability in the ancient Galactic disc that produced a puffed-up, buckled bar. The chemistry of bulge stars is similar to that of local thick disc stars, which additionally supports this hypothesis (see the many references in Barbuy et al., 2018).

1.3.2 Different metallicity populations in the bulge

The majority of the stars in the Galactic bulge are relatively metal-rich. Barbuy et al. (2018) present an overview of the metallicity distribution functions (MDFs) from twelve different papers studying the bulge spectroscopically. All samples almost exclusively contain stars with metallicities larger than 10% of the solar metallicity ([Fe/H] > -1.0), and all have multiple peaks in the MDF (although they do not agree on the number and the location of those peaks).

There are several indications that there are differences in the behaviour of stars of different metallicities. For example, Ness et al. (2013b) found that in the ARGOS data, all populations of stars with [Fe/H] > -1.0 rotate cylindrically, although the velocity dispersion of the more metal-rich stars is smaller than that of the more metal-poor stars. The population of stars with [Fe/H] < -1.0 showed slower rotation, but there are not many such stars in the ARGOS data. Using APOGEE and ARGOS data, Portail et al. (2017) make chemo-dynamical models of the bulge and find that the stellar populations with super-solar metallicities and with metallicities between $-0.5 <$ [Fe/H] < 0.0 are strongly bar-shaped, but the more metal-poor populations of stars are exceedingly less bar-shaped, more vertically extended and strongly centrally concentrated. The authors note that the number of stars with [Fe/H] < -1.0 is small and more data is needed to draw stronger conclusions about the nature of this population – whether these stars could come from the extension of the thick disc, the centre of the Galactic halo and/or a classical bulge.

A common theme appears that if there is a (small) classical bulge component present in the Milky Way, it might be hiding at metallicities lower than where most typical bulge surveys reach. Dedicated surveys for metal-poor stars in the inner Galaxy have focused on RR Lyrae stars – old, metal-poor stars that are relatively easy to select due to their typical variable light curves. They have the additional advantage that they are standard candles, their distances can be derived with high precision. Using data from the photometric, multi-epoch VVV and OGLE surveys, Dékány et al. (2013) and Pietrukowicz et al. (2015), respectively, selected large samples of RR Lyrae stars in the bulge. Both teams found the RR Lyrae to be centrally concentrated, although the OGLE team found the population to be bar shaped and the VVV team found that they have a spheroidal shape. Kunder et al. (2016) used the radial velocities of a sample of RR Lyrae stars to study their rotation around the Galactic centre, and they found no significant rotation which they interpreted as the signature of a present (small) classical bulge. However, these stars could also be part of the inner extension of the Galactic halo even if they had a small amount of rotation, as discussed in Pérez-Villegas et al. (2017).

1.3.3 Contribution of this thesis to the field

Clearly larger samples of low-metallicity stars in the bulge region are necessary to resolve some of the open questions regarding the nature of the metal-poor inner Galaxy. This thesis contributes significantly to the number of known metal-poor stars in the inner Galaxy ($\sim$ 6000 stars with [Fe/H] < -1.0), which is presented in Chapter 5, including a number of horizontal branch stars which are metal-poor standard candles. It also includes the first study of the inner Galaxy kinematics as a

function of metallicity for stars with [Fe/H] < -1.0 in Chapter 4. This chapter shows, for the first time, that the rotational velocity around the Galactic centre decreases for more metal-poor stars, and that the very metal-poor stars do not appear to rotate at all. At the same time, the velocity dispersion increases strongly with decreasing metallicity. These observations provide important constraints to inner Milky Way models.

1.4 Low/medium-resolution spectroscopy

Almost all of the results described in previous sections have, at one point or another, involved the use of low/medium-resolution (L/MR) spectroscopic observations. Here, L/MR is used to indicate a resolving power $R = \lambda/\Delta\lambda \sim 1\,000-10\,000$, where $\Delta\lambda$ is the full width at half maximum of the line-spread function. L/MR spectroscopic observations are commonly used to determine the stellar atmospheric parameters of stars, typically the effective temperature $T_{\rm eff}$, surface gravity $\log g$ and metallicity [Fe/H] (and sometimes other chemical abundances), and their radial velocities. This information is crucial for chemo-dynamical studies, where especially metallicities and radial velocities (and where possible, other abundances) for large numbers of stars are key ingredients. L/MR spectra are also useful for example for the confirmation of the extremely metal-poor nature of a star from a preselection method, or to get an estimate of the carbon-enhancement of stars since strong carbon features are present even in low-resolution spectra. Naturally, it would be ideal to have high-resolution spectroscopic observations which contain more information for any star, but high-resolution spectroscopy is very expensive in terms of telescope time and it is therefore difficult to create large samples. To summarise, L/MR spectroscopy is an important tool in Galactic archaeology, which can determine multiple useful parameters at a relatively low cost.

Two key regions used in L/MR spectroscopy are the infrared calcium triplet region (between $\sim 8400-8800$ Å) observed at medium resolution, and the optical/infrared (between $\sim 3800-9000$ Å). The former is particularly useful for the derivation of stellar radial velocities because there are three strong calcium lines close together, which are present in almost all types of stars. It can also be used for the derivation of stellar parameters and even chemical abundances of a few elements, although there are some degeneracies (see e.g. the results from the RAdial Velocity Experiment RAVE and the ARGOS survey, Steinmetz et al., 2020a,b; Freeman et al., 2013). The optical range can be used at lower resolution and is sensitive to the basic stellar parameters $T_{\rm eff}$, $\log g$ and [Fe/H], as well as to for example the carbon and α-abundances. It has been observed in many large spectroscopic surveys (for example SDSS and LAMOST, Yanny et al., 2009; Deng et al., 2012), including surveys targeting the lowest metallicity stars (for example in *Pristine*, Aguado et al., 2019).

1.4.1 Spectral analysis

Analysing spectra is a complex task, where the results often strongly depend on the methods used and assumptions adopted. This became particularly clear in

the efforts of the *Gaia*-ESO survey who used > 20 different methods from different groups to analyse high-resolution spectra of FGK stars, in the hope of producing the best stellar parameters (Smiljanic et al., 2014). They found that there were significant differences between the many methods (larger than the provided uncertainties from the various analyses), and a homogenisation was very challenging. This indicates that there are often hidden systematic biases playing a role. Despite these biases, however, spectroscopic analyses are extremely useful and they are typically trusted to a high degree.

The analysis of L/MR spectra often makes use of full-spectrum fitting methods, especially at lower resolution where individual spectral lines are typically blended. The advantage of full-spectrum fitting is that it uses as much information from the spectra as possible, compared to only using selected features. There are a large number of full-spectrum fitting codes available in the literature employing many different approaches. One of the main choices is which reference spectral library to use.

Many approaches rely on the usage of synthetic spectral libraries. These have the advantage that they are regular and noise-less, that they can be made at any resolution and for any wavelength range, and that they cover as much of the parameter space as desired. However, they are limited by both computational power and our incomplete theoretical knowledge. Examples of codes that rely on synthetic libraries are MATISSE (MATrix Inversion for Spectral SynthEsis, Recio-Blanco et al., 2006) which uses a projection method inspired on principal component analysis, and FERRE (Allende Prieto et al., 2006) which is a χ^2 minimisation code that interpolates in a model grid.

Another option is to use data-driven methods which have the advantage that they use real spectra and can represent observed spectra very well. They are, however, limited in their coverage of the parameter space, causing the results to strongly depend on the set of stars the model was trained on. Examples of data-driven methods are ULySS (University of Lyon Spectroscopic Software, Koleva et al., 2009) which is a a χ^2 minimisation method using model interpolators created from empirical spectral libraries, and The Cannon (Ness et al., 2015) which is trained on a set of stars with stellar parameters known from elsewhere that are observed with the same instrument.

1.4.2 Contribution of this thesis to the field

Each spectral analysis method has its own strengths and weaknesses, and the method of choice often depends on the scientific question of interest. This thesis contains different L/MR spectral analysis approaches. Chapter 3 is dedicated to the determination of stellar atmospheric parameters for the recent empirical X-shooter Spectral Library (XSL). This medium-resolution spectral library has been created mainly to be used in stellar population analysis, for which a homogeneous library of stellar spectra with homogeneously derived stellar parameters is crucial. The chapter contains a robust determination of the stellar parameters and their uncertainties for a large variety of stars in XSL (covering a wide range in $T_{\rm eff}$, $\log g$ and [Fe/H]), using the data-driven ULySS method. XSL itself will also be a valuable resource for

the stellar community, allowing for a homogeneous comparison between observed and synthetic spectra across a huge wavelength range (from the UV to the infrared).

In Chapter 5, several thousand L/MR optical and infrared calcium triplet spectra from the *Pristine* Inner Galaxy Survey are analysed with two independent methods: one data-driven (ULySS) and one using a synthetic model grid (FERRE). The comparison between the two methods is a powerful tool for determining realistic uncertainties on the stellar atmospheric parameters and identifying reliable regions of the parameter space. The advantage of using a synthetic library for the PIGS analysis is that it includes stars down to the lowest metallicities which are missing from empirical libraries, and that it is possible to vary additional parameters – in this case the carbon abundance, which is particularly interesting for metal-poor stars.

1.5 Thesis overview

In summary, this thesis aims to provide significant contributions to the study of the First Stars, to Galactic archaeology with (very) metal-poor stars, and to the study of the ancient inner Galaxy; employing low/medium-resolution spectroscopy as one of the main tools. The overarching theme is that of using the oldest stars in the Milky Way to learn about the ancient history of our Galaxy and the conditions in the early Universe.

Chapters 2, 3, 4 and 5 have been published as Arentsen et al. (2019a), Arentsen et al. (2019b), Arentsen et al. (2020a) and Arentsen et al. (2020b), respectively. Only their format has been changed to fit the thesis. Chapter 6 is a paper in an advanced stage of preparation, and will be submitted to MNRAS at a later point in time.

2 Binarity in CEMP-no stars: an indication of multiple formation pathways?

A. Arentsen, E. Starkenburg, M. D. Shetrone, K. A. Venn, É. Depagne, A. W. McConnachie

ABSTRACT

Carbon-enhanced metal-poor (CEMP) stars comprise a high percentage of stars at the lowest metallicities. The stars in the CEMP-no subcategory do not show any *s*-process enhancement and therefore cannot easily be explained by transfer of carbon and *s*-process elements from a binary AGB companion. We have performed radial velocity monitoring of a sample of 22 CEMP-no stars to further study the role that binarity plays in this type of CEMP star. We find four new binary CEMP-no stars based on their radial velocity variations; this significantly enlarges the population of known binaries to a total of 11. One of the new stars found to be in a binary system is HE 0107–5240, which is one of the most iron-poor stars known. This supports the binary transfer model for the origin of the abundance pattern of this star. We find a difference in binary fraction in our sample that depends on the absolute carbon abundance, with a binary fraction of 47^{+15}_{-14}% for stars with a higher absolute carbon abundance and 18^{+14}_{-9}% for stars with a lower absolute carbon abundance. This might imply a relation between a high carbon abundance and the binarity of a metal-poor star. Although binarity does not equate to mass transfer, there is a possibility that a CEMP-no star in a binary system has been polluted, and care has to be taken in the interpretation of their abundance patterns. We furthermore demonstrate the potential of Gaia of discovering additional binary candidates.

2.1 Introduction

To study the earliest times in the Universe, we do not have to go to high redshift. Our Milky Way still hosts remnants from these early times in the form of extremely metal-poor stars that are expected to be almost as old as the Universe, and we can study them in detail. At the lowest metallicities, the fraction of stars enhanced in carbon increases dramatically (Beers et al. 1992; Norris et al. 1997). These carbon-enhanced metal-poor (CEMP) stars comprise 15 – 20% of the very metal-poor stars ([Fe/H][1] < −2.0), which increases to ∼ 40% for extremely metal-poor stars ([Fe/H] < −3.0) and even higher percentages at lower metallicities (Yong et al. 2013a; Lee et al. 2013; Placco et al. 2014).

Different types of CEMP stars have initially been defined by Beers & Christlieb (2005). The two main classes are CEMP-*s* stars, which show additional enhancement in s-process elements (with [C/Fe] > +0.7 and [Ba/Fe] > +1.0), and the CEMP-no stars, which do not show any s-process enhancement and usually occur at lower metallicities (with [C/Fe] > +0.7 and [Ba/Fe] < 0.0). A subclass of the CEMP-*s* stars are the CEMP-*r*/*s* stars, which are additionally enhanced in r-process elements. It was reported by Spite et al. (2013) that CEMP stars seemed to occupy two bands in absolute carbon versus metallicity space. The more metal-rich CEMP stars have higher absolute carbon clustering around an absolute carbon abundance A(C)[2] ∼ 8.25, and they turned out to be mainly CEMP-*s* stars, whereas the more metal-poor CEMP stars are located at a lower A(C) ∼ 6.5, and they are mainly CEMP-no stars. Larger samples of CEMP stars have confirmed this trend (e.g. Bonifacio et al. 2015; Hansen et al. 2015), although there are always some outliers.

Through radial velocity monitoring, it was found that the CEMP-*s* stars are almost always in a binary system (e.g. McClure & Woodsworth 1990; Preston & Sneden 2001; Lucatello et al. 2005; Hansen et al. 2016b), while the CEMP-no stars more often appear to be single stars (Norris et al. 2013b; Starkenburg et al. 2014; Hansen et al. 2016a, afterwards S14 and H16a). CEMP-*s* stars are thought to have received their carbon and s-process elements through mass-transfer from an evolved companion that has gone through the asymptotic giant branch (AGB) phase (Abate et al., 2015).

The exact origin of the CEMP-no stars is not yet clear. CEMP-no stars are not generally considered to be in binary systems, but the data indicate that at least some of them are: ∼ 17% of the sample in H16a. This is close to the binary frequency of 16% ± 4% found by Carney et al. (2003) for 91 carbon-normal metal-poor ([Fe/H] ≤ −1.4) field red giants. Since most of the CEMP-no stars do not have a binary companion, it is often assumed that the carbon abundance in these stars is intrinsic and therefore reflects the composition of the gas out of which they are formed. The 13 stars with the lowest known metallicities ([Fe/H] < −4.5) are all CEMP stars, with two exceptions from Caffau et al. (2011) and (likely) Starkenburg et al. (2018). Moreover, most of them do not show clear signatures of s-process enhancement.

[1] $[X/Y] = \log(N_X/N_Y)_* - \log(N_X/N_Y)_\odot$, where the asterisk subscript refers to the considered star, and N is the number density.

[2] $A(X) = \log\epsilon_X = \log(N_X/N_H) + 12$. Throughout this paper, we assume the Asplund et al. (2009) solar abundances.

This combination of the most metal-poor stars being enhanced in carbon and not in s-process elements suggests that their abundances may be “original". The CEMP-no stars may be early-generation stars born from gas that was polluted by the first generation(s) of massive stars.

One of the possible progenitors of carbon in the early universe are the so-called spinstars (e.g. Meynet et al. 2006 2010; Chiappini 2013). These are rapidly rotating massive ultra metal-poor stars with strong winds, and they can form large amounts of carbon. Another possibility for the progenitors of carbon are the so-called faint supernovae with mixing-and-fallback models (Umeda & Nomoto 2003; 2005; Nomoto et al. 2013; Tominaga et al. 2014), in which a supernova does not have sufficient energy to eject all its material into its surroundings, but only the outer layers with the lightest elements are ejected, while the inner part falls back onto the neutron star or black hole at the centre. Yoon et al. (2016) recently suggested that there are two types of CEMP-no stars based on their absolute carbon abundance; they might correspond to the two different progenitors.

It is also possible that some CEMP-no stars have been polluted by a companion, but the binary fraction of CEMP-no stars is not well constrained so far. Studying the CEMP-no binary fraction and binary properties of the population provides us with more information on star formation processes at early times. Additionally, knowledge about the binarity of each individual CEMP-no star is important because it may aid the interpretation of the chemical properties of the star. Key in determining the binarity of stars is radial velocity monitoring, a laborious effort. In this paper we present the results of a large radial velocity monitoring program for CEMP-no stars. The initial sample (described in S14) has been extended with additional spectra for 22 CEMP-no stars, including nine new stars that are not in S14 or H16a, which are mainly located in the southern hemisphere.

This paper is organised as follows. The new observations from this work are described in Section 2.2. In Section 2.3 we present the results of the radial velocity monitoring, and in Section 2.4 we summarise the properties of the CEMP-no binary population. We discuss the results in Section 2.5, give an outlook about what can be achieved with *Gaia* in Section 2.6, and our conclusions are briefly summarised in Section 2.7.

2.2 Data

2.2.1 Sample selection and observations

We monitored 22 CEMP-no stars for radial velocity variations. The stars were chosen to be additional follow-up for Starkenburg et al. (2014) and to extend the sample to the southern hemisphere. Stars were originally selected from Norris et al. (2013b), and then the sample was expanded with additional stars from different literature sources. The list of targeted stars with some of their properties can be found in Table 2.1. All stars in our sample have [Fe/H] < -2.5, and more than 80% of the sample has [Fe/H] < -3.0. All stars meet the CEMP criterion [C/Fe] $\geq +0.7$, and more than 70% of the sample meets the stricter CEMP criterion of [C/Fe] $\geq +1.0$. Almost all stars satisfy the classical CEMP-no criterion by having [Ba/Fe] ≤ 0.0, within the

Table 2.1 — The 22 program stars

Name	n[a]		V (mag)	RA (J2000)	DEC (J2000)	[Fe/H]	[C/Fe][b]	A(C)[b]	[Ba/Fe]	ref	bin?[c]
BD+44°493	C	5	9.1	02 26 49.7	+44 57 47	−3.83	1.35	5.95	−0.60	2	1
BS 16929–005	C	4	13.6	13 03 29.5	+33 51 09	−3.34	0.99	6.09	−0.41	1	1
CS 22878–027	C	4	14.4	16 37 35.9	+10 22 08	−2.51	0.86[d]	6.78[d]	< −0.75	1	1
CS 22949–037	C	5	14.4	23 26 29.8	−02 39 58	−4.38	1.16	5.97	−0.60	3	1
CS 22957–027	C	5	13.6	23 59 13.1	−03 53 48	−3.19	2.61	7.87	−0.81	3	2
CS 29498–043	S	4	13.7	21 03 52.1	−29 42 50	−3.87	2.75	7.62	−0.49	3	1
CS 29502–092	C	6	11.9	22 22 36.0	−01 38 28	−3.30	1.06	6.59	−1.36	3	1
HE 0057–5959	S	2	15.8	00 59 54.1	−59 43 30	−4.08	0.86	5.21	−0.46	1	
HE 0107–5240	S	4	15.1	01 09 29.2	−52 24 34	−5.44	3.97	7.03	< +0.93	4	**3**
HE 0557–4840	S	3	15.5	05 58 39.3	−48 39 57	−4.73	1.59	5.29	< +0.07	5	
HE 1012–1540	C/S	5/1	14.0	10 14 53.5	−15 55 53	−4.17	2.40	6.67	−0.28	3	1
HE 1150–0428	C	7	14.9	11 53 06.6	−04 45 03	−3.47	2.37	7.35	−0.48	1	2
HE 1201–1512[e]	C/S	4/2	13.8	12 03 37.1	−15 29 32	−3.86	1.14	5.71	< +0.05	1	1
HE 1300+0157	C	4	14.1	13 02 56.2	+01 41 52	−3.75	1.31	5.99	< −0.85	1	1
HE 1327–2326	S	3	13.6	13 30 05.9	−23 41 50	−5.71	4.18	6.90	< +1.39	6	1
HE 1506–0113	C/S	7/1	14.4	15 09 14.3	−01 24 57	−3.54	1.47	6.38	−0.80	1	2
HE 2139–5432	S	2	15.4	21 42 42.5	−54 18 43	−4.02	2.59	7.01	< −0.33	1	**3**
HE 2142–5656	S	3	13.7	21 46 20.5	−56 42 18	−2.87	0.95	6.61	−0.63	1	
HE 2202–4831	S	2	15.6	22 06 06.0	−48 16 53	−2.78	2.41	8.08	−1.28	1	
HE 2247–7400	S	1	13.3	22 51 19.6	−73 44 21	−2.87	0.70	6.58	−0.94	1	
SDSS J0140+2344[e,f]	C	4	15.1	01 40 36.2	+23 44 58	−4.00	1.13	5.56	< +0.34	1	**3**
SDSS J1422+0031	S	3	16.3	14 22 37.4	+00 31 05	−3.03	1.70	7.11	−1.18	7	**3**

Notes. References: (1) Yong et al. (2013a), (2) Ito et al. (2013), (3) Roederer et al. (2014), (4) Christlieb et al. (2004), (5) Norris et al. (2007), (6) Frebel et al. (2008), (7) Aoki et al. (2013)
(*a*) Number of radial velocity measurements added in this program observed with CFHT (C) or SALT (S)
(*b*) Values corrected for evolutionary status, as reported in Yoon et al. (2016)
(*c*) 1 = single, 2 = binary, from Preston & Sneden (2001), S14 and H16a, **3** = binary from this work
(*d*) This star is not in the Yoon et al. (2016) compilation, we report the [C/Fe] from Yong et al. (2013a) (without evolutionary correction, which is fine since this is not an evolved star), and we computed the A(C) using the Asplund et al. (2009) solar carbon abundance.
(*e*) These are the dwarf solutions.
(*f*) Sometimes named 53327–2044–515 (e.g. in Yong et al. 2013a), but here we use its official SDSS name.

uncertainties. Two notable exceptions are the hyper metal-poor stars HE 0107–5240 and HE 1327–2326, whose upper limits on [Ba/Fe] are higher than +0.9. However, Matsuno et al. (2017) have revised the CEMP-no definition, taking into account the increasing trend in [Ba/Fe] with [Fe/H] among CEMP-s stars. The new definition is different from the classical definition for stars with [C/Fe] > +2, where in this region stars are classified as CEMP-no if they have [Ba/C] < −2. Both HE 0107–5240 and HE 1327–2326 satisfy this revised CEMP-no criterion. Additionally, Norris et al. (2013b) pointed out that other chemical properties for these stars are consistent with being CEMP-no. One other star that does not satisfy even the new CEMP-no criterion is SDSS 0140+2344 ([Ba/Fe] < +0.34). This star has an absolute carbon abundance of 5.6, however, which is much lower than the typical value for CEMP-*s* stars. It is therefore more likely to be CEMP-no.

Between August 2013 and April 2015, we gathered a total of 98 high-resolution spectra with a low signal-to-noise ratio of our target stars, plus spectra of radial velocity standard stars. We made use of the Echelle SpectroPolarimetric Device for the Observation of Stars (ESPaDOnS, Donati 2003; Manset & Donati 2003) at the Canada-France-Hawaii Telescope (CFHT), with a resolving power of R ~ 68 000 covering the wavelength range 370–1050 nm. The other spectrograph we used was the High Resolution Spectrograph (HRS, Bramall et al. 2010; Bramall et al. 2012; Crause et al. 2014) at the Southern African Large Telescope (SALT, Buckley et al. 2006), which we used in its low-resolution mode with R ~ 16 000. Our observations started during commissioning of HRS. The HRS is a fibre-fed dual-beam white-pupil echelle spectrograph that yields two spectra: a blue arm that covers from 370–550 nm, and a red arm that covers from 550–890 nm. The number of observed spectra per star for each telescope is indicated in Table 2.1.

The stars that were observed with CFHT largely overlap with the sample of H16a, which we could not coordinate because our programs were executed at around the same time. We typically have a shorter baseline and a more heterogeneous sample of measurements.

2.2.2 Data reduction

The CFHT spectra were reduced using the dedicated software package LIBRE-ESPRIT (Donati et al., 1997), which includes an automatic wavelength correction using telluric lines. We used the normalised spectra in our radial velocity measurements.

For the SALT data we have adopted the results of the standard HRS pipeline for the spectra taken after commissioning of HRS was completed in late 2013 (80% of the sample). The spectra obtained during commissioning (eight science observations in total) were reduced with the standard IRAF[3] reduction scripts from the ECHELLE package. These shared-risk spectra had to be addressed individually and were not well suited for reduction with the preliminary HRS pipeline at that time.

2.2.3 Radial velocity determination

We determined radial velocities using the IRAF FXCOR package. This package Fourier cross-correlates the observed spectrum with a template spectrum, measuring the relative shift between the two spectra. For each of the stars, we created template spectra using the MARCS (Model Atmospheres in Radiative and Convective Scheme) stellar atmospheres and the Turbospectrum spectral synthesis code (Alvarez & Plez 1998; Gustafsson et al. 2008; Plez 2008) with stellar parameters $T_{\rm eff}$, $\log g$, and [Fe/H] as given in Table 2.1. In FXCOR, we fitted a Gaussian to the cross-correlation peak, from which the formal radial velocity uncertainties were determined following the method described in Tonry & Davis (1979).

[3] IRAF (Image Reduction and Analysis Facility) is distributed by the National Optical Astronomy Observatories, which are operated by the Association of Universities for Research in Astronomy, Inc., under contract with the National Science Foundation.

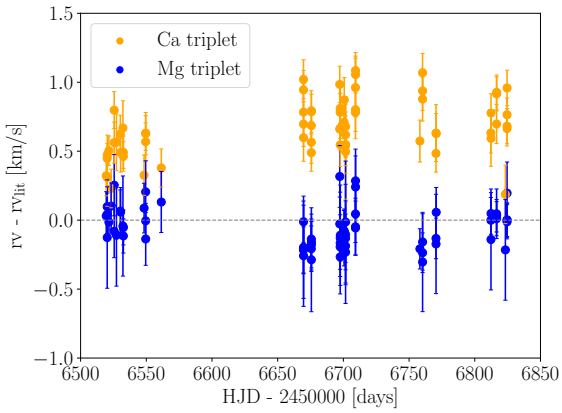

Figure 2.1 — Radial velocities of standard stars observed with CFHT compared to their literature values. The expected zero-line is indicated.

In stars that are so metal-poor as those in our sample, not many lines are present in the spectrum. Only a few features can be used to determine robust radial velocities, the main features being the calcium triplet (at 8498, 8542 and 8662 Å), the Hα line (6563 Å), and the magnesium triplet (5167, 5173 and 5184 Å). Blueward of these features, the signal-to-noise ratios tend to be too low for good radial velocity measurements.

CFHT sample

For our CFHT sample, we used the magnesium triplet region to determine good radial velocities. We found that the Hα line is too broad for precise radial velocities, and when we used the calcium triplet, we found a slight offset ($\sim$ 0.8 km s^{-1}) for the standard stars with respect to the literature (see Figure 2.1). This figure shows that although the formal uncertainties on the radial velocities derived from the magnesium triplet are larger than those from the calcium triplet, the velocities are more accurate. Additionally, for the CEMP-no stars that overlap with the H16a sample, the radial velocities of the magnesium triplet agree better with the H16a velocities than those from the calcium triplet. Our supposition is that the difference between the radial velocities of the calcium and magnesium triplet is the result of a faulty wavelength calibration in the red part of the ESPaDOnS spectra. Therefore we decided to use the radial velocities of the magnesium triplet in our analysis for the CFHT spectra, with uncertainties as provided by FXCOR.

SALT sample

The SALT spectra have lower signal-to-noise ratios than the CFHT spectra and were taken at lower resolution. For these observations we therefore used the spectra from the red and blue arms to obtain more precise radial velocities.

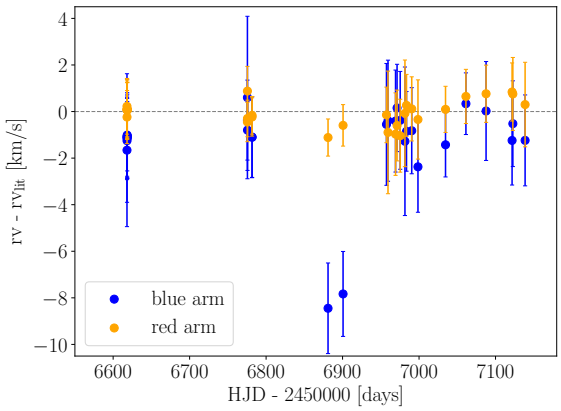

Figure 2.2 — Radial velocities of standard stars observed with SALT compared to their literature values. The expected zero-line is indicated.

To correct for any instabilities in the instrument, we computed two radial velocity corrections. First of all, we computed a correction using the telluric lines in the red spectrum. Telluric lines have fixed wavelengths and can be used to correct for exposure-to-exposure differences in the instrument that may cause changes in the wavelength solution. We applied this correction to the blue and red spectrum of that observation, since the blue spectra show no telluric lines. For the observed radial velocity standard stars, we present the telluric-corrected radial velocities compared to the literature velocity in Figure 2.2. The red arm velocities agree well with the literature within the uncertainties of about 1 $\mathrm{km\,s^{-1}}$ for all standard stars throughout the full time-span, demonstrating that our radial velocity determination, when combined with the telluric correction, is robust and that the uncertainties are realistic.

The blue arm velocities for the standard stars show a small offset in most of the measurements. Furthermore, the blue-red difference around HJD − 2450000 = 6900 days (August 2014) is particularly large for the two observed standard stars. The history of maintenance operations on HRS shows that in August 2014, the instrument was plagued by several issues. The vacuum was lost a few times during the first weeks of August, and afterwards, the cameras needed to be heated up by more than 150 degrees to remove possible contaminants. Since this was done at least twice in this period, it is possible that in the process, one of the CCDs moved slightly. This could lead to a discrepancy between the two arms.

However, we can correct for the blue arm differences using the standard star observations. We applied a correction to the blue arm radial velocities for our science observations, which is the difference between the literature and measured radial velocity from the blue arm of the standard star(s) observed on the same night. Especially for the two science stars observed in August 2014, this drastically improves the consistency between the blue and red arm radial velocities. During one night, the blue arm correction may vary by up to 1 $\mathrm{km\,s^{-1}}$, and unfortunately, not

every science observation always has its own radial velocity standard observation. Therefore, we inflated the FXCOR uncertainties on the blue arm radial velocities of the science observations by 1 $\mathrm{km\,s^{-1}}$.

The final radial velocities are computed as the weighted average of the (telluric and standard corrected) red and blue velocities, where the weights are the uncertainties as provided by FXCOR (with the blue uncertainties inflated). Final radial velocity uncertainties are estimated by the standard deviation of the two velocities derived from the blue and red arm.

For almost half of the spectra no radial velocity standard star was observed on the same night. For these stars we did not use the blue arm radial velocities, but accepted the radial velocities from the red arm with uncertainties as provided by FXCOR. This resulted in lower precision for these stars, but as illustrated in Figure 2.2, we are confident that the red arm velocities are accurate. Additionally, for two nights (five spectra) no red spectrum was available for science or standard stars, and therefore also no telluric correction. We excluded these measurements from this work entirely. For the five stars with SALT data that overlap with the H16a sample, the derived radial velocities agree with those from H16a within the uncertainties.

2.2.4 CEMP compilation

For an overview of known CEMP stars, we have used data from Yoon et al. (2016) as a basis. These authors have compiled a large number of CEMP stars from the literature. The sample contains 127 CEMP-no stars, 147 CEMP-*s* stars, and 31 unclassified CEMP stars based on upper limits on their [Ba/Fe]. The carbon abundances in this compilation were corrected for evolutionary phase (following Placco et al. 2014), and throughout this paper, we use their corrected [C/Fe] and A(C) values for the stars in our sample (Table 2.1) and when we refer to the compilation.

We added six stars to this compilation: the recently discovered hyper metal-poor star SDSS J0815+4729 from Aguado et al. (2018), which is extremely enhanced in carbon (with [Fe/H] < -5.8 and [C/Fe] $> +5.0$), the recently discovered CEMP-no binary star SDSS J1341+4741 from Bandyopadhyay et al. (2018), CS 22166–016 (Giridhar et al., 2001) and CS 22878–027 (Yong et al., 2013a), which are two CEMP-no stars that were monitored in radial velocity by H16a and us and which are missing in the compilation, and G64–12 and G64–37, which were found to be CEMP-no stars by Placco et al. (2016a). For SDSS J0929+0238 we updated the $\log g$ (to the main-sequence solution), [Fe/H], [C/Fe], A(C), upper limit for [Ba/Fe], and binary status to the values in Caffau et al. (2016). We updated the [Fe/H], [C/Fe], and A(C) of HE 2319–5228 to the values from Beers et al. (2017). HD 135148 is a known binary star (Carney et al., 2003), therefore we updated its binary status in the compilation. The star has a [Ba/Fe] = +0.3 (Simmerer et al., 2004) and is not clearly classified as CEMP-no or CEMP-s, therefore we did not consider this star in our analysis. For SMSS 0313–6708 we updated the [Fe/H] upper limit to −6.5 (Nordlander et al., 2017)
.

For HE 1201–1512 and SDSS J0140+2344, Yoon et al. (2016) only provided the subgiant solutions, even though Yong et al. (2013a) provided both dwarf and subgiant solutions since the evolutionary status of this star was unknown at the

time. With *Gaia* DR2 (Gaia Collaboration et al., 2018), we can determine which solution is likely the best one. We compared the BP−RP and absolute G magnitude (converted using the parallax) to a MIST isochrone[4] (Dotter 2016; Choi et al. 2016) with [Fe/H] = −4.0 at an age of 12.5 Gyr. We find that both stars are more consistent with being dwarfs, therefore we accept the dwarf solutions.

2.3 Results

2.3.1 Radial velocity database

We present all derived radial velocities for the stars in our CFHT/SALT sample in Table 2.3. We supplemented our radial velocities with values from the literature, to obtain a time span as long as possible and as many radial velocities for as many stars as possible. We compiled a list with all available radial velocity measurements from S14, H16a, and this work, and added five stars from the literature. The CEMP-no stars G77–61 (Dearborn et al., 1986), SDSS J0929+0238 (Caffau et al., 2016), and SDSS J1341+4741 (Bandyopadhyay et al., 2018) are known to vary in radial velocity. G77–61 and SDSS J0929+0238 only have upper limits for [Ba/Fe], but are assumed to be CEMP-no stars because they are not on the high-carbon band. SDSS J0929+0238 has been discovered as a double-lined (possibly even triple-lined) spectroscopic binary, and it was monitored for radial velocity variations after. For this star, two or three radial velocities per spectrum are given for spectra that had multiple components (as in Caffau et al. 2016). The two stars G64–12 and G64–37 are CEMP-no stars that are constant in radial velocity (Latham et al., 2002). Additionally, we kindly received several unpublished radial velocity measurements from N. Christlieb for HE 0557–4840 and HE 0107–5240, which we have added to the compilation.

We supplemented our literature sample by deriving a radial velocity for other available spectra, using the same method as for the CFHT spectra. For HE 1201–1512, we derived the radial velocity from a FEROS spectrum that was taken during follow-up efforts from the Pristine survey (Starkenburg et al. 2017b; Caffau et al. 2017). We also searched the ESO archive and found a UVES spectrum for SDSS J0140+2344 taken as part of the TOPoS survey (Bonifacio et al., 2018) and 34 UVES spectra over the course of one year for the most iron-poor star SMSS J0313–6708, which was observed as part of the SkyMapper extremely metal-poor star survey (Keller et al. 2014; Bessell et al. 2015). No radial velocities for SMSS J0313–6708 have previously been published.

Our efforts result in a sample of 710 individual radial velocity measurements (including this work) for 45 CEMP-no stars. The stars are listed in Table 2.4 with their radial velocity properties, stellar parameters, and carbon and barium abundances. The individual radial velocity measurements can be found in Table 2.5.

[4] `http://waps.cfa.harvard.edu/MIST/interp_isos.html`

2.3.2 Radial velocity variation in the sample

For each of the 45 CEMP-no stars in the compilation, we determined the χ^2 of the radial velocity distribution,

$$\chi^2 = \sum_{i=1}^{n} \left(\frac{v_i - \bar{v}}{\sigma_{v_i}} \right)^2, \tag{2.1}$$

and used it to compute the probability that the radial velocity is constant, the p-value $P(\chi^2)$. Before computing the χ^2, we quadratically added to the radial velocity uncertainties from H16a a floor uncertainty of 0.1 $\mathrm{km\,s^{-1}}$ to account for external uncertainty sources, as H16 did when computing their χ^2. The final probability for each of the stars is presented in the fifth column of Table 2.4. Carney et al. (2003) found that all binary stars in their sample have $P(\chi^2) < 10^{-6}$, which is what we take as our binary candidate selection criterion.

Among the stars with $P(\chi^2) < 10^{-6}$, we find the six known binary systems from the literature: CS 22957–027, HE 0219–1739, HE 1150–0428, and HE 1506–0113, which are the four binaries discussed in S14 and H16a, and additionally G77–61 and SDSS J1341+4741 (see Section 2.3.1). SDSS J0929+0238 is also binary, but is not included in this analysis since it is a spectroscopic double-lined system.

New binary candidates

There are five additional stars with $P(\chi^2) < 10^{-6}$, which are good binary candidates. Three of them, HE 0107–5240, HE 2139–5432 and SDSS J1422+0031, are in our southern hemisphere SALT sample. The fourth star, SDSS J0140+2344, is in our CFHT sample and is one of the few stars in that sample that has not been monitored by H16a. Finally, SDSS J1313–0019 has not been observed by us, but comes from the literature.

We present the individual radial velocity measurements for the three stars with > 10 $\mathrm{km\,s^{-1}}$ variation that include measurements from this work in Figure 2.3. SDSS J1422+0031 and SDSS J0140+2344 have been mentioned before as possible interesting candidates in S14.

The fourth star that includes measurements from this work, HE 0107–5240, is presented in Figure 2.4. This star was long thought to be non-variable in radial velocity, but when we included our new measurements, this star appears to be varying on a long timescale (> 10 years). Our supposition is that it is part of a (wide) binary system.

The final star, SDSS J1313–0019, has three radial velocity measurements in the literature, of which two come from low-resolution spectra (268 ± 4 $\mathrm{km\,s^{-1}}$ and 242 ± 4 $\mathrm{km\,s^{-1}}$ from SEGUE and BOSS, respectively, Allende Prieto et al. 2015) and one from a high-resolution spectrum (274.6 $\mathrm{km\,s^{-1}}$, no uncertainty given, Frebel et al. 2015). Both teams of authors have suggested that this star might be in a binary system, but more measurements are needed to confirm or refute this. We do not treat this star as a binary system in this work because it has only one measurement from high-resolution spectroscopy.

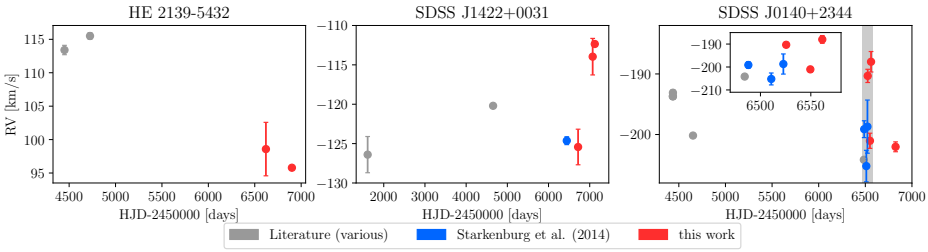

Figure 2.3 — Radial velocities for the three stars in our sample that strongly vary in radial velocity ($> 10\,\mathrm{km\,s^{-1}}$) and were not previously identified as binaries. For SDSS J0140+2344, a zoom-in of the shaded region is shown.

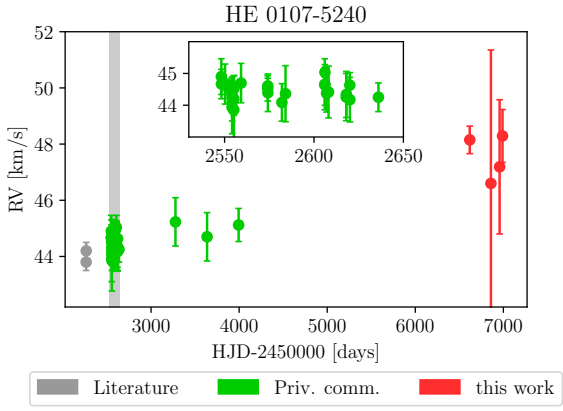

Figure 2.4 — Radial velocities for HE 0107–5240, including those unpublished values that we received through private communication from N. Christlieb. A zoom-in of the shaded region is shown.

Other stars with low $P(\chi^2)$

Two additional stars had $P(\chi^2) < 10^{-6}$. The first, HE 1410+0213, was observed extensively by H16a, and after much analysis, they concluded that the star is most likely single. They assumed that the velocity variation comes from low-amplitude pulsations in the star and suggested adding a velocity jitter of $0.15\,\mathrm{km\,s^{-1}}$. When we add such a jitter, $P(\chi^2)$ is increased (as presented in Table 2.4).

The second star is the most iron-poor star of the compilation, SMSS 0313–6708. Its 34 radial velocities (which we derived from archive UVES spectra) measured over the course of one year have a dispersion of $0.4\,\mathrm{km\,s^{-1}}$, with two measurements that have difference of $2.3\,\mathrm{km\,s^{-1}}$ (see Figure 2.12 in the appendix). We were not able to fit an orbit through all points using the method in Section 2.3.3 and, excluding the two outliers, the other measurements seem compatible with a constant radial velocity. We therefore conclude that it is likely that the radial velocity uncertainties are underestimated. The ESO archive lists no radial velocity standard stars that are

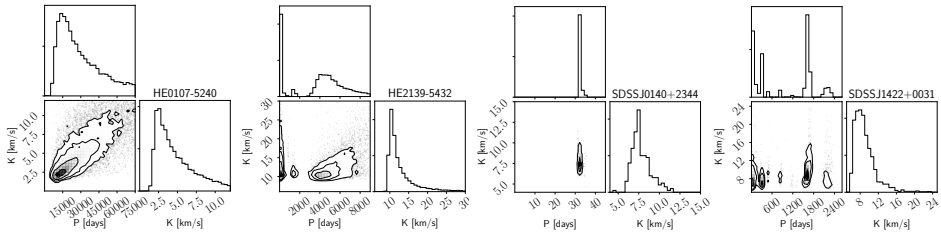

Figure 2.5 — Orbits solutions from THE JOKER for the period P and the semi-amplitude K for the new binaries. The ranges on the x- and y-axes have been truncated for clarity, but at least the two largest peaks of the distribution are always shown.

observed on the same nights as the two outliers, therefore we cannot correct for any systematics. Instead, we estimate an uncertainty floor by assuming that the star does not vary in radial velocity. We quadratically added a constant to each of the the uncertainties until a final reduced χ^2 of 1 was reached. This leads to an uncertainty floor of 0.35 $\mathrm{km\,s^{-1}}$, which we have added to each measurement. We provide these inflated uncertainties for SMSS 0313–6708 in Table 2.5. After this correction, this star no longer has $P(\chi^2) < 10^{-6}$ (the updated value is presented in Table 2.4). In this work we treat SMSS 0313–6708 as single, although it could still vary in radial velocity on a timescale longer than one year.

Final notes on radial velocity variations

Radial velocity variations are not only caused by binarity, they can also be caused by inhomogeneities on the surfaces of stars or stellar pulsations, for example. Carney et al. (2008) found that the velocity "jitter" that is due to inhomogeneities mainly affects evolved stars with $M_V \leq -1.4$ ($\log g \lesssim 1.0$). None of our four new binary candidates are in this regime, nor do they lie in parts of the HR diagram that are known for stellar pulsations. We therefore conclude that their radial velocity variations are due to binarity.

For all remaining stars in our CFHT/SALT sample we present the individual radial velocity measurements in Figure 2.13. Our measurements agree with previous measurements when there is overlap.

2.3.3 Orbit properties of the new binaries

We applied the code THE JOKER (Price-Whelan & Hogg 2017; Price-Whelan et al. 2017) to the radial velocity data of our four newly discovered binary systems: HE 0107–5240, HE 2139–5432, SDSS J0140+2344, and SDSS J1422+0031. THE JOKER is a Monte Carlo sampler for orbital parameters of binary systems that can also be applied to sparse and/or low-quality radial velocity data. It produces a posterior sampling of the period, eccentricity, pericentre phase and argument, velocity semi-amplitude, and the barycentre velocity. For all four of our stars, the eccentricity and pericentre phase and argument were not well constrained in the analysis. The resulting corner plots (Foreman-Mackey, 2016) for the periods and semi-amplitudes

provide insight, however, and can be found in Figure 2.5. We took 10^6 samples per star, except for SDSS J0140+2344, where we took 10^8 because the orbit is relatively well determined with the available radial velocity measurements, so that few samples are accepted.

The analysis with THE JOKER for HE 0107–5240 results in a period distribution that peaks between 10000 and 30000 days (27−82 years) and a semi-amplitude of the order of 2–5 $\mathrm{km\,s^{-1}}$. HE 2139–5432 has sparse radial velocity data that allow for many possible short-period orbits up to 300 days, or longer period orbits of ∼4000 days, both with semi-amplitudes of ∼11 $\mathrm{km\,s^{-1}}$. For SDSS J0140+2344 we find a narrow peak of the period distribution at 32 days, and a semi-amplitude of 7.5 $\mathrm{km\,s^{-1}}$. Finally, for SDSS J1422+0031 we find multiple peaks, the most pronounced one producing a period of ∼1600 days and a semi-amplitude of ∼8 $\mathrm{km\,s^{-1}}$. Clearly, for at least three of these stars, more radial velocity measurements are needed to determine better orbital solutions.

2.4 Properties of the CEMP-no radial velocity sample

By combining our four new CEMP-no binaries with the four known binaries discussed in S14 and H16a (CS 22957–027, HE 0219–1739, HE 1150–0428, and HE1506–0113) and the three literature stars G77–61 (Dearborn et al., 1986), SDSS J0929+0238 (Caffau et al., 2016) and SDSS J1341+4741 (Bandyopadhyay et al., 2018), we have a sample of eleven CEMP-no binary stars. To obtain to a binary fraction, the number of single stars needs to be determined as well. Long monitoring time-scales and high radial velocity precision are needed to rule out the binarity of a star. If the timescale is too short or the uncertainties are too large, a long-period low-amplitude signal might be hiding in the data. For all practical purposes, however, we assumed that the monitored stars that do not show indications of radial velocity variations are single. We excluded from the single-star sample those stars with fewer than five radial velocity measurements, because the radial velocity precision and/or temporal coverage of those measurements is not sufficient to claim that a star is single based on so few data points. Combining the single and binary stars results in a binary fraction of 32^{+10}_{-9} % (11 out of 34) for the whole sample of radial velocity monitored CEMP-no stars, using binomial statistics to derive the $\pm1\sigma$ uncertainties. This binary fraction is larger than 17^{+11}_{-8} % (4 out of 24) as found by H16a for CEMP-no stars, but agrees within 1σ. The discrepancy of our result with the binary fraction of 16^{+5}_{-4} % (14 out of 85) for carbon-normal metal-poor ($-3.0 \lesssim$ [Fe/H] $\lesssim -1.4$) giants by Carney et al. (2003) is slightly larger than 1σ. However, both of these are not statistically significant differences.

The sample of H16a appears to be more homogeneously monitored than the complete combined sample in this work, because we and others in the literature may have preferentially monitored stars that already showed some indication of radial velocity variation. The binary fraction in this work might not necessarily be representative for the whole population.

All these binary fractions (including those from H16a and Carney et al. 2003) are more correctly thought of as lower limits, given that long-period binaries or binaries

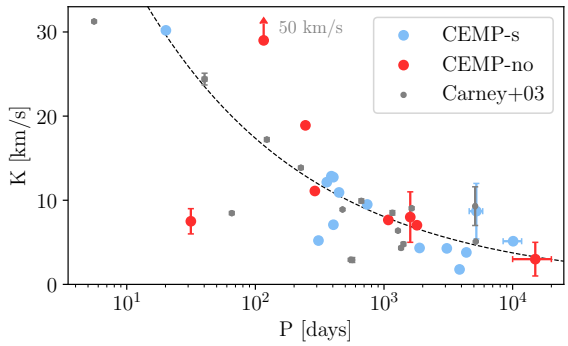

Figure 2.6 — Periods and semi-amplitudes of carbon-normal metal-poor binaries from Carney et al. (2003), CEMP-*s* binaries from Hansen et al. (2016b) (excluding their CEMP-r/s stars), and CEMP-no binaries (compilation from this work). HE 1506–0113 (see Figure 2.13) and SDSS J0929+0238 are not shown in this figure since they do not have any derived orbits, HE2139-5432 is not shown because it either has P < 300 or P ≈ 4000 days (with K ≈ 11 km s^{-1}). The line indicates what would be expected of Keplerian orbits of a 0.8 $M_\odot$ star with a 0.5 $M_\odot$ companion, for an eccentricity of 0.3 (typical for the stars in the Carney et al. 2003 sample) under an inclination of 60°.

at high inclinations may still be present among the assumed single stars. It is much easier to confirm the binarity of a star than to rule out its binarity, since fewer measurements are needed to find that a star is variable in radial velocity, especially if the amplitude of the variation is large.

However, the collection of binary stars we now have is interesting to study in itself. In the following subsections we discuss some of the properties of the CEMP-no binary population.

2.4.1 Orbit characteristics

How do the orbit properties of CEMP-no stars compare to those of CEMP-*s* stars and other metal-poor binary systems? We compare the periods and semi-amplitudes in Figure 2.6. The uncertainties for the binaries from this work are taken from the 1σ contours of the most significant peaks from the probability distributions in Figure 2.5. There is no indication that the CEMP-no binaries are of a different distribution than the CEMP-*s* binaries or the stars from Carney et al. (2003). The typical companion mass for stars in the latter sample is 0.5 $M_\odot$ with eccentricities of ~ 0.3. Only three of the CEMP-no binaries have known eccentricities, H16a claimed that their distribution is not different from normal metal-poor stars.

One odd star is SDSS J0140+2344 with its short period of 31.5 days and a relatively low semi-amplitude of 7.5 km s^{-1}. This system may be observed relatively face-on. Another odd star is SDSS J1341+4741, which has a reported period of 116 days and a semi-amplitude of 50 km s^{-1} (Bandyopadhyay et al., 2018). If this is confirmed with more radial velocity measurements, this star would have to have a more massive companion than the other stars or be on a highly eccentric orbit.

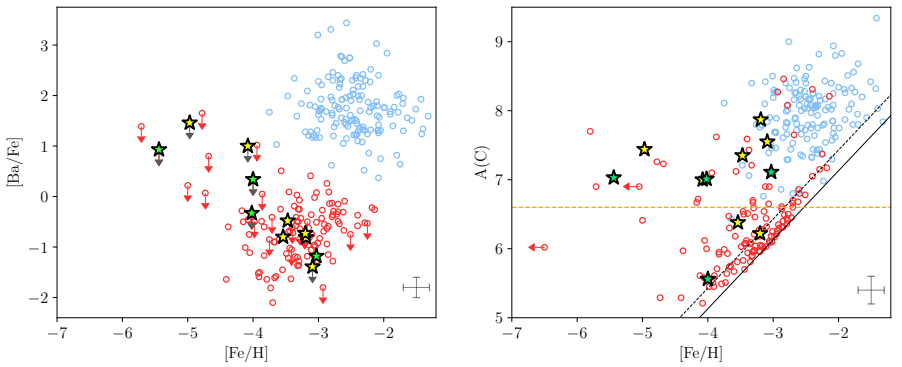

Figure 2.7 — Left: [Ba/Fe] as a function of [Fe/H] for the compilation of CEMP stars from Yoon et al. (2016) down to [Fe/H] = −6, where CEMP-*s* stars are shown in blue and the CEMP-no stars in red. The known and new CEMP-no binaries are indicated as yellow and green stars, respectively. Right: The same, but for A(C) on the y-axis. The solid and dotted black lines indicate the [C/Fe] > +0.7 and [C/Fe] > +1.0 CEMP criteria, respectively. The orange dashed line indicates the separation of the low- and the intermediate-/high-carbon band. For both panels, typical error bars on the abundances are shown in the lower right corner.

H16a were unable to derive an orbital solution for HE 1506–0113, despite the large number of radial velocity measurements and its clear variability. This star seems to vary on a short timescale (∼ 20 days) in the data from Norris et al. (2013a), which have been reanalysed by H16a, and a longer timescale (∼ 1000 days) on the basis of data from S14 and H16a, see Figure 2.13. Our new radial velocities for this star fill the gap between the measurements of S14 and H16a, but do not help to clarify its orbit.

2.4.2 Enhancement in s-process elements

Enhancement in the s-process element barium is usually a sign of mass transfer from an AGB companion. We present [Ba/Fe] as a function of [Fe/H] in the left panel of Figure 2.7 for our binary stars on top of the CEMP compilation of Yoon et al. (2016), where the CEMP-no stars are shown in red and the CEMP-*s* stars in blue. The CEMP-no binaries from the literature (from S14, H16a, Dearborn et al. 1986, Caffau et al. 2016, and Bandyopadhyay et al. 2018) are shown as yellow stars, and the new binaries uncovered in this work are plotted as green stars. CEMP star classes are defined mainly by the barium abundance, therefore the CEMP-*s* stars (blue points) and the CEMP-no stars (red points) are almost perfectly separated in this diagram. Four binaries have upper limits on [Ba/Fe] that are above zero. HE 0107–5240 and SDSS J0140+2344 were discussed in Section 2.2.1, and taking the revised CEMP-no definition of Matsuno et al. (2017), SDSS J0929+0238 is also classified as CEMP-no. Even though it does not satisfy the revised definition, the dwarf G77–61 ([Ba/Fe] < +1.0) is likely a CEMP-no star as well, assuming that all ultra metal-poor low-

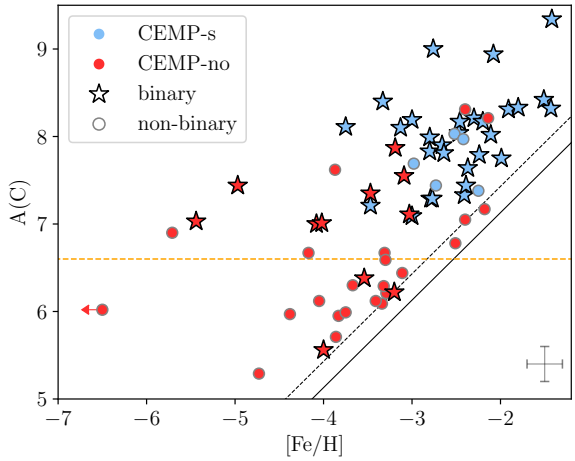

Figure 2.8 — A(C) as a function of [Fe/H] for CEMP stars, where again CEMP-no stars are shown in red and CEMP-*s* stars in blue. Binary stars are indicated by a star. The orange dashed line is the same as in the right panel of Figure 2.7.

carbon band stars are. Alternatively, it could be the first ultra metal-poor ([Fe/H] ≤ -4.0) CEMP-*s* star. However, since no ultra metal-poor CEMP-*s* stars are known to date, we assume that it belongs to the CEMP-no class.

The binaries seem to be part of the normal CEMP-no distribution in the left panel of Figure 2.7. The low [Ba/Fe] values (or upper limits) of most the binary stars are consistent with them having had no “classical" binary interaction with an AGB star in which s-process elements were transferred together with carbon.

2.4.3 Absolute carbon abundance

As discussed in the introduction, in general CEMP-*s* and CEMP-no stars have different absolute carbon abundances. This can be seen in the right panel of Figure 2.7 for the compilation of CEMP stars. Yoon et al. (2016) suggested that there may be three different groups of CEMP stars based on their A(C) and [Fe/H]. First, there are the Group I stars that cover the region of the CEMP-*s* stars at large A(C) and higher [Fe/H]. Then there are two different groups of CEMP-no stars, the Group II stars, that in general have lower A(C) and exhibit a clear dependence of A(C) on [Fe/H], and the Group III stars that seem to centre on a higher A(C) without a clear dependence on [Fe/H].

One might expect that like the CEMP-*s* stars, most high-carbon band CEMP-no stars would be in binary systems. However, H16a did not find a strong correlation between the binary status of CEMP-no stars and their location on the A(C) versus [Fe/H] plane (although that is difficult to say with such a small sample). In the right panel of Figure 2.7 we highlight the 11 currently known CEMP-no binaries on the A(C) versus [Fe/H] plane. It appears that most of the CEMP-no binaries have relatively high A(C) values in between the high- and low-carbon bands of Spite et al.

(2013), which seems to correspond roughly to the region of the Group III stars of Yoon et al. (2016) (although four of the binary stars are classified as Group I stars).

This does not seem to be a selection effect of only monitoring stars with the highest carbon enhancement, which can be seen from Figure 2.8. There we present the same A(C) versus [Fe/H] plane as in Figure 2.7, but now only for stars that have sufficient radial velocity data to determine with some confidence whether they are in a binary system or not. Typically, the stars that we assume to be single have been observed as thoroughly as the other stars, but we cannot fully exclude the possibility that they are in a binary system with a long period or low amplitude. For the CEMP-*s* stars, we used the binarity information as documented in Yoon et al. (2016).

In Figure 2.8 the fraction of CEMP-no stars that are in binary systems seems higher for stars on the intermediate- or high-carbon band compared to the stars on the low-carbon band. Splitting our sample of well-monitored stars in half based on A(C), as illustrated by the orange dashed line in Figure 2.8, we find that for the CEMP-no stars with A(C) > 6.6 the binary fraction is 47^{+15}_{-14}% (8 out of 17), and for A(C) ≤ 6.6 it is 18^{+14}_{-9}% (3 out of 17). The difference between these two fractions is 1σ.

If we conservatively assume that except for the known binary CEMP-no stars, all the known CEMP-no stars with A(C) > 6.6 are single stars (even if they do not have any radial velocity information), we find a binary fraction of 18^{+8}_{-6}% (8 out of 44). This conservative lower limit for the binary fraction of high-carbon CEMP-no stars is independent of the selection for radial velocity monitoring or the quality of the determination of single stars.

The periods for CEMP-no binary stars with A(C) > 6.6 and derived orbits are similar to the periods for CEMP-*s* binary stars, which typically are of the order of a few 100 to a few 1000 days (see Figure 2.6). The three CEMP-no binaries with A(C) < 6.6 are HE 1506–0113, SDSS J0140+2344 and SDSS J1341+4741. It is curious that each of these three stars was described in Section 2.4.1 because they have no or odd orbital solutions.

We end this section with a note of caution: the (absolute) carbon abundances need to be interpreted with caution, since most of the measurements were not made using non-local thermodynamic equilibrium (non-LTE) and/or 3D models, and such corrections may be especially important for carbon when comparing stars of different metallicities and evolutionary stages.

2.4.4 Hertzsprung-Russell diagram

We highlight the location of the CEMP stars on the (spectroscopic) Hertzsprung-Russell diagram in Figure 2.9, where again we only show the stars that have sufficient radial velocity information available. Almost all the stars in the compilation are giant stars, since these are intrinsically brighter and easier to analyse. Additionally, CEMP stars with lower effective temperatures are easier to recognise from the spectra because the CH features are more distinct. Three CEMP-no binary stars lie on the main sequence (or close to the turn-off), G77–61 with $T_{\rm eff}$ = 4000 K, SDSS J0140+2344 with $T_{\rm eff}$ = 5703 and $\log g$ = 4.7, and SDSS J0929+0238 with $T_{\rm eff}$ = 5894 K and $\log g$ = 4.5. Another possibility is that SDSS J0929+0238 is a sub-giant

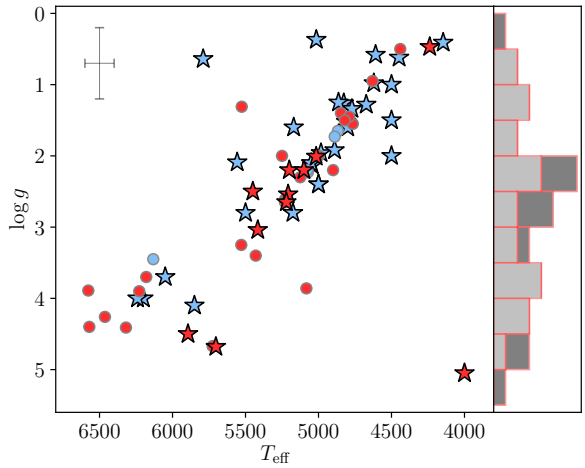

Figure 2.9 — Hertzsprung-Russell diagram for all CEMP-no and CEMP-*s* stars, with the same symbols and colour-coding as in Figure 2.8. Because the narrow giant branch is very crowded, we additionally show for the CEMP-no stars the stacked histogram for $\log g$ on the side, where dark grey are binary and light grey are single stars. Typical error bars are indicated in the top left corner.

branch star with $\log g = 3.7$, but it has been argued by Caffau et al. (2016) that the main-sequence solution is more likely (unfortunately, the *Gaia* DR2 parallax for this star is uncertain).

One of the CEMP-no binary stars, HE 0219–1739, is at the tip of the giant branch. The stellar parameters for this star are somewhat uncertain, however. T. Hansen found $T_{\rm eff} = 4600$ and $\log g = 2.3$ with stacked high-resolution radial velocity monitoring spectra (priv. comm.). Unfortunately, the *Gaia* parallax for this star is negative and does not help to constrain the $\log g$. The question arises whether this star is a real CEMP star, or if it might be an intrinsic (pulsating) carbon star. The well-determined radial velocity period of this star is 1800 days, which is longer than typical pulsation periods of long-period variable (LPV) stars. This star is also indicated as variable in its photometry by PanSTARRS (Hernitschek et al., 2016), but the given variability timescale (0.13 days) is too short and the magnitude amplitude (0.034 mag in r) is too small to represent LPV pulsations. We conclude that this star is most likely a bona fide CEMP star in a binary system.

The apparent over-density of CEMP-no binary stars between $\log g$ = 2–3 as illustrated in a histogram in the right panel of Figure 2.9 seems curious, even though we have monitored stars along the entire giant branch and turn-off. In comparison, the general sample of CEMP-no stars (from the Yoon et al. 2016 compilation) does not show an over-density between $\log g$ = 2–3. Larger samples are needed to put this tentative result on firmer footing.

We note that compared to CEMP-no stars, a larger number of monitored CEMP-s stars appear to lie on the upper part of the red giant branch. It is unlikely that this is a brightness selection-effect, since the stars in the samples of H16a and Hansen et al.

(2016b) for CEMP-no and CEMP-*s* stars cover similar ranges in V magnitudes (and they make up most of the stars in this diagram). Other unknown selection effects might play a role, however.

2.5 Discussion

2.5.1 CEMP-no stars and binary mass transfer

Each of the CEMP-no binary stars must have a companion that causes its radial velocity variations. Since none of the stars except SDSS J0929+0238 seem to be double-lined spectroscopic binaries and no visual counterpart is seen in photometry of any of the stars, the companion must be a fainter star. For the dwarf star G77–61 it has been argued that the companion is most likely a white dwarf (Dearborn et al., 1986). For the giants, the companion can be expected to be a main-sequence star or a white dwarf (which has gone through the AGB phase in the past). Would it therefore not be likely that if some of the CEMP-no stars have white dwarf companions, they might have been polluted by mass transfer from an AGB companion at some point in their life?

For CEMP-*s* stars, mass transfer from an AGB star is the main formation scenario, which has been confirmed by the number of them that is in a binary system ($82 \pm 10\%$, Hansen et al. 2016b). Different types of mass-transfer are effective at different initial separations of the stars in the binary system, where Roche-lobe overflow can occur in the closest systems, wind-assisted Roche-lobe overflow in systems of intermediate separation, and wind transfer by itself in wider systems. As shown in Figure 2.6, typical periods and radial velocity amplitudes for binary CEMP-*s* and CEMP-no stars are similar. How many of the CEMP-no stars would have experienced binary interaction?

A simple estimate of the general fraction of metal-poor stars that interact with a binary companion can be made using the CEMP-*s* stars, assuming that they all became CEMP-*s* by mass-transfer from a former AGB star. Of all stars with [Fe/H] < -2.0, 13% are CEMP-*s* stars (Placco et al., 2014) and therefore in a formerly interacting binary system. There is no reason (yet) to assume that at lower metallicity, binary stars suddenly start to interact less. By re-examining different surveys, Moe et al. (2018) have found that the close binary fraction ($P < 10^4$ days) of low-mass stars (0.6-1.5 $M_\odot$) increases with decreasing metallicity. Therefore, in the regime of the CEMP-no stars, which are at lower metallicity than the CEMP-*s* stars, an even larger fraction of all stars might be expected to have had interaction with a companion, simply because the binary fraction is higher. We see almost no CEMP-*s* stars with [Fe/H] < -3.0, however, and none at all with [Fe/H] < -4.0. What do extremely metal-poor stars look like that underwent mass-transfer from a former extremely metal-poor AGB companion?

Our CEMP-no binaries are not enhanced in s-process elements (specifically barium), which has usually been taken as a sign that they have not had any interaction with a binary companion. However, much is unknown about ultra metal-poor AGB stars (see the recent review by Gil-Pons et al. 2018). Models of AGB transfer among metal-poor stars have focussed on CEMP-*s* stars (as in Abate

et al. 2015), which are mostly found at higher metallicities than the CEMP-no stars (see Figure 2.7). The most metal-poor AGB yields available with s-process elements only extend to [Fe/H] = −2.3 (Lugaro et al., 2012). Extremely or even more metal-poor AGB stars might produce fewer s-process elements, for example in the (non-rotating) models of Suda et al. (2004), Lau et al. (2007), and Cruz et al. (2013). Additionally, rotation can strongly affect the s-process element production, for example in intermediate-mass spinstars (Meynet et al., 2010). Furthermore, the mass of the AGB star is important. It is expected that intermediate-mass AGB stars produce fewer s-process elements than AGB stars of lower mass, which especially affects s-process elements beyond the first s-process peak (Karakas & Lattanzio, 2014). If these are the polluting companion stars, no barium excess should be expected. Finally, Busso et al. (1999) suggested that in very metal-poor AGB stars, the *s*-process mainly produces third-peak *s*-process elements, particularly lead, instead of first or second *s*-process peak elements (like barium). However, lead is extremely hard to measure in carbon-enhanced metal-poor stars.

To summarise, AGB stars have ways to produce less barium and/or other s-process elements than usual. It is unclear what abundance patterns exactly are expected in extremely metal-poor AGB stars, and therefore what their companions should look like that have received mass-transfer from such a star.

2.5.2 High fraction of binaries among intermediate- and high-carbon band CEMP-no stars

In a scenario in which a carbon-normal metal-poor star or an existing low-carbon band CEMP-no star in a binary system is (further) enriched in carbon by mass-transfer from such an AGB star, this would bring them up to the intermediate- or high-A(C) band without enhancing their barium. Some or all of the carbon for these CEMP-no stars can be intrinsic, but likewise, some or all of it can come from mass transfer from a former AGB companion. If a number of CEMP-no stars were additionally enhanced in carbon over their lifetime and some were only intrinsically carbon-enhanced, this might be a possible explanation for the potential discrepancy in binary fraction between the higher A(C) and the low-A(C) populations of CEMP-no stars.

It is not likely that mass-transfer from a companion has occurred in all the intermediate- or high-A(C) CEMP-no binary stars. For example, SDSS J0929+0238 with A(C) = 7.44 is a double-lined (possibly even triple-lined) spectroscopic binary of two main-sequence stars with similar temperatures (Caffau et al., 2016). If the carbon comes from mass-transfer from an AGB companion, these stars were born in a hierarchical triple system with the third star more massive and finally polluting the other two. This scenario decreases in likelihood if it were confirmed that SDSS J0929+0238 is a triple-lined system, which means that it consists of three main-sequence CEMP-no stars. In this case, the system would have had to been born as a quadruple system with one star being more massive and having evolved through the AGB phase. A better scenario probably is that these stars were born with an intrinsically high A(C), with the carbon formed in the previous generation of stars (as in the spinstar and/or faint supernova models).

Interestingly, five CEMP-*s* stars do not show any radial velocity variation. The binary fraction of CEMP-*s* stars determined in Hansen et al. (2016b), 82 ± 10%, is not necessarily consistent with 100 % binarity. The authors claimed that even with the uncertainties on the inclination, it is unlikely that all the apparently single stars are actually in binary systems. We note that in Figure 2.8 the single CEMP-*s* stars seem to be preferentially located on the lower side of the A(C) distribution of the CEMP-*s* stars. Choplin et al. (2017) modelled the abundances of the single CEMP-s stars with massive spinstar models, and succeed for three out of the four modelled stars. Spinstar models are also employed to explain the abundances of CEMP-no stars (e.g. Meynet et al. 2010). Potentially, single intermediate- or high-carbon band CEMP-no stars (or binaries that have not had any interaction) and single CEMP-s stars are the product of a similar type of progenitor.

A takeaway from this section is that a combination of one or more of the "classical" scenarios for the formation of CEMP-no stars and binary interaction complicates the interpretation of the abundance patterns of these stars. CEMP-no stars are usually thought to be direct probes of nucleosynthesis in the first stars and supernovae, but they might also be probes of extremely metal-poor AGB stars.

Scenario without binary interaction

An alternative (or supplement) to the mass-transfer scenario is a scenario where binary stars form more easily in a carbon-enhanced environment. For example, Chiaki et al. (2017) have shown that for [C/Fe] < +2.30, silicate dust grains dominate the cooling during star formation of extremely metal-poor stars, while for [C/Fe] > +2.30, carbon grains dominate. It is not known how this would affect the binary fraction, but there might a difference between these environments of different dust cooling. Unfortunately, little work has been done on the binary fraction of carbon-normal extremely metal-poor stars, and more observations are needed to study whether there is a difference in binary fraction between carbon-rich and carbon-normal extremely metal-poor environments.

2.5.3 HE 0107–5240

HE 0107–5240 is the most iron-deficient binary in our sample, and at the time of its discovery, it was the most iron-deficient star known (Christlieb et al., 2002). Since then, many different scenarios have been proposed to explain its chemical properties, including its high carbon abundance. There are two main scenarios: 1) the abundance pattern of the star reflects the interstellar medium from which it was born, which has been polluted by one or more primordial core-collapse supernovae; alternatively, 2) the surface of the star has been polluted by material from a binary companion. So far, none of the scenarios can completely explain the abundance pattern of HE 0107–5240. It might also be a combination of the two.

In the first scenario, different possible sources produce the necessary amount of carbon and the peculiar abundance pattern of HE 0107–5240, for example, spinstars (Takahashi et al., 2014), faint supernovae (Umeda & Nomoto 2003; Iwamoto et al. 2005), or a combination of normal and faint supernovae (Limongi et al., 2003). These

scenarios seem to be relatively successful, but their predictions are not entirely in agreement with the observations, especially for the oxygen abundance (Bessell et al., 2004).

The alternative scenario of a binary companion transfer has been investigated by Suda et al. (2004), Lau et al. (2007) and Cruz et al. (2013). In the last work, the *s*-process abundance pattern and enhancement of carbon of HE 0107–5240 are explained by invoking mass transfer from a low-mass companion AGB star (both stars have some initial metallicity higher than zero). These models seem to fit the abundance pattern well, except for nitrogen, which is overproduced in the models. In the first two works, HE 0107–5240 starts out as a Population III (originally metal-free) star, where mass transfer from the companion star is fully responsible for the abundance pattern of HE 0107–5240. These models are also relatively successful at reproducing the chemical properties of this star. A prediction of the models is that the period of the binary is currently at least 30 years (Lau et al., 2007) and up to 150 years (Suda et al., 2004), with a maximum radial velocity variation of 6.5 – 7 $\mathrm{km\,s^{-1}}$. Their period range of 11000 – 55000 days and semi-amplitude of ~ 3.5 $\mathrm{km\,s^{-1}}$ are in good agreement with the results of this work; see the first panel of Figure 2.5. Additionally, Venn et al. (2014) have found a marginal detection of mid-IR excess of this star. They speculate that if this excess is real, it might be a possible indication for a debris disk formed in a binary interaction.

In summary, our observations support the binary transfer model for the origin of HE 0107–5240, where this star is potentially a true first-generation star whose pristine atmosphere has been spoiled during its lifetime. In the binary transfer scenario, it can also be a second-generation star whose surface is additionally polluted by mass-transfer from a companion, which would complicate the interpretation of its abundance pattern.

2.5.4 Magnesium

In their comparison of the two different CEMP-no sub-groups, Yoon et al. (2016) examined magnesium and found that in A(C) versus A(Mg) space, the Group II stars scale roughly with A(C), whereas the Group III stars do not and appear offset to lower A(Mg) values. Based on this behaviour (and similar behaviours for other elements), the authors suggested that the Group II and Group III CEMP-no stars could be associated with different classes of progenitors, possibly the faint mixing-and-fallback supernovae and spinstar, respectively. They reported this as a tentative conclusion, and that there may be other factors at play. Several of the CEMP-no binaries fall in the Group III subclass, suggesting that binarity may be one of those other factors.

Recently, Hartwig et al. (2018) have presented a novel diagnostic to identify second-generation stars whose birth gas cloud was enriched by only one supernova. They use the so-called divergence of the chemical displacement to identify regions in chemical space where it is likely to find this type of stars. This divergence does not depend on many assumptions in addition to the input supernovae yields for core-collapse, pair-instability, and faint supernovae. Hartwig and collaborators did not include rotating first stars or any mass-transfer scenarios as possible sources of

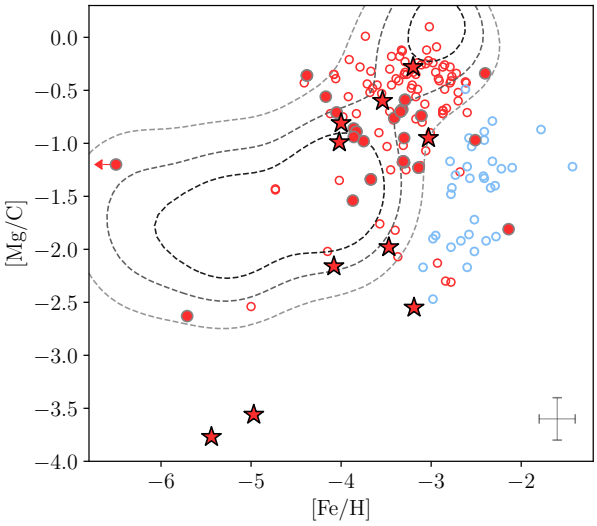

Figure 2.10 — Following Hartwig et al. (2018), we present [Mg/C] values for CEMP-no and CEMP-*s* stars against [Fe/H]. The symbols are the same as in Figures 2.8 and 2.9, while open symbols represent stars without binarity information. Typical error bars are indicated in the lower right corner. Contours of likely mono-enrichment are over-plotted (priv. comm. T. Hartwig).

metals in their model, but reported that they plan to add these in later work. One of the abundance spaces they identify as useful is [Fe/H] versus [Mg/C].

To determine what the CEMP stars look like in this space, we compiled their magnesium abundances. For the single and binary CEMP-no stars, [Mg/C] values are listed in Table 2.4. For further Group II and III stars we used the compilation of Yoon et al. (2016), which we supplemented with [Mg/Fe] for Group I stars. For the CEMP-*s* stars, we compiled [Mg/Fe] from Yong et al. (2013a) and Roederer et al. (2014) to obtain a representative sample of CEMP-*s* stars for comparison (both used the Asplund et al. (2009) solar abundances). We cross-matched these stars with Yoon et al. (2016) to derive the corrected carbon abundances for consistency. We did not include the binary information for the CEMP-*s* stars since only a few stars with binarity information are included in the combined Yong and Roederer sample, and it can be assumed that almost all of them are in fact in binary systems.

The result is shown in Figure 2.10. The CEMP-*s* stars all lie outside the range where Hartwig et al. (2018) claimed that mono-enrichment is likely. This is not surprising since they are expected to have received mass-transfer from a binary companion, and the models do not include this. The CEMP-*s* stars are offset towards lower [Mg/C] than most of the CEMP-no stars at similar [Fe/H], which is consistent with their formation scenario of binary transfer from a former AGB companion. This transfer mainly enhances C, not Mg, in the companion star. This diagram may be a useful tool for uncovering stars that have undergone mass-transfer.

Most of the CEMP-no stars lie in the mono-enrichment range. Five of the CEMP-no binary stars, however, have relative low values of [Mg/C] ($\lesssim -2.0$). Like the CEMP-*s* stars, these stars may have experienced mass transfer from a binary companion that enhanced C, but not Mg. These five stars are HE 0107–5240, SDSS J0929+0238, G77–61, HE 1150–0428, and CS 22957–027 (in order of increasing [Fe/H]). For HE 0107–5240, the very low [Mg/C] ratio was also reproduced in the mass-transfer model by Cruz et al. (2013). G77–61 most likely has a white dwarf as a companion (Dearborn et al., 1986), so that past mass transfer is also likely. For SDSS J0929+0238 we argued earlier that the mass-transfer scenario is unlikely (see Section 2.5.1), but it is still possible. If it is has not experienced AGB mass transfer, some other explanation needs to be found for its low [Mg/C].

All CEMP-no stars that overlap with the location of the CEMP-*s* stars in this diagram are Group I stars, regardless of their binary status. CEMP-no stars in Group I have A(C) and [Fe/H] similar to those of the CEMP-*s* stars, but low [Ba/Fe]. The source of these high carbon abundances is unclear, especially for the single stars, but it is interesting that in this space they also share properties with CEMP-*s* stars. However, it also shows that interpretation of this diagram is not trivial, and we should be careful to draw strong conclusions.

Finally, we emphasise that further caution should be taken when interpreting this figure, since most of the abundance measurements were not computed using non-LTE and/or 3D models, and such corrections can be important for both C and Mg.

2.6 Radial velocity outlook with *Gaia*

More data are needed to increase the sample of CEMP-no stars with multiple radial velocity measurements and to place more stringent constraints on the orbits for several of the CEMP-no binaries. This might also shed light on the evolutionary status of the companion stars and constrain mass transfer models. Additionally, more long-period variable stars might be hiding in the current sample. The ESA *Gaia* mission will have several epochs of radial velocity data for all the brightest stars in the Galaxy down to $V \approx 16.2$ (Gaia Collaboration et al., 2016). For the faintest metal-poor ([Fe/H] $= -1.5$) stars, *Gaia* will have end-of-mission radial velocity uncertainties larger than 15 km s^{-1}, whereas for stars brighter than $V = 14$, the expected uncertainty is between $0.5 - 2$ km s^{-1}.[5] This is unfortunately not the uncertainty on the individual radial velocity measurements, but that of the combined end-of-mission radial velocity. Moreover, only for the brightest stars will the single epoch radial velocities be probably released in a future *Gaia* data release. It is unclear how much *Gaia* will contribute to providing multiple good radial velocity measurements that can constrain orbits of CEMP stars. It is therefore still important to continue the radial velocity monitoring effort with high-resolution spectrographs here on Earth.

[5] https://www.cosmos.esa.int/web/gaia/rvsperformance

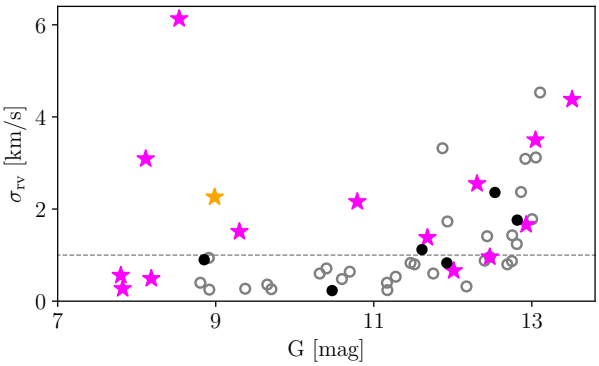

Figure 2.11 — Radial velocity uncertainty from *Gaia* vs. the *Gaia G* magnitude. Stars are labelled by binarity using the information from the Yoon et al. (2016) compilation, where magenta stars are binaries, black circles are non-binaries, and open grey circles represent stars of unknown binarity. The orange star is HD 135148. At fainter magnitudes, the radial velocity uncertainties in *Gaia* increase. The 1 km s^{-1} limit is marked by the grey dotted line.

2.6.1 Method

Gaia data can, however, be used to find new binary systems, even in *Gaia* DR2 (Gaia Collaboration et al., 2018). The radial velocity uncertainties provided in DR2 are the result of the combination of multiple radial velocity measurements, and if stars vary in radial velocity over the course of the *Gaia* observations, they will have higher radial velocity uncertainties than expected from the precision for stars of their magnitude and effective temperature. This approach is similar to what was done to investigate binarity in CEMP stars discovered in the APOGEE survey (Kielty et al., 2017).

An example of this type of analysis is shown in Figure 2.11, where we cross-matched the Yoon et al. (2016) CEMP star sample with *Gaia* DR2 and present the uncertainty in radial velocity versus the *G* magnitude for the stars that are sufficiently bright to be included in the current data release. At the faintest end, the precision is expected to be a maximum of ~ 2 km s^{-1} for the hottest stars in our sample, and at the bright end, the precision should be less than 1 km s^{-1} (Katz et al., 2018). In the figure we indicate binarity information from the compilation, where the magenta stars are known binaries, the black circles are known non-binaries, and open grey symbols represent stars of unknown binarity. The orange star in the Figure is HD 135148, for which the binary information was not provided in the Yoon et al. (2016) compilation. We “rediscovered" this binary using the *Gaia* information and found that it was already known from Carney et al. (2003). It is clear that several of the binaries indeed have larger radial velocity uncertainties than expected from the precision alone.

Table 2.2 — CEMP stars that have Gaia radial velocity uncertainties > 1 $\mathrm{km\,s^{-1}}$, with new binary candidates in bold-face.

Name	CEMP class	G (mag)	rv_{Gaia} ($\mathrm{km\,s^{-1}}$)	σ_{Gaia} ($\mathrm{km\,s^{-1}}$)	rv_{lit}[a] ($\mathrm{km\,s^{-1}}$)	σ_{lit} ($\mathrm{km\,s^{-1}}$)	n_{lit}	ref	T_{eff}[b] (K)	[Fe/H][b]	$T_{\mathrm{eff,T}}$ (K)	$[\mathrm{Fe/H}]_{\mathrm{T}}$
HE 2155–3750	s	13.1	77.5	4.5	27.7	10.0[c]	1	1	5000	−2.64	5500	0.0
HE 1305+0007	s	11.9	228.5	3.3	217.8	1.5	1	2	4750	−2.08	4750	−2.0
HE 2123–0329	no	13.1	−217.7	3.1	−219.1	0.4	2	3	4725	−3.22	6500	−1.5
SMSS J1738–1457	no	12.9	43.7	3.1	−26.9	2.0	1	4	4600	−3.58	5700	0.0
HKII 17435–00532	r/s	12.8	39.3	2.4	38.9	0.3	4	5	5200	−2.23	6000	−1.5
CS 30301–015	s	12.8	87.0	1.8	86.6	0.1	18	6	4900	−2.73	6000	−1.5
HE 2319–5228	no	13.0	286.2	1.8	294.3	4.0	2	7	4900	−2.60	6000	−1.5
BS 16077–077	s	11.9	68.3	1.7	...	...	...	...	5900	−2.05	6000	−1.5
CS 22947–187	s	12.8	−252.3	1.4	−251.9	0.9	2	8,9	5300	−2.58	6000	−1.5
HE 1305+0132	s	12.4	157.0	1.4	...	...	...	...	4462	−2.45	4500	0.0
CS 22873–128	no	12.8	207.15	1.2	205.5	0.3	2	8,9	4710	−3.32	6000	−1.5

Notes. References: (radial velocities) (1) Placco et al. (2011), (2) Goswami et al. (2006), (3) Hollek et al. (2011), (4) Jacobson et al. (2015), (5) Roederer et al. (2008), (6) Hansen et al. (2016b), (7) Beers et al. (2017), (8) Roederer et al. (2014), (9) McWilliam et al. (1995)
(*a*) For stars with only one measurement, this is the radial velocity as presented in the literature. For stars with multiple measurements (see column n_{lit}), it is the (weighted) average of the different measurements. Similarly, for the uncertainty, it is either the uncertainty reported in the literature or the (weighted) standard deviation between different literature values.
(*b*) As reported in the Yoon et al. (2016) compilation.
(*c*) No uncertainty is given in the reference, but since it is a measurement from an intermediate-resolution spectrum, we assume $\sigma = 10\,\mathrm{km\,s^{-1}}$.

2.6.2 New CEMP binary candidates

We investigated stars of unknown binarity with high σ_{Gaia} values (> 1 $\mathrm{km\,s^{-1}}$), see a summary in Table 2.2. We included the $T_{\mathrm{eff,T}}$ and $[\mathrm{Fe/H}]_{\mathrm{T}}$ of the template that was used in the Gaia radial velocity determination. A poor template with an incorrect shape of the spectral lines might not necessarily result in a poor radial velocity, but will most probably influence the radial velocity uncertainty. The standard Gaia radial velocity templates have [Fe/H] of either 0.0 or −1.5, except when the metallicity of the star is known (Katz et al., 2018). Even though most of our stars are more metal-poor than [Fe/H] = −1.5, the radial velocity precision seems to be good with the [Fe/H] = −1.5 templates, since for several stars in Table 2.2 the literature and *Gaia* radial velocities agree to within 1 $\mathrm{km\,s^{-1}}$. This is even the case for stars where $T_{\mathrm{eff,T}}$ differs by more than 1000 K from the literature (see CS 30301–015 and CS 22873–128). It is unclear how good the velocities are with the [Fe/H] = 0.0 templates, since for two stars with such a template the literature radial velocities are highly discrepant with those from *Gaia*. In future *Gaia* data releases the stellar parameters from the *Gaia* spectra (Bp, Rp, and RVS) will be used to select better radial velocity templates, which should reduce the mismatch between observations and templates and improve the radial velocity quality (Katz et al., 2018).

In the cross-match between the Yoon et al. (2016) CEMP sample and the *Gaia* data are two CEMP-*s* stars that are good new binary candidates: HE 2155–3750 and HE 1305+0007. They have large σ_{Gaia} and large discrepancies (>10 $\mathrm{km\,s^{-1}}$)

between the *Gaia* radial velocity and the literature. The $[Fe/H]_T$ of HE 2155–3750 is a poor match, which may cause part of the discrepancy, but probably not the full $\sim$50 km s^{-1}. These two stars seem good binary candidates.

Additionally, and of more interest for this work, two CEMP-no stars seem to vary in radial velocity: SMSS J1738–1457 and HE 2319–5228. The applied radial velocity template for SMSS J1738–1457 is a poor match in both [Fe/H] and $T_{\rm eff}$. It is unlikely, however, that this causes a difference of $\sim$ 60 km s^{-1}. This star is therefore still a good binary candidate. With its A(C) = 6.18 and [Fe/H] = $-$3.58 (Jacobson et al., 2015), it lies on the lower carbon band. Then HE 2319–5228 shows a modest radial velocity variation of $\sim$ 8 km s^{-1}. We showed that a mismatch between $T_{\rm eff}$ and $T_{\rm eff,T}$ is not likely to cause such large differences (e.g. compare to CS 30301–015), therefore this star remains a good binary candidate. It has A(C) = 6.51 and [Fe/H] = $-$3.4 (Beers et al., 2017), therefore it also lies on the lower carbon band.

Another way to find binary stars using *Gaia* is through the astrometric excess noise (D) and the goodness of fit of the *Gaia* astrometry. This selects stars with poor astrometric solutions that are caused by a companion star (as demonstrated e.g. in Evans et al. 2018). This method works best for nearby stars, and unfortunately, most of the extremely metal-poor CEMP-no stars are too far away. However, two CEMP-no stars in the Yoon et al. (2016) sample, G77–61 and CS 22958–042, have significant astrometric excess noise ($D > 3$). G77–61 is a nearby, high proper motion, known binary star with a poor goodness of fit and D = 207.9. CS 22958–042 has D = 9.7 and also a poor goodness of fit, therefore this star might be in a binary system as well.

The analysis in this section shows that *Gaia* can be used to find new candidate binary CEMP systems. Follow-up spectroscopy is still needed, however, to verify the results and characterise the orbits of the new binary systems.

2.7 Conclusions

We have discussed the results of extending a radial velocity monitoring program for CEMP-no stars that started with Starkenburg et al. (2014). We identified four new CEMP-no stars in binary systems based on their radial velocity variations. Together with stars from the literature, we now have a sample of 11 CEMP-no binaries and 23 likely single CEMP-no stars, resulting in a binary fraction of 32^{+10}_{-9}%. This only marginally agrees with the previous estimate for CEMP-no stars by Hansen et al. (2016a), which was similar to the binary fraction of metal-poor carbon-normal giants (16^{+5}_{-4}%, Carney et al. 2003).

The periods of the CEMP-no binaries are similar to the typical periods of CEMP-*s* stars, ranging from several 100 to several 1000 days for most of the stars. It applies to all the binaries in our sample that if the companion of the main star is currently a white dwarf, it is probable that the current CEMP-no star has been polluted during the AGB phase of the companion. This enhances the amount of carbon in the star and changes its abundance pattern. None of the CEMP-no binary stars show a clear enhancement in [Ba/Fe] that would be indicative of s-process element transfer. Therefore, if binary transfer from an AGB companion has occurred, it must have

been an extremely metal-poor AGB star that has not produced a significant amount of s-process elements.

Our small CEMP-no radial velocity sample shows an apparent difference in binary fraction between the CEMP-no stars with lower A(C) (18^{+14}_{-9} %) and those with higher A(C) (47^{+15}_{-14} %). This higher binary fraction of stars with high absolute carbon abundances can have interesting implications for the origins of CEMP-no stars. We propose that some of the high A(C) binaries started out as carbon-normal stars or CEMP-no stars on the low-carbon band and received extra carbon from a companion, which moved them to the intermediate- to high-carbon band. Alternatively, star formation might have a tendency to form more binaries at high A(C) or extremely low [Fe/H].

The detection of radial velocity variations in the hyper-metal-poor star HE 0107–5240 is very interesting. Some models have tried to explain its abundance pattern based on the assumption that its completely pristine surface has been polluted by a former AGB companion, which currently is a white dwarf. Previous to this current detection, there was no clear evidence for its variability in radial velocity. This makes the binary formation scenario as probable as or even more probable than scenarios invoking faint supernovae or spinstars.

Further monitoring of our new CEMP-no binary stars would allow deriving better orbit parameters, which is necessary to constrain possible mass transfer models. Monitoring of additional stars is needed to investigate wether there truly is a larger fraction of CEMP-no binary stars among stars with high absolute carbon abundance and/or extremely low metallicity. Although *Gaia* may not (yet) be instrumental in studying specific binary systems in detail or in constraining the binary fraction, it shows promise in discovering new binary systems. We have highlighted some new binary candidates.

Some (although not necessarily all) CEMP-no binary stars might have been polluted by a companion star, which affects and complicates the interpretation of their abundance patterns. Their abundances may not only be probes of faint supernovae and/or spinstars, but also of extremely metal-poor AGB stars.

Acknowledgements.

AA and ES gratefully acknowledge funding by the Emmy Noether program from the Deutsche Forschungsgemeinschaft (DFG). KAV thanks the National Science and Engineering Research Council for partial funding through their Discovery Grants program. We thank Lison Malo for her help with the CFHT ESPaDOnS spectra, Norbert Christlieb for sharing his radial velocity data for HE 0557–4840 and HE 0107–5240 with us, Terese Hansen for her re-determination of the stellar parameters for HE 0219–1739 and Tilman Hartwig for sharing his mono-enrichment contours for Figure 2.10. We thank John Norris, Jay Farihi and Terese Hansen for their useful comments on a draft of this work. The observations reported in this paper were obtained with the Southern African Large Telescope (SALT) and the Canada France Hawaii Telescope (CFHT). It also made use of data obtained from the ESO Science Archive Facility under request numbers *aarentsen* 312315 and 358299. This work has made use of data from the European Space Agency (ESA) mission *Gaia* (`https://www.cosmos.esa.int/gaia`), processed by the *Gaia* Data Processing and Analysis Consortium (DPAC, `https://www.cosmos.esa.int/web/gaia/dpac/consortium`). Funding for the DPAC has been provided by national institutions, in particular the institutions participating in the *Gaia*

Multilateral Agreement. This research made extensive use of the MATPLOTLIB (Hunter, 2007) and PANDAS (McKinney, 2010a) Python packages.

2.8 Appendix

2.8.1 Additional figures

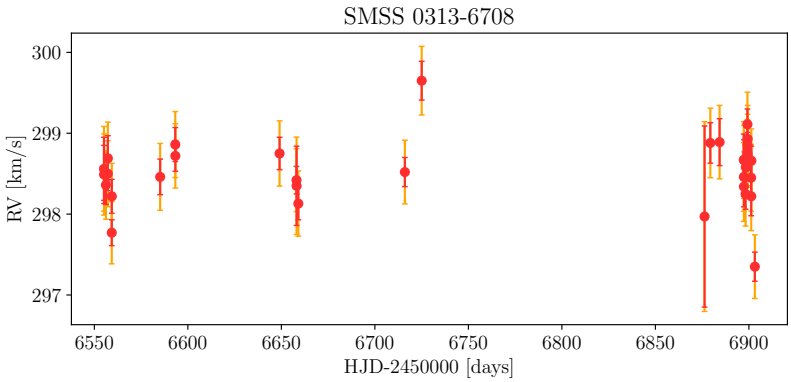

Figure 2.12 — Radial velocities for SMSS 0313–6708, derived from archive UVES spectra. The red error bars represent the uncertainties coming from FXCOR, and the orange error bars include an uncertainty floor of 0.35 km s^{-1}.

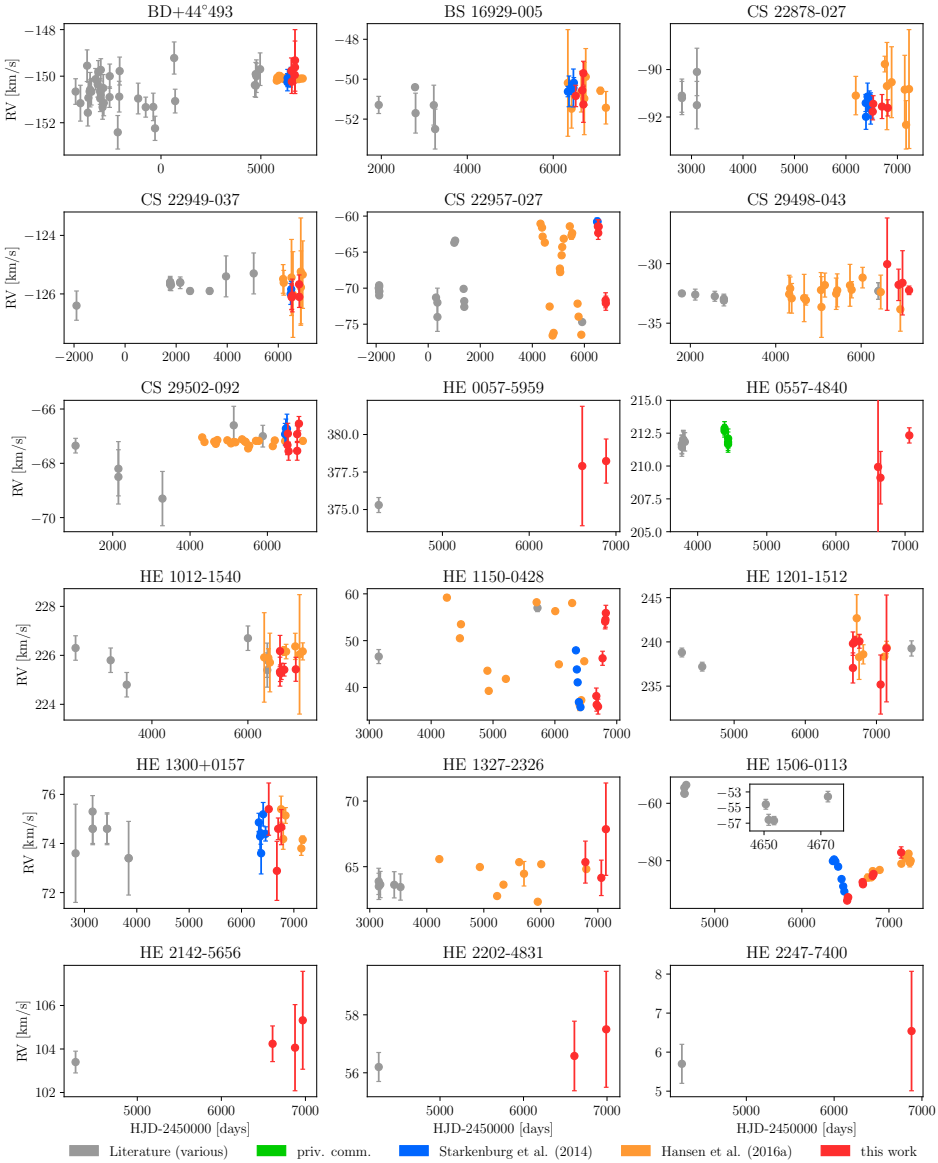

Figure 2.13 — Radial velocities of the 18 program stars that have not yet been shown in the main text, ordered alphabetically. For seven measurements of HE 1327–2326 reported by Hansen et al. (2016a), no uncertainties are provided.

2.8.2 Tables

Table 2.3 — Radial velocities determined from the CFHT and SALT spectra in this work.

Name	rv ($km\,s^{-1}$)	err ($km\,s^{-1}$)	HJD −2450000	flag[a]
BD+44°493	−149.77	0.55	6525.58	C
BD+44°493	−150.24	0.51	6549.55	C
BD+44°493	−149.95	0.35	6697.25	C
BD+44°493	−149.32	1.32	6709.21	C
BD+44°493	−149.62	1.13	6709.21	C
BS 16929–005	−50.84	0.54	6523.22	C
BS 16929–005	−50.56	0.76	6675.68	C
BS 16929–005	−51.27	0.90	6701.62	C
BS 16929–005	−49.70	0.60	6701.63	C
CS 22878–027	−91.77	0.35	6520.32	C
CS 22878–027	−91.45	0.34	6530.23	C
CS 22878–027	−91.56	0.51	6700.64	C
CS 22878–027	−91.62	0.34	6812.32	C
CS 22949–037	−126.10	0.44	6521.53	C
CS 22949–037	−126.12	0.41	6532.54	C
CS 22949–037	−126.05	0.56	6549.50	C
CS 22949–037	−125.67	0.32	6816.59	C
CS 22949–037	−126.10	0.36	6824.54	C
CS 22957–027	−61.43	0.94	6519.53	C
CS 22957–027	−62.34	0.89	6532.55	C
CS 22957–027	−61.46	0.92	6549.52	C
CS 22957–027	−71.68	1.05	6816.61	C
CS 22957–027	−72.09	0.98	6824.56	C
CS 29498–043	−30.04	3.88	6609.25	S
CS 29498–043	−31.78	1.32	6876.25	S
CS 29498–043	−31.61	2.70	6968.25	S
CS 29498–043	−32.24	0.36	7121.64	S

Notes. [(a)] C is observed with CFHT, S is observed with SALT

Table 2.3 — (continued)

Name	rv ($km\,s^{-1}$)	err ($km\,s^{-1}$)	HJD −2450000	flag[a]
CS 29502–092	−67.33	0.35	6519.53	C
CS 29502–092	−66.91	0.38	6530.43	C
CS 29502–092	−67.55	0.33	6548.33	C
CS 29502–092	−66.93	0.31	6770.64	C
CS 29502–092	−67.54	0.35	6770.64	C
CS 29502–092	−66.54	0.26	6816.58	C
HE 0057–5959	377.90	3.98	6611.50	S
HE 0057–5959	378.23	1.47	6886.50	S
HE 0107–5240	48.15	0.49	6618.50	S
HE 0107–5240	46.60	4.75	6858.50	S
HE 0107–5240	47.19	2.39	6957.25	S
HE 0107–5240	48.29	0.94	6990.50	S
HE 0557–4840	209.11	2.00	6644.25	S
HE 0557–4840	212.33	0.58	6923.50	S
HE 1012–1540	226.17	0.64	6669.61	C
HE 1012–1540	225.33	0.59	6669.62	C
HE 1012–1540	225.27	0.34	6675.60	C
HE 1012–1540	225.35	0.33	6697.51	C
HE 1012–1540	225.41	0.26	6758.22	C
HE 1012–1540	225.43	0.49	6998.50	S
HE 1150–0428	38.17	1.70	6669.64	C
HE 1150–0428	36.31	1.38	6675.62	C
HE 1150–0428	35.90	1.59	6697.53	C
HE 1150–0428	46.23	1.51	6770.44	C
HE 1150–0428	54.06	1.55	6812.25	C
HE 1150–0428	54.49	1.62	6817.23	C
HE 1150–0428	55.91	1.65	6823.24	C
HE 1201–1512	239.80	1.32	6669.67	C
HE 1201–1512	237.06	1.70	6669.67	C
HE 1201–1512	240.11	0.52	6697.56	C
HE 1201–1512	240.07	0.79	6760.26	C
HE 1201–1512	235.18	3.34	7058.47	S
HE 1201–1512	239.26	6.04	7141.24	S

Notes. [(a)] C is observed with CFHT, S is observed with SALT

Table 2.3 — (continued)

Name	rv ($km\,s^{-1}$)	err ($km\,s^{-1}$)	HJD −2450000	flag[a]
HE 1300+0157	75.40	1.06	6520.22	C
HE 1300+0157	72.89	1.20	6675.67	C
HE 1300+0157	74.60	0.44	6700.53	C
HE 1300+0157	74.67	0.72	6760.28	C
HE 1327–2326	65.35	1.60	6781.25	S
HE 1327–2326	64.15	1.35	7060.50	S
HE 1327–2326	67.86	3.52	7140.53	S
HE 1506–0113	−93.91	0.54	6520.24	C
HE 1506–0113	−92.80	0.46	6527.22	C
HE 1506–0113	−92.75	0.51	6532.22	C
HE 1506–0113	−87.43	0.46	6697.63	C
HE 1506–0113	−88.23	0.46	6701.64	C
HE 1506–0113	−85.32	0.34	6812.29	C
HE 1506–0113	−84.61	0.37	6823.27	C
HE 1506–0113	−77.13	1.97	7140.54	S
HE 2139–5432	98.58	4.00	6620.25	S
HE 2139–5432	95.79	0.29	6900.25	S
HE 2142–5656	104.24	0.82	6609.25	S
HE 2142–5656	104.06	1.98	6876.25	S
HE 2142–5656	105.32	2.25	6968.25	S
HE 2202–4831	56.58	1.20	6609.25	S
HE 2202–4831	57.50	2.00	6990.25	S
HE 2247–7400	6.54	1.53	6881.50	S
SDSS J0140+2344	−190.32	1.09	6525.55	C
SDSS J0140+2344	−201.03	1.25	6549.52	C
SDSS J0140+2344	−187.99	1.69	6561.38	C
SDSS J0140+2344	−202.03	0.82	6824.57	C
SDSS J1422+0031	−125.43	2.26	6717.50	S
SDSS J1422+0031	−113.96	2.32	7071.59	S
SDSS J1422+0031	−112.35	0.23	7122.52	S

Notes. [(a)] C is observed with CFHT, S is observed with SALT

Table 2.4 — List of 45 CEMP-no stars with multiple radial velocity measurements.

Name	n_{rv}	rv_w ($km\,s^{-1}$)	σ_{rv} ($km\,s^{-1}$)	$P(\chi^2)$	bin?	T_{eff} (K)	log g	[Fe/H]	[C/Fe]	A(C)	[Ba/Fe]	[Mg/C]	ref
BD+44°493	61	−150.09	0.63	0.015	1	5430	3.4	−3.83	1.35	5.95	−0.60	−0.89	1
BS 16929–005	21	−50.77	0.66	0.629	1	5229	2.6	−3.34	0.99	6.09	−0.41	−0.70	2
CD–24°17504	2	136.25	0.49	0.227	1	6228	3.9	−3.41	1.10	6.12	<−1.05	−0.76	3
CS 22166–016	9	−210.39	0.77	0.607	1	5250	2.0	−2.40	1.02[a]	7.05[a]	−0.37	−0.34[a]	4
CS 22877–001	16	166.25	0.12	0.790	1	4790	1.5	−3.31	1.10	6.67	−0.50	−1.17	5
CS 22878–027	21	−91.28	0.61	0.058	1	6319	4.4	−2.51	0.86[a]	6.78[a]	<−0.75	−0.97[a]	2
CS 22949–037	26	−125.74	0.29	0.889	1	4630	1.0	−4.38	1.16	5.97	−0.60	−0.36	5
CS 22957–027	40	−66.87	5.16	$<10^{-6}$	2	5220	2.7	−3.19	2.61	7.87	−0.81	−2.55	5
CS 29498–043	26	−32.55	0.60	0.994	1	4440	0.5	−3.87	2.75	7.62	−0.49	−1.54	5
CS 29502–092	35	−67.22	0.51	0.575	1	4820	1.5	−3.30	1.06	6.59	−1.36	−1.18	5
CS 29527–015	6	47.13	0.42	0.988	1	6577	3.9	−3.32	1.18	6.29		−0.68	2
G64–12	33	442.55	1.05	0.009	1	6463	4.3	−3.29	1.07[a]	6.21[a]	−0.07	−0.59[a]	6
G64–37	22	81.49	0.95	0.312	1	6570	4.4	−3.11	1.12[a]	6.44[a]	−0.36	−0.74[a]	6
G77–61	13	−23.94	11.35	$<10^{-6}$	2	4000	5.1	−4.08	2.65	7.00	<+1.00	−2.16	7
HE 0020–1741	10	93.06	0.83	0.001	1	4765	1.6	−4.05	1.40	6.12	−1.11	−0.71	6
HE 0057–5959	3	375.64	1.60	0.143		5257	2.7	−4.08	0.86	5.21	−0.46	−0.35	2
HE 0107–5240	7	44.78	1.91	$<10^{-6}$	2	5100	2.2	−5.44	3.97	7.03	<+0.93	−3.77	8
HE 0219–1739	15	107.96	5.09	$<10^{-6}$	2	4238	0.5	−3.09	1.90	7.55	<−1.39		9
HE 0405–0526	13	165.66	0.04	1.000	1	5083	3.9	−2.18	0.92	7.17	−0.22		9
HE 0557–4840	22	211.94	0.80	0.965		4900	2.2	−4.73	1.59	5.29	<+0.07	−1.43	10
HE 1012–1540	20	225.84	0.47	0.217	1	5230	2.7	−4.17	2.40	6.67	−0.28	−0.56	5
HE 1133–0555	9	270.70	0.34	0.810	1	5526	1.3	−2.40	2.20	8.31	−0.58		9
HE 1150–0428	27	47.49	8.13	$<10^{-6}$	2	5208	2.5	−3.47	2.37	7.35	−0.48	−1.98	2
HE 1201–1512[b]	13	238.91	2.51	0.016	1	5725	4.7	−3.86	1.14	5.71	<+0.05	−0.86	2
HE 1300–0641	2	68.79	0.11	0.162	1	5308	3.0	−3.14	1.25	6.54	−0.82	−1.23	11
HE 1300+0157	20	74.40	0.70	0.871	1	5529	3.3	−3.75	1.31	5.99	<−0.85	−0.98	2
HE 1302–0954	3	32.56	0.04	0.973	1	5120	2.4	−2.25	1.17	7.37	<−0.53		9
HE 1327–2326	17	64.38	1.30	0.202	1	6180	3.7	−5.71	4.18	6.90	<+1.39	−2.63	12
HE 1410+0213	23	81.12	0.18	0.614	1	5000	2.0	−2.14	1.92	8.21	−0.26	−1.81	13
HE 1506–0113	29	−83.50	11.22	$<10^{-6}$	2	5016	2.0	−3.54	1.47	6.38	−0.80	−0.60	2
HE 2139–5432	4	102.18	10.07	$<10^{-6}$	2	5416	3.0	−4.02	2.59	7.01	<−0.33	−0.99	2
HE 2142–5656	4	103.70	0.80	0.718		4939	1.9	−2.87	0.95	6.61	−0.63	−0.72	2
HE 2202–4831	3	56.32	0.67	0.797		5331	3.0	−2.78	2.41	8.08	−1.28	−2.31	2
HE 2247–7400	2	5.78	0.59	0.602		4829	1.6	−2.87	0.70	6.58	−0.94	−0.69	2
HE 2318–1621	7	−41.77	0.28	0.218	1	4846	1.4	−3.67	1.04	6.30	−1.61	−1.34	14
SDSS J0140+2344[b]	8	−198.65	4.54	$<10^{-6}$	2	5703	4.7	−4.00	1.13	5.56	<+0.34	−0.81	2
SDSS J0929+0238	26	388.33	10.40		2	5894	4.5	−4.97	3.91[a]	7.44[a]	<+1.46	−3.56[a]	15
SDSS J1313–0019	3	255.50	13.50	$<10^{-6}$	2?	5200	2.6	−5.00	2.98	6.41	<+0.22	−2.45	16
SDSS J1341+4741	5	−194.68	26.63	$<10^{-6}$	2	5450	2.5	−3.20	0.99[a]	6.22[a]	−0.73	−0.28[a]	17
SDSS J1422+0031	6	−118.97	6.09	$<10^{-6}$	2	5200	2.2	−3.03	1.70	7.11	−1.18	−0.95	18
SDSS J1613+5309	4	0.01	0.89	0.745		5350	2.1	−3.33	2.09	7.21	+0.03	−1.18	18
SDSS J1746+2455	5	78.45	0.54	0.431		5350	2.6	−3.17	1.24	6.51	+0.26	−0.56	2
SDSS J2206–0925	3	14.83	0.90	0.626		5100	2.1	−3.17	0.64[a]	5.90[a]	−0.85	+0.61[a]	18
Segue 1–7	4	204.86	0.59	0.580		4960	1.9	−3.52	2.30[a]	7.21[a]	<−0.96	+0.94[a]	19
SMSS 0313–6708	34	298.50	0.35	0.592	1	5125	2.3	<−6.50	>5.39	6.02		−1.20	20

Notes. See the next page for notes.

Table 2.4 — Notes

Name	n_{rv}	rv_w ($km\,s^{-1}$)	σ_{rv} ($km\,s^{-1}$)	$P(\chi^2)$	bin?	T_{eff} (K)	$\log g$	[Fe/H]	[C/Fe]	A(C)	[Ba/Fe]	[Mg/C]	ref

Columns: star name; number of radial velocity measurements in Table 2.5; weighted average of radial velocity measurements in Table 2.5; standard deviation of radial velocity measurements in Table 2.5; variability criterion $P(\chi^2)$; binary status (1 = single, 2 = binary, labels as collected by Yoon et al. (2016) and updated in this work); effective temperature; surface gravity; iron abundance; carbon-to-iron ratio; absolute carbon abundance; barium-to-iron ratio, magnesium-to-carbon ratio; literature reference.
$^{(a)}$ These carbon abundances have not been corrected for evolutionary status (all other measurements have been, as reported in Yoon et al. (2016)). However, all of these stars have $\log g \gtrsim 2.0$, where the correction is expected to be small.
$^{(b)}$ Of the two provided solutions in the reference, these are the dwarf solutions.
References: (1) Ito et al. (2013), (2) Yong et al. (2013a), (3) Jacobson et al. (2015), (4) Giridhar et al. (2001), (5) Roederer et al. (2014), (6) Placco et al. (2016b), (7) Plez & Cohen (2005), (8) Christlieb et al. (2004), (9) H16a, (10) Norris et al. (2007), (11) Barklem et al. (2005), (12) Frebel et al. (2008), (13) Cohen et al. (2013), (14) Placco et al. (2014), (15) Bonifacio et al. (2015) and for magnesium Caffau et al. (2011), (16) Frebel et al. (2015), (17) Bandyopadhyay et al. (2018), (18) Aoki et al. (2013), (19) Norris et al. (2010), (20) Bessell et al. (2015), and for magnesium Keller et al. (2014)
(This table is available in electronic form at the CDS via anonymous ftp to `cdsarc.u-strasbg.fr` (130.79.128.5) or via `http://cdsweb.u-strasbg.fr/cgi-bin/qcat?J/A+A/627/A138`)

Table 2.5 — Compilation of 710 radial velocity measurements for 45 CEMP-no stars.

name	rv ($km\,s^{-1}$)	err ($km\,s^{-1}$)	HJD −2450000	ref	bibcode
BD+44°493	−150.66	0.55	−4273.25	Carney+03	2003AJ....125..293C
BD+44°493	−151.16	0.77	−4034.25	Carney+03	2003AJ....125..293C
BD+44°493	−149.55	0.68	−3698.25	Carney+03	2003AJ....125..293C
BD+44°493	−151.57	0.57	−3662.25	Carney+03	2003AJ....125..293C
BD+44°493	−150.93	0.67	−3634.25	Carney+03	2003AJ....125..293C
...	...	...	...	...	...

Notes. We do not include *Gaia* DR2 radial velocities in this table because they are averages over multiple measurements in time.
(This table is only available in electronic form at the CDS via anonymous ftp to `cdsarc.u-strasbg.fr` (130.79.128.5) or via `http://cdsweb.u-strasbg.fr/cgi-bin/qcat?J/A+A/627/A138`)

3 Stellar atmospheric parameters for 754 spectra from the X-shooter Spectral Library

Anke Arentsen, Philippe Prugniel, Anais Gonneau, Ariane Lançon, Scott Trager, Reynier Peletier, Mariya Lyubenova, Yan-Ping Chen, Jesús Falcón Barroso, Patricia Sánchez Blázquez, Alejandro Vazdekis

ABSTRACT

The X-shooter Spectral Library (XSL) is an empirical stellar library at medium spectral resolution covering the wavelength range from 3000 Å to 24 800 Å. This library aims to provide a benchmark for stellar population studies. In this work, we present a uniform set of stellar atmospheric parameters, effective temperatures, surface gravities, and iron abundances for 754 spectra of 616 XSL stars. We used the full-spectrum fitting package ULySS with the empirical MILES library as reference to fit the ultraviolet-blue (UVB) and visible (VIS) spectra. We tested the internal consistency and we compared our results with compilations from the literature. The stars cover a range of effective temperature $2900 < T_{\rm eff} < 38\,000$ K, surface gravity $0 < \log g < 5.7$, and iron abundance $-2.5 <$ [Fe/H] $< +1.0$, with a couple of stars extending down to [Fe/H] $= -3.9$. The precisions of the measurements for the G- and K-type stars are 0.9%, 0.14, and 0.06 in $T_{\rm eff}$, $\log g$, and [Fe/H], respectively. For the cool giants with $\log g < 1$, the precisions are 2.1%, 0.21, and 0.22, and for the other cool stars these values are 1%, 0.14, and 0.10. For the hotter stars ($T_{\rm eff} > 6500$ K), these values are 2.6%, 0.20, and 0.10 for the three parameters.

3.1 Introduction

Libraries of stellar spectra are important resources in astronomy. They are used in stellar population models for the analysis of galaxies and star clusters, and they are used as templates of stellar spectra for example for the automatic determination of stellar atmospheric parameters or for the validation of synthetic stellar spectra. For each of these purposes it is important to have spectra of as many different types of stars as possible and, especially for stellar population modelling, a large spectral range is preferable.

The X-shooter Spectral Library (hereafter XSL; Chen et al. 2014) is a stellar spectral library consisting of a collection of medium resolution spectra for 668 stars spanning a wide range of effective temperature ($T_{\rm eff}$), surface gravity ($\log g$, where g is expressed in cm s^{-2}) and iron abundance ([Fe/H] = $\log(N_{\rm Fe}/N_{\rm H})_* - \log(N_{\rm Fe}/N_{\rm H})_\odot$ where N is the number density). The latter two parameters are written without units throughout. The spectra were observed with the X-shooter instrument (Vernet et al., 2011) mounted at the Very Large Telescope (VLT), at a resolving power $R = \lambda/\Delta\lambda$ of $\sim$ 10 000 in the wavelength range λ = 3000-24 800 Å, where $\Delta\lambda$ is the full width at half maximum of the line-spread function (LSF).

With XSL, it will be possible to build the first stellar population models fully consistent from the near the ultraviolet to the near infrared. Before XSL, in order to cover this wavelength region, the models had to combine different libraries made of different stars, observed at different spectral resolution, as for example in Vazdekis et al. (2016) or in Villaume et al. (2017). The resulting potential discontinuities limit the reliability and consistency of the predictions of the global spectral energy distributions. For other applications, the large wavelength coverage will also be valuable to validate synthetic stellar spectra, or to cross-calibrate surveys made in different, narrower spectral regions.

Knowledge of the atmospheric parameters is required to use a library either for stellar characterization or for population models. In the latter case, for instance, the models combine individual spectra according to the expected number of stars in each cell of the parameter space ($T_{\rm eff}$, $\log g$, [Fe/H]). The accuracy of the atmospheric parameters is in fact a recurring issue. For example, a modest bias of the temperature of the giant branch can change the determination of the age of old populations by several gigayear (e.g. Charlot et al., 1996; Koleva et al., 2007) and offsets in the three parameters can mimic abundance ratio variations (Percival & Salaris, 2009).

Different methods can be used to determine stellar atmospheric parameters. At medium resolution, a well-established approach is full-spectrum fitting using synthetic or empirical libraries. The full-spectrum fitting method consists of comparing an observed spectrum to a template spectrum from a reference library that can be either empirical or synthetic. After adjusting the continuum and line broadening, the minimization of the residuals enables the estimation of the atmospheric parameters. The greatest advantage of full-spectrum fitting is that it allows the use of the whole spectral range and many spectral features at the same time, instead of picking specific features, therefore making optimal usage of the available signal. Some examples of full-spectrum fitting codes are TGMET (for

Temperature, Gravity, MEtallicity, Katz et al. 1998, Soubiran et al. 2003), MATISSE (MATrix Inversion for Spectral SynthEsis, Recio-Blanco et al., 2006) and ULySS (University of Lyon Spectroscopic Software, Koleva et al., 2009).

Synthetic libraries, computed ab initio using stellar atmosphere models and synthesis of the spectral lines, provide references at any desired resolution and are free of noise or interference with peculiarities of real individual stars. Comparing synthesized and observed spectral lines is the only method to estimate the detailed abundances of stars. Therefore, synthetic libraries are a cornerstone of the characterization of stars. However, synthetic spectra cannot presently reproduce all the observed features of a stellar spectrum consistently across wavelength and parameter space (e.g. Martins & Coelho, 2007; Coelho, 2014). This is because of uncertainties and approximations in the treatment of the physics and because of an imperfect knowledge of the millions of atomic and molecular transitions needed to predict the spectral lines (see e.g. Kurucz, 2017). Some lines are not predicted at accurate enough wavelength and strength, other lines may simply be missing in the models. On the other hand, empirical libraries can reproduce an observed spectrum with a precision of a few tenths of a percent (Wu et al., 2011a), although these libraries suffer from a number of observational defects, are affected by the peculiarities on their stars (such as rotation, binarity, or particular abundance patterns), and their parameter space coverage is restricted. This precision is a valuable advantage over using synthetic spectra at medium spectral resolution and in the regime of low temperatures, such as for late-K and M type stars, where isolated and well-modelled lines cannot be cherry-picked.

The goal of this paper is to provide homogeneous atmospheric parameters of as many XSL stars as possible. For XSL, using full-spectrum fitting with empirical references appears to be the most appropriate choice because of its spectral resolution and because of its large coverage of spectral type, in particular for cool stars. In this paper we analyse the XSL spectra with the ULySS package[1] (Koleva et al., 2009), using the MILES empirical library (Sánchez-Blázquez et al., 2006a; Falcón-Barroso et al., 2011) as a reference. The spectrum to be analysed is compared to that computed with the MILES spectral interpolators (Prugniel et al., 2011; Sharma et al., 2016), and the minimization of the residuals leads to an estimation of the atmospheric parameters. The MILES library (resolving power $R \sim 2200$) was designed to cover the needs of population synthesis applications and has a wide coverage of the parameter space. Its atmospheric parameters are bound to literature compilations (e.g. PASTEL; Soubiran et al., 2016) and homogenized as in Cenarro et al. (2007).

In Section 3.2 we describe the current XSL spectral library and in Section 3.3 we describe the method we use to determine the parameters. In Section 3.4 we present the results and quantify the uncertainties, and we end with a summary in Section 3.5.

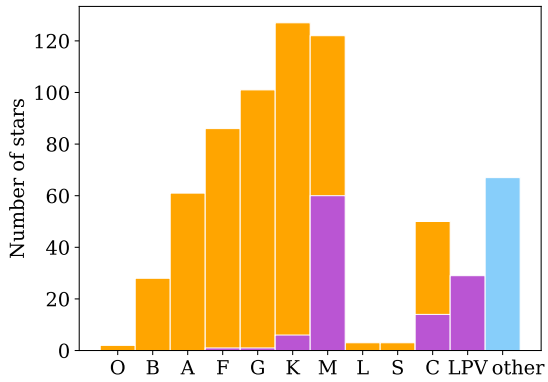

Figure 3.1 — Distribution of the spectral types present in XSL, as retrieved from SIMBAD. We highlight the number of stars known as LPV objects in purple. The stars in the 'LPV' bin have no given spectral type but have object types labelling them as LPV objects. The stars in the blue bin 'other' do not have spectral types in SIMBAD, nor have object types which label them as LPV objects.

3.2 Data

The spectra for XSL were obtained under an ESO Large Programme (run IDs 084.B-0869(A/B), 085.B-0751(A/B) and 189.B-0925(A/B/C/D) at the VLT with the X-shooter instrument (Vernet et al., 2011). The instrument splits the light using dichroics towards three echelle spectrographs: the ultraviolet-blue arm (UVB) covers the wavelength range 3000 – 5500 Å, the visible (VIS) covers 5300 – 10200 Å, and the infrared (NIR) covers 10000 – 24800 Å. The mean resolving powers of the spectral arms are ~ 9000, 11000, and 8000 for the UVB, VIS, and NIR arms, respectively.

The present work is based on a preliminary version of the second XSL data release (DR2: Gonneau et al., in prep). The DR2 consists of ~800 UVB, VIS, and NIR spectra of 668 stars, and it includes the re-reduced spectra of DR1. Differences between the version used in this work and that to be released in the final DR2 concern only details of the flux calibration and have no significant effect on the measured parameters. The DR2 does not contain merged spectra of the three arms. In this paper, we analyse separately the UVB and VIS arms.

The spectra have associated error spectra obtained by propagating the estimated noise (photon noise plus detector noise) through the data reduction process. Some spectra of cool stars have very low signal in the blue. The minimum wavelength that can reasonably be considered as usable (keyword WMIN) is indicated in the DR2 and we used this information to trim the blue end of the spectra in our analysis.

The details of the selection of stars for XSL will be described in the DR2 paper. In short, the XSL stars were selected to cover as much of the Hertzsprung-Russell

[1] `http://ulyss.univ-lyon1.fr`

diagram as possible; these stars have a wide range of metallicities. We did not attempt to provide our own spectral types based on the spectra. We retrieved the spectral types for as many stars as possible from the SIMBAD database (Wenger et al., 2000), and we show the distribution in Figure 3.1. We highlight the long period variable (LPV) stars in each of the bins in purple. Some stars do not have a spectral type in SIMBAD, but have an object type which labels the star as LPV. We included these stars in the LPV bin of the figure. Additionally, there are stars that fall into the 'other' category; these stars either do not have a spectral type and object type or they have one that labels them as a peculiar star (other than LPV).

Some stars are observed more than once. Several cool giant stars were re-observed to monitor their spectral variability, some stars were re-observed to assess the stability of the instrument and data reduction, and others were repeated because of (sometimes unfounded) concerns about the observing conditions.

3.3 Method

We used ULySS (Koleva et al. 2009, version 1.3.1) to determine the stellar atmospheric parameters for the spectra in XSL. This full-spectrum fitting package performs a χ^2 minimization between a model spectrum and an observed spectrum. The model spectrum $S(\lambda)$ in ULySS is described by

$$S(\lambda) = P_n(\lambda) \times G(v_r, \sigma) \otimes \mathrm{TGM}(T_{\mathrm{eff}}, \log g, [\mathrm{Fe/H}], \lambda), \tag{3.1}$$

where $P_n(\lambda)$ is a series of Legendre polynomials up to degree n, and $G(v_r, \sigma)$ is a Gaussian broadening function described by the radial velocity v_r and the broadening width[2] σ. The TGM function returns a model spectrum for given stellar atmospheric parameters T_{eff}, $\log g$, and [Fe/H] by interpolating a reference stellar spectral library. The spectra are binned in logarithmic wavelength, so that the kinematical effects (Doppler shift and rotational broadening) can be expressed by a single convolution to all pixels. The function $P_n(\lambda)$ corrects for the Galactic extinction and for any suboptimal flux calibration of the observed spectrum or the reference library. The free parameters in the fit of an observed spectrum to a model spectrum are T_{eff}, $\log g$, [Fe/H], v_r, σ, and the coefficients of $P_n(\lambda)$, which are all fit at the same time to deal consistently with degeneracies between the parameters.

The spectral interpolator approximates each wavelength bin of a spectrum with a polynomial function of T_{eff}, $\log g$, and [Fe/H]. Each term of the polynomial is a product of powers of the three parameters (see e.g. Section 2.5.2 in Prugniel et al., 2011). The interpolator combines three sets of polynomials corresponding to three temperature regimes, for OBA, FGK, and M stars, defined as follows:

$$\begin{aligned} &\text{OBA regime}: T_{\mathrm{eff}} > 7000\,\mathrm{K} \\ &\text{FGK regime}: 4000 < T_{\mathrm{eff}} < 9000\,\mathrm{K} \\ &\text{M regime}: T_{\mathrm{eff}} < 4550\,\mathrm{K} \end{aligned}$$

[2]When analysing a line-of-sight integrated galaxy spectrum, σ is the so-called velocity dispersion, while in the present case it is related to the rotational velocity. To some extent, G also absorbs uncertainties in the wavelength calibration and width of the LSF.

The three regimes are smoothly connected. For the hot stars the polynomials have 19 terms, and they have 26 terms for the warm and cool stars.

Several spectral interpolators have been constructed by members of our group over time for the different popular stellar libraries, and some improvements have emerged with the successive versions. Because the results obtained with the MILES interpolator used in this work are not independent of those obtained with previous versions, we provide a brief historical summary. The first interpolator was made at a resolving power $R = 10000$ for the ELODIE library (Prugniel & Soubiran, 2001). The library and the interpolator were later improved, and the current version 3.2 was described in Wu et al. (2011a). The latter interpolator is available on the ULySS website. The ELODIE interpolator covers the wavelength range 3900 – 6800 Å and uses input atmospheric parameters compiled from the literature; each individual published set of measurements was carefully examined to adopt a "best" set for each star. The self-inversion of the library, i.e. the redetermination of the stellar parameters by fitting the library spectra with its associated interpolator allows for a check of the self-consistency of the input parameters and in fact is used to detect and correct inaccurate measurements in the compilation (see e.g. Prugniel et al., 2011). The self-inverted parameters have a high internal consistency, which is a characteristic lacking in the heterogeneous literature compilation, but these self-inverted values are affected by the systematics of the interpolator. For example, the inverted parameters in some specific regions of the parameter space may display biases because the polynomials do not perfectly reproduce the physical variation. The choice of the terms in the polynomials, the definition of the temperature regimes, and the weighting of individual spectra were tuned to minimize those systematics.

We note that the polynomials do not strictly interpolate between the spectra of the library, but also perform some approximation. This is an important aspect for empirical libraries as it results in a smoothing of both the noise and the effects of "hidden" parameters. These hidden parameters include all the characteristics of the stars that are not reflected by the three fundamental parameters. They are for example the individual abundances, the rotation, chromospheric activity, binarity (although binaries are as far as possible avoided in spectral libraries), and also include flux calibration errors, or uncertainty in the correction of the Galactic extinction.

The polynomials naturally go wild outside the populated region of the parameter space. To alleviate the consequences, the interpolators therefore include extrapolation support, which is based on synthetic spectra differentially corrected to smoothly connect with the library (see Wu et al. 2011a).

Whereas the ELODIE interpolator was based on a literature compilation corrected for inconsistencies using a self-inversion, the MILES interpolator started from a catalogue of parameters obtained by fitting the MILES spectra using the ELODIE interpolator (Prugniel et al., 2011). Additionally, the MILES version was supplemented by literature values in regions of the parameter space in which the ELODIE parameters are not reliable. This approach took advantage of the high internal consistency in the FGK regime, where the ELODIE library is well populated and the interpolator is very reliable, but avoided being affected by the

ELODIE interpolator systematics in the outskirts of the parameter space. This input catalogue and the self-inversion were carefully checked against the literature compilation.

The last version of the MILES interpolator (Sharma et al., 2016) improved the modelling of cool stars, in particular by supplementing MILES with more spectra of M dwarfs. This feature is important for XSL, which contains a number of cool stars that are out of the range of ELODIE. Therefore we chose to use the MILES interpolator for the present analysis and we used the ELODIE interpolator for comparison tests. Our choice of the MILES interpolator sacrifices the original spectral resolution of XSL, which is higher than MILES. However Prugniel et al. (2011) and Koleva & Vazdekis (2012) have shown that the resolution does not have a strong influence on the precision of the derived parameters. The MILES library also offers a wider wavelength range (3500 – 7400 Å) than ELODIE, which is an advantage in this study.

The reliability of ULySS with these interpolators has been tested in various papers (in particular Wu et al. 2011a; Prugniel et al. 2011; Koleva & Vazdekis 2012; Sharma et al. 2016) by comparing the results with datasets from the literature. The method is robust for FGK stars over a wide range of iron abundances ($-2.5 <$ [Fe/H] < 0.3) and gravities ($0 < \log g < 5$). In this regime the ELODIE and MILES libraries are well populated and the associated stellar parameters are the most reliable. For hotter or cooler stars, and for extreme gravities or iron abundances, the situation is more complicated. There are both fewer stars in the libraries, their parameters are less securely determined in earlier detailed studies, and furthermore the physics of these stars often cannot appropriately be described by only the three parameters that we are using. For hot stars, in addition, the narrow and weak lines usually considered as markers of the chemical composition are typically smeared out at medium or low spectral resolution, hence affecting the possibility of measuring abundances; we note however that this effect has not been formally checked. Thanks to the careful tuning of the MILES interpolator, the method generally behaves well in an extended region of the parameter space, but comparisons with external measurements remain important to detect issues.

The only types of stars included in XSL that cannot a priori be measured with our method are (i) late-M and L-type dwarfs, (ii) carbon stars, and (iii) other peculiar stars. With the wavelength coverage from the MILES interpolator (3500 – 7400 Å) we can analyse the UVB and VIS spectra in XSL. We choose to fit the UVB between 4000 – 5500 Å, except for the hottest stars for which we use the range 3800 – 5500 Å to include a few more lines in these almost line-less spectra, and the VIS between 5600 – 7400 Å. Above 5500 Å for the UVB and below 5600 Å for the VIS the spectrum is too contaminated by the unstable response of the dichroic of the X-shooter instrument.

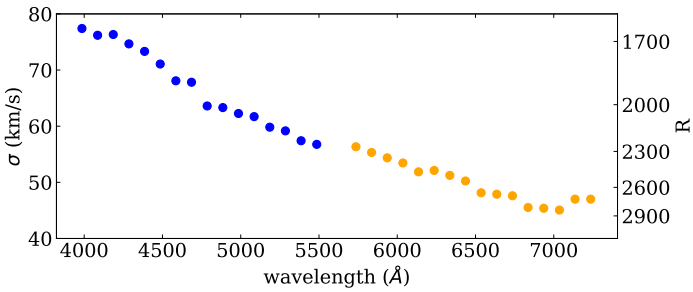

Figure 3.2 — Line spread function for the MILES interpolator, separated by colour for the UVB and VIS.

3.3.1 Resolution matching

If we used a reference stellar library with a higher spectral resolution than XSL, the procedure would be to use the relative LSF[3] of XSL with respect to the library to degrade the resolution of the reference library to match that of XSL. In the present case we have to do the opposite.

The LSF represents the broadening of spectral lines due to the instrumentation and data reduction. In the present paper we are assuming it is Gaussian, which is close to the actual shape, and the difference is not expected to influence the present analysis. The LSF of the MILES interpolator varies with wavelength, but as its determination in Sharma et al. (2016) does not cover the full wavelength range used in this paper, we redetermined it by comparing an interpolated spectrum for the parameters of the Sun to the National Solar Observatory solar spectrum stored in HyperLeda[4] (Makarov et al., 2014) and to a high resolution synthetic spectrum. The resulting MILES interpolator LSF is represented in Figure 3.2. Its Gaussian velocity dispersion varies from ~80 $\mathrm{km\,s^{-1}}$ ($R \sim 1600$) at 4000 Å to ~45 $\mathrm{km\,s^{-1}}$ ($R \sim 2800$) at 7000 Å.

The XSL LSF, described in the DR2 paper, has a Gaussian velocity dispersion of about 13 $\mathrm{km\,s^{-1}}$ and 11 $\mathrm{km\,s^{-1}}$, respectively, in the UVB and VIS regions that we are using. The variation and non-Gaussianity of the XSL LSF with wavelength can be neglected for our purposes. The velocity dispersion of the relative LSF of MILES with respect to XSL can be computed as $\sigma^2_{\mathrm{relative\,LSF}} = \sigma^2_{\mathrm{MILES\,LSF}} - \sigma^2_{\mathrm{XSL\,LSF}}$. The relative LSF is different from the MILES LSF by only ~2 $\mathrm{km\,s^{-1}}$ because $\sigma^2_{\mathrm{XSL\,LSF}}$ is much smaller than $\sigma^2_{\mathrm{MILES\,LSF}}$. However, a slight over-smoothing of the spectra is actually beneficial to the convergence of the radial velocities, therefore we simply convolve the XSL spectra with the MILES LSF instead of the relative LSF.

We used the ULySS function ULY_SPECT_LSFCONVOL to inject the MILES interpolator LSF in the XSL spectra. Because the resulting spectrum would be needlessly

[3] The relative LSF of spectrum A with respect to spectrum B is the broadening that shall be applied to spectrum B to match the resolution of spectrum A. In general, the LSF depends on the wavelength and it may depart from a Gaussian.

[4] http://leda.univ-lyon1.fr/

oversampled, we log-rebinned the spectra to a pixel value of 50 $\mathrm{km\,s^{-1}}$, which is comparable to the sampling of MILES (in the red spectral range, where MILES has the highest resolution, the pixel size is 2.25 times the full width at half maximum of the LSF).

3.3.2 Rest-frame reduction

Although our full spectrum fitting method adjusts the velocity (parameter v_r in Eq. 3.1), this velocity shift should not exceed, by a couple of times, the broadening of the library. As XSL includes stars with radial velocities up to almost 400 $\mathrm{km\,s^{-1}}$, it is necessary to reduce the spectra to the rest frame; this is achieved by changing the world-coordinate system of the spectra and does not require any additional rebinning. We corrected the spectra using the velocities which were determined as described in the DR2 paper.

3.3.3 Multiplicative polynomial

The optimal value for the degree n of $P_n(\lambda)$ mainly depends on the resolution, the fitted wavelength range, and the accuracy of the wavelength calibration of the spectra. We used the test described in Koleva et al. (2009) to find the best value for n for our spectra. We selected six stars of different spectral types and fit these with n ranging from 0 to 300 in the wavelength region 4000 – 5500 Å for the UVB arm, and 5600 – 7400 Å for the VIS, from which we determined the value for n where the parameters seem to become independent of n.

The solutions are nearly stable for $n \gtrsim 10$. When using echelle spectra, such as those from the ELODIE library or the present XSL spectra, the case for using higher values of n comes from the presence of residuals from the blaze correction that may leave wavy fluctuations in the flux calibration with an amplitude of the order of one percent. For high S/N observations, this effect is prominently visible in the residuals of the fit with ULySS, although these residuals barely affect the solution because these patterns are not correlated with any physical feature. High values of n correct this effect, but they sometimes tend to absorb physical features, in particular for hot stars for which the wings of broad H lines are partly fitted by the polynomial. This raises concerns that the exact degree of the polynomial may affect the solution. However, we analysed the spectra in this work both with $n = 10$ and $n = 30$, and it appears that taking a higher degree does not bias the parameters. Stars between ~7000–9000 K are an exception; for these stars the resulting T_eff from the UVB fit clearly depends on the choice of n. We estimate the bias introduced in Section 3.4.4.

With $n = 30$, most of the echelle residuals and features of imperfect flux calibrations are taken out. Therefore we adopt $n = 30$ as the degree for $P_n(\lambda)$, for both the UVB and the VIS spectra. For some low S/N spectra for which the blue sections of our wavelength range are below the S/N threshold, n is reduced proportionally to the wavelength range actually used.

If the multiplicative polynomial goes to negative values or ULySS cannot find a fit, ULySS automatically reduces n. This mainly happens for some of our cool giant stars.

3.3.4 Fitting a spectrum

The ULySS package performs a local minimization, starting with a set of parameter guesses. The convergence region is generally very wide, meaning that starting with a guess very distant from the actual parameters, the program still converges to the right solution. However, in some cases the solution may be trapped in a local minimum. This mainly happens when the star lies in the margins of the parameter space. The solution to find the absolute minimum is to repeat the minimization starting from a variety of initial guesses, and adopt local solutions with the best χ^2. In ULySS, this is easily achieved by providing a grid of guesses rather than a single value. We use the following grid:

$$T_{\rm eff} \in [3000, 4000, 5600, 7000, 13000, 30000]$$
$$\log g \in [0.5, 1.8, 3.8]$$
$$[{\rm Fe/H}] \in [-1.7, -0.3, 0.5]$$

The bounds of the parameter space are set to [2700, 40000] K, [−0.5, 5.9], and [−4.0, 1.0] for $T_{\rm eff}$, $\log g$, and [Fe/H], respectively. The complete algorithm is

- Mask emission lines that may prevent the convergence, or make it slower
- Run the minimization with the above grid of guesses
- Do another minimization starting from the best solution of the run with multiple guesses, using the `/CLEAN` option, which automatically rejects bad regions in the fit (owing to e.g. bad pixels, emission lines, and telluric lines) to improve the final solution.

We include an extra step for stars hotter than 8000 K, for which we found that including the `/CLEAN` option sometimes results in a bad fit indicated by unphysical σ (broadening width) values. The reason for this is that hot stars only have a few spectral lines, and if they are cleaned out because they are not well fitted, a low χ^2 is achieved by smoothing the spectra. Therefore, if σ is higher than 500 $\mathrm{km\,s^{-1}}$, we redo the fit without the `/CLEAN` option on. This results in a much better fit for many of these hot stars.

3.4 Results

We fitted 814/815 UVB/VIS spectra of 668 unique stars included in XSL DR2 to obtain their stellar atmospheric parameters. In this section we select the acceptable measurements, analyse the errors, and combine the measurements in the UVB and VIS arms.

3.4.1 Selection of the reliable solutions

In this section, we establish criteria to identify the cases in which the derived parameters are unreliable either because the observation has an insufficient quality (in the wavelength region used) or for other reasons. Our analysis method is valid

only for stars that can be modelled with the interpolator. Some special stars in particular, such as carbon stars (but see Gonneau et al. 2016, 2017 for a different approach) and other peculiar stars, cannot be modelled well.

The reduced χ^2 of the fit, which compares the magnitude of the residuals to the fit with the expected error from the noise spectrum, indicates the quality of the fit. But as the interpolator has a limited capability to represent real spectra, very high S/N spectra are unavoidably fitted with a large χ^2 ; reciprocally, very low S/N observations may be fitted with $\chi^2 \approx 1$, even if the parameters of the stars are not correctly matched. Therefore, the criterion cannot simply be to reject the solutions with χ^2 larger than a threshold. A more realistic approach is to set a threshold on the signal to residuals ratio (SRR; computed over the whole wavelength range of the fit; normally SRR < S/N).

The fitted broadening width σ (see Eq. 3.1) is related to the stellar rotation for some hot stars, but high values generally indicate a failed fit. When no proper match is found in the library, the minimum χ^2 is obtained by strongly smoothing the model spectrum.

We empirically determined the following recipe to consider a solution as acceptable for the UVB arm:

- Reject solutions with $\sigma > 500\ \mathrm{km\,s^{-1}}$
- Reject solutions with $\sigma > 300\ \mathrm{km\,s^{-1}}$ and $T_{\mathrm{eff}} < 10\,000$ K
- For $T_{\mathrm{eff}} < 3600$ K, reject solutions with SRR< 1.5
- For $T_{\mathrm{eff}} > 3600$ K, reject solutions with SRR< 15

And for the VIS arm:

- Reject solutions with $\sigma > 300\ \mathrm{km\,s^{-1}}$
- For $T_{\mathrm{eff}} < 3600$ K, reject solutions with SRR< 3
- For $T_{\mathrm{eff}} > 3600$ K, reject solutions with SRR< 25

These criteria were tuned after visual inspection of the residuals to the fits to exclude the solutions that did not converge (they generally went to high σ) or where, because of the low quality of the spectra, we could not see any match of the spectral features. These criteria also rejected most of the carbon stars because the carbon features cause large residuals, and for those that were accepted, the non-carbon features are well fitted. Parameter estimations from 734 UVB and 737 VIS observations are considered reliable according to these criteria.

3.4.2 Error analysis

The propagation of the errors from the noise in the observations provides us with error estimates on the parameters computed by the ULySS software. This is what we call the formal error (or precision). However, the error propagation through the complex data reduction and analysis may suffer from some approximations or

inaccuracies, and therefore the formal errors may not be an unbiased estimator of the actual effect of the noise. Therefore, in Sect. 3.4.3, we use the repeated observations to correct the formal errors and derive what we call the internal errors.

It is well known that the internal errors in stellar parameter determination strongly underestimate the real errors. There are some clear reasons for this. Several observational effects (e.g. non-linearity of the detector and imperfect subtraction of diffuse light in the spectrograph), peculiarities of the individual stars, hidden parameters (e.g. abundance patterns, rotation, and binarity), and inaccuracies and systematics of the models (in this case the spectral interpolator) all contribute to the final error budget. These effects are at the origin of systematics between series of measurements obtained with different data or methods. They have been studied in a number of literature studies (e.g. Smiljanic et al., 2014), and a working group of the International Astronomical Union has been tasked to propose practices to bring a better understanding of this error budget[5]. In Sections 3.4.4 and 3.4.5 we complete our error analysis to estimate the total error.

Finally, our results are compared to some literature compilations in Section 3.4.6 and 3.4.7 to provide us with some hints of the external errors, although attributing the fair share of responsibility of the differences between our measurements and the used reference is mostly a subjective choice.

3.4.3 Internal precision

The validity of the formal errors returned by ULySS relies on the estimated variance of each bin of the spectrum and on the correlation of the noise between successive bins[6]. Using a long series of observations of the same star, Sharma et al. (2016) showed that if the noise on the spectrum and its correlation are well estimated, the formal fitting errors on the derived parameters match the internal errors, i.e. the errors resulting solely from the noise.

In our sample we do not have one star with a long series of observations, but we do have many stars with multiple observations, observed either two, three, or four times. We use the difference in determined parameters between in total 135 pairs of observations that we consider reliable to estimate the validity of the formal errors returned by ULySS, where we have excluded stars with $T_{\rm eff} < 3700$ K, which are likely variable.

Not all spectra have the same S/N, therefore we compute the following weighted difference for each pair of observations i:

$$\Delta \mathrm{P}_{w,i} = \frac{\mathrm{P}_{1,i} - \mathrm{P}_{2,i}}{\sqrt{\epsilon_{1,i}^2 + \epsilon_{2,i}^2}}, \tag{3.2}$$

where P can be $T_{\rm eff}$, $\log g$ or [Fe/H], ϵ is the formal ULySS error on the respective parameters, and 1 and 2 indicate two observations of the pair. Statistically, it

[5] `http://svo2.cab.inta-csic.es/projects/iaug5wg`

[6] The rebinning of the spectrum results in a correlation of the noise over adjacent pixels which appear as non-diagonal terms in the co-variance matrix. The error spectrum is the square root of the diagonal of this matrix. In ULySS, this effect can be modelled using a factor that corrects the number of independent pixels; neglecting this correlation results in underestimating the errors.

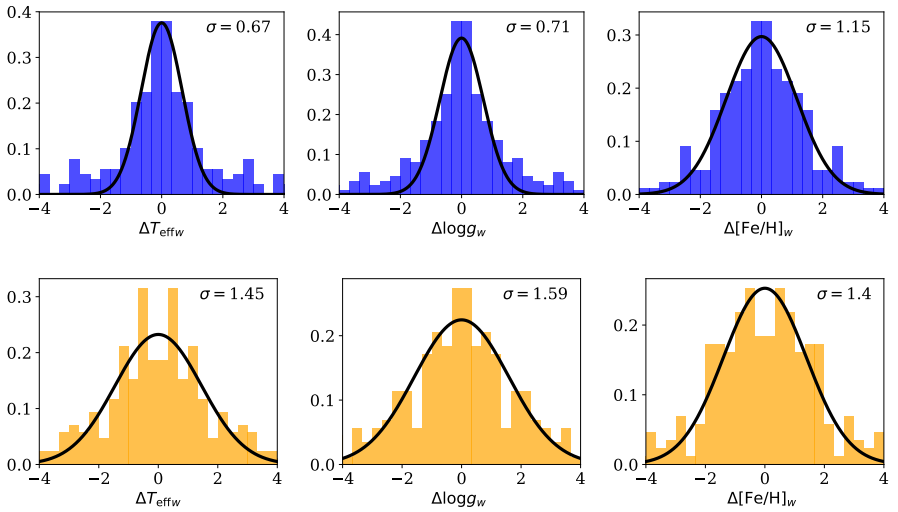

Figure 3.3 — Distributions of ΔP_w for pairs of observations of the same star. The UVB and VIS analyses are presented in the top and bottom row, respectively. The Gaussians with a mean of zero and a standard deviation computed as described in the text are shown, the standard deviations of these Gaussians are given in the top right corner of each panel.

should follow a Student's t distribution, which is close to a Gaussian but has heavier tails. If the formal and internal errors are equal, we would expect a standard deviation of one for the distribution of ΔP_w. A deviation from one indicates that the estimated noise spectra may be incorrect. We computed standard deviations using the python `sigma_clip` function with a clipping sigma of 2.2. We present the results in Figure 3.3, in which each pair is shown twice to produce symmetrical distributions.

The standard deviations are of the order of 0.7 for the UVB and of 1.5 for the VIS. Experimenting with the degree of the multiplicative polynomial (see Sect. 3.3.3) we found that these standard deviations change by about 10%. The prominent difference between the two arms is likely due to an incorrect estimate of the noise spectra in DR2. The suspected reasons are that the noise variance was interpolated rather than rebinned when the spectra were transformed into evenly distributed wavelength bins, and that we did not take into account the correlation of the noise. Both effects depend on the ratio of the size of the pixels on the detector and in the final spectrum, which varies with wavelength and between the arms. We did not investigate the effect further because it belongs to the data reduction. We can rule out that the arms contrast is from causes other than the noise propagation, for example to different sensitivity to degeneracy or systematics of the interpolator, because those effects would change significantly over the parameter space, which we do not observe. We therefore use the above factors to rescale the formal errors into internal errors.

We finally note that the variations in the stellar parameters between repeated observations of stars are very small. After 3σ clipping (which excludes 8 out of 135 pairs), the dispersion is 0.5% for differences in $T_{\rm eff}$, 0.05 for differences in $\log g$, and 0.03 for differences in [Fe/H].

3.4.4 Systematics and total errors

In this section we investigate the systematic effects introduced by the spectral interpolators and the other effects that contribute to the total error. First we compare the UVB solutions obtained with the MILES and ELODIE interpolators in the same wavelength range. The two interpolators were computed from two different libraries (different stars and spectra, and different distribution in the parameter space), and therefore we may expect different systematic effects.

Then, we compare the analysis in the two arms with the MILES interpolator, which, as they correspond to two non-overlapping wavelength regions, can also be regarded as two different interpolators. Indeed, as each spectral bin is independently modelled with a specific polynomial, the interpolator in two spectral regions may have unrelated systematic effects, even if the library is the same. As two separate wavelength regions were used, the effect of hidden parameters, such as rotation, binarity, contamination by the light of nearby stars, or detailed abundances, are likely to be different.

While the first test addresses only the question of the systematics of the interpolators, the second is also sensitive to the other observational and physical effects. The second test is a more complete assessment of the total error.

Comparison between MILES and ELODIE solutions (UVB)

We computed the parameters again with the higher resolution ELODIE interpolator for our UVB spectral range; the ELODIE range is limited to 6800 Å in the red, and therefore we cannot perform the test for our VIS range. We used the same procedure, except that in this case the resolution of XSL spectra did not have to be reduced and we only corrected for the changing of the XSL LSF with wavelength. The comparison with the parameters derived using the MILES interpolator is shown in Figure 3.4, i.e. for stars with $T_{\rm eff} > 4000$ K, since the ELODIE interpolator has not been optimized for cooler stars. The standard deviations for stars with $4000 < T_{\rm eff} < 5500$ K and $\log g > 1$ are 1%, 0.12, and 0.08 for $T_{\rm eff}$, $\log g$, and [Fe/H], respectively, after clipping 3σ outliers.

There are several trends worth noting. For the coolest stars ($T_{\rm eff} < 5500$ K), the MILES $\log g$ is systematically higher than that from ELODIE by 0.1, and the MILES [Fe/H] is systematically lower by 0.1. For $5500 < T_{\rm eff} < 7000$ K, the biases are smaller; MILES $\log g$ is systematically higher by 0.05 and the MILES [Fe/H] is systematically lower than the ELODIE values by 0.05. Finally for the hottest stars ($T_{\rm eff} > 7000$ K) the most notable bias is in $T_{\rm eff}$, where the MILES values are on average 3% higher. The magnitudes of these biases are comparable to the standard deviations of the difference between the two series. The MILES interpolator has been carefully tuned (Prugniel et al., 2011; Sharma et al., 2016) to minimize the

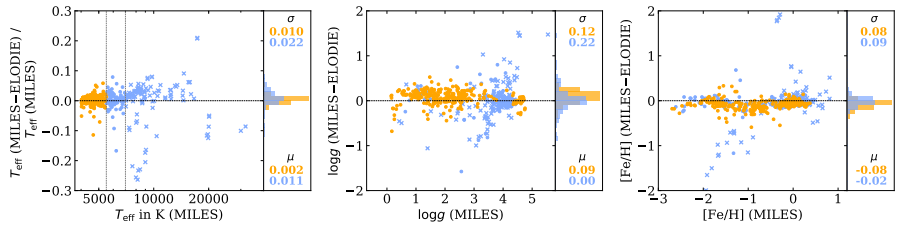

Figure 3.4 — Comparison between the MILES and ELODIE solutions in the UVB for the stars with $T_{\rm eff}$ (MILES) > 4000 K. Each atmospheric parameter is shown in a separate panel, and the colour of the symbols identify two temperature ranges (dividing at 5500 K). Stars hotter than 7000 K are shown as crosses. In the $T_{\rm eff}$ and log$g$ panels, seven and two outliers, respectively, are not shown (all hot stars). The dispersion σ and mean offset μ for the two temperature ranges are indicated.

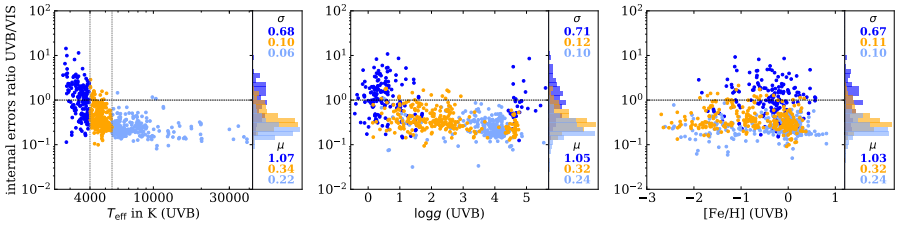

Figure 3.5 — Ratio of the internal errors between the UVB and VIS for each atmospheric parameter, in separate panels. The stars with $T_{\rm eff}$ < 4000 K, 4000 < $T_{\rm eff}$ < 5500 K, and $T_{\rm eff}$ > 5500 K are shown with dark blue, orange, and light blue symbols, respectively. The dispersion σ and mean offset μ for the three temperature ranges are indicated.

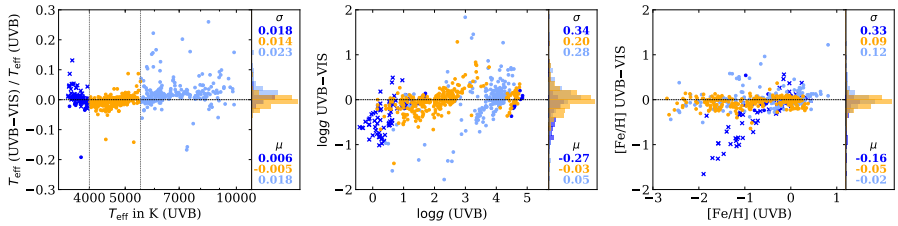

Figure 3.6 — Difference between the parameters determined from the UVB and VIS spectra for stars with 3500 K < $T_{\rm eff}$ (UVB) < 10 000 K. The colour-coding is the same as in Figure 3.5, and for the coolest stars (< 4000 K) the giants are shown with crosses. In the log$g$ panel, two outliers (hot stars) are not shown. The dispersion σ and mean offset μ for the three temperature ranges are indicated.

biases between the parameters of the input catalogue and those obtained after a self-inversion of the library, and we may suppose that the biases observed are mostly due to the ELODIE interpolator. However, including the biases and the random dispersion, the rms between the two series are 1.4%, 0.18, and 0.11 for $T_{\rm eff}$, $\log g$, and [Fe/H], respectively (after a 3σ clipping), and if we conservatively assume that the systematics are equally shared between the two interpolators, the quoted dispersions shall be divided by $\sqrt{2}$ to estimate the magnitude of the errors introduced by the interpolators. Those are 1.0%, 0.13, and 0.08 for the three parameters.

Comparison between UVB and VIS solutions

In this section we investigate differences between the UVB and VIS solutions. We first compare the internal uncertainties from the fit to the UVB and VIS spectra. In Figure 3.5 we present for each observation the UVB internal error divided by the VIS internal error for the three atmospheric parameters. For cool stars with $T_{\rm eff} < 5500$ K there is a decrease with temperature in the UVB/VIS internal errors ratio. This reflects the fact that the spectra of the coolest stars have lower S/N in the UVB compared to the VIS. For stars hotter than 5500 K the ratio of the UVB to VIS internal errors is constant and the UVB precisions are about four times higher. In Figure 3.6 we compare the solutions from the UVB and VIS, differentiating the three $T_{\rm eff}$ ranges 3500 – 4000 K, 4000 – 5500 K, and 5500 – 10000 K with different colours. We are not comparing the solutions for the coolest and hottest stars because in the first case the VIS solution can a priori be considered superior because these cool stars have very little flux in the UVB, and in the latter case the UVB is likely superior because there are almost no lines in the VIS. The two solutions appear essentially consistent, except these marginally significant biases: (i) the UVB $T_{\rm eff}$ is higher than the VIS for the stars hotter than 5500 K, reaching a bias of 3% at 10 000 K; (ii) the VIS $T_{\rm eff}$ is higher than the UBV by about 1% for $3800 < T_{\rm eff} < 4800$ K; and (iii) the UVB [Fe/H] are systematically lower than the VIS [Fe/H] by about 0.045. A comparison with a literature compilation (see Sect. 3.4.6) suggests that in the first case the bias is in the UVB solution, and in the two latter the bias is in the VIS solution. Our sample contains 161 spectra in the region of cool giants ($T_{\rm eff} < 4000$ K, and $\log g < 3$), represented as blue crosses in Figure 3.6. For the 129 of these with UVB solutions $T_{\rm eff} < 3800$ K, the UVB [Fe/H] are spread too low [Fe/H] (down to -1.9), while the VIS [Fe/H] is closer to solar. This produces the diagonal plume, with slope -1, stretching in the right panel, and for these spectra the UVB $\log g$ are reaching extreme negative values. Many of these stars are cool Miras, and their flux in the UVB arm is low, so we tend to a priori dismiss those measurements. The comparison with the literature for 14 spectra of stars having high resolution estimates confirms that standard deviation between UVB and literature is higher than between VIS and literature. But it also appears that the VIS [Fe/H] are biased to higher values with respect to the literature by about 0.2. We correct for these biases when we combine the two solutions in Sect. 3.4.5.

For 239 spectra with $4000 < T_{\rm eff} < 5500$ K and $\log g > 1$, the rms deviations between the UVB and VIS solutions are 1.3% (or 62 K), and 0.20 and 0.08 for $T_{\rm eff}$, $\log g$

and [Fe/H], respectively, after clipping the 3σ outliers. Accordingly, estimated total errors are 0.9% (or 44 K), 0.14 and 0.06 (the rms divided by $\sqrt{2}$). This is comparable with the external errors quoted in Wu et al. (2011a) for the stars of spectral types F, G, and K: 43 K, 0.13 and 0.05 for the three parameters.

For the cooler stars, $T_{\rm eff} < 4000$ K and $\log g > 1$ (58 spectra after clipping the outliers), the rms deviations are 2.0%, 0.19, and 0.13. The temperature and metallicity consistency degrades by about a factor 1.5. For the stars with $log g < 1$ (130 spectra after clipping the outliers), the deviations are 2.0 %, 0.29, and 0.28. Finally, for the warmest stars, $6500 < T_{\rm eff} < 10\,000$ K (90 spectra after clipping the outliers), the deviations are 2.3%, 0.30, and 0.12, i.e. 1.5 to 2 times less consistent than the GK stars. The consistency further degrades at higher temperature, down to 3.7%, 0.29, and 0.13 for all 117 spectra warmer than 6500 K, including those warmer than 10 000 K. For the cool stars, the UVB measurements are less accurate than the VIS ones, and the opposite is true for the hot stars, in particular above 10 000 K. Therefore, the comparison between the two arms may overestimate the total errors, but as we lack other indicators, we conservatively derive the total errors from these comparisons.

3.4.5 Combination of the UVB and VIS solutions: Adopted parameters and total error

The adopted parameters are finally derived by combining together the UVB and VIS solutions that satisfy the acceptance criteria stated in Section 3.4.1, after correcting the solutions for the biases described in Section 3.4.4. As we have seen above, and as we could logically expect, the UVB solution is generally better for the hot stars, and the VIS solution is better for the cool stars. We therefore adopted the following scheme:

- Use the UVB solution alone if $T_{\rm eff}$ (VIS) > 4500 K, or if the VIS solution is rejected.
- Use the VIS solution alone if $T_{\rm eff}$ (VIS) < 10 000 K and either the UVB solution is rejected or if $T_{\rm eff}$ (UVB) < 3800 K.
- Otherwise use the average of the two solutions weighted by the inverse of the square of the internal errors.

We use the comparison between the UVB and VIS solutions to derive the total error. We computed statistics of the differences between the two solutions in different regions of the parameter space, assuming this represents the total errors. After subtracting quadratically the internal errors we derive models of the errors due to the interpolator and effects of the hidden parameters, and finally we combine these errors with the internal errors to estimate the total errors for each measurement.

We adopted one set of parameters for each observation, therefore, in the case a star has repeated observations, we have multiple sets of parameters for the star. As the stars may be variable, we do not attempt to combine these measurements. If necessary, averaging the different values may be the best approach.

Table 3.1 gives the derived atmospheric parameters for 754 observations of 616 stars. Their distribution in the $T_{\rm eff}$ versus $\log g$, $T_{\rm eff}$ versus [Fe/H] and [Fe/H] versus $\log g$ planes are presented in Figure 3.7, to show that XSL contains a wide variety of stars. The library includes many normal dwarf and giant stars with a wide range in metallicity, and there are very hot stars, a significant number of AGB stars (with $T_{\rm eff}$ < 4000 K and $\log g$ < 1.0), Cepheids, RR Lyrae stars, post-AGB stars, and horizontal branch stars.

There is a twiddle around $\log g$ = 4.8 and $T_{\rm eff}$ = 5000 K, which is also seen in analyses of the Large Sky Area Multi-Object Fiber Spectroscopic Telescope (LAMOST) survey data by Wu et al. (2011b), Xiang et al. (2015), and Ho et al. (2017), which use a similar analysis approach. This is certainly an artefact due to the limited number of stars with accurate gravity measurements in the ELODIE and MILES stellar libraries, which were used to create the interpolator. A fit of the solar spectrum returns a gravity that is slightly too low for the Sun. Improving the interpolator in this region is possible, but beyond the scope of the current work. The effect is worse at the transition where we accept the UVB solution alone instead of a combination of the UVB and VIS solutions (at 4500 K). The effect is however within the $\log g$ uncertainties.

3.4.6 External precision: Comparisons with the general literature

The most inclusive assessment of the precision of our determination is a comparison with measurements published in the literature. For this purpose we assembled a compilation based on the PASTEL catalogue (Soubiran et al., 2016), which compiles published atmosphere analysis from high resolution spectra and atmosphere models. We supplemented the catalogue by other series of measurements missing in PASTEL (but satisfying its selection criteria) and measurements that extend the boundaries of PASTEL. These latter measurements include analyses of medium or low resolution spectra, using either synthetic spectra or observed stellar templates, and they also include photometric measurements. This compilation is a long-term effort, and to verify its completeness we checked the literature for each star using SIMBAD. The compilation, listed in Table 3.2 (available in full only in electronic form in Vizier), contains 4123 measurements of the XSL stars from 445 references. Half of these measurements (2069) are in PASTEL. For each star we computed a single set of parameters by averaging the available measurements, giving priority to those resulting from recent studies at high spectral resolution, and using other measurements only when no such measurements are available or when the high resolution measurements are not internally consistent. This procedure produces parameters classified in four quality classes. The Q0 class has the best values. They are based on high resolution spectroscopic original measurements published after 1985 and they are consistent within 6% for $T_{\rm eff}$, 0.7 for $\log g$, and 0.4 for [Fe/H]. The Q1 class contains measurements from low resolution spectra and the older or less consistent high resolution spectra. The Q2 class also includes photometric measurements and Q3 are from compilations (from measurements not included otherwise). The average literature parameters for the present sample, their standard

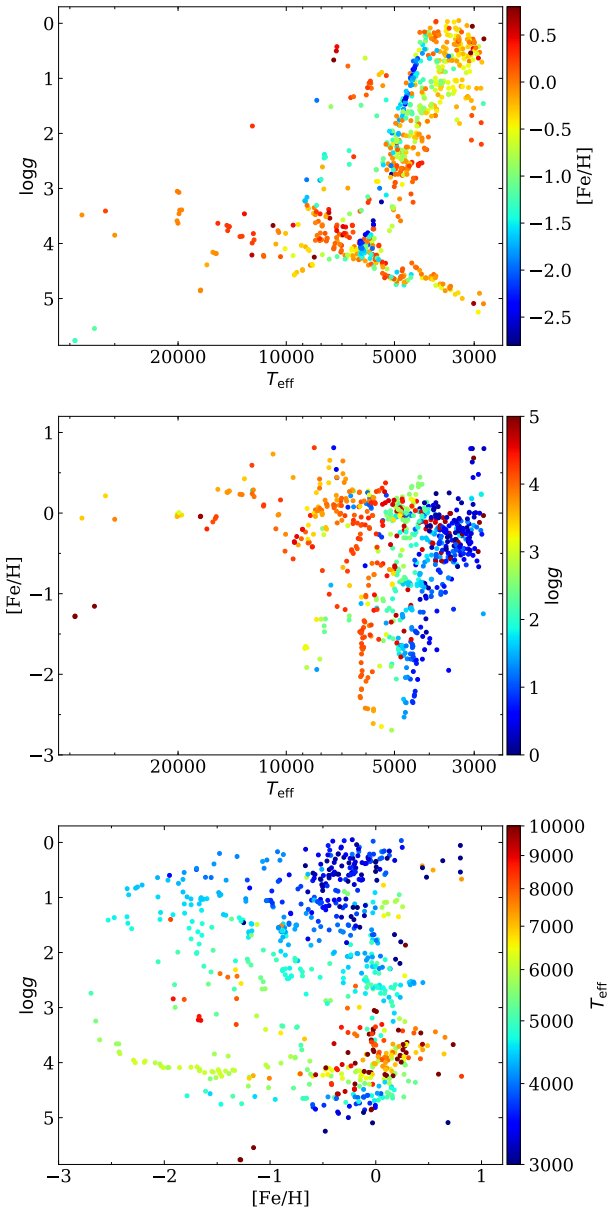

Figure 3.7 — Final parameters in this paper for XSL. Top panel: Hertzsprung-Russell diagram for XSL, colour-coded by [Fe/H]. Middle: Distribution in the $T_{\rm eff}$– [Fe/H] plane, colour-coded by $\log g$. Bottom: Distribution in the [Fe/H]– $\log g$ plane, colour-coded by $\log T_{\rm eff}$. One star with a $\log g$ error larger than 2.0 is not shown (carbon star [ABC89] Cir 18).

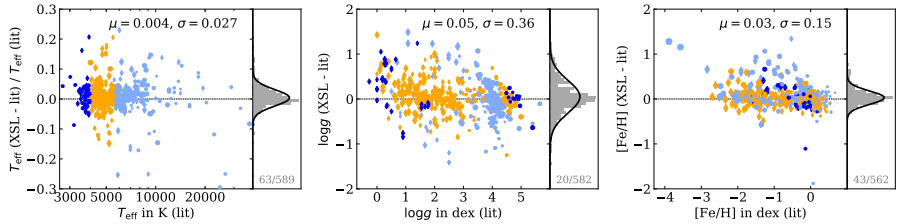

Figure 3.8 — Comparison between our adopted parameters and the literature compilation. The standard deviation and mean of the differences are written and the corresponding curve is shown. The number of clipped observations compared to the total number of literature values is presented in the lower right corner of each of the panels. The colour of the points relates to $T_{\rm eff}$; the size of the points to [Fe/H], and giants and dwarfs (log$g$ limit 3.0) are indicated by diamonds and circles, respectively. In the $T_{\rm eff}$ and log$g$ panels, two and four outliers, respectively, are not shown (various types of stars).

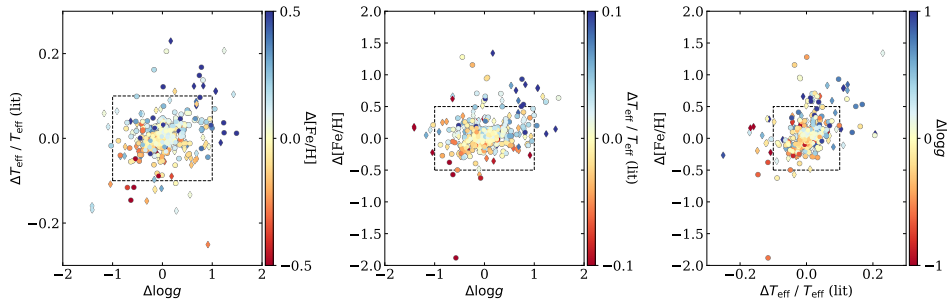

Figure 3.9 — Comparison of different Δs (our adopted parameter minus the literature value) for $T_{\rm eff}$, log$g$, and [Fe/H]. Stars with multiple literature references are shown as circles, whereas stars with only one reference are shown as diamonds. The observations outside the boxes that have more than one literature reference are discussed in Section 3.4.6.

deviation, the number of measurements used, and the quality parameters are presented in Table 3.3.

In this compilation, $T_{\rm eff}$, log$g$, and [Fe/H] are available, respectively, for 493, 487, and 466 of the 668 XSL stars. Including the repeated observations, 586 of the 786 measurements that we obtained can be compared to a measurement of $T_{\rm eff}$ from the compilation. If we reject those of our measurements departing from the literature compilation by more than 10% in $T_{\rm eff}$, or 1.0 and 0.5, respectively, in log$g$ or [Fe/H], the 450 remaining measurements have a standard deviation of 3% in $T_{\rm eff}$, and 0.33 and 0.16, respectively, in the two other parameters. Of these measurements 329 are for FGK stars, and for those the standard deviations are slightly lower.

The difference between the literature and our measurements is presented in Figure 3.8. We computed standard deviations and means using the python `sigma_clip` function with a clipping sigma of 3.0, where the number of stars rejected compared to the total available literature measurements is shown in the bottom right corner of

the figure. The consistency between our measurements and the literature is better for the GK stars, and it degrades for the hotter, cooler, and lowest gravity stars.

In Figure 3.9, we present our adopted parameter minus the literature value (Δ) in combinations of all three parameters. The dashed boxes represent deviations of 10%, 1, and 0.5 on the three parameters, respectively, corresponding approximately to three times the clipped standard deviations. A mild correlation is seen along the expected temperature-metallicity degeneracy line (right panel), but this accounts only for a minor fraction of the variance. The outliers in each projection (outside the dashed boxes) are most often discrepant on all the three parameters, and we note that their distribution is asymmetric. There are more outliers for which we measure $T_{\rm eff}$, $\log g$, and [Fe/H] values higher than in the literature than there are outliers with lower values. We do not think this asymmetry is physically significant. In an attempt to identify cases or regions of the parameter space for which our method may fail, we discuss below the outliers for which the literature reports more than one set of values considered reliable; these outliers are shown as circles outside the boxes.

Cases with Δ [Fe/H] > 0.5

There are 20 observations with a [Fe/H] difference larger than 0.5. Many of these observations belong to peculiar stars (that are not covered by the interpolator), for example two $\alpha 2$ CVn variable stars (hot stars with abnormal chemical compositions), two extremely metal-poor stars ([Fe/H] < -3.0), and a very metal-poor cool subdwarf ([Fe/H] $= -2.5$), a brown dwarf, a Herbig Ae/Be star with many emission lines, a hot (12 000 K) metal-poor (-0.4) star, and a high proper motion cool flare star.

There are also a few metal-poor stars ([Fe/H] < -1.5) that ULySS has confused for a different evolutionary state, which also has a large $\log g$ discrepancy. Two of these are horizontal branch stars that we place on the main sequence (HD074721, for which the $T_{\rm eff}$ is also discrepant by 10%) or on the giant branch (HD184266). Then there is a post-AGB star that is placed on the horizontal branch (HD116745). We carefully checked that our solutions were not trapped in a local minimum, and we suppose that the interpolator simply fails to reproduce these stars because they are not represented in the reference libraries.

Additionally, there are three observations (of two stars) that do not seem to have an obvious reason to be discrepant with the literature in [Fe/H]. The first star, HD184571, has a good fit in ULySS; the two arms give consistent solutions, but there are only low resolution spectroscopic [Fe/H] values available in the literature with a spread of 0.19. Therefore it is not clear whether our measurements or the literature measurements are better. The second star is CL* NGC 330 ROB A3 in the globular cluster NGC 330 in the Small Magellanic Cloud, which has two XSL observations. The $T_{\rm eff}$ and $\log g$ for this star are also discrepant with the literature, but the fits are very good and consistent with each other between the two observations. There may be a possibility that we are comparing this star to the wrong literature star in the cluster. Finally, there are five stars for which the dispersion of [Fe/H] from different literature studies is ≥ 0.20 and a good comparison cannot be made.

Cases with $\Delta T_{\rm eff} > 10\%$

There are 20 observations with a $T_{\rm eff}$ difference larger than 10%. Three stars are cool supergiants in the Magellanic Clouds with literature $T_{\rm eff} < 3600$ K: [M2002] LMC 150040, [M2002] LMC 158646, and [M2002] SMC 52334. Each of these stars has a high $T_{\rm eff}$ dispersion in the literature (200–350 K), and each of the literature $T_{\rm eff}$ values comes from comparing intermediate resolution spectroscopy to synthetic spectra; this kind of comparison is subject to many uncertainties (e.g. Davies et al., 2013). Another cool star, the red supergiant HD050877 with literature $T_{\rm eff}$ = 3550 K, has multiple high resolution spectroscopic measurements, however their dispersion is 500 K.

Then there is the warmer giant star HD058790 (literature $T_{\rm eff}$ 5275 K) which is well fitted, consistent between the UVB and VIS, and there is no reason to believe its fitted parameters are wrong. The fitted $T_{\rm eff}$ is 600 K cooler than the literature value, which is an average of two papers from 1989 and 1999 by the same group (Luck & Bond 1989; Luck & Lambert 1992). The fitted $\log g$ is also 0.7 lower than the literature. The spectrum of this star and its fit are very comparable to other XSL stars in this parameter region, therefore we assume our measurement is better.

The spectrum of the F giant HD161770 is well fitted, but it disagrees with the literature $T_{\rm eff}$ by 600 K. The literature $T_{\rm eff}$ includes seven photometric measurements that are all relatively consistent with each other, and one spectroscopic measurement from Bensby et al. (2014) which is higher. Remarkably, our determined temperature agrees relatively well with that from that spectroscopic work.

For HD188262, a warm giant, we have two observations, which in both cases show a large discrepancy between the UVB and VIS $T_{\rm eff}$ values. For both observations, we adopt the UVB solution which is 800 K warmer than the literature. However, the VIS solutions agree much better with the literature, although the literature values show a high dispersion of 600 K.

There are two horizontal branch stars HD143459 and HD128801 with $T_{\rm eff} >$ 9000 K, which both have a large difference in the $T_{\rm eff}$ derived from the UVB or the VIS (> 800 K). The VIS barely contributes to our final adopted parameters in hot stars like these. In the case of HD128801, the UVB is closer to the literature $T_{\rm eff}$. For HD143459, the literature $T_{\rm eff}$ is in between the UVB and VIS $T_{\rm eff}$. However, for both stars either the literature values have a high dispersion, or they are different measurements from one single paper (and thus not from independent methods).

There are also two observations of the hot subdwarf HD004539 that are off from the literature by 5000 K, where the literature $T_{\rm eff}$ = 24570 K with a dispersion of 1200 K. However, all four measurements are from the same reference and therefore are also not independent.

Finally there are some discrepant stars which are peculiar stars. Examples are a post-AGB star which is an RV Tauri variable star, two Herbig Ae/Be stars, a Cepheid, an RR Lyrae star, and one hot variable supergiant.

Cases with $\Delta \log g > 1.0$

There are four observations with multiple literature measurements that agree with the literature for $T_{\rm eff}$ and [Fe/H] within 10% and 0.5, respectively, but are discrepant in $\log g$ by more than 1.0. However, the literature dispersions in $\log g$ for these stars

are generally high. One is the very cool giant HD065354, which has a literature dispersion for $\log g$ of 1.2. Secondly, there is another very cool giant [M2002] SMC 55188, for which we find a difference in $\log g$ of 1.03. For this type of star there is very little reliable literature information available. Another is the post-AGB star HD112374, however the literature dispersion is high with 0.8 in $\log g$. The fourth observation is one of the three observations for Feige 110, a hot subdwarf with $T_{\rm eff}$ = 39 000 K. The $\log g$ values of the other two observations agree with the literature, but this one has a difference of 2, placing it at 3.5 instead of 5.5. It is however remarkable that the other two observations agree with the literature both in $\log g$ and $T_{\rm eff}$ because this type of star is not represented in the MILES library, and the success of our analysis is due to the theoretical extrapolation support spectra used to compute the interpolator.

Summary of the literature comparison

Overall, our measurements agree with the literature within 2.7%, 0.36, and 0.15 for $T_{\rm eff}$, $\log g$, and [Fe/H], respectively. The largest share of the dispersion is likely due to the inhomogeneity of the literature compilation. We generally trust our parameters for stars on the main sequence and those on the giant branch with $T_{\rm eff} > 3800$ K. Compared to previous stellar libraries, in XSL there is a relatively large group AGB stars and other giants cooler than 3800 K. For these stars, there is very little reliable information in the literature with which to compare.

We find that many of the parameters that are discrepant with the literature are for peculiar stars which are not well represented by the MILES interpolator, such as extremely metal-poor stars, brown dwarfs, stars with peculiar chemistry, and variable stars. Additionally, there are a significant number of stars for which the literature has a high dispersion itself. For some other stars, we have good fits and find no obvious reason for the discrepancy with the literature. There may be issues with the literature values themselves, or we might be comparing two different stars without knowing. Finally, we found that some of the stars discrepant with the literature also show discrepancies between our UVB and VIS measurements.

3.4.7 Comparison with previous ULySS determinations

To test the consistency of our approach, we compare our determinations with three previous studies using ULySS and the MILES or ELODIE interpolators. These comparisons also cannot be regarded as estimates of the external errors because these series may be affected by similar systematic because the same methods were used.

Wu et al. (2011a)

Wu et al. (2011a) used the ELODIE interpolator to determine parameters for the CFLIB (also known as the Indo-US library). Including the repeated observations, 109 measurements that we obtained can be compared to a measurement in that study; see Figure 3.10. The standard deviations in $T_{\rm eff}$, $\log g$, and [Fe/H] are 1.4%, 0.16, and 0.09, respectively (clipping with a sigma of 3.0). There do not appear to be

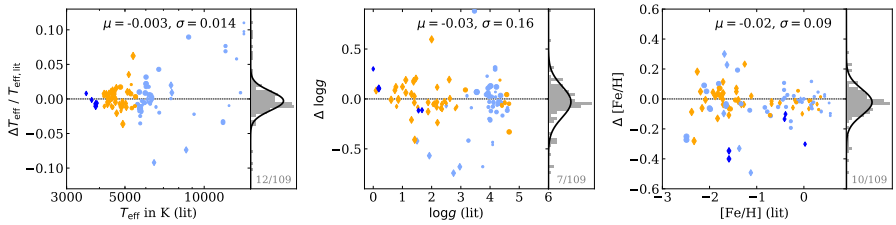

Figure 3.10 — Comparison between our adopted parameters and the parameters from Wu et al. (2011a). One and three outliers are not shown for $\log g$ and [Fe/H], respectively, and one measurement at 29000 K is not shown (its $\Delta\ T_{\rm eff}/\ T_{\rm eff\ lit}$ is +0.027.). The axes and symbols are explained in Figure 3.8.

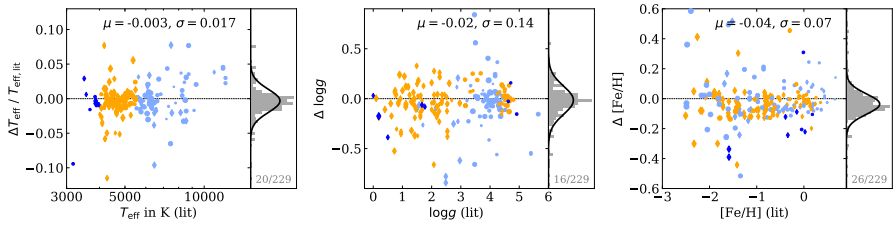

Figure 3.11 — Same as Figure 3.10, but compared to Prugniel et al. (2011). There are eight, four, and three outliers not shown for $T_{\rm eff}$, $\log g$, and [Fe/H], respectively, and three additional measurements above 20000 K are not shown; they have differences between −0.04 and −0.06.

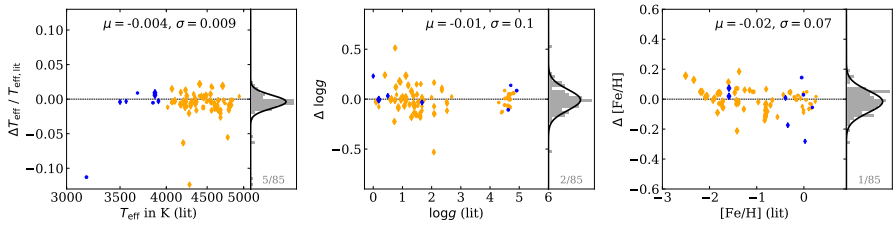

Figure 3.12 — Same as Figure 3.10, but compared to Sharma et al. (2016). All measurements from XSL in common with that study are shown.

any biases. Wu et al. (2011a) compared their determined parameters for FGK stars to many different literature compilations and determined robustly their external errors. They claim a precision of 43 K, 0.13, and 0.05 for $T_{\rm eff}$, $\log g$, and [Fe/H], respectively. Our standard deviations with respect to Wu et al. (2011a) are slightly higher.

Prugniel et al. (2011)

Prugniel et al. (2011) used the first version of the MILES interpolator to determine uniform parameters for the MILES library. Including repeated observations, 229 observations can be compared to a measurement from that study; see Figure 3.11. The standard deviations are 1.7%, 0.14, and 0.07 in $T_{\rm eff}$, $\log g$, and [Fe/H], respectively, although especially for $T_{\rm eff}$ a large fraction of the stars are clipped from computing the standard deviation. There may be a small bias in [Fe/H], where our measurements are on average 0.04 lower.

Sharma et al. (2016)

Finally, we compare to the study by (Sharma et al., 2016, hereafter S16), who improved the MILES interpolator for the cool stars (< 5000 K). This is the version of the interpolator we are using. For 85 observations in our sample we can compare to that study, which only contains cool stars; see Figure 3.12. The standard deviations are 0.9%, 0.1, and 0.07 in $T_{\rm eff}$, $\log g$, and [Fe/H], respectively. There are only five observations with differences larger than 5% in $T_{\rm eff}$; one of these is a flare star with a high proper motion (BD+19 5116B; our $T_{\rm eff}$, $\log g$ and [Fe/H] 2900 K, 4.9, and −0.12 respectively), and the other three stars (one of these has two observations) are all giants between $4100 - 4500$ K in the same globular cluster NGC 6838: CL* NGC 6838 AH A9 (twice), NGC 6838 1009, and NGC 6838 1053. The S16 authors have fixed [Fe/H] to the cluster [Fe/H] while fitting $\log g$ and $T_{\rm eff}$, whereas we fit [Fe/H] as a free parameter. This affects the final solutions, although the difference between our values and the adopted cluster [Fe/H] is small (0.08 – 0.14). It is therefore unclear why the effective temperatures are discrepant. Additionally, S16 reanalysed their spectra without fixing [Fe/H]. The effective temperatures do not change much, so likely fixing [Fe/H] is not the only reason our measurements are discrepant with S16. CL* NGC 6838 AH A9 and NGC 6838 1053 are also in the literature compilation we compared to in Section 3.4.6 and have multiple $T_{\rm eff}$ determinations from high resolution spectroscopy. Our $T_{\rm eff}$ agrees better (within 50–100 K) with those literature values than the S16 $T_{\rm eff}$ values, which are different from the literature by 200 and 400 K for CL* NGC 6838 AH A9 and NGC 6838 1053, respectively.

3.5 Summary

In this paper we have presented uniformly derived stellar atmospheric parameters for XSL. We used two spectral regions from the UVB and VIS arm spectra of the instrument and performed full-spectrum fitting with the ULySS package and the

MILES spectral interpolator. We compared the solutions obtained for repeated observations of the same object to assess the accuracy of the internal errors. We compared the solutions obtained using the two spectral regions, and those obtained using another interpolator based on the ELODIE library to evaluate the systematics introduced by the method and the effects due to particular characteristics of individual stars. This analysis indicates that for $\log g > 1$ and $4000 < T_{\rm eff} < 5500$ K the total errors are 0.9% (or 44 K), 0.14, and 0.06 for $T_{\rm eff}$, $\log g$, and [Fe/H], respectively, and for lower temperatures the [Fe/H] total error increases to 0.1. For the hotter stars the estimated total errors are 2.6%, 0.20, and 0.10 on the three parameters, and for $\log g < 1$, they are 2.1%, 0.21, and 0.22. These errors are consistent with those previously reported in papers using the same method (Prugniel et al., 2011; Wu et al., 2011a; Koleva & Vazdekis, 2012).

The XSL spectra in combination with these atmospheric parameters can be used to create spectral interpolators and stellar population models. This library has an important value because it has a large wavelength coverage obtained in a single observation, medium resolution (between R=8 000 and 11 000), and a wide coverage of the parameter space.

Acknowledgements.

AA gratefully acknowledges funding by the Emmy Noether programme from the Deutsche Forschungsgemeinschaft (DFG). PhP and AL acknowledge financial support from the Programme National Cosmology and Galaxies (INSU/CNRS) in 2017 and 2018. AG is supported by the European Union FP7 programme through ERC grant number 320360. JFB and AV acknowledge support from grant AYA2016-77237-C3-1-P from the Spanish Ministry of Economy and Competitiveness (MINECO). We thank Matthijs Dries for help with telluric corrections in XSL DR2. We thank Paula Coelho for her useful comments on a draft of this work. This research has made use of the SIMBAD database, operated at CDS, Strasbourg, France.

3.6 Appendix

Table 3.1 — Derived atmospheric parameters of the XSL stars

Name	Obs[a]	UVB solution			VIS solution			Adopted parameters						flag[b]
		$T_{\rm eff}$ (K)	log g ([$cm\,s^{-2}$])	[Fe/H] ([Sun])	$T_{\rm eff}$ (K)	log g ([$cm\,s^{-2}$])	[Fe/H] ([Sun])	$T_{\rm eff}$ (K)	err	log g ([$cm\,s^{-2}$])	err	[Fe/H] ([Sun])	err	
2MASS J17535707−2931427	247	4723	2.03	−0.04	4722	2.31	−0.02	4723	37	2.03	0.15	−0.04	0.05	
2MASS J18024572−3001120	255	4495	1.57	1.00	3296	1.82	−0.08	3296	35	1.82	0.82	−0.28	2.27	
2MASS J18024611−3004509	256	2700	5.71	1.00	3096	0.79	0.21	3096	67	0.69	0.30	0.01	0.25	
2MASS J18025277−2954335	257	3328	1.44	0.39	3368	0.33	−0.25	3368	56	0.23	0.20	−0.45	0.20	
2MASS J18032525−2959483	169				3270	0.50	−0.32	3270	56	0.40	0.22	−0.52	0.24	
2MASS J18033716−2954227	152	4237	2.49	0.34	4297	2.56	0.52	4250	30	2.55	0.15	0.45	0.05	
2MASS J18040638−3010497	153	3354	1.19	0.57	3384	0.39	−0.04	3384	56	0.29	0.20	−0.24	0.19	
2MASS J18042244−3000534	154	2958	0.88	−0.09	3240	1.03	−0.08	3240	41	1.03	0.21	−0.28	0.20	
...	...	...	...	...	...	...	...	...	...	...	...	...	...	

Notes. [(a)] XSL observation identifier. Internal unique number for an observation; repeated observations of the same target have different numbers, so this number should not be used to identify a star.
[(b)] Flag for stars that show large differences with their literature stellar parameters (if there are at least two literature measurements available), as discussed in Sect. 3.4.6.
This table is available in its entirety at the CDS.

Table 3.2 — 4123 individual atmospheric parameters from the literature compilation[a]

Name	J2000	$T_{\rm eff}$ (K)	err	log g ([$cm\,s^{-2}$])	err	[Fe/H] ([Sun])	err	r	c	m	bibcode
2MASS J18033716−2954227	J180337.1−295422	4300		1.67		0.54	0.37	L	O	A	2008A&A...486..177Z
2MASS J18351799−3428093	J183518.0−342809	4750		1.98		−0.19	0.12	L	O	A	2008A&A...486..177Z
2MASS J18352206−3429112	J183522.1−342911	4850		2.03		0.01	0.14	L	O	A	2008A&A...486..177Z
2MASS J18352834−3444085	J183528.3−344409	4900		2.00		−1.40	0.18	L	O	A	2008A&A...486..177Z
2MASS J18355679−3434481	J183556.8−343448	4350		1.81		−0.67	0.10	L	O	A	2008A&A...486..177Z
BD+01 2916	J142145.3+004659	4150		0.1		−1.99		H	O	A	2000ApJ...544..302B
BD+01 2916	J142145.3+004659	4150		0.1		−1.99		H	O	A	1996AJ....111.1689P
BD+01 2916	J142145.3+004659					−1.48		H	O	A	1983ApJ...271L..75L
...	...	...	...	...	...	...	...	...	...	...	...

Notes. [(a)] These measurements are compiled as described in Section 3.4.6. There are three quality measures, indicated in columns r, c and m. The column r indicates the resolution class, high (H), low (L) or photometry (P). The column c describes the origin, original measurement (O) or compilation (C). Column m describes the method, referenced to model atmosphere (A), isochrones (I) or empirical calibration (T).
This table is available in its entirety at the CDS.

Table 3.3 — Mean atmospheric parameters from the literature comparison for 487 stars[a]

Name	$T_{\rm eff}$ (K)				log g ([$cm\,s^{-2}$])				[Fe/H] ([Sun])			
	μ	σ	n	Q	μ	σ	n	Q	μ	σ	n	Q
2MASS J18033716−2954227	4300		1	1	1.67		1	1	0.54		1	1
2MASS J18351799−3428093	4750		1	1	1.98		1	1	−0.19		1	1
2MASS J18352206−3429112	4850		1	1	2.03		1	1	0.01		1	1
2MASS J18352834−3444085	4900		1	1	2.00		1	1	−1.40		1	1
2MASS J18355679−3434481	4350		1	1	1.81		1	1	−0.67		1	1
BD+01 2916	4167	29	3	0	0.10	0.00	3	0	−1.93	0.11	3	0
BD+03 2688	4300		1	0	0.00		1	0	−1.42		1	0
BD+04 2466	5031	137	8	0	1.61	0.54	3	0	−1.99	0.12	4	0
...	...	...	...	...	...	...	...	...	...	...	...	...

Notes. [(a)] These measurements are compiled as described in Section 3.4.6. Column names μ, σ, n and Q refer to the average of the measurements in the literature, their standard deviation, the number of included measurements and the quality of the combined measurement (as described in the main text), respectively.
This table is available in its entirety at the CDS.

4 The Pristine Inner Galaxy Survey (PIGS) I: Tracing the kinematics of metal-poor stars in the Galactic bulge

A. Arentsen, E. Starkenburg, N. F. Martin, V. Hill, R. Ibata, A. Kunder, M. Schultheis, K. A. Venn, D. B. Zucker, D. Aguado, R. Carlberg, J. I. González Hernández, C. Lardo, N. Longeard, K. Malhan, J. F. Navarro, R. Sánchez-Janssen, F. Sestito, G. Thomas, K. Youakim, G. F. Lewis, J. D. Simpson, Z. Wan

— Published as Arentsen et al., 2020, MNRAS, 491L, 11, Oxford University Press —

ABSTRACT

Our Galaxy is known to contain a central boxy/peanut-shaped bulge, yet the importance of a classical, pressure-supported component within the central part of the Milky Way is still being debated. It should be most visible at low metallicity, a regime that has not yet been studied in detail. Using metallicity-sensitive narrow-band photometry, the Pristine Inner Galaxy Survey (PIGS) has collected a large sample of metal-poor ([Fe/H] < -1.0) stars in the inner Galaxy to address this open question. We use PIGS to trace the metal-poor inner Galaxy kinematics as function of metallicity for the first time. We find that the rotational signal decreases with decreasing [Fe/H], until it becomes negligible for the most metal-poor stars. Additionally, the velocity dispersion increases with decreasing metallicity for $-3.0 <$ [Fe/H] < -0.5, with a gradient of $-44 \pm 4\,\mathrm{km\,s^{-1}\,dex^{-1}}$. These observations may signal a transition between Galactic components of different metallicities and kinematics, a different mapping onto the boxy/peanut-shaped bulge for former disk stars of different metallicities and/or the secular dynamical and gravitational influence of the bar on the pressure-supported component. Our results provide strong constraints on models that attempt to explain the properties of the inner Galaxy.

4.1 Introduction

The central few kiloparsecs of the Milky Way are a unique place for Galactic studies as there multiple Galactic components overlap with each other. Most of the mass appears to be in a rotation supported boxy/peanut-shaped bulge that rotates like a solid body, indicative of a bar origin (Howard et al., 2009; Ness et al., 2013b). In recent years, a debate has been ongoing about the importance of an additional classical, pressure-supported component in the bulge (Zoccali et al., 2008; Babusiaux et al., 2010; Kunder et al., 2016). If present, it can only be a small percentage of the mass of the bulge, as constrained by the line-of-sight velocity profiles (Shen et al., 2010; Ness et al., 2013b). However, these profiles are mainly based on metal-rich stars. At lower metallicity the pressure-supported component may be expected to play a larger role. Additionally, the halo continues down into the central regions of our Galaxy and contributes to the metal-poor inner Galaxy.

Most bulge studies have been based on samples with stars of fairly high metallicity ([Fe/H] > -0.5), since such stars are the most abundant. They already found that sub-solar metallicity stars are more spherically distributed than super-solar metallicity stars (e.g. Zoccali et al., 2017), although they show the same amount of rotation (Ness et al., 2013b). The few studies focussing on metal-poor stars in the inner Galaxy used RR Lyrae stars, a population with mean [Fe/H] $= -1.0$ and age > 11 Gyr (Dékány et al., 2013; Kunder et al., 2016). They find that these stars are more spherically distributed than the metal-rich stars and rotate only slightly (if at all). The ARGOS red clump bulge survey contains only 4.4 per cent (522 stars) with [Fe/H] < -1.0 and 0.7 per cent (84 stars) with [Fe/H] < -1.5 (Ness et al., 2013a), not sufficient to study this population in detail.

What is missing from the literature is a comprehensive study of the behaviour of the (very) metal-poor tail of the inner Galaxy. In this Letter we present for the first time the kinematics as a function of metallicity for a large sample of metal-poor stars (mainly [Fe/H] < -1.0) from the Pristine Inner Galaxy Survey (PIGS, Chapter 5).

4.2 Data

Since metal-poor stars in the Galactic bulge are extremely rare, targeted selection is necessary to obtain a large sample of them. PIGS is a sub-survey of the Pristine survey (Starkenburg et al., 2017b), which uses a narrow-band $CaHK$ filter for MegaCam on the 3.6m Canada-France-Hawaii Telescope (CFHT) to photometrically search for the most metal-poor stars. The $CaHK$ photometry is highly sensitive to metallicity for FGK stars. Candidate metal-poor stars selected from this photometry are followed up using the AAOmega+2dF multi-fibre spectrograph on the 3.9m Anglo-Australian Telescope (AAT) in low/intermediate resolution, which has 400 fibres in a two-degree field of view.

For the selection, we combine our $CaHK$ photometry with $Gaia$ DR2 broad-band BP, RP and G photometry (Gaia Collaboration et al., 2016, 2018), or in some later fields with Pan-STARRS1 DR1 g and r photometry (Chambers et al., 2016). We checked that there are no strong systematic effects between the two selections that affect the results of this Letter. We deredden the photometry using the 3D extinction

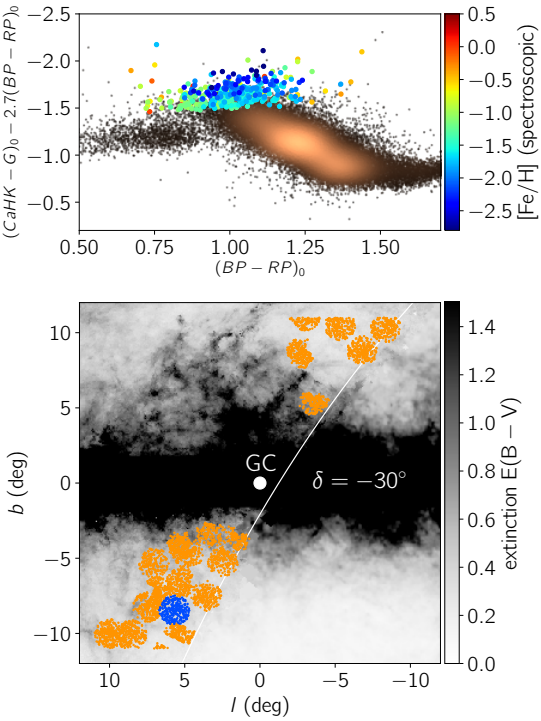

Figure 4.1 — Top: Pristine colour-colour diagram for one field (blue in bottom panel). Metal-poor stars lie towards the top. All stars in this field in our magnitude range that pass the parallax cut are shown (~ 40 000 stars), of which we observed 350 with the AAT (coloured points). Bottom: Coverage of the sample of stars used in this work (after quality cuts). The extinction in the background is a combination of the 3D extinction map from Green et al. (2018) at 8 kpc, available above a declination of −30° (white curve) and reliable at $|b| > 2°$, and the Schlegel et al. (1998) extinction map elsewhere. The colour bar is truncated at E(B−V) = 1.5 for clarity.

map of Green et al. (2015, 2018), assuming a distance of 8 kpc. To probe giants in the bulge region we select stars with $13.5 < G_0 < 16.5$ (*Gaia*) or $14.0 < g_0 < 17.0$ (Pan-STARRS), excluding those that have *Gaia* (parallax − parallax_error) > 0.25 mas to avoid stars closer to us than ~4 kpc. We do not make any cuts based on the proper motions. The top panel of Figure 4.1 shows the location of spectroscopically followed-up metal-poor candidates in a colour-colour diagram. We select stars moving down from the top of the diagram, until there are enough targets to fill all 2dF fibres.

The spectroscopic observations were performed in August 2017, June 2018, August 2018 and April 2019 with the 580V and 1700D gratings. The blue spectra cover a wavelength range of 3800–5800 Å at a resolution R~1300, the red spectra cover the calcium triplet (CaT) with a wavelength range of 8350–8850 Å at a resolution R~10 000. Total exposure times were generally two hours, with sub-exposures of 30

minutes, to reach a minimum signal to noise ratio (SNR) of 20 for the faintest stars. The data were reduced and combined using the AAT `2dfdr` pipeline[1] (v. 6.46) with the standard settings. The spatial coverage of the sample used in this work is shown in the bottom panel of Figure 4.1. The PIGS footprint only reaches a declination of $-30°$ since the *CaHK* photometry is obtained from the Northern hemisphere.

We used the FXCOR package in IRAF[2] to determine line-of-sight velocities from the CaT spectra. As templates we use synthetic spectra created using the MARCS (Model Atmospheres in Radiative and Convective Scheme) stellar atmospheres and the Turbospectrum spectral synthesis code (Alvarez & Plez, 1998; Gustafsson et al., 2008; Plez, 2008). We first derive velocities using a fixed template, then derive stellar parameters with the zero-shifted spectra, and finally rederive velocities using templates with stellar parameters close to those of each star, in the following grid: $T_{\rm eff}$ = [5000, 5500] K, $\log g$ = 2.5 and [Fe/H] = [0.0, −1.0, −2.0, −3.0]. Uncertainties are of order 2 km s^{-1}, combining the formal FXCOR uncertainties with an estimate of the systematic uncertainties derived from repeated observations. Stars with large line-of-sight velocity uncertainties ($\varepsilon_{\rm FXCOR} > 5$ km s^{-1}) and double-lined spectra are discarded from our sample. The line-of-sight velocity converted to the Galactic Standard of Rest $v_{\rm gsr}$ is determined using ASTROPY (v3.0, Astropy Collaboration et al., 2013; Price-Whelan et al., 2018), assuming the peculiar velocity of the Sun from Schönrich et al. (2010) and circular velocity at the solar radius from Bovy (2015).

To determine stellar parameters $T_{\rm eff}$, $\log g$ and [Fe/H] from the blue spectra, we use the full-spectrum fitting University of Lyon Spectroscopic Software (ULySS, Koleva et al. 2009). We use the well-tested model interpolator created from the empirical MILES library (Prugniel et al., 2011; Sharma et al., 2016), which has for example been used to determine stellar parameters for the X-shooter Spectral Library (Arentsen et al., 2019b, Chapter 3). This interpolator is calibrated down to [Fe/H] = −2.8, which is perfect for the sample in this work. For more details on the stellar parameter determination, see Section 4.5.1 in the Appendix. Typical uncertainties on $T_{\rm eff}$, $\log g$ and [Fe/H] are 120 K, 0.35 dex and 0.2 dex, respectively.

The $T_{\rm eff}$–$\log g$ diagram of the sample passing our quality criteria is shown in the top panel of Figure 4.2. In this Letter, we only consider stars with $1.8 < \log g < 3.2$ (black dotted lines), to constrain the sample to stars likely in the bulge volume. This $\log g$ range is the same as that used in Ness et al. (2013a) for red clump stars. This cut removes a significant number of the (very) metal-poor stars, since many of those have low surface gravities and may be located further into the halo on the far side of the bulge. For a discussion on the distances of our sample stars, see Section 4.5.3 in the Appendix. Furthermore, the region where the horizontal branch (HB) stars are located is highlighted in red (see Section 4.5.2 in the Appendix for more details on the selection and metallicities of the HB stars).

The metallicity distribution of all stars is shown in the bottom panel of Figure 4.2. At the low-[Fe/H] end there is an excess of stars at the limit of the interpolator; several of these may be even more metal-poor than [Fe/H] = −2.8. There are two

[1] https://aat.anu.edu.au/science/software/2dfdr

[2] IRAF (Image Reduction and Analysis Facility) is distributed by the National Optical Astronomy Observatories, which are operated by the Association of Universities for Research in Astronomy, Inc., under contract with the National Science Foundation.

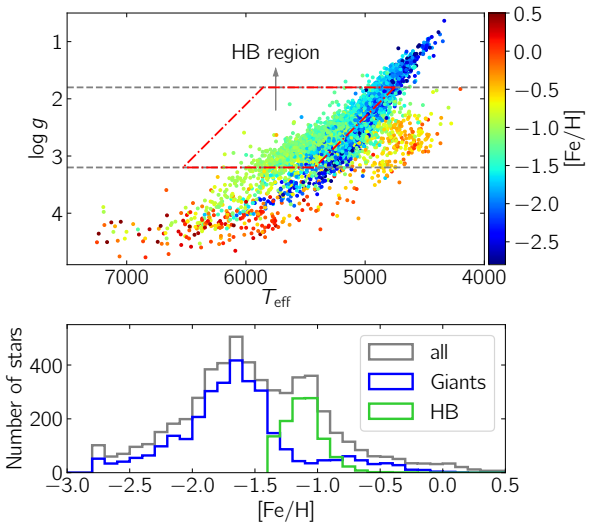

Figure 4.2 — Top: $T_{\rm eff}$–log g diagram colour-coded by [Fe/H], for the sample making our quality cuts. The the log g cuts are indicated in grey, and the box containing HB stars is shown in red (see Section 4.5.2 in the Appendix). Bottom: Metallicity distribution of our full sample in grey, with the 4200 stars that have $1.8 < \log g < 3.2$ highlighted in blue (giants) and green (HB stars). The lower [Fe/H] limit of the interpolator is −2.8, causing an apparent excess of stars there.

peaks in the distribution, which can be attributed to two different types of stars: the HB stars and the normal giants. The more metal-rich peak around [Fe/H] ~ -1.1 is that of the HB stars. Although the exact metallicities for the HB stars are somewhat uncertain, they are clearly distinct from the normal giants. The second peak at [Fe/H] = −1.6 is that of the normal giants in the sample and illustrates the success of PIGS in selecting this rare metal-poor population. The overall shape of the metallicity distribution is the result of our specific photometric selection and does not necessarily represent the metallicity distribution function of the underlying population.

4.3 Results

We use our sample to study the kinematics in the inner Galaxy at different metallicities. We investigate the rotation curve and the velocity dispersion as a function of metallicity.

We present the mean line-of-sight velocity as a function of the Galactic longitude in Figure 4.3, with the metallicity decreasing from the left to the right panels. The top row combines all latitudes per longitude bin, the second row shows each AAT field individually, colour-coded by latitude. The dashed lines in these rows are the rotation curves from Shen et al. (2010), who modelled a purely barred bulge which

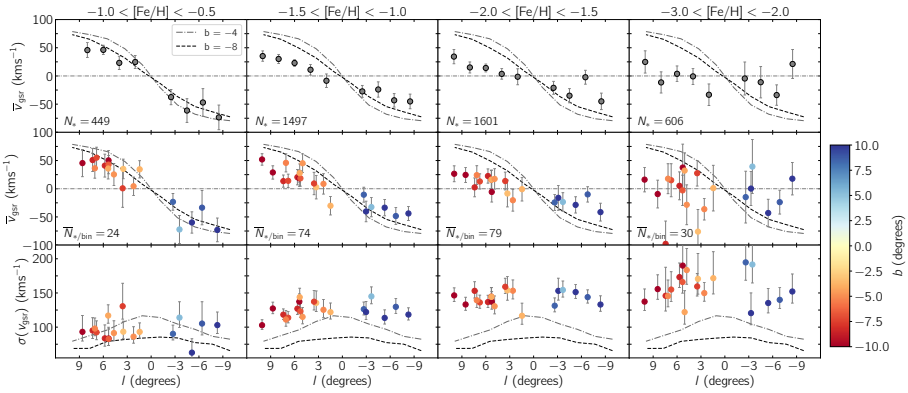

Figure 4.3 — Top row: longitude versus mean line-of-sight velocity in the GSR ($v_{\rm gsr}$) for different metallicity ranges from left to right (see column title) in bins of 2 degrees. This includes both the normal giants and the HB stars. Lines from the bar model from Shen et al. (2010) have been over-plotted. Error bars are $\sigma/\sqrt{N}$. Middle row: the same, but separately for each AAT field where the colour indicates the latitude. Bottom row: similar, but for the standard deviation of $v_{\rm gsr}$. In each of the panels, only bins with at least 10 stars are shown. The (asymmetric) error bars are $\sqrt{\sigma^2(N-1)/\chi^2_{\pm}}$, with $\chi_{\pm}$ determined for a 68% confidence interval and $N-1$ degrees of freedom.

fits the BRAVA data (Howard et al., 2008, 2009). In the bottom row of the figure we present the corresponding velocity dispersions for both the data and the bar model.

The motions of stars in the most metal-rich bin ($-1.0 <$ [Fe/H] < -0.5) appear quite consistent with the bar models. The more metal-poor stars also show signatures of rotation, but the mean velocity is smaller and decreases with decreasing metallicity until it disappears completely for the most metal-poor stars ([Fe/H] < -2.0).

The rotation of metal-poor stars in the inner Galaxy has previously been seen in the ARGOS data (Ness et al., 2013b), although their sample of metal-poor stars is small and has only one bin ([Fe/H] < -1.0). They find line-of-sight velocities of 20–40 km s^{-1} at $|l| = 10°$, consistent with what we find in our $-1.5 <$ [Fe/H] < -1.0 bin. Additionally, Kunder et al. (2016) showed that the RR Lyrae stars in the inner Galaxy may be rotating slowly, although their sample only contains stars with $|l| < 4°$ so they cannot trace the rotation beyond this. We clearly see for the first time how the rotation changes, and then disappears, as a function of metallicity in the metal-poor tail of the inner Galaxy.

Additionally, it is striking how strongly the velocity dispersion increases with decreasing metallicity. The behaviour of the velocity dispersion as a function of [Fe/H] is shown in more detail in Figure 4.4. Here we excluded the HB stars, since their metallicity is less well-determined. The increase in velocity dispersion with decreasing [Fe/H] appears gradual. The lower dispersions in the range $-10° < l < -5°$ with [Fe/H] < -2.3 could be an indication of substructure, but the sample

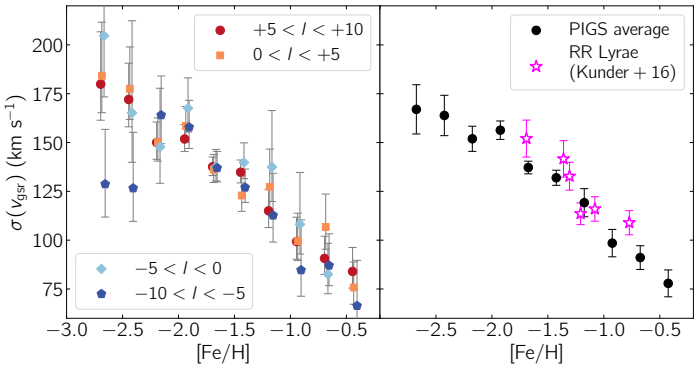

Figure 4.4 — Left: $v_{\rm gsr}$ dispersion as a function of [Fe/H] (bins of 0.25 dex), for four ranges in l. The HB stars are excluded. Different l ranges are offset by 0.01 dex for clarity. Only bins with at least 10 stars are shown. Right: weighted average of the different l ranges, with the bulge RR Lyrae results from Kunder et al. (2016).

is small. A linear fit to the average velocity dispersions provides a gradient of $-44 \pm 4\,{\rm km\,s^{-1}\,dex^{-1}}$.

Kunder et al. (2016) have previously shown that for inner Galaxy RR Lyrae stars the velocity dispersion increases with decreasing metallicity. Their results have been over-plotted in the right panel of Figure 4.4 and they generally agree with our findings, although their dispersions appear slightly higher. Ness et al. (2013b) also investigate the velocity dispersion as a function of [Fe/H], with lower [Fe/H] resolution and mainly for higher metallicity stars. For fields with $|l| \leqslant 10^\circ$ and $b \leqslant -7.5^\circ$, their relations appear to have similar slopes between $-1.0 <$ [Fe/H] $< +0.5$. Their velocity dispersion at [Fe/H] $= -1.0$ of $\sim 100\,{\rm km\,s^{-1}}$ is similar to our findings. Combining the results of PIGS and ARGOS, we find an almost continuous increase in velocity dispersion from [Fe/H] $= +0.5$ down to [Fe/H] $= -3.0$.

4.4 Discussion

With our large PIGS sample of metal-poor inner Galaxy stars, we can trace for the first time their rotation and velocity dispersion as a function of the metallicity for $-3.0 <$ [Fe/H] < -0.5. We find that the metal-poor stars show a signature of rotation, which decreases in magnitude with decreasing [Fe/H], until it disappears for the most metal-poor stars. The line-of-sight velocity dispersion is continuously increasing with decreasing metallicity. What is the interpretation of the behaviour of these metal-poor inner Galaxy stars? We present a number of possible scenarios.

Firstly, we note that our sample is not completely free of selection effects. Metal-poor stars are generally brighter and thus we may preferentially select stars that are further away at lower metallicity (and therefore less dominated by "the bulge").

Although we have tried to mitigate this effect through our selection of stars based on surface gravity, a small effect is potentially still present.

If we take our results at face value, a possible explanation is a smooth transition of how much each of the Galactic components (with fixed velocity dispersions) contributes at a certain metallicity. In this case there is a change from being dominated by a rotation-supported population of a bar or disc at higher metallicities ([Fe/H] > -1.0, Ness et al. 2013b) to being fully dominated by the pressure-supported component like the halo or classical bulge at the lowest metallicities ([Fe/H] < -2.0). Additionally, the stars in our sample are not necessarily confined to the bulge. At the lowest metallicities the fraction of stars that have large apocentres, and therefore only pass through the bulge, may increase. A transition between components can naturally explain an increase in velocity dispersion and a decreasing rotational signal with decreasing metallicity. This scenario would also work if the pressure-supported component itself does not rotate at all.

It has been shown that in the solar neighbourhood the thick disc has a metal-poor tail with [Fe/H] < -1.5 (Kordopatis et al., 2013a), possibly extending all the way down to [Fe/H] < -4.0, (Sestito et al., 2019). If this tail is also present in the inner Galaxy, these stars could contribute to the rotational signal that we see in Figure 4.4. Kordopatis et al. (2013a) estimate that in the solar neighbourhood, the fractions of stars with [Fe/H] < -1.5 belonging to the thick disc or the halo are equal (selecting stars with $1 < |Z/\mathrm{kpc}| < 2$ from DR4 of the RAVE survey, Kordopatis et al. 2013b). If we make the simple assumption that this fraction is the same in the inner Galaxy and we combine this with a halo/thick disc mass fraction of 0.10 locally (Kordopatis et al., 2013a) and 0.15 in the inner Galaxy (as derived by Schiavon et al. 2017 based on the Besançon model within a height of 4 kpc and $R_{GC} = 2$ kpc, from Robin et al. 2012, 2014), we estimate that the halo has ~ 1.5 times more stars in this region than the thick disc for [Fe/H] < -1.5. Many assumptions are made here, but this argument shows that at these metallicities the densities of the halo and thick disc only differ by a factor of a few. At higher (lower) [Fe/H], the thick disc (halo) contribution will dominate over the other.

Alternatively, stars of all [Fe/H] could originate from the disc without an additional halo component, where stars have been mapped into the boxy/peanut bulge in different ways because of their different velocity distributions at the time of the bar formation (e.g. Di Matteo, 2016; Debattista et al., 2017). This fits with a continuous increase in velocity dispersion all the way from [Fe/H] $= +0.5$ down to [Fe/H] $= -3.0$ (where this is almost like an age-[Fe/H] relation).

Additionally, a present pressure-supported component can itself be rotating. This can be original rotation from the collapse of a slightly rotating cloud for an in-situ classical bulge/halo, or alternatively stars in the spheroidal component could have been spun up and/or caught by the bar. The strong dynamical and gravitational effects of the bar should secularly affect all populations in the inner Galaxy (Saha et al., 2012; Saha, 2015). Recently, Pérez-Villegas et al. (2017) used N-body simulations to study the influence of the bar and boxy/peanut bulge on the central part of the halo. They find that due to angular momentum transfer, an initially non-rotating halo starts rotating with line-of-sight velocity signatures of $\sim$15–25 $\mathrm{km\,s^{-1}}$ for $|l| > 5^\circ$ with a velocity dispersion of $\sim$120 $\mathrm{km\,s^{-1}}$. They also find

that a small fraction of the stars (~12 per cent) are moving on bar-following orbits at the end of their simulation. The exact values of these numbers depend on the model details, but it shows that there can be some rotation in the halo component which is (much) slower than that of the bar. In order for this scenario to explain our metallicity-dependent results, the velocity dispersions for more metal-poor stars had to have been already (much) higher to begin with.

To further disentangle this complex region of our Galaxy, and e.g. to distinguish between an accreted and in-situ pressure-supported component, additional information is needed. Better distances (e.g. using a combination of parallaxes, spectroscopy and photometry with the StarHorse code, Santiago et al. 2016; Queiroz et al. 2018) are necessary to derive detailed dynamical properties. Additionally, high-resolution spectroscopic follow-up is necessary to get detailed chemistry of stars, which contains important information not present in metallicities and kinematics alone.

Acknowledgements.

We thank the referee for their helpful comments. We thank Chris Wegg, Tobias Buck and Jan Rybizki for helpful discussions and suggestions, and we thank Gail Zasowski for suggesting the PIGS acronym. We thank the organisers of the ESO conference "The Galactic Bulge at the crossroads" in Pucón, Chile, in December 2018, where the idea of this Letter was conceived.

We thank the Australian Astronomical Observatory, which have made these observations possible. We acknowledge the traditional owners of the land on which the AAT stands, the Gamilaraay people, and pay our respects to elders past and present. Based on data obtained at Siding Spring Observatory (via programs S/2017B/01, A/2018A/01, OPTICON 2018B/029 and OPTICON 2019A/045, PI: A. Arentsen). Based on observations obtained with MegaPrime/MegaCam, a joint project of CFHT and CEA/DAPNIA, at the Canada-France-Hawaii Telescope (CFHT) which is operated by the National Research Council (NRC) of Canada, the Institut National des Science de l'Univers of the Centre National de la Recherche Scientifique (CNRS) of France, and the University of Hawaii.

AA, ES and KY gratefully acknowledge funding by the Emmy Noether program from the Deutsche Forschungsgemeinschaft (DFG). NFM, RI, NL, and FS gratefully acknowledge support from the French National Research Agency (ANR) funded project "Pristine" (ANR-18-CE31-0017) along with funding from CNRS/INSU through the Programme National Galaxies et Cosmologie and through the CNRS grant PICS07708. FS thanks the Initiative dExcellence IdEx from the University of Strasbourg and the Programme Doctoral International PDI for funding his PhD. This work has been published under the framework of the IdEx Unistra and benefits from a funding from the state managed by the French National Research Agency as part of the investments for the future program. CL thanks the Swiss National Science Foundation for supporting this research through the Ambizione grant number PZ00P2 168065. DBZ and JDS acknowledge the support of the Australian Research Council through Discovery Project grant DP180101791. JIGH acknowledges financial support from the Spanish Ministry of Science, Innovation and Universities (MICIU) under the 2013 Ramón y Cajal program MICIU RYC-2013-14875, and also from the Spanish ministry project MICIU AYA2017-86389-P. Horizon 2020: This project has received funding from the European Union's Horizon 2020 research and innovation programme under grant agreement No 730890. This material reflects only the authors views and the Commission is not liable for any use that may be made of the information contained therein.

The authors thank the International Space Science Institute, Bern, Switzerland for providing financial support and meeting facilities to the international team "Pristine".

This work has made use of data from the European Space Agency (ESA) mission *Gaia* (`https://www.cosmos.esa.int/gaia`), processed by the *Gaia* Data Processing and Analysis Consortium (DPAC, `https://www.cosmos.esa.int/web/gaia/dpac/consortium`). Funding for the DPAC has been provided by national institutions, in particular the institutions participating in the *Gaia* Multilateral Agreement.

The Pan-STARRS1 Surveys (PS1) and the PS1 public science archive have been made possible through contributions by the Institute for Astronomy, the University of Hawaii, the Pan-STARRS Project Office, the Max-Planck Society and its participating institutes, the Max Planck Institute for Astronomy, Heidelberg and the Max Planck Institute for Extraterrestrial Physics, Garching, The Johns Hopkins University, Durham University, the University of Edinburgh, the Queen's University Belfast, the Harvard-Smithsonian Center for Astrophysics, the Las Cumbres Observatory Global Telescope Network Incorporated, the National Central University of Taiwan, the Space Telescope Science Institute, the National Aeronautics and Space Administration under Grant No. NNX08AR22G issued through the Planetary Science Division of the NASA Science Mission Directorate, the National Science Foundation Grant No. AST-1238877, the University of Maryland, Eotvos Lorand University (ELTE), the Los Alamos National Laboratory, and the Gordon and Betty Moore Foundation.

4.5 Appendix

4.5.1 Analysis of the spectra

To determine stellar atmospheric parameters, we use the ULySS code (Koleva et al., 2009) with the empirical MILES spectral library interpolator (Prugniel et al., 2011; Sharma et al., 2016). One advantage of using an empirical reference grid of stellar spectra in the determination of stellar atmospheric parameters, is that the grid only contains spectra with existing combinations of $T_{\rm eff}$, $\log g$ and [Fe/H], and therefore one only obtains physically sensible solutions. This especially an advantage at low resolution, where the sensitivity to $\log g$ is small. An extensive description of our analysis will be published in the PIGS II paper (Chapter 5), but some relevant details are summarised here.

We use only the blue arm in the fit, because the maximum wavelength in the MILES library is 7400 Å. In the future, we will explore the possibility of fitting together the blue and the red arm with a different reference library. The spectra are corrected for their radial velocities, but they are not continuum-normalised, before feeding them into ULySS. Inside ULySS, the continuum, stellar parameters, line broadening, and residual velocities are fitted simultaneously. In the fit, we mask the CH-band around 4300 Å, since [C/Fe] varies widely at low [Fe/H] (e.g. Beers & Christlieb, 2005, and references therein). Additionally, ULySS iteratively clips regions from the fit that are large outliers, excluding e.g. dead pixels and other unphysical features in the spectra.

We select stars with good fits on the basis of a set of (empirically determined) quality criteria. These are the following:

- $\mathrm{SNR}_{4000-4100} > 7$, to keep only spectra that have large enough signal-to-noise-ratio (SNR) between 4000–4100 Å,

- signal-to-residual ratio (SRR) > 15, to exclude peculiar stars that have bad fits even though they have a good SNR,
- $\sigma < 150$ km s^{-1}, to exclude stars that were fit with a high line broadening in ULySS, which usually indicates a bad fit,
- fraction of pixels clipped-out in the fit between $4600 - 4800$ Å $< 10\%$ and between $5000 - 5200$ Å also $< 10\%$, this cuts out stars with very large carbon features in these wavelength regions. Carbon is not included as a variable in the model spectra which therefore results in bad fits for very carbon-rich stars,
- $T_{\rm eff} > 4200$ K, because we found that the fits below this temperature are badly fitted.

These quality cuts remove 10% of the spectra. External tests of the stellar atmospheric parameters show that the systematic uncertainties with our method at the given resolution are of the order of 120 K, 0.35 dex and 0.2 dex for $T_{\rm eff}$, $\log g$ and [Fe/H], respectively. Tests with repeated observations show that the statistical uncertainties for stars with $\mathrm{SNR}_{4000-4100} < 7$ are larger than this, therefore we take this as our lower limit in SNR. Details of the tests will be described in the PIGS II paper. The mean $\mathrm{SNR}_{4000-4100}$ of the full sample is 25. For the spectra passing the defined quality criteria, the SNR in the CaT is larger than 10, with a mean of 60.

Example fits for three stars of different metallicities are shown in Figure 4.5. Each of these spectra has $\mathrm{SNR}_{4000-4100} \approx 25$.

4.5.2 Horizontal Branch stars

A striking feature in the $T_{\rm eff}$–$\log g$ diagram (top panel of Figure 2 in the main paper) is that of the horizontal branch (HB) stars. HB stars are helium-burning stars like red clump stars, but at lower metallicity. They are located at hotter temperatures compared to normal giants of the same metallicity. They enter our selection box on the blue side of the red giant branch (see the top panel of Figure 1 in the main paper between $0.7 < (BP - RP)_0 < 1.0$).

The HB stars end up in a narrow range of metallicity around -1.1. Additionally the HB is not as horizontal in the $T_{\rm eff}$–$\log g$ diagram as it should be. Both of these effects may (partly) be artefacts of the reference library. We used the MILES library (Sánchez-Blázquez et al., 2006a; Falcón-Barroso et al., 2011), which contains only a small number of stars at $T_{\rm eff}$–$\log g$ combinations of HB stars, that, compounding the problem, only possess these metallicities. However, preliminary tests with synthetic spectra appear to converge on metallicities similar to those from ULySS. Additionally, the ULySS fits do look reasonable, see Figure 4.6 for two examples. We therefore assume that the metallicities are good enough to separate the stars in bins of 0.5 dex as in Figure 3 of the main paper, but we exclude them from our analysis in main paper Figure 4, which is divided in bins of 0.25 dex. We check that when we do include them, the results do not change significantly: another indication that the metallicities are reasonable.

To separate the HB stars from normal giants, we first draw a rough box in $T_{\rm eff}$–$\log g$ space where HB stars are located. This region also contains some normal

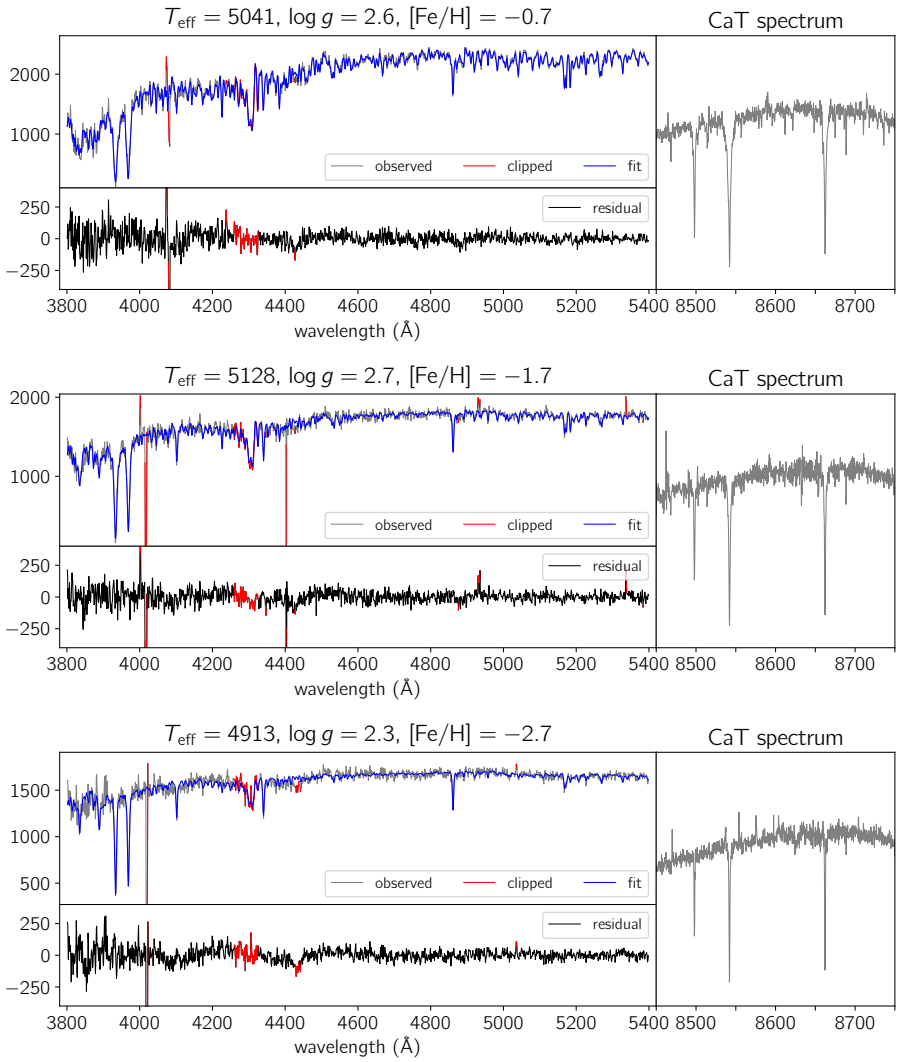

Figure 4.5 — Example fits of three spectra at different [Fe/H] and slightly different log g and $T_{\rm eff}$ (see titles). The units on the y-axis are an arbitrary flux unit. The spectra are normalised as determined in the fit. The CH-band around 4300 Å has been masked in all fits. The (non-normalised) CaT spectra are shown in the right-hand panels as examples of what they look like, they were not included in the fit.

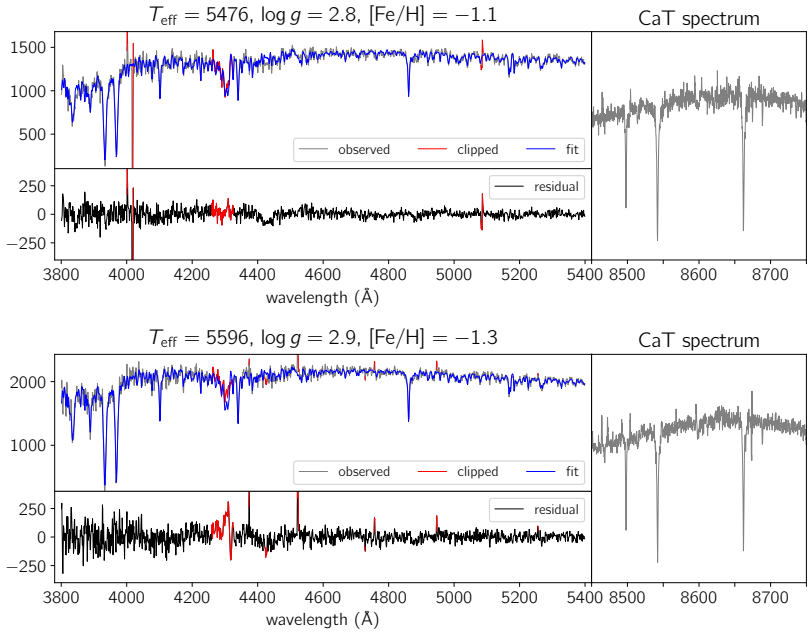

Figure 4.6 — Same as Figure 4.5, but for two HB stars, with slightly different temperatures and metallicities.

giants, but at these temperatures they are at lower [Fe/H] than the HB stars. Therefore we choose to split the two samples within this boxed region by [Fe/H]. From the metallicity distribution in Figure 2 of the main paper, we deduce that the [Fe/H] cut should be between [Fe/H] = −1.1 and −1.7 (the two peaks). We assume that the two types of stars should have roughly Gaussian distributions in [Fe/H] around their mean, with some tails. The best result is obtained when using a cut at [Fe/H] = −1.4.

To refine the exact HB selection box further, we take the stars with −1.4 < [Fe/H] < −0.5 to determine what $T_{\rm eff}$–log g combination results in the most natural split between normal and HB stars, see Figure 4.7. The red line runs through the valley between the HB stars and the giants, and has been set to be oriented along the giant branch. The functional form of this line is log $g = T_{\rm eff}/480 - 8.1$, which we use as the limit of our HB selection box.

4.5.3 Distances to our sample stars

To determine whether the stars in this sample are truly "in the bulge" (e.g. with R_{GC} < 3.5 kpc, as in Ness et al. 2013b), distances are needed. However, good distances to the stars in our sample are difficult to determine. *Gaia* DR2 (Gaia Collaboration et al., 2018) parallaxes by themselves are not good enough to estimate precise distances to sources further away than ∼4–5 kpc and our uncertainties on log g translate into large spectroscopic distance uncertainties.

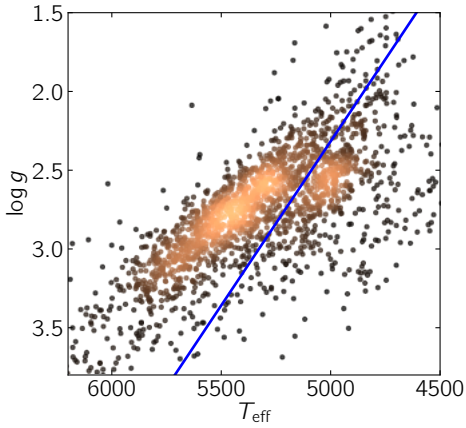

Figure 4.7 — Distribution of stars with $-1.4 < [\mathrm{Fe/H}] < -0.5$ in the $T_{\rm eff}$–$\log g$ diagram, colour-coded by density. We take the blue line ($\log g = T_{\rm eff}/480 - 8.1$) as the best separation between the normal giants and the HB stars in this metallicity range.

Since HB stars are standard candles, we can derive distances for this subset of stars from the photometry. We use the following HB absolute magnitude relation from Chen et al. (2009) for the SDSS i-band[3]:

$$M_{i,\mathrm{HB}} = (0.064 \times [\mathrm{Fe/H}]) + \big(0.049 \times \mathrm{age}\big) - 0.148 \tag{4.1}$$

with the age given in Gyr. We assume an age of 10 Gyr and the [Fe/H] from ULySS. We convert the absolute magnitude to distance using the distance-magnitude relation:

$$d = 10^{\frac{m_i - M_i}{5} + 1} \tag{4.2}$$

We derive distance uncertainties of ~0.8 kpc (≈ 10 per cent) by quadratically adding results from a 0.2 mag uncertainty in the i-band (estimated to cover the uncertainty on the extinction correction and the scatter in the relation) and a 2 Gyr uncertainty in age. The dependence on metallicity is almost negligible. The resulting distance distribution is shown in magenta in the top right panel of Figure 4.8, with an average of 7.7 kpc and a Gaussian width of 1.5 kpc, they lie perfectly in the bulge region.

We compare our standard candle HB distances with distances from the *Gaia* DR2 Bailer-Jones et al. (2018, hereafter BJ18) distance catalogue, which is based on parallaxes only in combination with a density prior. We remove stars which have $ruwe > 1.4$. The histograms of BJ18 distances for both the HB stars and the giants are shown in the top right panel of Figure 4.8, and the individual HB stars in the top left panel. It is clear that the BJ18 distances are generally too small and that their average uncertainties are much larger ($^{+2.9}_{-1.8}$ kpc). These distances should not be used for stars towards/in the bulge. The BJ18 distributions of the giants and HB stars look

[3]We convert the Pan-STARRS i-band magnitude to the SDSS photometric system using the relation from Tonry et al. (2012).

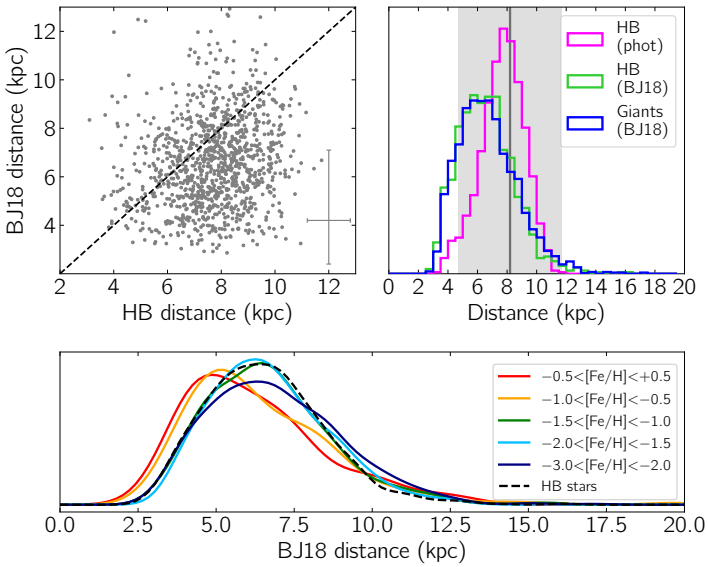

Figure 4.8 — Top left: Comparison of the Bailer-Jones and the standard candle HB distances. A typical error bar is indicated in the lower right corner. Top right: Comparison of the normalised distributions of the Bailer-Jones distances for the HB stars and the giants in our sample, and the HB standard candle distances from photometry. The shaded region indicates the Galactic centre distance of 8.2 kpc (Gravity Collaboration et al., 2019) ± 3.5 kpc. Bottom: kernel density estimate BJ18 distance distributions for the giants in different metallicity ranges, and for the HB stars.

similar, indicating that these samples either occupy the same distance range, and/or are too dominated by the assumed density prior.

There is still some relative information present in the distributions. We see an effect with metallicity as shown in the bottom panel of Figure 4.8. The stars in the two most metal-rich bins have smaller BJ18 distances, consistent with them being part of the bar which is pointing towards us in this part of the sky. The most metal-poor stars with [Fe/H] < -2.0 may have a more pronounced tail towards larger distances.

In a future work we will derive better individual distances, combining parallax information with spectroscopy and photometry. By themselves each of these methods have their problems and challenges (too far away for good parallax information, too large uncertainties on $\log g$ and/or extinction for good photometric or spectroscopic distances), but together they can break the degeneracies.

5 The Pristine Inner Galaxy Survey (PIGS) II: Uncovering the most metal-poor populations in the inner Milky Way

A. Arentsen, E. Starkenburg, N. F. Martin, D. S. Aguado, K. A. Venn, D. B. Zucker, V. Hill, C. Allende Prieto, R. Carlberg, E. Fernandez-Alvar J. I. González Hernández, L. I. Mashonkina, J. F. Navarro, R. Sánchez-Janssen, M. Schultheis, G. F. Thomas, K. Youakim, G. F. Lewis, J. D. Simpson, Z. Wan, D. Geisler, R. E. Cohen, J. O'Connell

— Published as Arentsen et al., 2020, MNRAS, 496, 4964, Oxford University Press —

ABSTRACT

Metal-poor stars are important tools for tracing the early history of the Milky Way, and for learning about the first generations of stars. Simulations suggest that the oldest metal-poor stars are to be found in the inner Galaxy. Typical bulge surveys, however, lack low metallicity ([Fe/H] < -1.0) stars because the inner Galaxy is predominantly metal-rich. The aim of the Pristine Inner Galaxy Survey (PIGS) is to study the metal-poor and very metal-poor (VMP, [Fe/H] < -2.0) stars in this region. In PIGS, metal-poor targets for spectroscopic follow-up are selected from metallicity-sensitive $CaHK$ photometry from the CFHT. This work presents the $\sim$ 250 deg^2 photometric survey as well as intermediate-resolution spectroscopic follow-up observations for $\sim$ 8000 stars using AAOmega on the AAT. The spectra are analysed using two independent tools: ULySS with an empirical spectral library, and FERRE with a library of synthetic spectra. The comparison between the two methods enables a robust determination of the stellar parameters and their uncertainties. We present a sample of 1300 VMP stars – the largest sample of VMP stars in the inner Galaxy to date. Additionally, our spectroscopic dataset includes $\sim$ 1700 horizontal branch stars, which are useful metal-poor standard candles. We furthermore show that PIGS photometry selects VMP stars with unprecedented efficiency: 86%/80% (lower/higher extinction) of the best candidates satisfy [Fe/H] < -2.0, as do 80%/63% of a larger, less strictly selected sample. We discuss future applications of this unique dataset that will further our understanding of the chemical and dynamical evolution of the innermost regions of our Galaxy.

5.1 Introduction

The oldest, metal-poor stars that still exist today formed in relatively pristine environments and are unique probes of the conditions in the early universe. These stars carry the imprint of the first supernovae and are local windows into the first episodes of star formation. Studying their chemistry in detail advances our understanding of the first generations of stars and their supernovae, and, combined with kinematic information, metal-poor stars provide clues to the early formation history of the Milky Way and its different components (see reviews by Freeman & Bland-Hawthorn, 2002; Tolstoy et al., 2009; Frebel & Norris, 2015).

The Λ cold dark matter simulations of Diemand et al. (2005) predict that, if any of the very first stars have survived to the present day, 30 − 60% of them would be within 3 kpc of the Galactic centre. Similarly, the simulations of Tumlinson (2010) suggest that metal-poor stars below [Fe/H][1] = −3.5 (all formed at redshifts > 15) would be most frequently found within the bulge, because dark matter haloes grow inside-out. These stars are not necessarily born in the bulge, but they have ended up in the central regions because of their dynamical history. Using hydrodynamical simulations, Starkenburg et al. (2017a) also find that the fraction of stars that are both metal-poor ([Fe/H] < −2.5) and old (formed within the first 0.8 Gyr) is highest towards the centres of galaxies, even though the relative fractions of just metal-poor stars or just old stars increase with galactic radius. Hence, a clear picture emerges that the central part of our Galaxy is a privileged location to look for the oldest and most metal-poor stars.

A complication in studying old, metal-poor stars in the Galactic bulge is that the overwhelming majority of stars are metal-rich ([Fe/H] > −0.5). This metal-rich component has been studied in detail in previous surveys such as the GIRAFFE Inner Bulge Survey (GIBS, Zoccali et al., 2014), the Bulge Radial Velocity Assay (BRAVA, Kunder et al., 2012), the Abundances and Radial velocity Galactic Origins Survey (ARGOS, Ness et al., 2012; Freeman et al., 2013) and the Apache Point Observatory Galactic Evolution Experiment (APOGEE, e.g. Schultheis et al., 2017; García Pérez et al., 2018; Zasowski et al., 2019). The general conclusion from these previous studies is that the Galactic bulge is a rotating, boxy/peanut-shaped pseudo-bulge, with little room for a pressure-supported, classical bulge (e.g. Howard et al., 2009; Hill et al., 2011; Shen et al., 2010; Ness et al., 2013b). If there is a classical component, it can only contain a fraction of the mass of the entire bulge and it is likely more dominant at lower metallicities.

The kinematics of the metal-poor tail of the bulge are still largely unexplored, with the exception of some RR Lyrae studies (e.g. Dékány et al., 2013; Kunder et al., 2016). The ARGOS survey of bulge red clump stars, with a survey strategy aimed to be metallicity-unbiased, found only 16 out of 14 150 stars with −2.6 < [Fe/H] < −2.0, and only 84 stars with [Fe/H] < −1.5 (Ness et al., 2013a). This emphasises that targeted surveys are necessary for the discovery of large samples of metal-poor stars in the inner Galaxy.

[1] $[X/Y] = \log(N_X/N_Y)_* - \log(N_X/N_Y)_\odot$, where the asterisk subscript refers to the considered star, and N is the number density.

There have been several efforts to find very metal-poor ([Fe/H] < -2.0) stars in the inner Galaxy using photometry. Casey & Schlaufman (2015) employed a combination of infrared 2MASS and WISE photometry. These authors found and studied three [Fe/H] < -2.7 stars with high-resolution spectroscopy, but it was limited to bright stars only (V < 14). Another study by Koch et al. (2016), used a filter focused on the Ca II K line to select candidate metal-poor stars. They found four stars with $-2.7 <$ [Fe/H] < -2.3, among them the first carbon-enhanced metal-poor star in the inner Galaxy.

So far, the largest effort to search for metal-poor stars in the inner Galaxy has been the Extremely Metal-poor BuLge stars with AAOmega (EMBLA) survey (Howes et al., 2014, 2015, 2016), which used SkyMapper photometry. The SkyMapper filter set includes a narrow-band v filter containing the Ca H&K lines. These lines are good metallicity indicators, and in combination with broad-band photometry, metal-poor stars can be selected efficiently using this v filter (Wolf et al., 2018). The EMBLA team has performed low-resolution follow-up spectroscopy of photometrically selected candidates and identified $\sim$ 150 stars with [Fe/H] < -2.5 (L. Howes, priv. comm.). From this sample, 37 stars were selected for high-resolution spectroscopic follow-up, and of those, 30 have [Fe/H] ≤ -2.5, and 9 have [Fe/H] ≤ -3.0. These stars are the first known extremely metal-poor stars in the inner Galaxy. The recent Chemical Origins of Metal-poor Bulge Stars (COMBS) survey also analysed stars selected using SkyMapper photometry. Their high-resolution spectroscopic sample contains five stars with [Fe/H] < -2.0 (Lucey et al., 2019).

A striking difference between the metal-poor EMBLA stars in the inner Galaxy and typical Galactic halo stars is that only a small fraction of EMBLA stars appear to be enhanced in carbon (Howes et al., 2015, 2016). In the Galactic halo, the number of stars with enhanced carbon increases with decreasing metallicity. These carbon-enhanced metal-poor (CEMP) stars comprise 15–20% of stars with [Fe/H] < -2 and up to 70% of stars with [Fe/H] < -4 (Yong et al., 2013b; Placco et al., 2014). One of the reasons for the lack of CEMP stars in EMBLA could be that the survey is biased against carbon-rich stars. The SkyMapper v filter includes a region of the spectrum where a CN-band can be present in carbon-enhanced stars, which makes such stars appear more metal-rich and fail the selection for follow-up (Da Costa et al., 2019).

The low number of known metal-poor stars in the bulge, the apparent lack of CEMP stars in the inner Galaxy, the possibility to uncover the oldest, metal-poor stars in the Milky Way, and the opportunity to study the metal-poor tail of the Galactic bulge are all good reasons to expand the search for metal-poor stars in the inner Galaxy. The Pristine Inner Galaxy Survey (PIGS) aims to build an unprecedentedly large sample of old, metal-poor stars for detailed chemo-dynamical studies. The Pristine survey (Starkenburg et al., 2017b, hereafter S17b) is very efficient at uncovering metal-poor stars photometrically. It has reported success rates of 56% and 23% from spectroscopic follow-up studies for finding stars in the Galactic halo with [Fe/H] < -2.5 and [Fe/H] < -3.0, respectively (Youakim et al., 2017; Aguado et al., 2019; Venn et al., 2020). In the Pristine survey, a narrow-band Ca H&K filter on MegaCam at the Canada-France-Hawaii Telescope (CFHT) is used to provide photometric metallicities down into the extremely metal-poor regime. The $CaHK$ photometry is combined with available broadband photometry

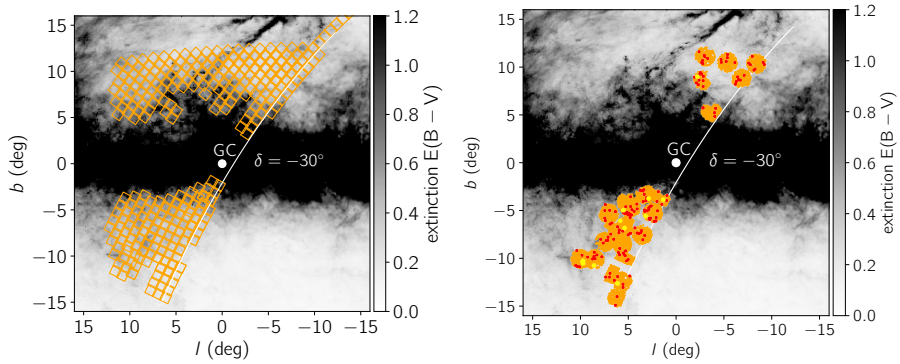

Figure 5.1 — PIGS footprints, on top of the extinction map from Green et al. (2018) (where available and reliable, which is above a declination of −30° and at $|b| > 2°$) and Schlegel et al. (1998) (elsewhere). A truncation of the colour bar at E(B−V) = 1.2 is set for clarity. Left: photometric footprint, where each square is one MegaCam field. Right: spectroscopic footprint, located within the photometric footprint from 2017 and 2018. Stars with [Fe/H] < −2.5 are marked in red, and those with [Fe/H] < −3.0 in yellow.

for colour/temperature information to compute these photometric metallicities. The Pristine filter is narrower than the SkyMapper filter, and should be less biased against CEMP stars (see Figure 2 in S17b).

Compared to the halo, the inner Galaxy has a much higher density of (mainly metal-rich) stars. It is therefore significantly more crowded, there is a larger foreground population, and there is much more (inhomogeneous) reddening due to the presence of dust. These challenges, together with the unique science case, have led to a change in strategy between the main Pristine survey and PIGS, which we will describe in this paper. The first scientific results from PIGS were published in a Letter in this journal (Arentsen et al., 2020a) / Chapter 4, and it focused solely on the kinematics of the metal-poor ([Fe/H] < −1.0) tail of the inner Galaxy using a sample of several thousand low- and intermediate resolution spectroscopic observations.

In this work, we present the PIGS data collection and analysis in detail and focus on our results and success rates to find and analyse the most metal-poor stars in the inner Galaxy. The photometric $CaHK$ observations and selection of metal-poor candidates are described in Section 5.2. The analysis of low-/medium resolution spectroscopic follow-up observations are described in Section 5.3, the results for the stellar parameters are discussed in Section 5.4, and the survey performance is determined in Section 5.5. A summary of our PIGS survey and future plans are provided in Section 5.6.

5.2 Photometric observations

In this section, the photometric PIGS data is presented. We discuss the data reduction and calibration, and the target selections for the spectroscopic follow-up.

With MegaCam on CFHT, we have obtained ~250 square degrees of metallicity-sensitive $CaHK$ photometry in the Galactic bulge region. The footprint covers a region of $|l|$ and $|b| \lesssim 12^\circ$ above a declination of -30° (because we observe from the Northern hemisphere), and we limited it to areas with E(B−V) $\lesssim 0.7$ to avoid regions with too much extinction. A pilot program was initiated in 2017A, and extended to a larger program in 2018A and 2019A. The final photometric PIGS footprint is shown in the left panel of Figure 5.1. A small overlap between neighbouring MegaCam fields is included for calibration purposes.

5.2.1 Data reduction and calibration

Reduction

The PIGS MegaCam images are processed similarly to the Pristine images, as presented in S17b. All downloaded images are pre-processed by CFHT with the Elixir pipeline, whose role is to remove instrumental signatures from the data (Magnier & Cuillandre, 2004). The images were processed with a version of the Cambridge Astronomical Survey Unit pipeline (CASU, Irwin & Lewis, 2001) tailored to MegaCam images. The astrometry is performed on a CCD to CCD basis and using 2MASS (Skrutskie et al., 2006) for reference. While we could also use the *Gaia* DR2 (Gaia Collaboration et al., 2016, 2018) astrometry, the shallower 2MASS data works well for the densely populated regions of the survey and has the benefit of converging more quickly on a good astrometric solution, accurate at the $0.1''$ level. This accuracy is more than enough to cross-match the sources to *Gaia* DR2 positions, and we use the *Gaia* positions for the stars throughout this paper. With the CASU pipeline, aperture photometry is carried out on the individual CCDs to build a catalogue of sources that are at least 5σ above the background threshold.

The following quality cuts are made on the *Gaia* cross-matched catalogue to create our final non-calibrated catalogues:

- casu_flag = −1 or casu_flag = −2
- *Gaia* phot_variable_flag ≠ VARIABLE
- *Gaia* phot_bp_mean_mag and phot_rp_mean_mag > 0
- *Gaia* duplicated_source = false

The first cut only keeps point-sources from the CASU $CaHK$ photometry data reduction. The other three are quality cuts on the *Gaia* data, removing variable stars, stars that do not have BP and/or RP photometry, and stars that are flagged to be duplicated sources. The last flag proved to be unnecessary in hindsight. The full catalogue consists of more than 34 million objects with a *Gaia* DR2 counterpart (there are fewer unique stars; some stars have multiple entries due to the overlap between fields).

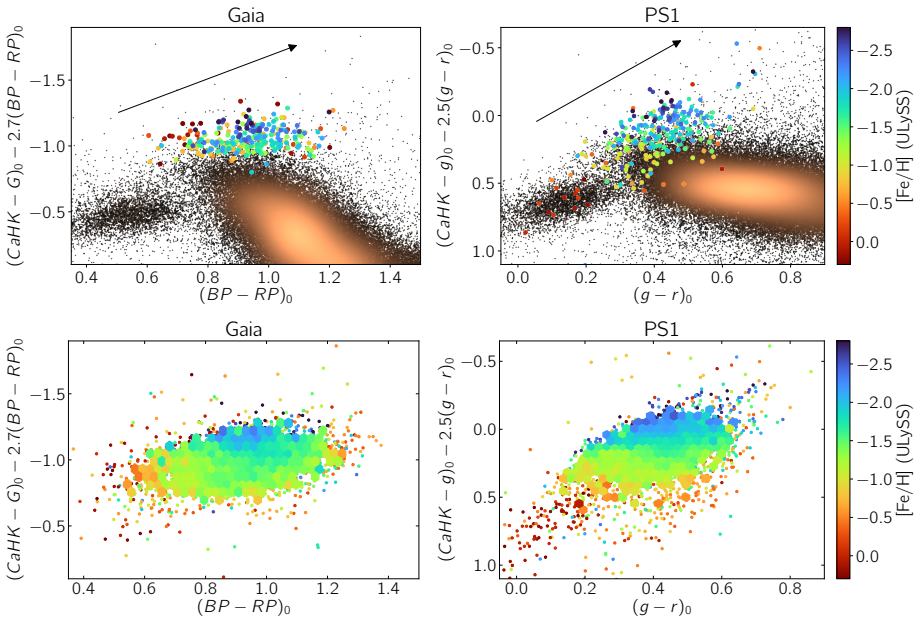

Figure 5.2 — Pristine colour-colour diagrams combining our *CaHK* photometry with broad-band photometry from *Gaia* (left) and PS1 (right). Top row: stars within our selected magnitude range and passing the parallax cut for a two-degree field of view centred on $(l, b) = (2.4°, -5.2°)$. We show our spectroscopic follow-up for this field, where the selection was originally made using *Gaia*. These stars are colour-coded by their ULySS [Fe/H] (for details on the spectroscopic analysis, see Section 5.3.4). The extinction vector for E(B−V) = 0.45 (the average in this field) is indicated by the arrow in the top left. Bottom row: 4300 stars in the Southern spectroscopic PIGS sample ($b < 0°$) that pass the ULySS quality criteria. Each hexbin contains at least five stars and is coloured by its average ULySS [Fe/H]. Single stars are plotted as additional points.

Calibration

The (non-calibrated) catalogue produced after the data reduction steps described above needs to be calibrated with several additional steps. Firstly, because the MegaCam images show subtle variations in magnitude that depend on the location in the field of view, a flat-field correction is applied as determined in Section 2.4.2 of S17b. Secondly, all MegaCam fields are put on the same scale. S17b used the determination of the stellar locus in the SDSS dereddened $((g - i)_0, (\mathrm{CaHK} - g)_0)$ colour-colour space to shift all fields to the scale of one reference field. The stellar locus consists mainly of metal-rich foreground stars. Unfortunately this method does not work for our footprint towards the inner Galaxy. The stellar locus is less well-defined since we look through a larger part of the disk, and, additionally, correcting for 3D extinction is a challenge. Thus, our MegaCam pointings are placed to create an overlap between neighbouring *CaHK* fields of ~ 0.1°, and these overlapping regions are used for a relative photometric calibration. All *Gaia* DR2

source_id's that have multiple $CaHK$ matches within 1" are identified, and we assume that these sources are the same stars observed in two (or more) different MegaCam fields. These are then used to determine the relative offsets between fields.

The 2017 and 2018 data sets and calibration are primarily used to select stars for our spectroscopic follow-up program (described in Section 5.3). As an initial (crude) calibration, we set one central field as the reference and started by determining offsets for the directly neighbouring fields with respect to the reference. For each pair of fields, all stars in common were used to compute the minimum χ^2 and the best offset. This process was repeated for each of those fields and their neighbours that had not yet been calibrated, until all fields are on the same scale. In this calibration, each field is calibrated with respect to only one other field.

In 2019, the calibration was changed to a more homogeneous approach, minimising the χ^2 for the overlapping regions of all fields simultaneously (using only the stars with $CaHK$ uncertainties less than 0.01), using the iterative method of Magnier et al. (1992) to find the best solution. We have since re-calibrated all our photometry using this approach, including the fields in the 2017 and 2018 footprint.

It is important to note that since we perform a relative calibration, the $CaHK$ photometry is not on the same scale as the $CaHK$ photometry in S17b. It is only homogeneous for continuous regions; thus, fields with $b > 0°$ and $b < 0°$ are not necessarily on the same scale as the two regions do not overlap.

5.2.2 Target selection for spectroscopic follow-up

Choice of broad-band photometry

The calibrated $CaHK$ photometry was combined with broad-band photometry to determine the best metal-poor candidates. The $CaHK$ lines are not only sensitive to metallicity, but they also depend strongly on the temperature of the star, which can be approximated using broad-band colours. In S17b, SDSS photometry was used, but there is no SDSS photometry towards the Galactic bulge (York et al., 2000). Instead, *Gaia* DR2 (Gaia Collaboration et al., 2018) and Pan-STARRS1 (PS1, Chambers et al., 2016) photometry were used to select targets. To select giant stars that are roughly at the distance of the bulge (for the typical extinction in our fields), we limited our magnitude range to $13.5 < G < 16.5$ when using *Gaia*, and $14.0 < g < 17.0$ when using PS1 (see Section 5.3.1). An additional cut was imposed on the *Gaia* parallaxes (ϖ) to remove foreground stars. This cut has slightly changed during the progress of the survey, from no cut in our spectroscopic follow-up pilot, in August 2017, to $\varpi > 0.25$ mas in 2018A, $\varpi - \Delta\varpi > 0.30$ mas in 2018B and $\varpi - \Delta\varpi > 0.25$ mas in 2019A.

The use of broad-band colour systems has evolved as well as we gained further insight by collecting larger spectroscopic samples. In 2018, after the pilot program, we enthusiastically switched from PS1 photometry to Gaia DR2 photometry when it became available, because the latter has the advantage of being more precise and having all-sky coverage. The bulk of our spectroscopic follow-up to date has thus been selected with the help of *Gaia* photometry. Further analysis of the results of these *Gaia*-selected runs, however, showed that the PS1 photometry performs

better for our purposes, especially in regions with high extinction. The reason for this is that even though the *Gaia* photometry is much more precise than PS1, it is much harder to correct for extinction. We have used *Gaia* extinction coefficients determined by F. Anders [2] for stars of $T_{\rm eff}$ = 5250 K and an extinction of A_V = 1.5 (which corresponds to an E(B−V) ≈ 0.5), together with the Green et al. (2018) reddening map. Because the *Gaia* filters are so broad, their extinction coefficients depend non-negligibly on the amount of extinction itself and on the temperature of the star. The coefficients are therefore not constant throughout our footprint, which covers a range of extinction values.

For these reasons, we switched back to using PS1 for our follow-up in 2019 and indeed noticed that it reduced the contamination from more metal-rich stars. The PS1 filters are narrower and therefore less dependent on the temperature of the star and the extinction. Additionally, the Green et al. (2018) reddening map has been made using PS1 photometry and they provide up-to-date PS1 extinction coefficients to go with this map, making the broad-band de-reddened photometry more self-consistent. For the $CaHK$ photometry, the extinction coefficient 3.924 from S17b was used, which is on the Schlafly & Finkbeiner (2011, hereafter SF11) scale.

Green et al. (2018) provide a 3D map that can be queried at different distances. For our purposes, we assume that all dust is located in the foreground disk (which should be valid in the PIGS latitude range), and query the map at a distance of 8 kpc. Another assumption is that the extinction law is constant (and correct). However, Schlafly et al. (2016) have shown that there appear to be spatial variations, which have not yet been characterised in detail. Finally, the extinction correction is limited by the pixel scale of the map used, while the extinction may vary on even smaller scales.

In this paper, whenever photometry is shown (in Figure 5.2 and 5.9), the updated PS1 reddening map by Green et al. (2019, hereafter G19) was used. The difference between the extinction coefficients for the PS1 *g* and *r* filters provided by the authors and those from SF11 is significant (0.35 for both), due to differences in the adopted reddening vector and scaling of their map. The extinction coefficients for $CaHK$ and the *Gaia* photometry are, however, on the SF11 scale. To convert the *Gaia* photometry to the G19 reddening scale, 0.35 was added to the A_V as used in Footnote 2 (assuming that the difference is same as for the PS1 *g* and *r* filters, which overlap in wavelength range with V). The $CaHK$ wavelength range lies outside the PS1 coverage and is bluer (more affected by extinction), therefore extrapolation is likely invalid for this filter. To estimate the G19 $CaHK$ coefficient, we instead tested a range of coefficients and determined for which value the dispersion in our photometric metallicity bins was the smallest (see Section 5.5.2 for a description of the photometric metallicities). A minimum was found for A_{CaHK} = 4.5, which was therefore adopted as the coefficient to use with the G19 map.

[2] These coefficients are A_G/A_V = 0.718, A_{BP}/A_V = 0.9785 and A_{RP}/A_V = 0.576. They were derived by interpolating between coefficients for stars of 4000 K and 6500 K. The Schlafly & Finkbeiner (2011) value for A_V = 2.742 (R_V = 3.1) was used.

Metallicity-sensitive photometric selection

In S17b, photometric metallicities for individual stars were determined from the $CaHK$ and broad-band photometry. This was not done for PIGS for multiple reasons: our $CaHK$ photometry is not all on the same absolute scale, the method had not been calibrated for *Gaia* broad-band photometry, and the photometric metallicities would in any case be much less precise than in the halo because of uncertainties in the reddening correction.

Instead, a relative selection was applied in each follow-up field. An example selection for follow-up with *Gaia* is shown in the top left panel of Figure 5.2, for a two-degree field of view. In this Pristine colour-colour diagram, the metal-poor stars are roughly expected to lie towards the top. Targets were therefore simply selected by their vertical location in this diagram, within a certain $(BP - RP)_0$ range corresponding to the expected location of metal-poor giant stars. The coloured points are stars followed up spectroscopically, which have been colour-coded according to their spectroscopic metallicity (for details on the spectroscopy, see the next section). The top-right panel of the figure shows the same stars, but now with PS1 broad-band photometry instead of *Gaia*. The contamination of metal-rich stars would have been lower, if this field had been selected using PS1. In the bottom row of the figure we present the same diagrams, now for all stars in our spectroscopic follow-up program with $b < 0°$ (a homogeneously calibrated region of the photometry). There is a much clearer gradient with [Fe/H] in the case of PS1 photometry compared to the *Gaia* photometry. The main culprit of this difference is the extinction, which – as explained above – is difficult to correct for in the broad-band *Gaia* filters.

5.3 Spectroscopic follow-up observations

We performed low-/intermediate-resolution spectroscopic follow-up of our metal-poor candidates with the 3.9m Anglo-Australian Telescope (AAT). The follow-up was done with the dual-beam AAOmega spectrograph (Saunders et al., 2004) with the Two Degree Field (2dF) multi-object instrument, which has roughly 360 fibres for science targets (plus ~40 sky and guide fibres) over a 2-degree diameter field of view (Lewis et al., 2002; Sharp et al., 2006). To date, 23 fields have been observed, yielding spectra for 8350 stars. The right panel of Figure 5.1 shows the current spectroscopic PIGS footprint. Three fields were observed in service mode in August 2017 and June 2018, the rest was observed during three observing runs in June 2018, August 2018 and April 2019. The observations of two fields in August 2017 were our spectroscopic pilot program.

In this section, our observing strategy, the data reduction, the determination of radial velocities, and two independent methods of analysing the spectra are described. We first describe the derivation of $T_{\rm eff}$, $\log g$ and [Fe/H] with ULySS (Koleva et al., 2009), which is a data-driven method using empirical reference model spectra. In our second analysis, the employed method is FERRE (Allende Prieto et al., 2006) with a grid of synthetic model spectra to determine $T_{\rm eff}$, $\log g$, [Fe/H], and [C/Fe]. The parameters from ULySS for the sample in this work were used in

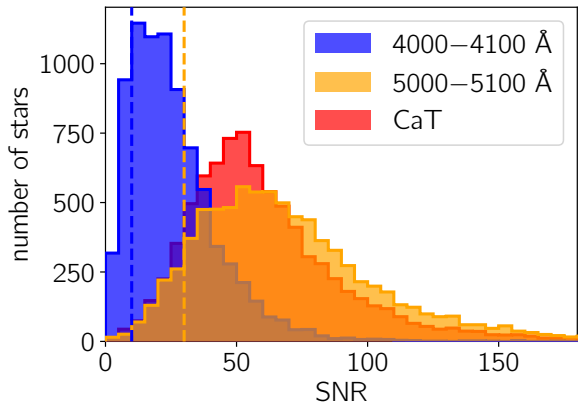

Figure 5.3 — Distribution of the SNR in different regions of the AAT spectra. The CaT range is from ~ 8400 – 8800 Å. The $SNR_{4000-4100}$ = 10 and $SNR_{5000-5100}$ = 30 quality cuts (see Section 5.3.4) are indicated by the vertical dashed lines.

Arentsen et al. (2020a)/Chapter 4, although we note that if the FERRE parameters had been used instead this would not have altered the results of that paper.

5.3.1 Observing strategy

For each field, the top 200 candidates from the photometry were provided and they were given the highest priority in the configuration of 2dF. Generally, ~95% of those candidates were allocated a fibre. The next best 200 candidates were provided with intermediate priority and the next best 200 candidates with low priority to fill the remaining ~ 160 science fibres. Stars already in the EMBLA survey were removed from our selection in most fields. 25 fibres were allocated to sky positions, the input catalogue for these was created by hand using the Aladin tool (Bonnarel et al., 2000) and PS1 images. Finally there are 8 fibres for guide stars, which were selected from *Gaia* DR2.

The stars were observed with the 580V and 1700D gratings, resulting in blue spectra at a resolving power R ~ 1300 covering ~ 3700 – 5500 Å, and near-infrared calcium triplet (CaT) spectra at R ~ 11 000 covering ~ 8400 – 8800 Å. The CaT spectra were used to determine radial velocities, and both spectra together to determine stellar parameters and metallicities.

The recommended magnitude range for stars in one 2dF field is ~3 magnitudes. When using *Gaia* photometry, stars between G = 13.5 and 16.5 were selected, and when using PS1, the selected stars were between g = 14.0 and 17.0. We aimed for a minimum signal-to-noise ratio (SNR) of 20 in the blue spectra, which meant integrating for 2 hours on each field. Because there were some fibre throughput issues (see below), this was not always successful for the faintest stars. The SNR in different regions of the spectra is summarised in Figure 5.3.

5.3.2 Data reduction

The spectra were reduced using the AAT 2DFDR[3] (v. 6.46) package. The standard settings for the 580V and 1700D spectra were used respectively, with the exception of two parameters that determine how spectra from multiple observations are combined.

The first setting which was changed is the FLUX_WEIGHT parameter, which determines how much weight is given to each individual exposure when combining to a single spectrum. The standard setting determines a frame zero-point by taking the median of the zero-points for each fibre. These fibre zero-points are derived using the difference between an empirical brightness from a smoothed version of the spectra and the expected brightness from provided external photometry. The frame zero-points are used to determine the relative weights of multiple exposures. This, however, is inappropriate when there is variation in throughput across the field. From the 2DFDR quality plots, we concluded such a variation is indeed present in most of our fields. There are often regions on the plate that have a reduced throughput. Although these regions are not always in the same location, they are usually in the outer regions of the plate. The effect is described in some detail in the appendix of Li et al. (2019). The root cause of the problem is the accuracy of the fibre placement, but exactly why the fibre placement is bad is unknown. There have been efforts at the AAT to resolve these problems, but so far no solution has been found (priv. comm. T. S. Li and C. Lidman). Because of the observed variation in throughput, we therefore decided to use the flux weighting by object instead of by frame, where each object is assigned its own weight in the combination of multiple frames.

Secondly, the ADJUST_CONTINUUM option was turned off. It was originally introduced into the software to fix a problem with the continuum of early 2dF spectra, which was solved in 1999. The 2DFDR documentation suggests it is worth using for data taken after the problem was fixed (it is the default), but it can also be turned off. We found that the default setting sometimes produced spurious, unphysical calcium triplet line shapes, therefore this option was disabled.

5.3.3 Radial velocities

Radial velocities were determined from the CaT spectra using the FXCOR package in IRAF[4]. The CaT spectra were cross-correlated with synthetic spectra, which were created using the MARCS (Model Atmospheres in Radiative and Convective Scheme) stellar atmospheres and the Turbospectrum spectral synthesis code (Alvarez & Plez, 1998; Gustafsson et al., 2008; Plez, 2008). A preliminary velocity was derived using a template with $T_{\rm eff} = 5000$ K, $\log g = 2.5$ and [Fe/H] $= -2.0$. After zero-shifting the spectra, we derive stellar parameters with ULySS (see Section 5.3.4). To improve the radial velocities, they were re-derived using the template that is the closest match to the ULySS parameters, from the following grid: $T_{\rm eff} = [4500, 5000, 5500]$ K, $\log g = 2.5$

[3] `https://aat.anu.edu.au/science/software/2dfdr`

[4] IRAF (Image Reduction and Analysis Facility) is distributed by the National Optical Astronomy Observatories, which are operated by the Association of Universities for Research in Astronomy, Inc., under contract with the National Science Foundation.

and [Fe/H] = [0.0, −1.0, −2.0, −3.0]. From the FXCOR formal uncertainties and a test of repeated observations, the radial velocity uncertainties are estimated to be of the order of 2 km s^{-1}.

5.3.4 Spectral analysis with ULySS

Method

For the first determination of stellar atmospheric parameters ($T_{\rm eff}$, log g and [Fe/H]) the University of Lyon Spectroscopic analysis Software (ULySS[5], Koleva et al. 2009, version 1.3.1) was used. ULySS is a full-spectrum fitting package that determines the best parameters by minimising the χ^2 of the residuals of the fit between an observed spectrum and model spectra. The model library used is the empirical MILES library (Sánchez-Blázquez et al., 2006b; Falcón-Barroso et al., 2011) with a resolving power of ∼2200, for which Prugniel et al. (2011) have computed a ULySS interpolator. We use the version of the interpolator as updated by Sharma et al. (2016), who improved it for cool stars. Recently, Arentsen et al. (2019b)/Chapter 3 have used ULySS with this interpolator to determine stellar atmospheric parameters for DR2 of the X-shooter Spectral Library (Gonneau et al., 2020). The reliability of the method has been tested extensively in the aforementioned works, and it has been found to be robust for FGK stars with $-2.5 <$ [Fe/H] < 0.5 and $0 <$ log $g < 5$. Details on how the method works can be found in Prugniel et al. (2011), it is briefly summarised here.

The model spectrum $S(\lambda)$ in ULySS is described by:

$$S(\lambda) = P_n(\lambda) \times G(v_{\rm r}, \sigma) \otimes {\rm TGM}(T_{\rm eff}, \log g, [{\rm Fe/H}], \lambda), \tag{5.1}$$

where $P_n(\lambda)$ is a series of Legendre polynomials up to degree n, and $G(v_{\rm r}, \sigma)$ is a Gaussian broadening function described by the radial velocity $v_{\rm r}$ and the broadening width σ. The σ is mainly related to the resolution of the spectra and to the rotational velocity of a star, sometimes it is also increased to smooth the spectra if no good fit can be found otherwise. The polynomial $P_n(\lambda)$ normalises the spectra, correcting for, e.g., the effects of the detector response and dust extinction. The TGM function represents the interpolator, which is a polynomial function that creates spectra from a reference library for a given combination of $T_{\rm eff}$, log g and [Fe/H]. In the fit, the free parameters are $T_{\rm eff}$, log g, [Fe/H], $v_{\rm r}$, σ and the coefficients of $P_n(\lambda)$.

The spectra reduced to the rest-frame with our preliminary CaT radial velocities were used, therefore $v_{\rm r}$ only absorbs uncertainties in the velocity. The degree of $P_n(\lambda)$ was set to 10, which is enough to correct for the response function of the detector and the extinction, but not so high that it starts affecting the parameters. The spectra were fit between 3800−5400 Å. The region of the CH G-band was masked between 4260 and 4325 Å, since carbon can be anomalous in metal-poor stars and it should be avoided that this drives the fit. The MILES library does not contain the region of the CaT, so the blue arm was fit alone.

We run ULySS with a grid of initial guesses to avoid getting trapped in local minima. The starting grid is $T_{\rm eff}$ = [4000, 5000, 6000] K, log g = [2.0, 4.0], and [Fe/H] = [−2.4, −1.7, −0.3], and the solution with the smallest χ^2 is finally adopted as the best

[5] ULySS is available at `http://ulyss.univ-lyon1.fr`

solution. Furthermore, the `/CLEAN` option was turned on, which rejects regions where the fit is bad due, for example, to bad pixels or features which are not in the model spectra such as strong carbon bands.

Some spectra do not pass through this first run or have extremely high σ values. They were rerun with a multiplicative polynomial of degree $n = 30$, which gives solutions for 89 additional stars. The main reason that these spectra fail, is that they either have a strong continuum shape that cannot be corrected with $n = 10$ or they are very carbon rich, in which case the higher polynomial degree tries to correct for the carbon features.

Example fits for seven stars are presented in Figure 5.4, in blue.

Selection of reliable results

The atmospheric parameters were determined for 8089 PIGS stars. To select reliable solutions, the following criteria were used:

- $\mathrm{SNR}_{4000-4100} > 10$ or $\mathrm{SNR}_{5000-5100} > 30$
- signal-to-residual ratio (SRR) > 15
- $\sigma < 150\ \mathrm{km\,s^{-1}}$
- fraction of rejected pixels in the fit between 4600 – 4800 Å< 10% and between 5000 – 5200 Åalso < 10%
- not double-lined

which leaves 7126 stars. The SNR cut was determined using repeated observations: above these SNR values, the dispersion in the results for individual observations is almost independent of SNR. This cut removes 677 stars, a relatively large fraction because of the flux-loss issues described in Sect. 5.3.2. The second and third cuts were set after inspecting the fits of stars that passed the SNR criterion, but had low SRR or very high σ which typically indicates a bad fit. Then the fraction of rejected pixels in the fit in the regions of two strong carbon bands were used to weed out a number of carbon-enhanced stars that had not been removed yet by the other cuts. The ULySS results are not reliable for such stars. These three cuts remove an additional 136 stars. The final cut removes stars with double-lined CaT spectra, based on a cross-correlation function (CCF) analysis. We cross-correlate the observed spectrum and the radial velocity synthetic template, and flag stars that have two or more clear peaks in the CCF (if the secondary is at least 50% as strong as the primary). This removes a final 150 stars. Given the crowding towards the bulge, the double-lined stars are probably more likely to be chance-alignments than spectroscopic binaries.

Stellar parameter uncertainties

The formal uncertainties provided by ULySS might under- or overestimate the statistical uncertainties if the uncertainty spectra are not perfect. To investigate

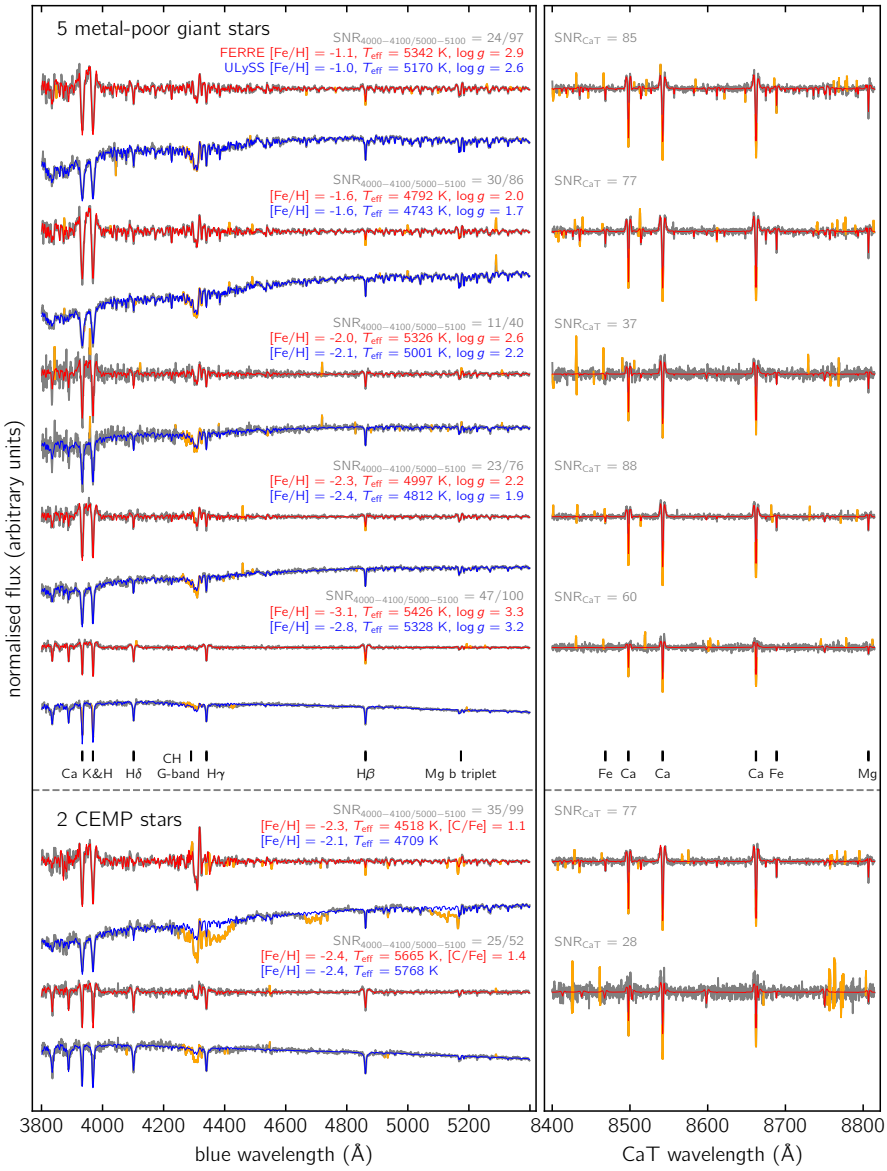

Figure 5.4 — Example fits for ULySS (blue) and FERRE (red) for five metal-poor giants and two CEMP stars. For both analyses, the observed (normalised) spectrum is shown in grey. Regions in the observed spectra which are masked in the fit are indicated in orange, these contain both a priori masks (the CH G-band in ULySS and the calcium triplet line cores in FERRE) and pixels that are masked iteratively. Several of the strongest spectral features have been indicated. For each star, the stellar parameters from both analyses are shown.

this, a repeat- observation test as in Arentsen et al. (2019b)/Chapter 3 was used. For each independent pair of observations of the same star, we computed the following weighted difference in the stellar parameters:

$$\Delta \mathrm{P}_{w,i} = \frac{\mathrm{P}_{1,i} - \mathrm{P}_{2,i}}{\sqrt{\epsilon_{1,i}^2 + \epsilon_{2,i}^2}}, \tag{5.2}$$

where P represents $T_{\rm eff}$, $\log g$ or [Fe/H], ϵ represents the formal uncertainty given by ULySS, and 1 and 2 indicate two observations of the same star. The distribution of ΔP should be close to Gaussian, with a standard deviation $\sigma_{\Delta \mathrm{P}} = 1$ if the uncertainties are properly scaled. A smaller/larger $\sigma_{\Delta \mathrm{P}}$ indicates over-/underestimated uncertainties.

We select two fields, one with four sub-exposures (F_273.7-27.1) and one with six sub-exposures (F_284.0_30.0). The stars in these fields are a representative subsample of the total. After applying the quality cuts for reliable solutions from the previous section, 2850 independent pairs of observations remain, which were used for the test. For all three parameters the distribution of ΔP is found to be close to Gaussian, with a standard deviation of 1.2. This indicates that the uncertainties are somewhat underestimated, therefore we multiply the formal ULySS uncertainties by this factor to derive proper internal uncertainties. The median of the internal uncertainties for the reliable set of ULySS parameters are 32 K, 0.08 dex and 0.04 dex for $T_{\rm eff}$, $\log g$ and [Fe/H], respectively.

5.3.5 Spectral analysis with FERRE

Method

The spectra were additionally analysed with the FERRE[6] code (Allende Prieto et al., 2006). FERRE performs full-spectrum fitting against a synthetic stellar model library, interpolating between the different nodes (the cubic algorithm was selected for the interpolation). In addition, the Boender-Timmer-Rinnoy-Kan (BTRK) algorithm was used as the global optimisation technique already included in the FERRE architecture. For each fit four different runs have been performed to avoid getting trapped in a local minimum. The $T_{\rm eff}$, $\log g$, [Fe/H] and [C/Fe] were derived simultaneously. In this work, we mainly focus on $T_{\rm eff}$, $\log g$, and [Fe/H]. The results with regards to [C/Fe] merit a separate discussion that is the subject of a forthcoming paper (see Chapter 6). The synthetic spectra in the reference grid were computed with the ASSET code (Koesterke et al., 2008), with the model atmospheres computed using the Kurucz code, described in Mészáros et al. (2012), assuming a microturbulence of 2 $\mathrm{km\,s^{-1}}$. The grid is similar to the carbon-rich ultra metal-poor (CRUMP) grid presented in Aguado et al. (2017), which has also been used in previous *Pristine* analyses (Youakim et al., 2017; Aguado et al., 2019), with two important differences: our current grid starts at $T_{\rm eff} = 4500$ K instead of 4750 K, and it extends up to [Fe/H] = +0.5 compared to −2.0 previously. The grid ranges and grid steps are the following:

[6] FERRE is available from `http://github.com/callendeprieto/ferre`

- $4500\,\mathrm{K} < T_{\mathrm{eff}} < 7000\,\mathrm{K}$, $\Delta T_{\mathrm{eff}} = 250\,\mathrm{K}$
- $1.0 < \log g < 5.0$, $\Delta \log g = 0.5$
- $-4.0 < [\mathrm{Fe/H}] < +0.5$, $\Delta[\mathrm{Fe/H}] = 0.5$
- $-1.0 < [\mathrm{C/Fe}] < +3.0$, $\Delta[\mathrm{C/Fe}] = 1.0$

where for all nodes $[\alpha/\mathrm{Fe}] = +0.4$. This value of $[\alpha/\mathrm{Fe}]$ is reasonable for bulge stars with $[\mathrm{Fe/H}] < -1.0$ or even -0.5 (Barbuy et al., 2018), but may result in biased results for more metal-rich stars. However, as the focus of this work is on metal-poor stars, this grid is the best choice for our science case. One of the advantages of the FERRE code is that it is able to fit different regions of the spectrum simultaneously even if they have different resolutions. That fact allows us to use all the information contained in both arms, fitting the blue and the CaT spectra together. We found, for instance, that including the CaT spectra reduces the scatter in the determined $\log g$ values considerably, likely because the wings of the calcium lines are sensitive to gravity. The blue and CaT spectra were corrected to rest-frame velocities using the CaT radial velocities. Several artefacts were removed from the spectra which are the result of dead pixels, and usually occur in the same place in the spectrum. The model spectra were smoothed to $R = 1300$ and $R = 11\,000$ for the blue and CaT spectra, respectively. The observed and model spectra were normalised using a running mean filter of 30 pixels.

We ran FERRE twice. First FERRE is run to get an estimate of the stellar parameters and a corresponding model spectrum for each observed spectrum. The cores of the calcium triplet lines were masked because they are strongly affected by non-local thermodynamical equilibrium (NLTE) processes[7]. The residuals between the observed and model spectrum were used to flag bad pixels. In the blue spectra, the standard deviation σ_f between model and observed spectrum was determined in chunks of 200 Å, because the SNR varies strongly throughout. Pixels were flagged as bad if they are discrepant by more than $3\sigma_f$, and added their neighbouring pixels if they are discrepant by more than $2\sigma_f$. Flagged regions are typically dead pixels that had not yet been removed, data reduction artefacts or other outliers. For the near-infrared spectra a single σ_f was computed since the SNR does not vary, and the pixels were flagged in the same way. The threshold was increased to $5\sigma_f$ around the three calcium triplet lines and the magnesium line at 8806 Å, to avoid these lines being removed entirely. The SNR is generally high enough that uncertainties in the spectral modelling start to affect the fit of the lines. Typically more pixels are flagged in the CaT spectra compared to the blue spectra because of faulty sky subtraction, which affects the infrared more. When we run FERRE for the second

[7] The line wings beyond 1.5 Å from the line centre can be safely used in LTE analyses, therefore the central 1.5 Å of each line were masked. However, because of the running mean normalisation, some of the NLTE information from the core may be spread to the neighbouring pixels. To test whether this significantly affects the analysis, we compare the results from FERRE runs with the blue arm only and with both arms together. There are no significant systematic changes in the metallicities between the two runs, although there are some systematic differences in $\log g$. It is unclear whether this is because the CaT spectra add necessary information to get better $\log g$ values, or whether this is a NLTE effect. Since there are no significant changes in the metallicities, we assume that it is sufficient to mask the cores of the lines.

time, the uncertainties on the pixels flagged as bad are increased to 10^9, in order to set their weight in the fit to practically zero. This second run resulted in significantly better fits for many stars. Example fits for seven stars are presented in Figure 5.4, in red.

Selection of reliable results

Reliable stellar parameters were selected using the following criteria:

- $\mathrm{SNR}_{4000-4100} > 10$ or $\mathrm{SNR}_{5000-5100} > 30$
- $\log \chi^2 < -2.4$
- not double-lined

which leaves 7186 stars. The SNR cut is the same as for the ULySS analysis, as is the cut on double-lined CaT spectra. The cut on the $\log \chi^2$ of the fit has been set to remove stars that are outliers by $> +3\sigma$ from the median. It removed 60 stars on top of the two other cuts.

Stellar parameter uncertainties

The same method was used as with the ULySS analysis to investigate the magnitude of the formal FERRE uncertainties, using 2785 independent pairs of observations. We find close-to-Gaussian distributions of ΔP (see Equation 5.2) with a standard deviation of 0.1 for each of the three main parameters (T_{eff}, $\log g$ and [Fe/H]) and 0.07 for [C/Fe]. This means that the formal FERRE uncertainties are severely overestimated, by a factor of ~10. No satisfactory explanation for this has been found. After re-scaling the formal uncertainties into internal uncertainties using the factors derived from the repeated-observations test, the values appear reasonable. The median internal FERRE uncertainties are 105 K, 0.34 dex, 0.09 dex and 0.12 dex for T_{eff}, $\log g$, [Fe/H] and [C/Fe], respectively. This is larger than for the ULySS analysis.

5.4 Stellar parameter results

The results of the ULySS and FERRE analyses of the PIGS low-/intermediate-resolution spectra are presented here. They are compared to each other to identify regions where the methods have issues and to derive the total uncertainties. The results are also compared to those in the SDSS APOGEE database for a sub-sample of stars.

5.4.1 Metallicity distribution and Kiel diagram

There are 7073 PIGS stars that passed the quality criteria for both the ULySS and FERRE analysis methods. The Kiel diagrams from ULySS and FERRE for these stars are shown in the top row of Figure 5.5, the metallicity distributions in the bottom

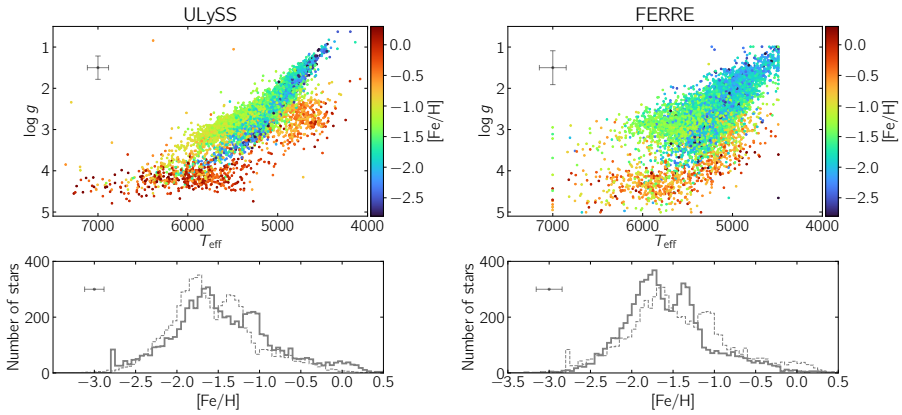

Figure 5.5 — Top row: Kiel diagram, colour-coded by [Fe/H] from ULySS (left) and FERRE (right). Each panel shows the stars that pass the quality criteria for both methods. Bottom row: metallicity distributions, where dashed histogram indicates the distribution with the other method. Median final uncertainties for metal-poor ([Fe/H] < -1.0) giants are shown in the top left corner of each panel. There are three grid effects visible in this figure: the [Fe/H] limit in the ULySS analysis is -2.8, and the FERRE grid limits are $4500 < T_{\rm eff} < 7000$ K and $1 < \log g < 5$.

row. There are several noteworthy features in the Kiel diagrams and metallicity distributions, seen in both analyses. There are a number of metal-rich dwarf stars ([Fe/H] > -0.5, $\log g > 3.5$) in our sample, which are in the sample mainly due to the *Gaia* selection (as can be seen in Figure 5.2; and more of these entered our selection box in higher extinction regions), or due to the selection testing in our two pilot fields. However, most of the stars in the sample are giants, consisting of three types. Firstly, there are the metal-poor red giant branch (RGB) stars which were the target of our survey ([Fe/H] < -1.5). These are the most numerous, and correspond to the largest peak in the metallicity distributions in Figure 5.5. Secondly, there are the hotter horizontal branch (HB) stars, with slightly higher metallicities ($-1.5 <$ [Fe/H] < -1.0). These are unintentionally part of our selection because they are relatively blue in colour and therefore also enter our selection box. They are less numerous than the RGB stars, but constitute a significant fraction of the sample and make up the second peak of the metallicity distribution. These stars are extremely useful, since they are metal-poor standard candles. Finally, there is a small number of metal-rich giants ([Fe/H] > -1.0), the result of "normal" contamination in our photometric selection. There is such a large number of metal-rich stars in the bulge that it is to be expected that some of them scatter into our selection box by accident, especially in higher extinction regions.

There are clear differences between the ULySS and FERRE analyses, which are the result of different strengths and limitations of the two methods. The features in the ULySS Kiel diagram are narrower, which we attribute to the data-driven nature of this method. Data-driven methods have two properties that contribute to creating such narrow features: the reference library contains only "physical"

stars that do indeed exist, and the differences in stellar parameters between each of the library spectra is irregular, i.e., not constant. The latter aids in the quality of the results by learning to interpolate between smaller offsets, unlike the use of synthetic grids, which have regular grid step spacing, thereby missing non-linear interpolation opportunities. Also, synthetic grids cover all possible combinations of stellar parameters (even those that should not exist), providing a larger parameter space for exploration, even non-physical regimes. And finally, most synthetic spectral grids are missing relevant physics, such as non-LTE corrections for some elements which can affect the stellar parameters (e.g., Kovalev et al., 2019).

Significant efforts are underway to create and/or extend existing empirical stellar spectral libraries to include more of the rarer stars (e.g. XSL, Gonneau et al., 2020), although they remain limited. In the PIGS sample, this limitation is particularly relevant for the HB stars and for the most metal-poor stars. In the MILES library and its interpolator (which is used in the ULySS analysis), only a limited number of HB stars are present, all with similar metallicities ([Fe/H] ≈ -1.1, Prugniel et al., 2011). It is therefore suspicious that in the ULySS analysis, we find a peak of HB stars at exactly the same metallicity. The FERRE analysis should be unbiased in this regime, and finds the HB metallicities to be ~ 0.3 dex lower. There are also only a handful of very metal-poor stars ([Fe/H] < -2.5) in MILES. The limit of the interpolator is at [Fe/H] $= -2.8$, hence the spike in the ULySS metallicity distribution there. In contrast, the FERRE synthetic grid goes to [Fe/H] $= -4.0$, therefore the results for the metal-poor tail are expected to be more trustworthy.

We highlight three final differences between the ULySS and FERRE analyses. First, the metal-rich dwarfs are more metal-rich in ULySS than in FERRE. This is due to the limitations of the FERRE grid chosen for this analysis, which only contains α-enhanced spectra. In our selected magnitude range, dwarf stars lie between us and the bulge and are likely part of the disk, and metal-rich disk stars are typically not enhanced in α-elements. Therefore our FERRE analysis does not derive the proper metallicity for these stars. Second, there are a number of relatively metal-rich stars that ULySS classifies as giants with $\log g \sim 3.0$, and FERRE as dwarfs/sub-giants ($\log g > 3.5$). Inspection of the spectra of these stars shows that they have Ca H&K in emission: these are active stars. This also explains why they ended up as contamination in our photometric selection: the emission filled in the Ca II H&K absorption lines, making them look metal-poor in the $CaHK$ photometry. Retrospectively, we found that many of these stars can be removed using a *Gaia* DR2 selection cut based on a combination of the mean flux over error for the G-band and the number of repeated observations. Finally, there are two sequences for the giants, which have different metallicities between ULySS and FERRE. In the ULySS analysis, there are a number of stars with slightly higher [Fe/H] and lower $\log g$ on the hot side of the RGB. In the FERRE analysis, these stars also have lower $\log g$ but similar [Fe/H] to the main RGB stars. These stars might be early asymptotic giant branch (AGB) stars. This hypothesis is strengthened by slightly lower carbon abundances for these stars (early AGB stars have lowered carbon abundances due to previous internal mixing processes on the RGB). This observation will be discussed in more detail in future work (Chapter 6).

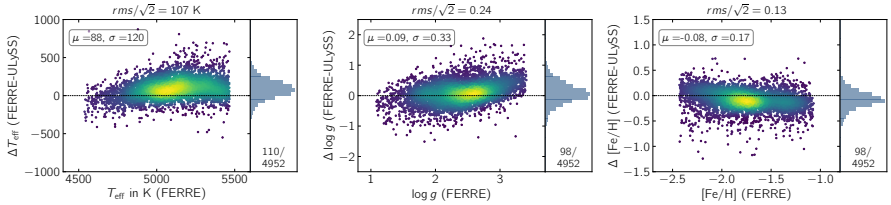

Figure 5.6 — Comparison of the parameters between ULySS and FERRE colour-coded by density, for giant stars ($\log g < 3.5$) cooler than 5500 K and with $-2.5 <$ [Fe/H] < -1.0. The zero-line is indicated. The mean difference and standard deviation are indicated in the top left corner of each main panel, after discarding 3σ outliers. The number of outliers versus the total number of stars are indicated on the bottom of the histogram panels. Finally, the title of each panel includes the corresponding $rms/\sqrt{2}$, which is quadratically added to the internal uncertainties from Section 5.3.4 and 5.3.5 to derive total uncertainties for both analyses.

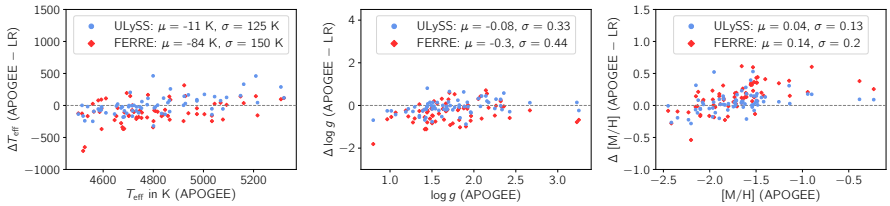

Figure 5.7 — Comparison of the parameters between APOGEE and ULySS and FERRE, for cool giants ($T_{\rm eff} < 5500$, $\log g < 3.5$). The mean difference and standard deviation, after discarding 3σ outliers, are indicated in the legend of each panel.

5.4.2 Total uncertainties

In Sections 5.3.4 and 5.3.5 we provided internal uncertainties for the ULySS and FERRE analyses. These indicate the precision of the derived stellar parameters in both methods. We can use the comparison between ULySS and FERRE to determine the *external* precision, which can be combined with the internal uncertainties to derive total uncertainties.

The difference in stellar parameters between the two methods is presented in Figure 5.6, in a region of the parameter space for which both methods are expected to behave well (based on the observations in the previous section). There are some systematic differences between the two analyses. The FERRE temperatures are on average 88 K higher than those from ULySS, where the discrepancy for the higher temperature stars is slightly larger. The mean difference for $\log g$ is 0.09 dex higher for FERRE, and it is somewhat larger for the highest $\log g$ stars. Finally, the mean difference in [Fe/H] is 0.08 dex (where FERRE is more metal-poor), varying slightly with [Fe/H]. The standard deviations around the mean are 120 K, 0.33 dex and 0.17 dex for $T_{\rm eff}$, $\log g$ and [Fe/H], respectively.

A better measure of the external precision than the standard deviation around the mean can be made using the root-mean-square (rms), which includes the biases

in the deviations from the mean. The external uncertainty can be estimated as $rms/\sqrt{2}$, which assumes that both methods contribute equally to the dispersion. These values have been indicated in the title of each panel in Figure 5.6, and are 107 K, 0.24 dex and 0.13 dex for $T_{\rm eff}$, $\log g$ and [Fe/H], respectively (after discarding 3σ outliers). Total uncertainties can now be derived by quadratically adding the internal ULySS or FERRE uncertainties and the $rms/\sqrt{2}$. This results in the following median total uncertainties for $T_{\rm eff}$, $\log g$ and [Fe/H] in the ULySS analysis: 111 K, 0.25 dex, and 0.14 dex, respectively, and in the FERRE analysis: 149 K, 0.41 dex and 0.16 dex, respectively.

The external uncertainties on [C/Fe] cannot be derived in the same way, since it is not a parameter in the ULySS analysis. Instead, they are estimated by scaling the [Fe/H] external uncertainties. In the FERRE analysis, the internal uncertainties on [C/Fe] are roughly 1.5 times larger than the [Fe/H] internal uncertainties. Assuming that the external uncertainties follow the same trend, an uncertainty floor of 1.5 × 0.13 dex = 0.20 dex is added to derive total uncertainties on [C/Fe]. The median of the total uncertainties for [C/Fe] is 0.23 dex.

5.4.3 Comparison with APOGEE

One additional comparison was made with fully external data, by comparing our derived stellar parameters with APOGEE for stars in common between the surveys. Because most bulge surveys contain mainly metal-rich stars, there generally is a lack of stars in common with this work. For instance, in APOGEE DR16 (Ahumada et al., 2019), there are only a handful of stars in common with PIGS. This is because APOGEE selects stars "randomly" with respect to metallicity, which in the bulge results in a predominantly metal-rich sample. However, we are collaborating with the bulge Cluster APOgee Survey (CAPOS, Geisler et al. in prep.) to obtain APOGEE follow-up of more PIGS stars. To date, one CAPOS field which includes PIGS targets has been fully observed (two additional fields are scheduled to be observed/finished) resulting in a total of 69 stars in common between PIGS and APOGEE DR16+CAPOS with good stellar parameters from both surveys (62 of these come from CAPOS, 7 from DR16). These stars have SNR in APOGEE between 30 and 150, and median uncertainties in $T_{\rm eff}$, $\log g$ and [M/H] are 134 K, 0.09 dex and 0.03 dex, respectively.

The AAT observations of the CAPOS field are unfortunately among the worst in the PIGS sample due to relatively bad weather conditions and the sky subtraction is sub-optimal. This affects our FERRE analysis more, because that includes the CaT spectra where the sky subtraction is more important. Additionally, the APOGEE pipeline struggles to provide good stellar parameters for very metal-poor stars (see, e.g., Figure 9 of Leung & Bovy, 2019, which shows that the median absolute error in [Fe/H] rises quickly for [Fe/H] < -1.7, even in very high signal-to-noise spectra, until it reaches about 0.4 dex at [Fe/H] $= -2.3$). The APOGEE-PIGS comparison should therefore not be over-interpreted, but it is still a useful additional indication of our external precision.

The comparison between the PIGS and APOGEE parameters is presented in Figure 5.7. The APOGEE [M/H] was used as metallicity, since for many metal-poor

stars no [Fe/H] is available or uncertain. The dispersion in the parameters between APOGEE and the ULySS analysis is comparable to that of the internal comparison (Figure 5.6), whereas the dispersions for our FERRE analysis are somewhat larger, as expected due to the lower quality CaT spectra. The biases in the ULySS-APOGEE comparison are negligible, but in the FERRE analysis they are more significant, and in the same direction as in the internal comparison (our FERRE analysis having larger $T_{\rm eff}$, larger $\log g$ and lower [Fe/H]). This could suggest that the biases in the internal comparison are mainly due to FERRE.

It is important to realise that this comparison with APOGEE is only in a limited range of the parameter space. However, it does show that the typical total uncertainties we have derived from our analysis appear to be realistic.

5.5 Discussion of PIGS survey performance

5.5.1 Metallicity distribution

Due to the nature of the PIGS selection, the sample is significantly more metal-poor than typical inner Galaxy surveys like for example ARGOS (Ness et al., 2013a) and APOGEE (Ahumada et al., 2019). The PIGS metallicity distribution relative to these two inner Galaxy surveys is presented in the top panel of Figure 5.8. The metallicity distribution from the low-resolution EMBLA survey sample is also included. It is clear that the PIGS sample is unique compared to existing bulge surveys in its large number of low-metallicity stars.

The PIGS sample contains $\sim 1300/160/10$ stars with [Fe/H] $< -2.0/-2.5/-3.0$, respectively (from the FERRE analysis). The ten most metal-poor stars are spread between $-3.5 <$ [Fe/H] < -3.0. This is the largest sample of confirmed very metal-poor (VMP, [Fe/H] < -2.0) stars towards the inner Galaxy, as shown in the bottom panel of Figure 5.8. It is also larger than the sample of VMP stars published by Aguado et al. (2019) for the main *Pristine* survey, although their sample contains many more stars with [Fe/H] < -2.5 compared to PIGS. In EMBLA there is a similar number of stars with [Fe/H] < -2.5 as in PIGS, but the total size of their sample is twice as large as PIGS. There is only one star in common between PIGS and EMBLA with [Fe/H] < -2.5 and twenty with [Fe/H] < -2.0, because in most fields we removed the EMBLA stars from our selection. The PIGS stars with [Fe/H] < -2.5 are distributed relatively homogeneously over the different fields, see the right panel of Figure 5.1.

In addition to the VMP stars, the PIGS sample contains ~ 4900 stars with $-2.0 <$ [Fe/H] < -1.0, an unprecedentedly large sample of metal-poor inner Galaxy stars to be used to study the metal-poor tail of the Galactic bulge. A first investigation of this population was presented in Arentsen et al. (2020a)/Chapter 4, using the metallicities and radial velocities to investigate the rotational signature in the inner Galaxy as a function of metallicity. That work shows that the rotational signal around the Galactic centre decreases with decreasing [Fe/H], while the velocity dispersion increases. Rotation then becomes negligible for the most metal-poor stars, providing a strong constraint for any models attempting to explain the formation and evolution of the inner Galaxy.

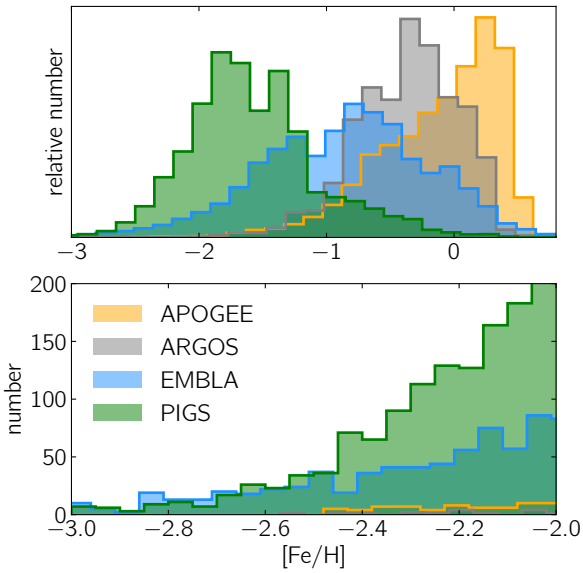

Figure 5.8 — Top panel: Relative metallicity distributions of the PIGS, EMBLA, ARGOS and APOGEE inner Galaxy surveys. For PIGS, the FERRE [Fe/H] for the AAT sample is shown, with the footprint as in Figure 5.1. The EMBLA metallicities are those for their AAT sample (provided by L. Howes, priv. comm.), with a footprint $|l| \lesssim 12^\circ$ and $3^\circ \lesssim |b| \lesssim 12^\circ$. The ARGOS sample consists of all fields with field centres $|l|, |b| \leq 10^\circ$ (metallicities provided by M. Ness, priv. comm.). The APOGEE sample shows the [M/H] of all DR16 stars in the region $|l|, |b| < 12^\circ$ (Ahumada et al., 2019). Bottom panel: absolute number of VMP stars in the same samples.

More detailed investigations of this metal-poor sample, including analysis of the orbits of these stars using (future) *Gaia* data, are planned for future work. Stars of special interest for dynamical studies are the ~ 1700 HB stars, for which, being standard candles, accurate distances may be inferred.

5.5.2 Survey success rates

Using our spectroscopic follow-up sample and spectroscopic observations from the literature, we investigate how well we can produce photometric metallicities in PIGS. For individual stars, photometric metallicities are likely not good, for the reasons described in Section 5.2. Instead, the average metallicity and the metallicity dispersion were determined in sub-regions of the Pristine colour-colour diagram and we investigate how clean a selection can be made for intermediate metal-poor (IMP, [Fe/H] < −1.5) and VMP ([Fe/H] < -2.0) stars.

In this test, the FERRE spectroscopic metallicities were used instead of those from ULySS, because they are typically better for the VMP stars. We have seen that FERRE is biased for [Fe/H] > −0.5/ − 1.0 because the synthetic grid used only includes alpha-enhanced spectra (see Section 5.3.5). However, for the purpose of the tests in this section we included data from three additional spectroscopic

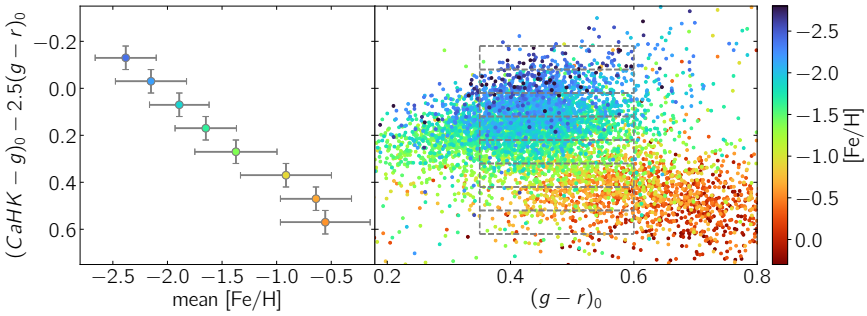

Figure 5.9 — Mean metallicity in bins of the y-axis of the Pristine colour-colour diagram (left) and the corresponding diagram with the indicated bins (right). Error bars in the left panel are the 1σ dispersion in each bin for [Fe/H], and for the y-axis they indicate the size of the bin. Included are stars from PIGS (using their FERRE [Fe/H]), and stars from EMBLA, APOGEE DR16 (using [M/H]) and ARGOS. Only stars with E(B−V) < 0.6 are included.

surveys that have many more stars with higher metallicities, making the small contribution of metal-rich PIGS stars irrelevant. The three surveys which were added are EMBLA (low-resolution sample, L. Howes priv. comm.), ARGOS (M. Ness priv. comm.) and APOGEE DR16 (Ahumada et al., 2019).

In the right panel of Figure 5.9 the Pristine colour-colour diagram is shown including all spectroscopic data samples described above. For stars with $0.35 < (g - r)_0 < 0.6$, where the discrimination between different metallicities appears to work best and where most of the stars of interest are located, it is sliced along the y-axis in bins of 0.1 mag. The left-hand panel shows the mean [Fe/H] and the dispersion in [Fe/H] in each bin. Only stars with E(B−V) < 0.6 are used (corresponding to roughly Galactic $b < -4.5°$) to avoid strong outliers in very high extinction regions. Additionally, a selection cut using the number of repeated observations and mean flux over error for the G-band photometry in *Gaia* DR2 was included, to remove stars with variable photometry from the PIGS sample.

Figure 5.9 shows that there is an almost linear relation between the y-axis colour and the metallicity in this regime, which confirms that our box selection for follow-up is a good way of selecting the most metal-poor stars. The [Fe/H] dispersion in the bins ranges from 0.30 − 0.45 dex, and the typical [Fe/H] difference between bins is ∼ 0.2 dex or more. The largest dispersion is in the intermediate metallicity range, possibly because it contains the largest mixture of stars of different surveys (and each has been analysed differently), or because the metallicity-sensitivity in this regime of the diagram is more non-linear.

We use the relative number of IMP and VMP stars in our best selection bins to estimate the PIGS selection efficiency for metal-poor stars in the inner Galaxy. In the most metal-poor bin, 86% and 80% of the stars have [Fe/H] < −2.0, for regions with E(B−V) < 0.4 and > 0.4, respectively. If, instead, the two most metal-poor bins are combined the number of stars is increased five-fold (to 500). In these bins, 80% of the stars have [Fe/H] < −2.0 and 98% have [Fe/H] < −1.5, for regions with E(B−V) < 0.4. This goes down to 63% and 93%, respectively, in E(B−V) > 0.4 regions.

These efficiencies do not change significantly when using $(g-i)$ as the effective temperature indicator instead of $(g-r)$. One might expect the former to work better because the g and i filters cover a longer wavelength baseline, and should thus yield better temperature estimates. However, because they are further apart, the extinction correction of the difference between the two filters is likely less good. These two effects appear to roughly cancel each other in PIGS.

We compare our efficiency to the results from Casey & Schlaufman (2015), using 2MASS and WISE photometry to identify VMP stars in the bulge region, who report a success rate of 20% of their candidates having $-3.0 <$ [Fe/H] < -2.0. The EMBLA survey has not published success rates, but the metallicity distribution of their low-resolution follow-up sample peaks around [Fe/H] $= -1.0$ (Howes et al. 2016, see also Figure 5.8), whereas PIGS peaks at lower metallicities. Additionally, as discussed in Section 5.5.1, their sample has a similar number of stars with [Fe/H] < -2.5, but twice as many stars in total. We therefore conclude that our selection is more efficient. Taken together, this shows that the efficiency of PIGS for selecting metal-poor stars in the bulge region is unprecedented.

5.6 Summary and outlook

In this paper, we have presented the Pristine Inner Galaxy Survey. The ~ 250 deg^2 of photometric $CaHK$ observations in the bulge region, the data reduction and calibration, and the low-/intermediate resolution spectroscopic follow-up of ~ 8000 metal-poor candidate stars were described in detail. Robust stellar parameters and metallicities were determined for the spectroscopic data using two completely independent analysis methods: 1) ULySS, a full-spectrum fitting package using an empirical library, and 2) FERRE, a full-spectrum fitting method employing a synthetic stellar model library. Our analysis with ULySS is restricted to the blue arm only, whereas FERRE can fit both blue and red arms of our observations simultaneously. The application of two methods allowed us to make an in-depth comparison between the merits and weaknesses of both methods in the context of analysing metal-poor stars, some of which are inherent to the empirical/synthetic nature of their model spectra. The use of these two complementary methods further enables the estimation of an external uncertainty on top of the internal uncertainties of each of the methods separately. An additional, completely independent, comparison has been carried out with overlapping stars observed with APOGEE.

As a result of its effective selection of metal-poor targets, PIGS data at the moment includes 1300 stars with spectroscopic [Fe/H] < -2.0, the largest sample of confirmed very metal-poor stars in the inner Galaxy to date. Combining spectroscopy and photometry, we tested the performance of our photometric selection of metal-poor stars. An efficient selection of [Fe/H] < -2.0 stars can be made; PIGS has a 86%/80% (intermediate/high extinction) success rate using the most conservative selection (producing only a small sample), and a success rate of 80%/63% for a sample five times larger. PIGS is therefore the perfect source of metal-poor candidate targets for future spectroscopic surveys in the inner Galaxy, such as

for instance the multi-object spectroscopic 4MOST Milky Way Disc and Bulge Low-Resolution Survey (4MIDABLE-LR, Chiappini et al., 2019).

Additionally, our sample includes a large sample of metal-poor horizontal branch stars. These stars are interesting in their own right, especially because of their standard candle nature.

Some follow-up work using the sample and analysis presented here is already underway. The third PIGS paper will present carbon abundance results from the FERRE analysis, including an investigation of the sensitivity of the Pristine filter to the carbon abundance, results on the carbon-enhanced metal-poor stars in the inner Galaxy, and an investigation of the evolution of the carbon abundance in metal-poor giant stars. A further paper in the PIGS series will focus in more detail on the dynamical properties of the metal-poor stars in the inner Galaxy using (future) *Gaia* data. We plan to derive distances and orbital properties for the spectroscopic metal-poor sample ([Fe/H] < -1.0). Additionally, as proper motions in the inner Galaxy become more reliable with future Gaia data releases, it may be possible to include the much larger photometric samples of metal-poor stars in kinematic analyses. Finally, we note that there is an ongoing high-resolution spectroscopic follow-up of PIGS stars that will be described elsewhere.

In the coming years, large samples of metal-poor inner Galaxy stars, such as provided through PIGS and other (future) surveys (for example *Gaia* DR3+ and 4MOST, de Jong et al. 2019) will provide a unique view of the central regions of the Milky Way. The chemistry and kinematics of these stars will lead to insights into the early history of the Milky Way, and large samples of them will allow for the discovery of rare stars whose abundance patterns teach us about previous, early generations of stars, all the way back to the First Stars.

Acknowledgements.

We thank Friedrich Anders for discussions on the extinction in *Gaia*, and for sharing his *Gaia* extinction coefficients. We thank Ting S. Li for valuable discussions and efforts regarding the fibre throughput issues of 2dF. We thank Louise Howes and Melissa Ness for sharing their spectroscopic catalogues with us, this was very helpful in the early development of PIGS and for this paper.

We thank the Australian Astronomical Observatory, which have made these observations possible. We acknowledge the traditional owners of the land on which the AAT stands, the Gamilaraay people, and pay our respects to elders past and present. Based on data obtained at Siding Spring Observatory (via programs S/2017B/01, A/2018A/01, OPTICON 2018B/029 and OPTICON 2019A/045, PI: A. Arentsen).

Based on observations obtained with MegaPrime/MegaCam, a joint project of CFHT and CEA/DAPNIA, at the Canada-France-Hawaii Telescope (CFHT) which is operated by the National Research Council (NRC) of Canada, the Institut National des Science de l'Univers of the Centre National de la Recherche Scientifique (CNRS) of France, and the University of Hawaii.

Based on observations obtained through the Chilean National Telescope Allocation Committee through programs CN2017B-37, CN2018A-20, CN2018B-46, CN2019A-98 and CN2019B-31.

AA, ES and KY gratefully acknowledge funding by the Emmy Noether program from the Deutsche Forschungsgemeinschaft (DFG). NFM gratefully acknowledges support from the French National Research Agency (ANR) funded project "Pristine" (ANR-18-CE31-0017) along

with funding from CNRS/INSU through the Programme National Galaxies et Cosmologie and through the CNRS grant PICS07708. DA thanks the Leverhulme Trust for financial support. KAV thank the Natural Sciences and Engineering Research Council for funding through the Discovery Grants program and the CREATE training program on New Technologies for Canadian Observatories. DBZ acknowledges the support of the Australian Research Council through Discovery Project grant DP180101791. CAP and JIGH acknowledge financial support from the Spanish Ministry of Science and Innovation (MICIIN) under the project MICIIN AYA2017-86389-P. JIGH also acknowledges the Spanish MICIIN under 2013 Ramón y Cajal program MICIIN RYC-2013-14875. D.G. gratefully acknowledges support from the Chilean Centro de Excelencia en Astrofísicay Tecnologías Afines (CATA) BASAL grant AFB-170002. D.G. also acknowledges financial support from the Dirección de Investigación y Desarrollo de la Universidad de La Serena through the Programa de Incentivo a la Investigación de Académicos (PIA-DIDULS). Horizon 2020: This project has received funding from the European Union's Horizon 2020 research and innovation programme under grant agreement No 730890. This material reflects only the authors views and the Commission is not liable for any use that may be made of the information contained therein.

The authors thank the International Space Science Institute, Bern, Switzerland for providing financial support and meeting facilities to the international team "Pristine".

This work has made use of data from the European Space Agency (ESA) mission *Gaia* (`https://www.cosmos.esa.int/gaia`), processed by the *Gaia* Data Processing and Analysis Consortium (DPAC, `https://www.cosmos.esa.int/web/gaia/dpac/consortium`). Funding for the DPAC has been provided by national institutions, in particular the institutions participating in the *Gaia* Multilateral Agreement.

The Pan-STARRS1 Surveys (PS1) and the PS1 public science archive have been made possible through contributions by the Institute for Astronomy, the University of Hawaii, the Pan-STARRS Project Office, the Max-Planck Society and its participating institutes, the Max Planck Institute for Astronomy, Heidelberg and the Max Planck Institute for Extraterrestrial Physics, Garching, The Johns Hopkins University, Durham University, the University of Edinburgh, the Queen's University Belfast, the Harvard-Smithsonian Center for Astrophysics, the Las Cumbres Observatory Global Telescope Network Incorporated, the National Central University of Taiwan, the Space Telescope Science Institute, the National Aeronautics and Space Administration under Grant No. NNX08AR22G issued through the Planetary Science Division of the NASA Science Mission Directorate, the National Science Foundation Grant No. AST-1238877, the University of Maryland, Eotvos Lorand University (ELTE), the Los Alamos National Laboratory, and the Gordon and Betty Moore Foundation.

This publication makes use of data products from the Two Micron All Sky Survey, which is a joint project of the University of Massachusetts and the Infrared Processing and Analysis Center/California Institute of Technology, funded by the National Aeronautics and Space Administration and the National Science Foundation.

This research has made use of "Aladin sky atlas" developed at CDS, Strasbourg Observatory, France (Bonnarel et al., 2000). It also made extensive use of the MATPLOTLIB (Hunter, 2007), PANDAS (McKinney, 2010b), ASTROPY (Astropy Collaboration et al., 2013; Price-Whelan et al., 2018) and DUSTMAPS (Green, 2018) Python packages, and of TOPCAT (Taylor, 2005).

6 The Pristine Inner Galaxy Survey (PIGS) III: carbon-enhanced metal-poor stars in the central regions of the Milky Way

A. Arentsen, E. Starkenburg, D. S. Aguado, K. Youakim, M. Fouesneau, et al.

— Paper in preparation —

ABSTRACT

The lowest metallicity stars provide important clues about the First Stars and early Galactic evolution. Many of the most metal-poor stars are over-abundant in carbon, and the fraction of carbon-enhanced metal-poor (CEMP) stars has been shown to increase with decreasing metallicity for stars in the Galactic halo. In this work, we use data from the *Pristine* Inner Galaxy Survey (PIGS) to investigate the CEMP stars in the inner regions of the Milky Way. We identify 66 new CEMP stars in the inner Galaxy, of which 31 are very metal-poor (VMP, [Fe/H] < -2.0); this is a thirty-fold increase compared to the two known CEMP stars in the literature. We then use the large sample of VMP stars in PIGS to study the occurrence of CEMP stars in the inner Galaxy. We find that the CEMP fractions appear lower than in the halo, but they could be compatible for CEMP-no stars. The very carbon-rich CEMP-s stars seem to be largely missing from PIGS – this could be an indication of different binarity properties of the stellar populations in the inner Galaxy and the halo, but more likely it is a selection effect in PIGS. Future exploitation of this data set will provide important constraints on the properties and the assembly of the old, metal-poor inner Galaxy.

6.1 Introduction

Carbon is a key element to study in the most metal-poor stars. A large majority of the most iron-poor stars show very large carbon over-abundances, painting a picture in which chemical evolution in the early Universe proceeded in a different manner compared to more recent times. In the Galactic halo, these carbon-enhanced metal-poor stars (CEMP, with [C/Fe] over +0.7, or even over +1.0 depending on the definition used, Beers & Christlieb, 2005; Aoki et al., 2007) are found to comprise 15–20% of stars with [Fe/H] < -2 and even up to 70% of stars with [Fe/H] < -4 (e.g., Yong et al., 2013b; Placco et al., 2014).

The existence of CEMP stars is generally understood to be related to binary mass-transfer for most CEMP stars in the $-3.0 <$ [Fe/H] < -2.0 range (e.g. Abate et al., 2015; Hansen et al., 2016a), and to unique nucleosynthesis in the First Stars and their supernovae for most CEMP stars with lower metallicities (e.g. Umeda & Nomoto, 2003; Meynet et al., 2006). These two populations can be separated by their chemical abundance patterns. Many of the CEMP stars with $-3.0 <$ [C/Fe] < -2.0 show enhancements in s-process elements and a very high absolute carbon abundance, in agreement with the hypothesis that they are chemically enriched by mass transfer from a companion star that has gone through the asymptotic giant branch (AGB) phase. Because of their high s-process signature, these stars are referred to as CEMP-s stars (Beers & Christlieb, 2005). Indeed, a very high fraction of these stars have radial velocity variations consistent with them being in binary systems (e.g., Lucatello et al., 2005; Hansen et al., 2016b). On the other hand, many of the most iron-poor stars show carbon enhancement without the accompanying s-process signature (e.g., for an overview see Norris et al., 2013b) and they lie on a different, lower, plateau in absolute carbon (Spite et al., 2013; Yoon et al., 2016). These are the CEMP-no stars which were likely born with their large carbon abundance and, in contrast to the CEMP-s stars, there are no similar populations known at higher metallicity (for the CEMP-s stars these are Barium and CH stars, Starkenburg et al., 2014), hinting at a different origin likely connected to First Stars physics.

There are some interesting exceptions to this picture. For instance, careful radial velocity monitoring programs (see e.g., Starkenburg et al. 2014; Hansen et al. 2016b; Arentsen et al. 2019a/Chapter 2) have shown that some of the CEMP-no stars do show evidence for binarity. Possible mass-transfer from a companion could have affected the current abundance pattern of the binary CEMP-no star, although it depends on the (unknown) current evolutionary state of the companion. Perhaps the most intriguing example here is HE 0107−5240, one of the most iron-poor stars known, which is in a very long period binary system with an unseen companion (Arentsen et al. 2019a/Chapter 2; Bonifacio et al. 2020). Additionally, some of the CEMP-s stars do appear to be single. They could be face-on binary systems which would not be detectable in a radial velocity monitoring program, but their number is larger than would be expected purely based on inclination arguments (Hansen et al., 2016a). Finally, what could also change the current picture is that typically one-dimensional models in local thermodynamic equilibrium (LTE) are used for the determination of chemical abundances from spectra, which appear

to be insufficient for proper determinations of [Fe/H] and [C/Fe] in such low metallicity stars (e.g. Norris & Yong, 2019; Amarsi et al., 2019).

The CEMP-no stars likely formed from gas clouds enriched by the First Stars. Two possible hypotheses for why the First Stars would produce so much carbon are that they might have higher spin rates and/or that they might explode as mixing and fallback (faint) supernovae rather than ordinary supernovae (Chiappini et al., 2006; Umeda & Nomoto, 2003). The exact abundance pattern these First Stars pass on to subsequent generations depends on their spin rate and mass, as well as the type of the supernova explosion. Studying more extremely metal-poor stars in detail will therefore allow us to put strong constraints on the processes of star formation and feedback in the very early Universe. For example, the SkyMapper Southern Sky Survey star SMSS J031300.36−670839.3 could be linked to a faint supernova of a zero metallicity star of ~ 60 solar masses (Keller et al., 2014; Bessell et al., 2015; Nordlander et al., 2017). This star, currently the record holder for the most iron-poor star at [Fe/H] < -7.1, shows an extremely high carbon abundance and a very peculiar abundance pattern in other elements as well.

Interestingly, the fraction of CEMP stars and the relative number of CEMP-s versus CEMP-no stars appear to vary throughout the Milky Way. Relatively small samples of several hundreds of very metal-poor stars studied in detail have indicated trends of increasing CEMP fraction with increasing height from the Galactic plane (Frebel et al., 2006), and a larger relative number of CEMP-no stars further away into the halo (Carollo et al., 2014). Similar results are seen in recent work using tens of thousands of stars with low resolution spectroscopy from the Sloan Digital Sky Survey (SDSS) and the AAOmega Evolution of Galactic Structure (AEGIS) survey, who produced "carbonicity" maps and found the average [C/Fe] to increase with increasing Galactic distance (Lee et al., 2017; Yoon et al., 2018). They also found that the relative number of CEMP-s stars is larger close-by, and that the CEMP-no stars appear to dominate more at further distances. These observations are most likely related to the inner part of the halo on average being more more metal-rich than the outer halo. Recent work using *Gaia* DR2 data (Gaia Collaboration et al., 2018) suggests that most of the inner halo may have originated from one large accretion event (Helmi et al., 2018; Belokurov et al., 2018). Since larger galaxies typically have higher metallicities, this is consistent with an observed metallicity gradient if the outer halo was built up by smaller accretion events. The spatial carbon trends give us valuable insight into the early chemical and dynamical evolution of the Milky Way and its building blocks.

The most striking result in this respect was found in the inner Galaxy by the Extremely Metal-poor BuLge stars with AAOmega (EMBLA) survey (Howes et al., 2014, 2015, 2016). They used photometry from a Strömgren v-filter – which includes the very metallicity sensitive Ca II H&K doublet (see Bessell et al., 2011) – from the 1.35m SkyMapper facility (Wolf et al., 2018) to select the most metal-poor stars in the bulge region, and followed these candidates up with medium and high-resolution spectrographs. Howes et al. (2015, 2016) derived the carbon abundances for 33 metal-poor stars (almost all [Fe/H] < -2.0) in the bulge region, and found only one of them to have a predicted natal [C/Fe] (corrected for stellar evolution effects)

above [C/Fe] = +0.7. This is in striking contrast with the much higher fraction of CEMP stars in the Galactic halo.

Given its important implications for early chemical evolution in our Galaxy, it is of importance that this result is verified with larger sample sizes and independent methods. One concern is that the result could be an effect of small number statistics. Another concern is that the SkyMapper v filter includes a wavelength region that contains a CN band in very carbon-enhanced stars, which could result in a selection bias against carbon-rich stars when selecting low-metallicity candidates based on them having little absorption in the v filter (Da Costa et al., 2019).

In this work, we present a complementary view of carbon abundances in the inner Galaxy from the *Pristine* Inner Galaxy Survey (Arentsen et al. (2020b)/Chapter 5, hereafter A20b/Ch5). PIGS contains a sample of ~1300 very metal-poor stars (VMP stars, [Fe/H] < -2.0) observed with the AAOmega spectrograph on the Anglo-Australian Telescope (AAT), with [Fe/H] and [C/Fe] determined from their low/intermediate resolution spectra. The candidate selection for metal-poor stars was done with the help of photometry using the *CaHK* narrow-band filter centred on the Ca II H&K lines on MegaCam at the Canada-France-Hawaii-Telescope (CFHT). As such, the PIGS selection process resembles very much the successful EMBLA approach. One difference is that the *CaHK* narrow-band filter used is much narrower than the SkyMapper v filter and is more centred around the Ca H&K features only (see Figure 6.1). It is therefore expected to be less affected by the CN and CH bands, although it is not completely unaffected for stars with very high carbon abundances because carbon affects the entire continuum changes in this wavelength range.

In this chapter, we discuss the carbon abundance results in PIGS. In Section 6.2, we introduce PIGS in more detail, and in Section 6.3 we consider the possible biases of our survey against carbon-enhanced stars in the candidate selection process. We subsequently focus on three different key results from our analysis: The evolutionary effects on the giant branch observed in PIGS in Section 6.4, a sample of newly discovered CEMP stars in the inner Galaxy and the resulting CEMP fraction with a comparison to the literature in Section 6.5. We discuss the results and end with our conclusions in Section 6.6.

6.2 The *Pristine* Inner Galaxy Survey (PIGS)

6.2.1 Survey overview

For details on the PIGS survey we refer the reader to A20b/Ch5. Here, we only briefly summarise the main goals and methods. PIGS was created as an extension of the *Pristine* survey (see for an overview Starkenburg et al., 2017b). The main goal of the *Pristine* survey is to find and study the underrepresented lowest metallicity population of stars using a tailor-made narrow-band filter centred on the strong Ca H&K stellar absorption lines, the filter is shown in Figure 6.1 on top of synthetic spectra of varying carbon abundance. The survey has an extensive spectroscopic follow-up campaign of its most promising candidates (Youakim et al., 2017; Caffau et al., 2017; Starkenburg et al., 2018; Aguado et al., 2019; Bonifacio et al., 2019;

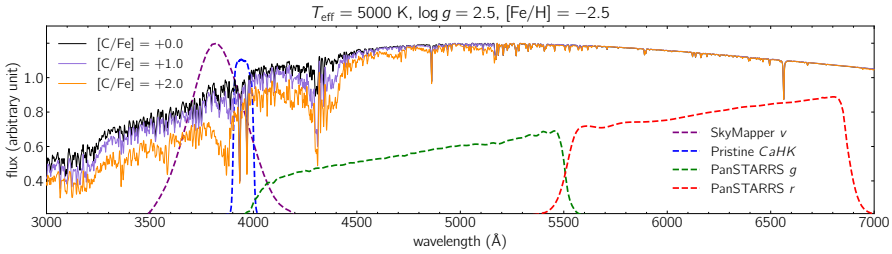

Figure 6.1 — Synthetic spectra (see text for details) for three stars with the same stellar parameters, listed on the top of the figure, but different C (and N and O) abundances. Four different filter curves from SkyMapper, *Pristine* and PanSTARRS are overplotted.

Venn et al., 2020; Caffau et al., 2020), and it has a dedicated dwarf galaxy program (Longeard et al., 2018, 2020). Instead of focusing on the Galactic halo and the satellites that reside in it, PIGS is looking towards the inner regions of the Galaxy – a far more challenging environment for various reasons. Firstly, the number of metal-poor stars are vastly overwhelmed by higher metallicity populations, much more so than in a halo environment as the bulge metallicity distribution peaks only slightly below solar (around $\sim -0.2/-0.5$ depending on the latitude, e.g. Ness et al., 2013a), whereas in the halo the mean metallicity lies around [Fe/H] $= -1.6$ (e.g., Youakim et al., 2020). Secondly, the amount of dust and therefore of extinction is far greater towards the inner Galaxy than towards the Galactic halo. The *Pristine* survey narrow-band filter covers a very blue wavelength range from $3900-4000$ Å and is therefore severely affected by the extinction. For this reason the footprint of PIGS is chosen such that it avoids the most extincted regions; it surveys all regions with E(B-V) < 0.7 for the part of the sky bound by declination $> -30°$ (because we use a Northern facility) and l and b roughly between $-12°$ and $+12°$ (for the detailed footprint, see Figure 1 in A20b/Ch5).

Much of the PIGS footprint has been followed-up spectroscopic observations using AAOmega at the AAT (see the right panel of Figure 1 in A20b/Ch5 for the coverage). As discussed in A20b/Ch5, the exact details of the target selection have varied throughout the progression of the survey with lessons learned and new *Gaia* data releases being available. In all instances, however, the targets are selected from a colour-colour space including broad-band colours either from PanSTARRS1 (PS1, Chambers et al., 2016) or from *Gaia* DR2 (Gaia Collaboration et al., 2018). The broad-band photometry is necessary as a proxy for the temperature of the star, and a combination of broad-band colours and *Pristine* $CaHK$ photometry is used as an indication of the metallicity. Because of unavoidable difficulties with differential reddening and the zero-point of the $CaHK$ photometry in this challenging Galactic region, we refrain from calculating photometric metallicities for each star. Instead, we select the most metal-poor populations in each field relatively and fill the fibres of the AAOmega spectrograph in order of increasing metallicity, starting from the best (most metal-poor) candidates. A20b/Ch5 has already shown that this selection has an unprecedentedly high efficiency in selecting

the most metal-poor populations: 90% of the best candidates are confirmed to satisfy [Fe/H] < -2.0 from the spectroscopy, as do 60-75% of the next best selection box (depending on the magnitude of extinction in the field). As we select stars with a limited magnitude range of $13.5 < G < 16.5$ for *Gaia*, or $14.0 < g < 17.0$ for PS1, and we deselect foreground dwarf stars using *Gaia* parallax information, we expect that these populations are roughly at the distance of the bulge. A more extensive kinematical analysis with (future) *Gaia* data is planned to investigate the detailed orbits of the PIGS stars.

Altogether, the sample contains ~ 8000 stars with low/medium-resolution spectra covering $3700-5500$ Å and $8400-8800$ Å. Careful analysis of these low/medium-resolution spectra with two independent and complementary spectroscopic analysis pipelines (ULySS and FERRE, Koleva et al., 2009; Allende Prieto et al., 2006, see A20b/Ch5 for details) reveals that our sample contains 1300 red giant branch stars with [Fe/H] < -2.0. It is this set of inner Galaxy VMP stars, the largest available in the literature, that we base this paper on. Paper I of this paper series (Arentsen et al. 2020a/Chapter 4) has investigated the kinematical signature of the metal-poor PIGS stars and compared it with the stars at higher metallicities. It shows for the first time how the rotational signature, observed in metal-rich stars, decreases with metallicity for metal-poor stars and completely disappears in this VMP sample. In this work, we focus instead on the carbon content of the PIGS stars, as measured from the AAOmega data with the FERRE pipeline.

6.2.2 Stellar parameters and [C/Fe] using FERRE

We employ the full-spectrum fitting code FERRE (Allende Prieto et al., 2006)[1] for the derivation of the effective temperature $T_{\rm eff}$, surface gravity $\log g$, metallicity [Fe/H] and the carbon abundance [C/Fe] from the PIGS AAOmega spectra. For details of the analysis, we refer the reader to A20b/Ch5, the method is summarised here. We fit the spectra against a synthetic stellar model library, interpolating between the nodes with a cubic algorithm. The blue and red arm of the spectra are fit together to simultaneously derive $T_{\rm eff}$, $\log g$, [Fe/H] and [C/Fe], using four different runs for each fit to avoid getting trapped in a local minimum. The reference grid used in this work consists of synthetic stellar spectra from Kurucz model atmospheres (see Mészáros et al., 2012), computed with the ASSET code (Koesterke et al., 2008). The grid is an extension of the grid described in Aguado et al. (2017), pushing to cooler effective temperatures ($T_{\rm eff} = 4500$ K) and higher metallicities ([Fe/H] = +0.5). Steps in $\log g$, [Fe/H], $T_{\rm eff}$, and [C/Fe] are 0.5 dex, 0.5 dex, 250 K, and 1.0 dex respectively. All stars are assumed to have $[\alpha/{\rm Fe}] = +0.4$, which is typically appropriate for the metal-poor populations we focus on in this work.

A first crude run of FERRE is used to get an estimate for the stellar parameters and to flag bad regions in the spectra (due to bad pixels, sky residuals, etc.). A second run is subsequently performed masking these bad regions out and presents the final results. We keep all stars that satisfy ${\rm SNR}_{4000-4100} > 10$ or ${\rm SNR}_{5000-5100} > 30$, that have $\log \chi^2$ of the fit < -2.4, and that do not show any strong evidence for double-lined features in their spectra. All stars have also been analysed with the completely

[1] FERRE is available from `http://github.com/callendeprieto/ferre`

independent, data-driven method ULySS (see A20b/Ch5), which we use to derive final uncertainties on the stellar parameters. However, this method does not give [C/Fe] and, as such, we do not have a straightforward measurement of the external uncertainty to derive final uncertainties for [C/Fe]. Nevertheless, we can quantify (especially at higher SNR), that the *internal* uncertainties on [C/Fe] are roughly 2 times larger than the internal uncertainties derived for [Fe/H]. Assuming that the external uncertainties on [C/Fe] will follow the same trend, we add an uncertainty floor of 2×0.11 dex = 0.22 dex to all FERRE [C/Fe] uncertainties. The median of the final [C/Fe] uncertainties for the sample passing our quality criteria is 0.27 dex, and 148 K, 0.41 dex and 0.14 dex for $T_{\rm eff}$, $\log g$ and [Fe/H], respectively.

6.3 The *Pristine* filter and its effect on CEMP selection

The *Pristine* narrow-band *CaHK* filter ranges in wavelength from $\sim 3900 - 4000$ Å and is nicely top-hat in shape. Its filter curve is shown in Figure 6.1, together with three synthetic spectra of a typical red giant branch star from the PIGS survey with different enhancements of carbon. These spectra are created using publicly available stellar atmosphere models from MARCS (Gustafsson et al., 2008; Plez, 2008), combined with the Turbospectrum spectral synthesis code (Alvarez & Plez, 1998). The strength of carbon bands also depends on nitrogen and oxygen; these are changed together with carbon following [C/O] = +0.5 and [C/N] = −0.5 (typical values in (E)MP stars in 1D/LTE analyses, from Norris et al., 2013b; Amarsi et al., 2019). This figure illustrates that it appears that it is not possible to construct a filter blueward of 5000 Å that is not affected by carbon features for stars that are very enhanced in C (and N and O). The region of the *Pristine* filter is probably the least affected region in this part of the spectrum. However, even here the placement of the continuum starts to be affected and there is consequently less flux measured in a very carbon-enhanced star than there would be from a star with a scaled down solar pattern. We thus expect that the *Pristine* filter is less sensitive compared to filters that cover more of the large CH band at ~ 4300 Å or the CN band centred just below ~ 3800 Å, such as the SkyMapper v filter, but that it will still be biased against finding highly carbon-enhanced stars.

Figure 6.2 projects the synthetic models onto the colour-colour spaces used in the selection of PIGS targets for one example AAT field, for both the *Gaia* and PS1 selections. Candidates for follow-up are selected starting at the top of the diagram where the most metal-poor stars are expected to lie, and then going down until all ~ 360 AAOmega fibres are filled. The vertical dashed lines indicate the $(g-r)_0$ limits of our selection box and the horizontal line indicates where the top 400 candidates end in both of the selections. Figure 6.2 is useful for giving us a qualitative understanding of the effect of CNO enhancements on the PIGS selection, but we refrain from interpreting this figure too literally for multiple reasons.

Firstly, there are uncertainties due to the modelling. The results of the synthetic spectra are to be taken with a grain of salt, because they are not calculated self-consistently. There are no MARCS stellar atmosphere models publicly available with these stellar parameters and CNO enhancements, hence we have taken non-

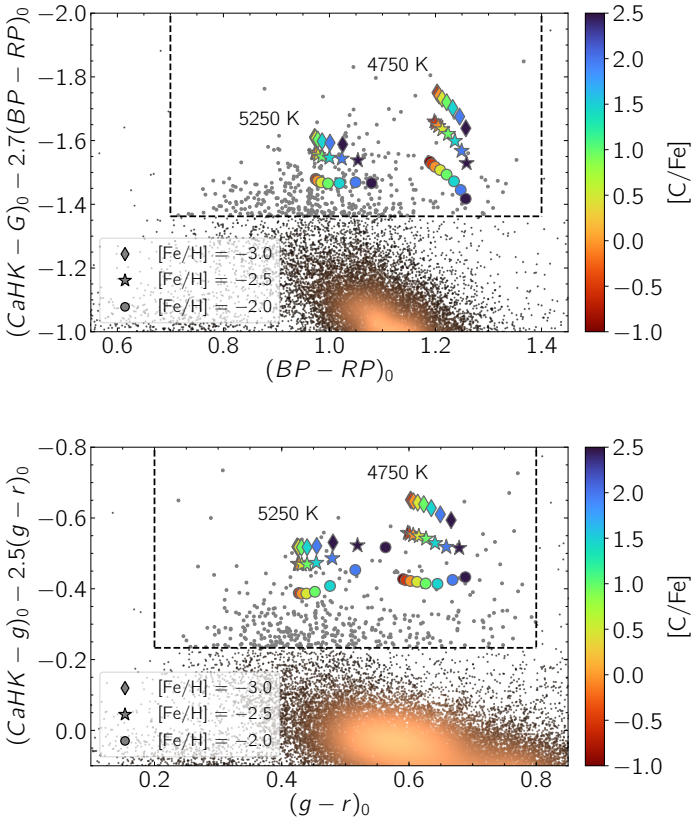

Figure 6.2 — Synthetic photometry from model spectra (coloured points) in the PIGS colour-colour space for the *Gaia* (top) and PS1 (bottom) broad-band photometric selection. Two different combinations of temperatures and log g are used ($T_{\rm eff}$ = 5250 K, log g = 2.5 as well as $T_{\rm eff}$ = 4750 K, log g = 2.0) and shown here are the results for different [Fe/H] (various symbols) and [C/Fe] (different colours). The [C/O] is fixed to +0.5 and the [C/N] to −0.5. Also shown is the photometric PIGS/broad-band data in a two-degree field centred at (RA, DEC) = (278.0, -28.0), together with the selection box for the best 400 candidate metal-poor stars in this field (dashed black line).

enhanced stellar atmosphere models and added the enhancement only in the step creating the stellar spectra. However, at these high enhancements, it is expected that the addition of so many more metals would also alter the internal structure of the star to a significant degree. In our calculations, we also do not take into account any effects from 3D or non-LTE. Additionally, the strength of the molecular CH and CN bands depends critically on the abundances for C, N, and O and the ratios of these abundances have a large scatter in the observations (e.g. Norris et al., 2013b), therefore, these models (where the [C/N] and [C/O] ratios are fixed) do not represent all carbon-enhanced stars. There is a stronger effect on the selection if N is increased or O is decreased. Finally, the accuracy of the synthetic results in Figure 6.2 hinges on the correctness of the photometric filter curves which were used to create the synthetic photometry and whether they take into account all atmospheric and instrumental effects.

Secondly, there are complications due to the data and our selection. As described in A20b/Ch5, the PIGS *CaHK* photometry is not calibrated in an "absolute" sense and the y-axis scale can therefore be slightly different compared to the models, which makes it difficult to place the models on top of the data. Additionally, the relative location of the models is also affected by the quality of the *Gaia* extinction correction, which was challenging (see Chapter 5 for details). To create this figure, we determined shifts for the synthetic photometry by matching the location of the [C/Fe] = 0.0 synthetic model points with the average location of spectroscopically observed stars with the same metallicity/temperature in this field. Furthermore, our selection box is a *relative* selection box and changes with the location of our fields, because it is dependent on the underlying metallicity distribution of the stars and the magnitude of the extinction. Finally, our photometric selection leading to the 1300 star VMP sample in this paper has not been homogeneous. Many of the follow-up fields were selected using *Gaia* photometry, some using PS1 photometry, and even within the *Gaia* selection the details of the selection box and the cuts for the removal of foreground contamination have evolved – all affecting where exactly the "best 400 stars" box ends.

Despite these caveats, our analysis is very useful for giving a qualitative estimate of the carbon-bias of the *Pristine CaHK* filter. The x-axis represents the "temperature" axis. In both the PS1 and *Gaia* spaces, there is a shift to higher $(g-r)_0$ and $(BP-RP)_0$, respectively. This is the result of large carbon features being present in the bluer filters but not in the redder filters. Such a shift makes the stars appear cooler; this is a well-known effect and has already been observed in Ba-stars and CH-stars many years ago (Bond & Neff, 1969). Fortunately, the PIGS selection box is chosen to be quite wide, such that even the most of the carbon-enhanced giants do not leave the selection box through this effect, except possibly at the tip of the giant branch.

The y-axis in the colour-colour diagrams represents the "metallicity" axis. It appears that we chose a PS1 colour combination where the change in $(g-r)_0$ largely cancels the change in $(CaHK-g)_0$ for carbon-rich stars – implying there should be little bias in our relative metallicity estimate of stars based on the vertical location in the PS1 diagram. In the *Gaia* space, for more carbon-rich stars there is a change on the metallicity axis, which depends strongly on the temperature.

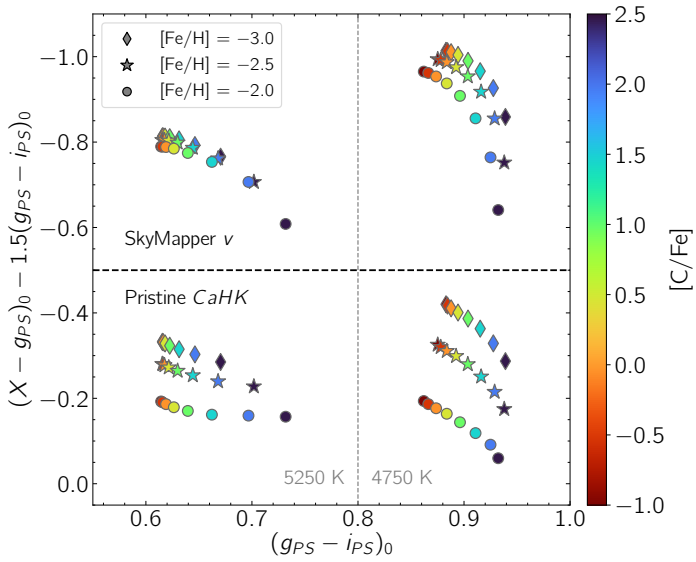

Figure 6.3 — Synthetic photometry from model spectra with the SkyMapper (top) and *Pristine* (bottom) filters, for the same $T_{\rm eff}$ and $\log g$ as the models in Figure 6.2 (5250 K on the left, and 4750 K on the right). The results for SkyMapper have been offset by 0.3 mag to separate the SkyMapper and *Pristine* results.

The cooler carbon-rich stars move down in the diagram, towards the border of the selection box. The larger effect in *Gaia* compared to PS1 is likely the result of the *Gaia* filters being much wider than the PS1 filters and therefore less sensitive to the carbon abundance – they cover more of the redder part of the spectrum which is less dominated by carbon features. The *CaHK* photometry is still affected significantly, and the difference between the colours on the y-axis is therefore larger. However, in this analysis, none of the models moves out of the metal-poor selection box.

The effect of carbon in the photometric selections of SkyMapper and *Pristine* is compared in Figure 6.3. The colour-colour space used here is that from Da Costa et al. (2019), with the difference that the broad-band colours are from PanSTARRS instead of SkyMapper. The top row shows the models when the SkyMapper v-filter is used, the bottom row presents the results from the $CaHK$ filter. The left- and the right-hand columns are models for stars of different temperatures. This confirms that the *Pristine* selection of metal-poor stars is expected to be less biased against carbon-rich stars than the SkyMapper selection.

Overall, it appears that the shifts of carbon-rich stars in the *Pristine* colour-colour diagrams are not expected to cause a significant bias in our selection – except possibly for the cooler, less metal-poor, most carbon-rich stars in the *Gaia* selection. This is a preliminary conclusion which depends on the uncertainties and caveats mentioned earlier in the section.

6.4 Stellar evolution on the giant branch

As stars evolve on the upper red giant branch (RGB), their surface carbon abundance changes. In the inner regions of an RGB star, carbon has been converted to nitrogen in the CN cycle. While ascending the RGB, the star experiences mixing episodes, in which material from layers deeper in the star are transported to the stellar surface. The first dredge up occurs at the start of the RGB, which does not significantly change the surface [C/Fe] for metal-poor stars (Vandenberg & Smith, 1988; Charbonnel, 1994; Gratton et al., 2000). No additional mixing is expected to take place from standard theoretical models, but observations have shown that the surface abundance of carbon and nitrogen changes significantly on the RGB for metal-poor stars. The strength of this "extra mixing" appears to depend on the initial metallicity and carbon and nitrogen abundances, and it has been found to be stronger in metal-poor stars (e.g. Gratton et al., 2000; Placco et al., 2014). One proposed mechanism is thermohaline mixing, which has been shown to reproduce the abundances in low-mass, low-metallicity evolved giants well (Charbonnel & Lagarde, 2010). A recent, in-depth, observational study of extra mixing in metal-poor giant branch stars has been done by Shetrone et al. (2019). They also nicely summarise our understanding of extra mixing in their introduction, including some criticism of the thermohaline mixing explanation. In this section, we investigate the change of carbon abundance on the RGB in PIGS.

6.4.1 [C/Fe] in the Kiel diagram

For this purpose, we select giant stars ($\log g < 3.5$) with $\mathrm{SNR}_{4000-4100} > 25$ to limit ourselves to a sample of stars with good quality carbon abundances. The median total uncertainty on [C/Fe] ($\epsilon_{[\mathrm{C/Fe}]}$) is 0.25 dex in this high SNR sample. Furthermore, we cut stars that have $\epsilon_{[\mathrm{C/Fe}]} > 0.4$ dex or $\epsilon_{\log g} > 0.5$ dex. We limit ourselves to stars with [Fe/H] < -1.5, because above this metallicity there are almost no upper RGB stars in PIGS. We split the sample in two: the intermediate metal-poor (IMP) stars with $-2.0 <$ [Fe/H] < -1.5 and the very metal-poor (VMP) stars with [Fe/H] < -2.0.

We present Kiel diagrams colour-coded by [C/Fe] for these two samples in Figure 6.4. For both the IMP and the VMP stars, the average value of [C/Fe] clearly decreases for stars higher up the RGB. There also appears to be population of stars above the RGB that shows lower [C/Fe] values (especially visible in the IMP sample). In the T_{eff}–$\log g$ diagram in the independent ULySS analysis of the spectra, there are also two sequences (there is no information on carbon in this analysis). We hypothesise that these stars are in fact not RGB stars, but that they lie on the parallel early asymptotic giant branch (AGB) instead. Early AGB stars are expected to have a lower carbon abundance than RGB stars because they have already travelled all the way up the RGB, before they became horizontal branch stars and now AGB stars. We make a rough separation of both populations indicated by a dashed line in Figure 6.4 (slightly different offset for the IMP and VMP stars). In line with our hypothesis, we will name the stars under this line RGB stars and the stars above the line AGB stars.

In the IMP sample, the number of RGB stars is three times larger than the number of AGB stars for stars between 5000 K $< T_{\mathrm{eff}} <$ 5300 K. It seems that the

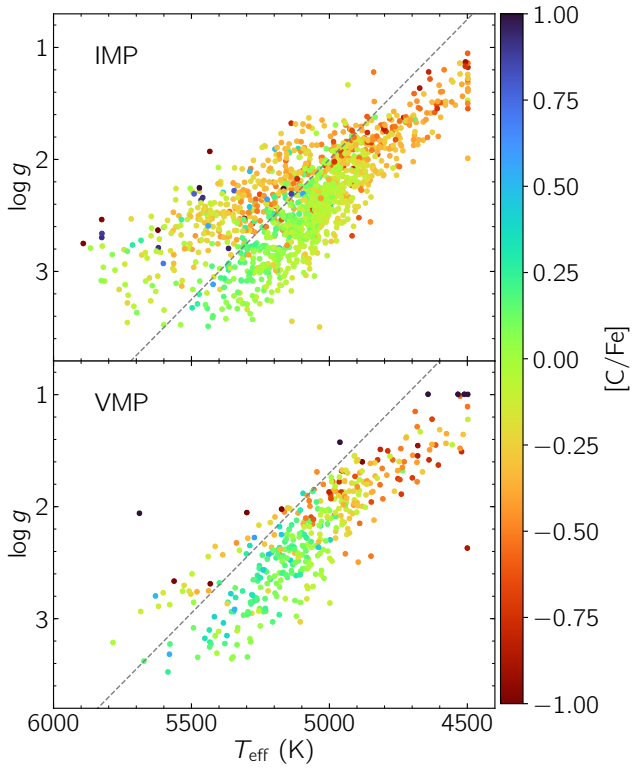

Figure 6.4 — Kiel diagram of PIGS giants with $\mathrm{SNR}_{4000-4100} > 25$ for stars with $-2.0 <$ [Fe/H] < -1.5 (IMP, top panel) and [Fe/H] < -2.0 (VMP, bottom panel), colour-coded by [C/Fe]. The dotted grey lines indicate a rough separation between the RGB and AGB stars.

fraction of AGB stars is relatively large, given the fact that stars generally live longer on the RGB than on the AGB. To quantify this, we performed a test with the MIST evolutionary tracks (Dotter, 2016; Choi et al., 2016). Using a track for a $0.8 M_{\odot}$ star with a [Z/H] of -1.4 (corresponding to [Fe/H] ~ -1.7, assuming $[\alpha/\mathrm{Fe}]$ is $+0.4$), the lifetime of stars on the RGB and AGB are compared in the same temperature range as was used for the data (5000 K $< T_{\rm eff} <$ 5300 K). We find that the time spent on the RGB in this temperature range is 100x larger than on the AGB. Given this large difference, it is curious that our sample contains so many early AGB stars. It might be that our metal-poor colour-colour selection somehow favours AGB stars over RGB stars, but it is not obvious why. A detailed investigation of this is beyond the scope of this work.

6.4.2 Quantifying the carbon depletion

Figure 6.5 presents the mean trends of [C/Fe] with $\log g$ for both the IMP and VMP RGB stars. The trend of decreasing [C/Fe] with the ascension on the RGB is clearly

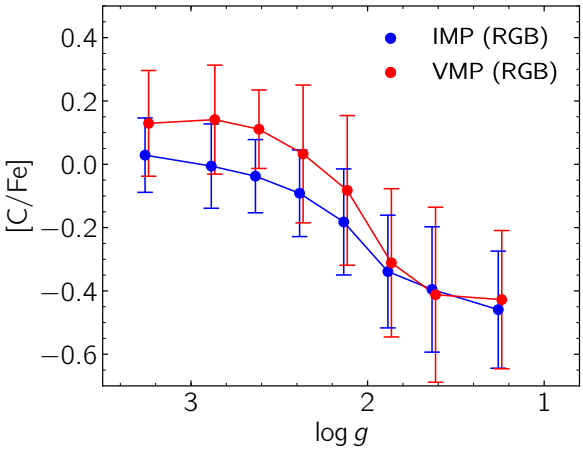

Figure 6.5 — The mean [C/Fe] versus $\log g$ in the IMP and VMP samples of RGB stars. The means are determined using a 3σ clipping of outliers.

visible; the magnitude of the carbon depletion (0.5 – 0.7 dex) and that it is stronger for more metal-poor stars is consistent with previous observations and modelling (e.g. Gratton et al., 2000; Placco et al., 2014). Additionally, the average [C/Fe] for the unevolved VMP stars is ∼ 0.10 – 0.15 dex higher than for the IMP stars. This is consistent with previously observed trends of increasing [C/Fe] with decreasing [Fe/H]; which might be real or might actually be the result of 1D/LTE instead of 3D/NLTE assumptions in the spectral modelling (Amarsi et al., 2019).

In the models by Placco et al. (2014), the extra depletion of carbon starts at $\log g = 2.0$ and is negligible at higher $\log g$ values. In our sample, we already see an effect at higher $\log g$. This could be real, but it would also be consistent with an offset in $\log g$ of ∼ 0.5 dex in the FERRE results. An indication of the latter is that the FERRE $\log g$ values appear to have an offset of a similar magnitude with stars in common with APOGEE, as discussed in A20b/Ch5. Additionally, also discussed in A20b/Ch5, there is a bias in the same direction (FERRE having $\log g$ values that are higher) in the comparison of the FERRE and ULySS analyses of the PIGS spectra. This bias, however, is not uniform throughout the parameter space. In both comparisons it appears to be larger for higher FERRE $\log g$. An additional check with MIST isochrones (Dotter, 2016; Choi et al., 2016) reveals that there could indeed be a $\log g$ bias in the FERRE analysis, mainly at the start of the RGB ($\log g > 2.5$).

For a very metal-poor population we expect that such a shift in $\log g$ has a negligible effect on the determination of [Fe/H], as most of the stronger Fe lines that are still visible in the more metal-poor stars are quite insensitive to $\log g$ (see, for instance, the discussion in Starkenburg et al., 2018). However, the carbon abundances might be affected by systematic differences in the $\log g$ determination. The strength of the CH band (which is the main carbon feature in the PIGS spectra) depends on the surface gravity. Aguado et al. (2019) tested how much [C/Fe] changes with $\log g$ for a sample of VMP stars from the *Pristine* survey, using a very

similar approach (FERRE with almost the same synthetic grid, and in the same blue wavelength range). Their Figure 5 shows the difference in [C/Fe] when they let $\log g$ be a free parameter versus when they fix $\log g$ to be 2.5. There is an almost linear relation between the difference in [C/Fe] and the $\log g$ for $1.0 < \log g < 3.5$, with an increase of 0.2 dex in [C/Fe] for a decrease in $\log g$ of 0.5 dex. If we assume that the PIGS $\log g$ values for giant stars are indeed 0.5 dex too high, the [C/Fe] are expected be of the order of 0.2 dex too low. We use this to correct our [C/Fe] abundances for part of the sample in the next section.

6.5 CEMP stars in the inner Galaxy

In this section, we report the discovery of several CEMP stars in the PIGS data set and discuss the fraction of CEMP stars in the inner Galaxy. Previously, only two CEMP stars were known in the bulge: one CEMP-s star (Koch et al., 2016) and one CEMP-no star (Howes et al., 2015). These two stars (and a slightly more metal-rich CH star from Koch et al. 2016), together with a large (halo) literature sample of CEMP stars observed with high-resolution spectroscopy from Yoon et al. (2016), are shown in the background of the [Fe/H]–A(C) diagram in Figure 6.6. The absolute carbon abundance A(C) represents the logarithm of the relative carbon abundance to hydrogen (in this system, A(H) is 12.0 per definition). As detailed in the introduction of this chapter, the different sub-populations of CEMP stars (CEMP-no and CEMP-s stars) show a typical separation in A(C) space.

6.5.1 New CEMP stars

To select CEMP stars from the PIGS data, we adopt a CEMP definition of [C/Fe] > +0.7. Only stars with $\log g > 1.5$ are included, since for the selected PIGS magnitude range more evolved stars might be in the halo on the other side of the bulge instead of in the inner Galaxy. For stars with $2.5 > \log g > 3.5$, 0.2 dex is added to the FERRE [C/Fe] values to correct for the bias in $\log g$ found in the previous section. No attempt is made at correcting for evolutionary effects in more evolved stars, due to uncertainties in the biases in $\log g$ in this regime and due to a difficulty in classifying the stars as true RGB or early AGB (the latter should have a larger correction). The correction would not drastically change the [C/Fe] of these stars, since most of these stars have $\log g > 2.0$ and based on Figure 6.5 the [C/Fe] correction should not be much larger than 0.3 dex. There are also a number of CEMP early AGB candidates, which could have larger corrections of up to ~ 0.5 dex (assuming the correction is the same as that for stars at the tip of the RGB, Placco et al. 2014[2]).

The stars passing the CEMP criterion are highlighted in Figure 6.6. The stars with $\log g > 2.5$ are shown in black, and the more evolved stars are shown in grey. For the latter, stars with [C/Fe] > +0.4 are also shown – these might be CEMP after correcting for evolutionary effects. In total, there are 66 metal-poor PIGS stars with [C/Fe] > +0.7, 32 of which have [C/Fe] > +1.0. These numbers are 31 and 14, respectively, for stars with [Fe/H] < −2.0. All of these are new carbon-enhanced star discoveries, and

[2] https://vplacco.pythonanywhere.com/

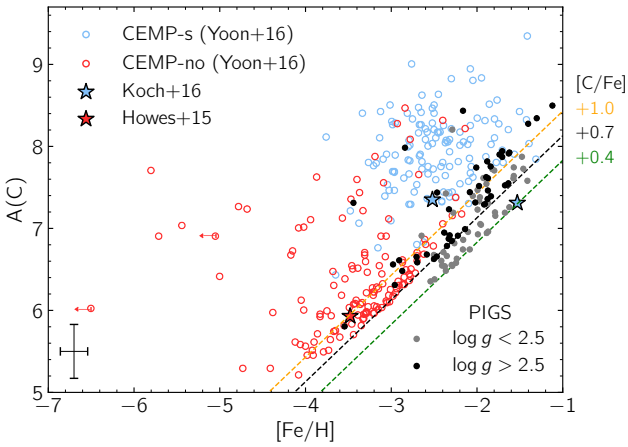

Figure 6.6 — A(C)–[Fe/H] diagram for CEMP stars. A literature halo sample from Yoon et al. (2016) is shown in red and blue circles, and the two previously known CEMP stars (and one CH star) in the bulge region are indicated with stars. The new PIGS CEMP stars are presented in black ($\log g > 2.5$) and grey ($\log g < 2.5$). Three lines of constant [C/Fe] are shown with dashed lines, with the [C/Fe] = +0.7 line indicating our adopted CEMP criterion. Typical uncertainties on the two parameters are shown in the bottom-left corner.

they increase the total sample of CEMP stars known in the inner Galaxy more than thirty-fold (fifteen-fold for very metal-poor CEMP stars).

In the absence of any s-process abundance information for our stars or any radial velocity monitoring, a different strategy is needed to classify the newly discovered CEMP stars. A first classification can be made based on the A(C) and [Fe/H] of the stars. Using limits of A(C) > 7.1 and [Fe/H] > −3.0, 46 stars are found to lie in the CEMP-s category. It is noteworthy that most of these lie at the lower A(C) edge of this space and at the more metal-rich end, whereas the known CEMP-s stars typically have much larger A(C) values and on average lower metallicities. The other 20 CEMP stars are located in the CEMP-no regime of the A(C)–[Fe/H] diagram. Most of these lie close to the [C/Fe] = +0.7 line, but – in contrast with the PIGS CEMP-s stars – here it is consistent with the space covered by halo CEMP-no stars.

The discrepant location of the PIGS CEMP-s stars might be related to our photometric narrow-band pre-selection. The *CaHK* photometry could be biased against the most carbon-enhanced stars, as discussed in Section 6.3. Although most of the effect of carbon-enhancement appears to be largely cancelled out in the colour-colour selection space, this is very sensitive to the assumptions of the modelling and the CNO abundance ratios, and it also depends on the employed broad-band photometry. It is therefore unclear whether the selection effect is the best explanation for the location of the PIGS CEMP stars in the [Fe/H]–A(C) diagram. It is possible that the sparsity of CEMP-s stars with higher carbon abundances in our sample is hinting at different binary fractions in the populations of stars we study,

when compared to similar populations in the halo. But more unbiased samples or better estimates of our selection biases would be needed to confirm this result.

We also report the discovery of four new CEMP stars that are likely in the halo on the opposite side of the bulge (not shown in Figure 6.6). Three of them have $\log g = 1.0$ (the $\log g$ edge of the FERRE grid) and one has $\log g = 1.4$. All four stars lie between $-3.0 <$ [Fe/H] < -2.0 and have A(C) values consistent with being CEMP-s stars. Their A(C) are larger than the bulk of the CEMP stars described above, but they are still located in the lower-carbon part of the CEMP-s region (even after applying Placco et al. 2014 corrections for tip-of-the-RGB stars, the corrections are only 0.2 – 0.3 dex for VMP stars with [C/Fe] $> +1.0$).

6.5.2 What is the CEMP fraction?

PIGS has significantly increased the number of known CEMP stars in the inner Galaxy, showing that these stars are also ubiquitous in this region of the Milky Way. However, the crucial comparison to be made with known samples of halo metal-poor stars is that of the fraction of CEMP stars compared to the total sample of (very/extremely) metal-poor stars.

To investigate the CEMP fraction, we select PIGS stars with $2.5 < \log g < 3.5$, because these are expected to be the least affected by extra mixing. Additionally, in this regime we have estimated the bias in the PIGS/FERRE $\log g$ and [C/Fe] results and corrected the carbon abundances accordingly (see Section 6.4). Finally, most of these stars are hotter than 5000 K; we therefore do not expect strong selection effects against carbon-rich stars, based on our tests in Section 6.3. We only use stars with $T_{\rm eff} < 5500$ K, in order to avoid a bias due to the inclusion of early AGB stars, and because the determination of [C/Fe] at lower temperatures is more robust. We also remove a small number of remaining likely early AGB candidates based on their location in the $T_{\rm eff} - \log g$ diagram and their very low [C/Fe].

We present the [C/Fe] as a function of [Fe/H] of the resulting sample in Figure 6.7, with the cumulative percentage of CEMP stars below four different [Fe/H] values indicated. For [Fe/H] $< -2.0, -2.5, -3.0$, we find CEMP fractions of $52 \pm 17\%$, $28 \pm 5\%$, $16 \pm 2\%$, respectively. These have been acquired through a Monte Carlo run in which the total uncertainties for the derived [Fe/H] and [C/Fe] are taken into account. The CEMP fractions determined by Placco et al. (2014) are indicated in red in the three most metal-poor bins, where the first number in each case is the combined fractions of CEMP-no and CEMP-s stars and the second number is for CEMP-no stars only. The PIGS fractions appear compatible with the literature for [Fe/H] < -2.5, but the fraction is strongly discrepant for [Fe/H] < -2.0. This is consistent with the apparent lack of CEMP-s stars with high A(C) compared to halo samples, as discussed in the previous sub-section. Placco et al. (2014) also provide the fractions of CEMP-no stars only; these are 20%, 24%, and 43% for [Fe/H] $< -2.0, -2.5$, and -3.0 respectively. These percentages are more consistent with the ones that we find.

If we would have calculated a simple ratio to estimate the CEMP fraction instead of the Monte Carlo approach, the CEMP fraction in the [Fe/H] < -2.5 bin would go down to 14% (9 out of 56). This difference is due to more stars lying just below the

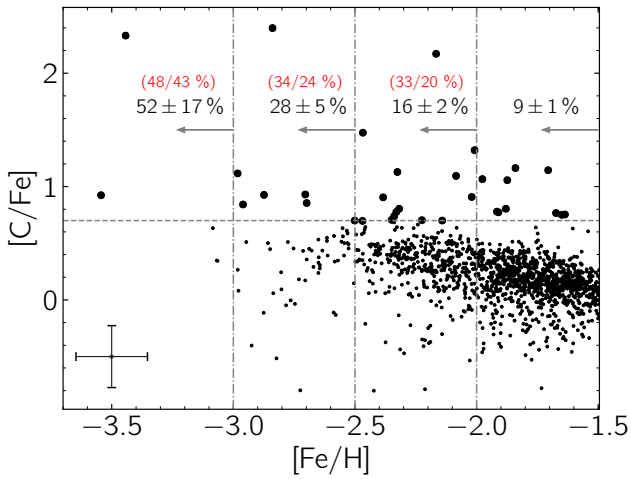

Figure 6.7 — PIGS stars with $2.5 < \log g < 3.5$. The horizontal dashed line indicates the CEMP criterion at [C/Fe] = +0.7, the CEMP stars (which are above this line) are shown with larger points. The PIGS cumulative CEMP fraction below four different [Fe/H] (vertical dot-dashed lines) is indicated in black, the CEMP fractions in the halo from Placco et al. (2014) are indicated in red (CEMP-no + CEMP-s/CEMP-no only). Typical uncertainties on the two parameters are shown in the bottom-left corner.

[C/Fe] = +0.7 border than above, and those stars scatter into the CEMP category in the Monte Carlo simulation. Additionally, compared to the literature halo CEMP star population, there is a lack of CEMP stars that are very enhanced in carbon also in this [Fe/H] regime. As can be seen in Figure 6.6, this applies mainly to the CEMP-s stars.

In summary, in this section we have shown that at face value, the CEMP fraction in the inner Galaxy from PIGS is lower than in the halo but that it could be compatible with the halo fraction at the lowest metallicities, especially for the CEMP-no stars. For CEMP-s stars with larger carbon-enhancement, there may be a difference between the inner Galaxy and the halo, and/or there could be stronger selection effects in PIGS resulting in a bias against these stars.

6.6 Discussion and conclusions

There are a number of avenues to investigate the results of this work in more detail, which are discussed in the first part of this section. In the second part we discuss possible interpretations of our observations, and we end with the conclusions.

6.6.1 Caveats and future tests

Firstly, only a crude estimate of the bias against carbon-rich stars in the photometric *Pristine* selection was performed. As described in Section 6.3, there are several

limitations in the current method on the modelling side (for example, varying CNO abundances, the assumption of 1D/LTE and challenges with the synthetic photometry) and on the observational side (for example, the varying limit of the selection box due to extinction and the underlying MDF and changes in follow-up strategy). In the coming years, the sample of observed (carbon-enhanced) metal-poor stars selected from the main *Pristine* survey in the halo is going to increase significantly through follow-up with WEAVE (the William Herschel Telescope Enhanced Area Velocity Explorer, a multi-object spectroscopic facility in the Northern hemisphere, Dalton et al. 2018). This will allow for a much more detailed empirical analysis of the selection effects due to the filter. Additionally, much better extinction maps will be available in the future derived from the *Gaia* spectrophotometry, which will help us to assess the full window function of the PIGS selection.

Another aspect which could be further developed is the determination of the stellar parameters and [C/Fe] with FERRE. We found that there are possible biases in $\log g$, which can affect the derived carbon abundance. In the FERRE analysis, the blue arm and the calcium triplet spectra are fit together and a running mean normalisation is used in order to compare the observations and synthetic spectra on the same scale. The cores of the calcium triplet lines are masked because they are sensitive to NLTE effects, but the wings of these lines are included in the fit. The wings are sensitive to gravity, and including the red arm in the analysis helps to get a better $\log g$. This is indicated by a smaller scatter with respect to the independent analysis as compared to when only the blue arm is used. However, the running mean spreads some of the information from the calcium triplet cores to the wings which might result in biased $\log g$ determinations. We plan to investigate this in the future by exploring other ways of normalising the calcium triplet spectra in the FERRE fit. Having more robust $\log g$ values would allow a proper correction for carbon depletion on the RGB, which will result in larger samples that can be used in the determination of the CEMP fraction.

Finally, a number of the CEMP stars in our sample may just be halo stars passing through the bulge instead of staying within the inner Galaxy. We plan to do a thorough investigation of the kinematics of these stars (and the rest of the PIGS sample) in the future using *Gaia* (E)DR3 information; this will allow us to refine the "true" inner Galaxy CEMP fraction.

6.6.2 Interpretations of the CEMP stars and fractions

The CEMP fractions in PIGS might be affected by small number statistics and/or by selection effects, but we can speculate what they would mean if we take them at face value. The fractions of CEMP-no stars appear compatible with those of the Galactic halo (although they have large uncertainties, especially at the lowest metallicities). This could imply that the First Stars polluted the gas in the same way in the building blocks that contributed to the inner Galaxy and those that contributed to the (local) Galactic halo. The inner Galaxy building blocks likely came into the Milky Way at an earlier time, and may have had different sizes. There have been some suggestions that the fraction of CEMP-no stars is lower in more massive building blocks, because of the observed (apparent) lack of CEMP-no stars in dwarf spheroidal galaxies,

whereas the CEMP-no stars are found in "usual" frequencies in ultra faint dwarf galaxies (e.g. Norris et al., 2010; Lai et al., 2011; Frebel et al., 2014; Skúladóttir et al., 2015). However, some have suggested that this is simply a selection effect related to the varying metallicity distribution functions in the different types of dwarf galaxies (Salvadori et al., 2015).

We also note that some of our CEMP-no stars might not be truly carbon-enhanced. Recently, Norris & Yong (2019) have cast doubts on the reported CEMP-no fractions in the literature. They found that once estimates for 3D and non-LTE effects on the CH G-band are taken into account (which are stronger for more metal-poor stars), the CEMP star carbon abundances decrease by up to ~ 0.5 dex, reducing the number of CEMP-no stars by ~ 70%. Similar results were found by Amarsi et al. (2019), who reported lower carbon abundances in a careful 3D/NLTE analysis of atomic carbon for a number of metal-poor stars. Most of the CEMP stars in PIGS would not be carbon-enhanced if their [C/Fe] was reduced significantly.

However, there are four CEMP stars in the sample that have [C/Fe] $\geq$ +2.0, which will stay carbon-enhanced even if strong corrections were applied. Based on their location in the [Fe/H]–A(C) diagram (see Figure 6.6), three of these are likely CEMP-s stars and one of them is potentially a CEMP-no star. These stars are very interesting targets for high-resolution spectroscopic follow-up; their abundance patterns will reveal information about mass-transfer from metal-poor AGB stars in the inner Galaxy and/or clues about First Star nucleosynthesis. It would also be interesting to monitor their radial velocities, to see if they fit in the standard binary mass-transfer/First Star picture. The potential CEMP-no star lies in the intermediate A(C) range between the bulk of CEMP-s and CEMP-no stars. Yoon et al. (2016) advocates treating stars in this part of parameter space as yet another population. Interestingly, Arentsen et al. (2019a)/Chapter 2 have shown that binarity among CEMP-no stars in this A(C) regime is higher than among the CEMP-no stars with lower A(C) (although this still has to be confirmed with more statistical rigour in larger samples). They hypothesise that some of these stars might have been born with less carbon initially, but might have obtained some additional carbon as their binary companion evolved. These CEMP-no stars do not show the typical s-process abundance enhancements, but it is questionable whether AGB stars at such low metallicities do produce s-process elements in the same way stars at higher metallicities do (see Arentsen et al. 2019a/Chapter 2, and references therein).

Finally, we ask the question: what if the apparent difference in the CEMP-s fraction between the inner Galaxy and the rest of the halo is real? The most obvious interpretation would be a smaller binary fraction among metal-poor stars in the inner Galaxy compared to the halo – if there are fewer binary stars, fewer stars will have experienced mass-transfer from a companion and fewer stars would turn into CEMP-s stars. However, there is no clear physical reason why the binary fraction in the bulge should be lower. The density of stars is higher than in the halo, but not so high that binary systems would get disrupted significantly more often. Alternatively, the typical separations of binary pairs could be different between the two populations, causing a difference in the efficiency of mass-transfer. It is, however, difficult to imagine what the cause of that would be. Another interpretation could be that, for some unknown reason, the metal-poor AGB stars

in the inner Galaxy did not produce as much carbon as those in the halo. However, this would be unexpected, since stellar evolution should not change with Galactic location. It appears that, at the moment, the *Pristine* selection effects are the most likely explanation for the low fraction of CEMP-s stars in the PIGS sample.

6.6.3 Conclusions

In this chapter, we discussed the carbon abundances of the PIGS sample of metal-poor stars in the inner Galaxy. We showed that in the inner Galaxy, the carbon in metal-poor giants decreases with the evolutionary stage of the stars. This effect has already been observed in the halo and is partly reproduced in stellar modelling. We presented a sample of 66 new CEMP stars, which is a significant increase compared to the only two known previous examples. These stars are unique tracers of binary mass-transfer and the fingerprints left by the First Stars, and a larger sample of them will allow for a closer investigation of these processes in the inner Galaxy. The fraction of CEMP-no stars appears consistent with the halo fraction – in contrast to previous results from the inner Galaxy SkyMapper/EMBLA survey (Howes et al., 2015, 2016). We do observe an (apparent) lack of very carbon-rich CEMP-s stars in the PIGS sample. We discussed various interpretations and concluded that it is likely a selection effect in the photometric pre-selection of PIGS stars, although there might be other explanations. Our biases and further properties of the inner Galaxy CEMP population will be investigated in more detail in future work, which will allow us to make more robust conclusions. This is only the start of a promising avenue to study the build-up of the old, metal-poor inner Galaxy using carbon-enhanced metal-poor stars.

7 Discussion and future perspectives

> *"When I look at the stars*
> *I see someone else*
> *When I look at the stars*
> *I feel like myself"*
>
> **— Switchfoot**
> (Stars)

The theme of this thesis is employing old, metal-poor stars to learn about the first generations of stars and how they have contributed to the build-up of the Milky Way galaxy. The individual contributions of each of the chapters to the current state of the field have been summarised in the Introduction. They include the study of the binarity properties of some of the most metal-poor stars, the analysis of stellar spectra for an empirical spectral library and a metal-poor star survey, the discovery of many new metal-poor stars in the inner regions of the Milky Way, and kinematical and chemical studies of the inner Galaxy metal-poor stars. These results are coming out in an exciting time for Galactic Archaeology, with many promising avenues to investigate them further in the near future.

7.1 The future for PIGS and metal-poor bulge studies

Three of the five chapters in this thesis are dedicated to the *Pristine* Inner Galaxy Survey (PIGS) – this survey started in the first year of doctoral studies of the thesis author and was developed further in the next three years. The first telescope proposal for *Pristine* in the bulge was submitted in the Spring of 2017, which resulted in a pilot program of ~ 40 deg^2 of *CaHK* photometry (containing several known metal-poor stars). The pilot results were promising, and within one month of receiving the first photometric data, a pilot spectroscopic follow-up proposal was submitted to the AAT and executed within days. This whirlwind start of the *Pristine* bulge survey (renamed to PIGS in 2019) was the beginning of an exciting journey – a journey that is still continuing.

While the observations of the planned photometric footprint have now been completed, the spectroscopic follow-up is still ongoing. An observing run at the AAT is scheduled towards the end of Semester 2020A, with the aim of observing an additional 12 fields. The added value of this additional follow-up is threefold. First, it allows studying a new bulge area. The fields will be placed mainly in the photometric footprint added in 2019 which covers much of the Northern bulge, whereas most of the current follow-up is in the Southern part. Most of the literature metal-poor inner Galaxy stars, dominantly from the EMBLA survey, are also in the South – meaning that the extension allows investigating a truly understudied stellar population. Secondly, it will increase our current sample by 50% (e.g. ~ 650 new stars with [Fe/H] < -2.0, extrapolating from our previous follow-up). This provides opportunities to discover more of the most metal-poor stars – a query of the JINAbase (Abohalima & Frebel, 2018) returns that only 7% of the stars with [Fe/H] < -3.0 have [Fe/H] < -4.0, which means that statistically we need much larger samples than the handful of currently known inner Galaxy stars with [Fe/H] < -3 to explore the ultra metal-poor tail. Additional follow-up will also increase the statistics for CEMP studies and kinematic studies with the most metal-poor stars. Finally, this expansion will create a more extended, symmetric coverage of the bulge which is important for future kinematic investigations. In this section, two important aspects of future (metal-poor) bulge studies are highlighted: dynamics and spectroscopy.

7.1.1 Dynamics of metal-poor bulge stars

We are planning more detailed dynamical studies of the metal-poor stars in the inner Galaxy in the near future, using PIGS and *Gaia*. Of particular interest are the orbits of the most metal-poor stars: do they stay within the bulge region or are they only passing through? What can their orbits tell us about their origin and the early evolution of the Milky Way? The addition of more AAT spectroscopic observations will be valuable for the reasons described above, but what is going to be crucial is the inclusion of more of the *Gaia* data – especially after the (E)DR3 data releases[1]. In the early DR3 (originally planned for the third quarter of 2020, but currently delayed), the *Gaia* team will provide updated astrometry and photometry for all sources. The parallaxes will improve in EDR3, but for stars in the bulge, the quality will not increase significantly (although a better removal of foreground stars will be possible). Proper motions, however, will be three times more precise compared to DR2, since the proper motion precision increases with time to the power 1.5 and the baseline will have more than doubled. The proper motions can be combined with radial velocities from PIGS and an estimate of the distance to derive orbital properties for our stars (assuming a particular Milky Way model). Early tests to derive distances for the PIGS stars have been conducted with the StarHorse code (Santiago et al., 2016; Queiroz et al., 2018), using available photometry, the *Gaia* parallaxes and our spectroscopic parameters (from ULySS). The code only converged for 2/3rd of the stars, and the quality of the results has not yet been

[1] (E)DR3 information from: `https://www.cosmos.esa.int/web/gaia/release` and `http://great.ast.cam.ac.uk/Greatwiki/GreatMeet-PM12`

investigated in detail. Future work will improve our distance estimates, and will allow a better investigation of the orbital properties of PIGS stars.

The full *Gaia* DR3 will include information from the BP/RP spectrophotometry (with an effective resolution $R < 100$), compared to only integrated BP, RP and G fluxes in DR2. This will have a profound impact the study of the (metal-poor) bulge and Galactic archaeology in general. The BP/RP spectrophotometry will allow the determination of astrophysical parameters for millions of stars. Combined with the parallax, these can be used to create superb extinction maps, better than any currently available. Including photometric information in the distance determination will allow significantly more robust distance estimates compared to using the parallaxes alone – allowing for better individual distances of stars and for a third dimension to the extinction map. Being able to correct for extinction properly is crucial in bulge studies. A large number of stars will also have available stellar parameters derived from the BP/RP spectrophotometry and/or the RVS spectra.

Gaia data will be very powerful by itself, but we also look forward to exploring synergies with PIGS; for example by adding the *CaHK* photometry that is very sensitive to metallicity at the low-metallicity end, or by adding our spectroscopy which will provide additional (chemical) dimensions. The improved quality of the proper motions also opens up possibilities for studying properties of the kinematics of the metal-poor tail of the bulge using the *CaHK* and broad-band photometry and proper motions *alone*. General bulge proper motion studies have already been undertaken with *Gaia* DR2 (Clarke et al., 2019; Sanders et al., 2019), but because the *Gaia* DR2 depth is limited (especially in the highly extincted bulge region), it has mainly been used to calibrate other, deeper proper motion surveys. With PIGS, we can provide a clean selection of metal-poor stars, a minority population in these regions that would be overshadowed by the overwhelmingly larger metal-rich populations in general bulge surveys. As we have shown in Chapter 4, such a study might lead to new insights into the kinematics of the old inner Galaxy.

7.1.2 Additional spectroscopic efforts

Chemistry from the AAT spectra

There is a limited amount of chemical information that can be derived from the low/intermediate resolution AAT spectra. In the analysis presented in this thesis we only derive the overall metallicity and the carbon abundance, but the spectra do contain more information. We have done some tests to derive additional abundances using FERRE, but have not yet explored it in detail. Of special interest is the calcium triplet region, which contains several spectral features that can be exploited for the derivation of chemical abundances. Interesting results in this respect have been published by the RAVE Survey in their sixth and final data release (Steinmetz et al., 2020a,b). From calcium triplet spectra at a resolution of $R \sim 7500$ they were able to derive reliable overall [α/Fe] ratios for stars in a large metallicity range, and iron, aluminum and nickel abundances mainly for stars with [M/H] > -1.0. We plan to further explore options for more chemical abundances from our AAT spectra, expecting to at least be able to derive general α-abundances or possibly individual magnesium abundances (combining information from the magnesium

triplet in the blue arm and a strong magnesium line in the calcium triplet region that is just outside the RAVE wavelength range). The α-abundances for metal-poor stars are typically expected to be enhanced by about $+0.4-0.5$ dex, but in the halo and dwarf galaxies some rare cases are known of metal-poor *and* α-poor stars (e.g. Caffau et al., 2013; Nagasawa et al., 2018). Exceptional stars like these hold unique clues about early star formation and Galactic evolution. For higher signal-to-noise spectra (SNR > 50), it should also be possible to derive additional elemental abundances. An alternative promising approach would be to employ machine-learning methods, which may be able to extract more information from (even relatively low signal-to-noise) low/medium resolution spectra. (e.g. Ting et al., 2017).

High-resolution follow-up

For detailed abundance patterns of individual stars, high-resolution spectroscopic observations are necessary. Currently there are three ongoing programs to follow-up stars from PIGS with high-resolution spectrographs. Two of these programs, with UVES on the VLT (accepted for Semester 2020A) and GRACES (part of the *Pristine* large program until Semester 2021B) on Gemini, focus on the most metal-poor candidates ([Fe/H] < -2.5) and target the optical wavelength range with $R \geq 40\,000$. These spectra contain many lines of elements representing various types of elemental groups: for example the α and iron-group elements, and neutron-capture elements in the rapid (r) and slow (s) categories. Deviations from halo-like abundance patterns in the iron-peak elements could indicate Population III enrichment, and those in r-process elements give insight into differences in nucleosynthesis between the inner Galaxy and the halo. Elements indicative of s-process enrichment can be used to distinguish between different types of CEMP stars.

The third follow-up effort at higher resolution is a collaboration with the bulge Cluster APOgee Survey (CAPOS, Geisler et al. in prep.), observing at $R \sim 22\,500$ in the near-infrared H-band. In this program, PIGS piggy-backs on fields targeted by CAPOS and fills ~ 100 fibres that they do not place on cluster stars in fields that are located in the PIGS footprint. It is limited to the relatively bright stars and the metallicity range is roughly $-2.5 <$ [Fe/H] < -1.5. Since there are not many spectral lines in the near-infrared in metal-poor stars, there will likely be only limited useful chemical information for these stars. This PIGS/CAPOS collaboration is estimated to double the number stars in the inner Galaxy with APOGEE spectra for [Fe/H] < -2.0, and increase it by 50% for stars with [Fe/H] < -1.5 (compared to DR16, Ahumada et al. 2019).

Large spectroscopic surveys

A very exciting development in the field is that of upcoming multi-object spectroscopic facilities, which have large surveys of millions of stars planned. The most relevant for Milky Way bulge studies are SDSS-V (Kollmeier et al., 2017), MOONS (the Multi-Object Optical and Near-infrared Spectrograph, Cirasuolo et al., 2011) and 4MOST (the 4-metre Multi-Object Spectroscopic Telescope, de Jong et al., 2019).

SDSS-V will use the existing BOSS and APOGEE spectrographs to perform an all-sky, multi-epoch survey of millions of stars in the Milky Way. In regions with high extinction, like the bulge, they will mainly use the APOGEE spectrograph – going more than one magnitude deeper than the current APOGEE surveys. Their unique strength lies in the multi-epoch observations, which will for example allow them to probe the binary properties of stars and track how they change with Galactic environment. MOONS will be able to observe simultaneously in the optical (> 6500 Å) and the near-infrared (H-band) at medium resolution, and it will have a high-resolution mode for the H-band similar to APOGEE. For their Galactic archaeology science case, MOONS will mainly target the inner regions of the bulge. They will produce precise radial velocities and chemical abundances, going more than 3 magnitudes deeper than APOGEE. There are discussions to include some metal-poor stars in their target lists, but in the inner regions the target selection will be difficult. The 4MOST survey in the bulge, however, will focus more on the optical wavelength regime and will therefore preferentially target regions with less extinction ($|b| \gtrsim 5°$). 4MOST also has a medium- and a high-resolution mode, and there are two dedicated consortium surveys studying the disc and bulge: the 4MOST Milky Way Disc and Bulge High-Resolution Survey (4MIDABLE-HR Bensby et al., 2019) and 4MIDABLE-LR (Chiappini et al., 2019). These surveys will revolutionise our understanding of the formation and evolution of the Milky Way bulge and bar, and will allow studying the interfaces between different Galactic components.

In the 4MOST low-resolution disk/bulge survey, a large number of (very) metal-poor stars are planned to be included. This sub-survey complements the high-resolution survey in the halo, which will also target very metal-poor stars (Christlieb et al., 2019). Target selection will be performed with the best information available, and in the inner Galaxy PIGS will likely be the main source of metal-poor stars. We expect to provide $100-200$ metal-poor targets per deg^2, of which we estimated 50% will have [Fe/H] < -2.0 (the other 50% is expected to be split equally between stars with $-2.0 <$ [Fe/H] < -1.5 and $-1.5 <$ [Fe/H] < -1.0). The coverage of the low-resolution spectra is $3700-9500$ Å, with a resolution varying from $R \sim 4000-7700$. The inclusion of the bluest wavelengths is crucial for the study of metal-poor stars – there are many lines of various elements here even in very metal-poor stars, and it includes some strong carbon-features. Recently, Hansen et al. (2019) used spectra from the X-shooter instrument (which has the most comparable resolution to the low-resolution 4MOST spectrograph) to study a sample of eleven very metal-poor stars, and they were able to derive abundances of 20 elements from high signal-to-noise spectra. They focus particularly on carbon and the neutron-capture elements Sr and Ba, and proposed a new scheme for CEMP-star classification based on these elements. Large samples of similar spectra from the 4MIDABLE-LR survey (in large part due to the excellent preselection with PIGS) will allow a thorough investigation of the (carbon-enhanced) metal-poor stars in the inner Galaxy.

7.2 The most metal-poor stars and CEMP stars in the coming years

The future is bright as well for the study of the very, extremely, ultra (etc.) metal-poor Milky Way. Studying the kinematics and chemistry of many EMP stars will provide insight into the formation history of the Galactic halo, and bring us closer to understanding the First Stars. This section discusses some future perspectives on having having larger spectroscopic samples and avenues to further study the role binarity plays in the most metal-poor stars.

7.2.1 Current and future samples of metal-poor stars

The number of known V/EMP stars has increased significantly in recent years, due to both metal-poor targeted spectroscopic surveys following up from photometry, like SkyMapper and *Pristine* (Da Costa et al., 2019; Aguado et al., 2019), and non-targeted large surveys, like LAMOST and SDSS (Li et al., 2018; Aguado et al., 2017). Most of these large spectroscopic samples only have low/medium-resolution spectroscopy available. These spectra are typically useful for a determination of the radial velocity, the stellar parameters including the metallicity, and for an estimate of the carbon abundance. For extremely metal-poor stars, it is difficult to get more information out of such low-resolution spectra (especially if the signal-to-noise is not very good, which is often the case).

Such samples are still valuable for many reasons. They are the place where exciting ultra-metal-poor objects are identified, which can then be followed up using higher resolution spectroscopy – a recent example is the ultra metal-poor star Pristine221 which is *not* very enhanced in carbon (Starkenburg et al., 2018). They can also be used to estimate the metallicity distribution function of the halo, either directly from the spectroscopic samples (Da Costa et al., 2019), or using the spectroscopy to calibrate larger photometric samples (Youakim et al., 2020). As a final example, the orbital properties of these stars (from combining their metallicities and radial velocities with *Gaia* DR2 information) contain a wealth of information about the formation history of the halo and, surprisingly, the disc. Yuan et al. (2020) used the VMP sample from LAMOST to search for dynamical substructures related to different accretion events in the halo, and Sestito et al. (2020) studied the orbits of stars in the *Pristine* and LAMOST samples and found that many of them appear to stay within the disc. More detailed dynamical investigations will be possible with future *Gaia* data releases and will undoubtedly lead to many new discoveries.

4MOST and WEAVE

The current samples of spectroscopic observations are incredibly useful, but as is typically the case, more and better data is expected to change the field once again. Important results will come from the large future multi-object spectroscopic facilities; especially WEAVE (Dalton et al., 2018) in the Northern Hemisphere and 4MOST (de Jong et al., 2019) in the Southern hemisphere are relevant here, but

other surveys are planned in the near or far future with the Subaru Prime Focus Spectrograph (PFS, Takada et al., 2014), the Dark Energy Spectroscopic Instrument (DESI, DESI Collaboration et al., 2016) and the Maunakea Spectroscopic Explorer (MSE, McConnachie et al., 2016).

As was briefly mentioned in the previous section, there is a consortium survey within 4MOST targeting the Galactic halo with the high-resolution ($R \geq 18\,000$) spectrograph (Christlieb et al., 2019). The main science goals are the study of the contents of the Galactic halo (identifying stars that formed *in situ*, in large and small halo building blocks and in globular clusters) to investigate the formation of the halo, and the study of early chemical evolution in the Milky Way using very metal-poor stars. They expect to observe $\sim 24\,000$ stars with [Fe/H] < -2.0 over the course of the survey (pre-selecting mainly from SkyMapper), and expect ~ 200 new stars with [Fe/H] < -4.0 – roughly a sixfold increase on the currently known number of ultra metal-poor stars (the current number is 43). Detailed chemical abundances will be available for this large sample (C, α-elements, neutron-capture elements).

Within WEAVE, there is both a dedicated low- and high-resolution survey for extremely metal-poor stars in the halo. They aim to target $> 60\,000$ candidate EMP stars, selected from various sources: *Gaia* DR3 (from BP/RP spectrophotometry and RVS spectra), SDSS and the *Pristine* survey. *Pristine* will be a very efficient source of the most metal-poor stars; based on three years of spectroscopic follow-up from the photometry they predict that 19% of EMP candidates will indeed have [Fe/H] < -3.0, and 53% and 78% will have [Fe/H] < -2.5 and -2.0, respectively (Youakim et al., 2017; Aguado et al., 2019). The *Pristine* survey currently has a footprint of ~ 5000 deg^2 (and it is still growing), of which a large fraction will overlap with the regions targeted in WEAVE. Estimates of EMP candidate densities are 20–30 per deg^2 in the low-resolution survey, and 1–2 in the brighter high-resolution survey. Whenever WEAVE points to a field with *Pristine* data, fibres will be allocated to EMP candidates from the *Pristine* survey. Aguado et al. (2019) estimate that the *Pristine*/WEAVE low-resolution survey will result in the discovery of ~ 3000 new stars with [Fe/H] < -3.0 and about $150 - 200$ with [Fe/H] < -4.0. The very wide wavelength coverage of the low-resolution spectra will provide at least metallicities, α-elements and an indication of the neutron-capture content of the stars. The high-resolution spectra will allow for a full investigation of the abundance patterns of EMP stars.

In summary, these very large samples of the most metal-poor stars from e.g. 4MOST and WEAVE are key additions to the field of Galactic Archaeology. They will provide exciting new insights into the properties of the First Stars and very early chemical evolution.

7.2.2 Binary properties of (C)EMP stars

Another important property of stars is whether they go through their life alone, or together with a companion. Not much is currently known about the binary fraction of stars at extremely low metallicities.

Importance of binary studies

We know that the abundance patterns of many stars with $-3.0 <$ [Fe/H] < -2.0 were affected by mass-transfer from a companion which is currently invisible; the companion can only be detected indirectly in the radial velocity variations of the primary star (these are the CEMP-s stars). Stars with [Fe/H] < -3.0 (and < -4.0) can still be in binary systems, but the general assumption is that their abundance patterns were not significantly affected and that they represent the gas out of which they formed. Studying the binary fraction and orbital properties of extremely and ultra metal-poor stars is crucial to estimate the validity of this assumption. The observations described in Chapter 2 show that the binary fraction among very carbon-rich CEMP-no stars is relatively high, which was a surprising result. Recent work shows that the binary fraction of stars appears to increase with decreasing metallicities (Moe et al., 2018; Price-Whelan et al., 2020). The high binary fraction among CEMP-no stars could simply be a reflection of the continuation of this relationship at the lowest metallicities. However, if the fraction of stars interacting with a companion is the same for [Fe/H] < -4.0 as for [Fe/H] < -2.0 stars, 13% of the ultra metal-poor stars should have had an interaction with a companion. If the binary fraction of ultra metal-poor stars is even higher, this percentage could also be higher. It appears unlikely that none of the ultra metal-poor stars interacted with a binary companion, although little is known about binary interaction at these metallicities so the end-product of such an interaction is uncertain. Future years should see improvements in the modelling of extremely metal-poor AGB stars and mass-transfer.

Binary stars can additionally provide information about the possible formation of low-mass stars at the lowest metallicities. Simulations of the First Stars mainly result in the formation of massive stars, but sometimes also smaller fragments can form – although it is unclear whether these survive to form low-mass stars (as discussed in the Introduction). The recent discovery of a ~ 0.14 $M_\odot$ companion to an ultra metal-poor star was used to estimate that solar-mass companions could be able to form around First Stars with masses between $10 - 100 M_\odot$ (Schlaufman et al., 2018). Estimating the mass of the companion of the most iron-poor star known to be in a binary system (HE 0107−5240, Arentsen et al. 2019a/Chapter 2; Bonifacio et al. 2020) would also provide valuable constraints.

Radial velocity monitoring

It is clearly worth investigating further what the binary properties of the most metal-poor stars are. Knowing the binary fraction better is necessary to investigate conditions for star formation in low-metallicity gas, and to estimate possible effects that the companions could have on each other. Monitoring the radial velocities of stars, however, is a laborious effort which should be continued for many years because stars can have very long orbits. Additionally, the radial velocities should be precise to be able to detect small variations. The largest ongoing multi-epoch spectroscopic survey is being conducted with the RVS instrument of *Gaia* (Gaia Collaboration et al., 2016). A discussion of what it will provide for the monitoring of CEMP-no stars is given in Chapter 2. Many of the extremely and ultra metal-poor

stars are unfortunately too faint, or their features in the calcium triplet spectra too weak, for precise radial velocities from *Gaia*. However, at the brighter end, *Gaia* will provide important constraints on the binary fraction and the variation of orbital properties as a function of metallicity. Similar types of constraints might come from SDSS-V (Kollmeier et al., 2017), although they note that they are not the optimal facility for stars that are faint or not very red (which unfortunately the most metal-poor stars typically are). Some promising results might also come from the 4MOST high-resolution survey, who aim to revisit targets on timescales of months to years (Christlieb et al., 2019).

It appears that there is still a need for dedicated, high-precision observing programs to investigate the binary properties of extremely metal-poor stars. One ongoing program to monitor the radial velocities of the most metal-poor stars ([Fe/H] < -4.5) is currently being undertaken with ESPRESSO at the VLT, yielding extremely precise velocities (Bonifacio et al., 2020). We are also continuing our own monitoring program for more CEMP-no stars to further test the results found in Arentsen et al. (2019a) (Chapter 2); using FEROS on the 2.2m at La Silla to monitor very carbon-rich CEMP-no stars with $V < 14.5$. It is a small, magnitude-limited sample, and unfortunately the structure of the time allocation and the observations is not ideal for monitoring programs – in an ideal situation one would do this in a more automated and structured way for much larger samples of stars.

7.3 Final remarks

The investigation of the most metal-poor stars and their connection to the First Stars will benefit enormously from upcoming surveys such as 4MOST and WEAVE. Many of the known ultra metal-poor stars have unique abundance patterns, and large samples are necessary to draw more general and robust conclusions about the first stellar populations in the Universe. It has also been the case that whenever larger samples of metal-poor stars became available, rare objects were discovered – such stars can provide unique insights into the environments of low-metallicity star formation and early chemical evolution. Combining the rich chemical information from spectroscopy with astrometric information from *Gaia* will allow a detailed reconstruction of the formation of the ancient Galactic halo.

Ongoing and future surveys will also revolutionise our understanding of the heart of our Galaxy. The combination of high quality proper motions, distances, radial velocities, metallicities and chemical abundances for thousands to millions of stars will open up an unprecedented, multi-dimensional view of the dynamical and chemical history of the inner Galaxy. Part of its earliest history can be traced using metal-poor stars; whereas previously only a small sample of them was known, their number has been significantly increased through this thesis and the future is even more promising. We study the Milky Way because we are curious about it and it is our home, but it is also the only Galaxy we can study in full detail. Having a better understanding of the history of the (inner) Milky Way will provide insights into the formation and evolution of other galaxies and their bulges.

Acknowledgements

It is great to see (and difficult to believe) that my thesis is really almost finished. What a journey it has been! Many people have been part of this journey one way or another, and I would like to thank them here.

First of all, I am extremely grateful to Else, my supervisor. You are an amazing person and a great supervisor, I love your enthusiasm and optimism! You trusted me so much in my work, which has been very encouraging. Thank you for giving me the chance to lead the PIGS project – it has been a challenging, interesting, scary and exciting experience. I always enjoy our (sometimes half English/half Dutch) conversations, and I am thankful for these years of working closely together with you. I think I hit the supervisor-jackpot!

I have been lucky to join the wonderful *Pristine* collaboration during my PhD. It is an honour and a joy to be a part of this group of nice people and excellent scientists, I always look forward to the *Pristine* meetings. Else and Nicolas, you are awesome PI's! Nicolas, it has been great working with you on PIGS and other *Pristine* projects. I enjoy discussing science with you, often leading to new ideas. Thanks for hosting me for a visit at the Strasbourg Observatory twice, and I look forward to spending the next few years there! Kim, thank you for your enthusiasm about my work and your encouraging support! It has been wonderful working with you, and I fondly remember my visit to Victoria. Vanessa, thank you for your interest in the *Pristine* bulge project, for the chance to visit Nice and for many nice interactions at *Pristine* meetings. David, I have had the pleasure of working more closely with over the past few months and it has been great! You are so encouraging even though you are sometimes drowning in work, I am so impressed! Thank you for the many hours you have poured into PIGS. Of course I should also thank the members of *Pristine*-Junior: Nicolas, Federico, Kris, Collin and recently Romain. Unfortunately we never had our shadow meeting in Hawaii, but who knows that the future brings. It has been a lot of fun to share the *Pristine*-PhD journey with you! Finally, not in *Pristine* but helping a lot with the PIGS AAT observations, thanks Dan for your support!

Also at AIP I've had the pleasure of interacting with many great people. Kris, I have enjoyed our time as PhD-siblings thoroughly! You are such a great person, full of excitement about life. It has been fun sharing an office with you during most of the PhD. We've had so many conversations about astronomy, work and life – I'm going to miss it a lot! Federico, thanks for the discussions and conversations we've had during your time in Potsdam, and for the time we shared an office. At the end of your stays I was sad to see you go back to Strasbourg! Anna, it has been a pleasure to share the office with you. Good luck for your PhD – I believe it will be a beautiful work! Alexey, it has been nice having a non-PhD student in the office. You always have such interesting stories to tell. And yes, also you, Friedrich, deserve a mention. Although has been interesting sharing an office, I enjoyed getting to know you. Marcel, I am thankful you joined AIP (I remember us meeting: "I think we follow each other on

Twitter"). You are a great person who cares a lot about others, and I want to thank you for the many conversations we've had. And thanks for checking my German summary! Dalal, I enjoy our chats and being able to share about the PhD journey. It was great representing the PhD students together with you. Thomas, I have enjoyed interacting with you, and thanks for the German/Python help every now and then. Guillaume, you are a fun person caring a lot about life outside work, also with colleagues. Thanks for that, and for the useful conversations about spectroscopy. Giacomo, it was a joy to have little chats in Dutch with you – I look forward to being able to do that again in Strasbourg. In Sung, I remember us arriving at AIP around the same time, both being new... I have enjoyed our interactions over the years. Florian, thanks for the company during many lunch breaks. Cameron, I appreciated your relaxed personality. Maria-Rosa, thank you for your group leadership. And thanks to all the other members of the MWLV & DGGH groups over the years for many interesting group meetings and enjoyable chats at coffee!

Of course there is also life outside of work – which has happened in a variety of languages. Pa en ma, bedankt voor jullie ondersteuning en liefde, en voor het toehoren bij mijn ellenlange verhalen over metaalarme sterren en de Melkweg! Mijn favoriete zus Hannah, ook jij hebt mijn verhalen aangehoord – bedankt voor het luisteren en meeleven, ik ben blij het met je te kunnen delen. Sietske, wat bijzonder dat we beide in Potsdam terecht kwamen voor onze PhD! Ik ben enorm dankbaar voor de regelmatige gezamenlijke maaltijden, en voor de gezellige gesprekken (wat fijn om Nederlands te praten!) met jou en Michael. Petra, Ruth, Aline, Rieneke – bedankt voor jullie vriendschap-op-afstand (elkaar maar één of twee keer per jaar zien is eigenlijk te weinig...). Annika, danke für die Zeit als Mitbewohnerinnen, es war schön die Wohnung mit dir zu teilen. Marie, danke für deine Freundschaft und viele gute Gespräche während unsere nach-Kleingruppe-Spaziergänge. Liebe Kleingruppe, danke das ihr meine Potsdamer Familie wart – Nate & Brittany and kids, Johann, Marie, Heidi, Lidia, Johanna, Sophia, Inga, Doro, Andreas, Anne Kristin. Ich werde euch vermissen! Ich habe eine super Zeit gehabt bei mittendrin, der cje und der SMD – es gibt zu viele Leute um einzeln zu nennen. Es war schön mit euch über Gott und die Welt zu reden und einfach spaß zu haben. My dear friend Tanya, it has been a blessing to get to know you through Cross-Current! Thank you for your friendship and the opportunity to share about the christian academic life. Christina, so toll dir besser kennen zu lernen und unsere Leidenschaft mit einander zu teilen! Alexander, thank you for your inspirational leadership and enthusiasm on the topic of science and faith in Germany and Europe. I am thankful for your support and interest in my path in life. And last but definitely not least, thank you Zachary. Thank you for your proofreading and your moral support. It has been a joy getting to know you and I am not sure how I would have gotten through the last "couple" of weeks without you.

Thank you!

Anke

The heavens declare the glory of God;
the skies proclaim the work of his hands.

— Psalm 19:1 (NIV)

Bibliography

Abate, C., Pols, O. R., Karakas, A. I., & Izzard, R. G. 2015, A&A, 576, A118
Abohalima, A., & Frebel, A. 2018, ApJS, 238, 36
Aguado, D. S., González Hernández, J. I., Allende Prieto, C., & Rebolo, R. 2017, A&A, 605, A40
—. 2018, ApJ, 852, L20
—. 2019, ApJ, 874, L21
Ahumada, R., Allende Prieto, C., Almeida, A., et al. 2019, arXiv e-prints, arXiv:1912.02905
Allende Prieto, C., Beers, T. C., Wilhelm, R., et al. 2006, ApJ, 636, 804
Allende Prieto, C., Fernández-Alvar, E., Schlesinger, K. J., et al. 2014, A&A, 568, A7
Allende Prieto, C., Fernández-Alvar, E., Aguado, D. S., et al. 2015, A&A, 579, A98
Alvarez, R., & Plez, B. 1998, A&A, 330, 1109
Amarsi, A. M., Nissen, P. E., Asplund, M., Lind, K., & Barklem, P. S. 2019, A&A, 622, L4
Aoki, W., Beers, T. C., Christlieb, N., et al. 2007, ApJ, 655, 492
Aoki, W., Beers, T. C., Lee, Y. S., et al. 2013, AJ, 145, 13
Arentsen, A., Starkenburg, E., Shetrone, M. D., et al. 2019a, A&A, 621, A108
Arentsen, A., Prugniel, P., Gonneau, A., et al. 2019b, A&A, 627, A138
Arentsen, A., Starkenburg, E., Martin, N. F., et al. 2020a, MNRAS, 491, L11
—. 2020b, MNRAS, 496, 4964
Asplund, M. 2005, ARA&A, 43, 481
Asplund, M., Grevesse, N., Sauval, A. J., & Scott, P. 2009, ARA&A, 47, 481
Astropy Collaboration, Robitaille, T. P., Tollerud, E. J., et al. 2013, A&A, 558, A33
Baade, W. 1944, ApJ, 100, 137
—. 1946, PASP, 58, 249
Babusiaux, C., Gómez, A., Hill, V., et al. 2010, A&A, 519, A77
Bailer-Jones, C. A. L., Rybizki, J., Fouesneau, M., Mantelet, G., & Andrae, R. 2018, AJ, 156, 58
Bandyopadhyay, A., Sivarani, T., Susmitha, A., et al. 2018, ApJ, 859, 114
Barbuy, B., Chiappini, C., & Gerhard, O. 2018, ARA&A, 56, 223
Barklem, P. S., Christlieb, N., Beers, T. C., et al. 2005, A&A, 439, 129
Beers, T. C., & Christlieb, N. 2005, ARA&A, 43, 531
Beers, T. C., Preston, G. W., & Shectman, S. A. 1985, AJ, 90, 2089
—. 1992, AJ, 103, 1987
Beers, T. C., Placco, V. M., Carollo, D., et al. 2017, ApJ, 835, 81
Belokurov, V., Erkal, D., Evans, N. W., Koposov, S. E., & Deason, A. J. 2018, MNRAS, 478, 611
Belokurov, V., Sanders, J. L., Fattahi, A., et al. 2019, arXiv e-prints, arXiv:1909.04679
Bensby, T., Feltzing, S., & Oey, M. S. 2014, A&A, 562, A71
Bensby, T., Bergemann, M., Rybizki, J., et al. 2019, The Messenger, 175, 35
Bessell, M., Bloxham, G., Schmidt, B., et al. 2011, PASP, 123, 789
Bessell, M. S., Christlieb, N., & Gustafsson, B. 2004, ApJ, 612, L61
Bessell, M. S., Collet, R., Keller, S. C., et al. 2015, ApJ, 806, L16
Bland-Hawthorn, J., & Gerhard, O. 2016, ARA&A, 54, 529
Bond, H. E., & Neff, J. S. 1969, ApJ, 158, 1235
Bonifacio, P., Caffau, E., Spite, M., et al. 2015, A&A, 579, A28
—. 2018, A&A, 612, A65
Bonifacio, P., Caffau, E., Sestito, F., et al. 2019, MNRAS, 487, 3797

Bonifacio, P., Molaro, P., Adibekyan, V., et al. 2020, A&A, 633, A129
Bonnarel, F., Fernique, P., Bienaymé, O., et al. 2000, AAPS, 143, 33
Bovy, J. 2015, ApJS, 216, 29
Bramall, D. G., Sharples, R., Tyas, L., et al. 2010, in SPIE Proceedings, Vol. 7735, Ground-based and Airborne Instrumentation for Astronomy III, 77354F
Bramall, D. G., Schmoll, J., Tyas, L. M. G., et al. 2012, in SPIE Proceedings, Vol. 8446, Ground-based and Airborne Instrumentation for Astronomy IV, 84460A
Bromm, V. 2013, Reports on Progress in Physics, 76, 112901
Bromm, V., & Larson, R. B. 2004, ARA&A, 42, 79
Buckley, D. A. H., Swart, G. P., & Meiring, J. G. 2006, in SPIE Proceedings, Vol. 6267, Society of Photo-Optical Instrumentation Engineers (SPIE) Conference Series, 62670Z
Busso, M., Gallino, R., & Wasserburg, G. J. 1999, ARA&A, 37, 239
Caffau, E., Bonifacio, P., François, P., et al. 2011, Nature, 477, 67
Caffau, E., Bonifacio, P., François, P., et al. 2013, A&A, 560, A15
Caffau, E., Bonifacio, P., Spite, M., et al. 2016, A&A, 595, L6
Caffau, E., Bonifacio, P., Starkenburg, E., et al. 2017, Astronomische Nachrichten, 338, 686
Caffau, E., Bonifacio, P., Sbordone, L., et al. 2020, MNRAS, 493, 4677
Carney, B. W., Latham, D. W., Stefanik, R. P., & Laird, J. B. 2008, AJ, 135, 196
Carney, B. W., Latham, D. W., Stefanik, R. P., Laird, J. B., & Morse, J. A. 2003, AJ, 125, 293
Carney, B. W., & Peterson, R. C. 1981, ApJ, 245, 238
Carollo, D., Freeman, K., Beers, T. C., et al. 2014, ApJ, 788, 180
Casagrande, L., Wolf, C., Mackey, A. D., et al. 2019, MNRAS, 482, 2770
Casey, A. R., & Schlaufman, K. C. 2015, ApJ, 809, 110
Cenarro, A. J., Peletier, R. F., Sánchez-Blázquez, P., et al. 2007, MNRAS, 374, 664
Chambers, K. C., Magnier, E. A., Metcalfe, N., et al. 2016, arXiv e-prints, arXiv:1612.05560
Charbonnel, C. 1994, A&A, 282, 811
Charbonnel, C., & Lagarde, N. 2010, A&A, 522, A10
Charlot, S., Worthey, G., & Bressan, A. 1996, ApJ, 457, 625
Chen, Y.-P., Trager, S. C., Peletier, R. F., et al. 2014, A&A, 565, A117
Chen, Y. Q., Zhao, G., & Zhao, J. K. 2009, ApJ, 702, 1336
Chiaki, G., Tominaga, N., & Nozawa, T. 2017, MNRAS, 472, L115
Chiappini, C. 2013, Astronomische Nachrichten, 334, 595
Chiappini, C., Hirschi, R., Meynet, G., et al. 2006, A&A, 449, L27
Chiappini, C., Minchev, I., Starkenburg, E., et al. 2019, The Messenger, 175, 30
Choi, J., Dotter, A., Conroy, C., et al. 2016, ApJ, 823, 102
Choplin, A., Hirschi, R., Meynet, G., & Ekström, S. 2017, A&A, 607, L3
Christlieb, N., Schörck, T., Frebel, A., et al. 2008, A&A, 484, 721
Christlieb, N., Bessell, M. S., Beers, T. C., et al. 2002, Nature, 419, 904
Christlieb, N., Beers, T. C., Barklem, P. S., et al. 2004, A&A, 428, 1027
Christlieb, N., Battistini, C., Bonifacio, P., et al. 2019, The Messenger, 175, 26
Cirasuolo, M., Afonso, J., Bender, R., et al. 2011, The Messenger, 145, 11
Clarke, J. P., Wegg, C., Gerhard, O., et al. 2019, MNRAS, 489, 3519
Coelho, P. R. T. 2014, MNRAS, 440, 1027
Cohen, J. G., Christlieb, N., Thompson, I., et al. 2013, ApJ, 778, 56
Crause, L. A., Sharples, R. M., Bramall, D. G., et al. 2014, in SPIE Proceedings, Vol. 9147, Ground-based and Airborne Instrumentation for Astronomy V, 91476T
Cruz, M. A., Serenelli, A., & Weiss, A. 2013, A&A, 559, A4
Da Costa, G. S., Bessell, M. S., Mackey, A. D., et al. 2019, MNRAS, 489, 5900
Dalton, G., Trager, S., Abrams, D. C., et al. 2018, in Society of Photo-Optical Instrumentation Engineers (SPIE) Conference Series, Vol. 10702, SPIE Proceedings, 107021B

Davies, B., Kudritzki, R.-P., Plez, B., et al. 2013, ApJ, 767, 3
de Jong, R. S., Agertz, O., Berbel, A. A., et al. 2019, The Messenger, 175, 3
Dearborn, D. S. P., Liebert, J., Aaronson, M., et al. 1986, ApJ, 300, 314
Debattista, V. P., Ness, M., Gonzalez, O. A., et al. 2017, MNRAS, 469, 1587
Dékány, I., Minniti, D., Catelan, M., et al. 2013, ApJ, 776, L19
Deng, L.-C., Newberg, H. J., Liu, C., et al. 2012, Research in Astronomy and Astrophysics, 12, 735
DESI Collaboration, Aghamousa, A., Aguilar, J., et al. 2016, arXiv e-prints, arXiv:1611.00036
Di Matteo, P. 2016, PASA, 33, e027
Di Matteo, P., Haywood, M., Lehnert, M. D., et al. 2019, A&A, 632, A4
Diemand, J., Madau, P., & Moore, B. 2005, MNRAS, 364, 367
Donati, J.-F. 2003, in Astronomical Society of the Pacific Conference Series, Vol. 307, Solar Polarization, ed. J. Trujillo-Bueno & J. Sanchez Almeida, 41
Donati, J.-F., Semel, M., Carter, B. D., Rees, D. E., & Collier Cameron, A. 1997, MNRAS, 291, 658
Dotter, A. 2016, ApJS, 222, 8
Eddington, A. S. 1920, The Observatory, 43, 341
Evans, D. W., Riello, M., De Angeli, F., et al. 2018, A&A, 616, A4
Falcón-Barroso, J., Sánchez-Blázquez, P., Vazdekis, A., et al. 2011, A&A, 532, A95
Foreman-Mackey, D. 2016, The Journal of Open Source Software, 1, doi:10.21105/joss.00024
Fragkoudi, F., Di Matteo, P., Haywood, M., et al. 2018, A&A, 616, A180
Frebel, A., Chiti, A., Ji, A. P., Jacobson, H. R., & Placco, V. M. 2015, ApJ, 810, L27
Frebel, A., Collet, R., Eriksson, K., Christlieb, N., & Aoki, W. 2008, ApJ, 684, 588
Frebel, A., & Norris, J. E. 2015, ARA&A, 53, 631
Frebel, A., Simon, J. D., & Kirby, E. N. 2014, ApJ, 786, 74
Frebel, A., Aoki, W., Christlieb, N., et al. 2005, Nature, 434, 871
Frebel, A., Christlieb, N., Norris, J. E., et al. 2006, ApJ, 652, 1585
Freeman, K., & Bland-Hawthorn, J. 2002, ARA&A, 40, 487
Freeman, K., Ness, M., Wylie-de-Boer, E., et al. 2013, MNRAS, 428, 3660
Gaia Collaboration, Prusti, T., de Bruijne, J. H. J., et al. 2016, A&A, 595, A1
Gaia Collaboration, Brown, A. G. A., Vallenari, A., et al. 2018, A&A, 616, A1
Gallart, C., Bernard, E. J., Brook, C. B., et al. 2019, Nature Astronomy, 3, 932
García Pérez, A. E., Ness, M., Robin, A. C., et al. 2018, ApJ, 852, 91
Gil-Pons, P., Doherty, C. L., Gutiérrez, J. L., et al. 2018, ArXiv e-prints, arXiv:1810.00982
Giridhar, S., Lambert, D. L., Gonzalez, G., & Pandey, G. 2001, PASP, 113, 519
Gonneau, A., et al., & et al. 2020, A&A
Gonneau, A., Lançon, A., Trager, S. C., et al. 2016, A&A, 589, A36
—. 2017, A&A, 601, A141
Goswami, A., Aoki, W., Beers, T. C., et al. 2006, MNRAS, 372, 343
Gratton, R. G., Sneden, C., Carretta, E., & Bragaglia, A. 2000, A&A, 354, 169
Gravity Collaboration, Abuter, R., Amorim, A., et al. 2019, A&A, 625, L10
Green, G. 2018, The Journal of Open Source Software, 3, 695
Green, G. M., Schlafly, E., Zucker, C., Speagle, J. S., & Finkbeiner, D. 2019, ApJ, 887, 93
Green, G. M., Schlafly, E. F., Finkbeiner, D. P., et al. 2015, ApJ, 810, 25
Green, G. M., Schlafly, E. F., Finkbeiner, D., et al. 2018, MNRAS, 478, 651
Greif, T. H., Bromm, V., Clark, P. C., et al. 2012, MNRAS, 424, 399
Gustafsson, B., Edvardsson, B., Eriksson, K., et al. 2008, A&A, 486, 951
Hansen, C. J., Hansen, T. T., Koch, A., et al. 2019, A&A, 623, A128
Hansen, T., Hansen, C. J., Christlieb, N., et al. 2015, ApJ, 807, 173

Hansen, T. T., Andersen, J., Nordström, B., et al. 2016a, A&A, 586, A160
—. 2016b, A&A, 588, A3
Hartwig, T., Yoshida, N., Magg, M., et al. 2018, MNRAS, 478, 1795
Heger, A., & Woosley, S. E. 2002, ApJ, 567, 532
Helmi, A., Babusiaux, C., Koppelman, H. H., et al. 2018, Nature, 563, 85
Hernitschek, N., Schlafly, E. F., Sesar, B., et al. 2016, ApJ, 817, 73
Hill, V., Lecureur, A., Gómez, A., et al. 2011, A&A, 534, A80
Hirano, S., & Bromm, V. 2017, MNRAS, 470, 898
Ho, A. Y. Q., Ness, M. K., Hogg, D. W., et al. 2017, ApJ, 836, 5
Hollek, J. K., Frebel, A., Roederer, I. U., et al. 2011, ApJ, 742, 54
Howard, C. D., Rich, R. M., Reitzel, D. B., et al. 2008, ApJ, 688, 1060
Howard, C. D., Rich, R. M., Clarkson, W., et al. 2009, ApJ, 702, L153
Howes, L. M., Asplund, M., Casey, A. R., et al. 2014, MNRAS, 445, 4241
Howes, L. M., Casey, A. R., Asplund, M., et al. 2015, Nature, 527, 484
Howes, L. M., Asplund, M., Keller, S. C., et al. 2016, MNRAS, 460, 884
Hunter, J. D. 2007, Computing In Science & Engineering, 9, 90
Irwin, M., & Lewis, J. 2001, NAR, 45, 105
Ishigaki, M. N., Tominaga, N., Kobayashi, C., & Nomoto, K. 2018, ApJ, 857, 46
Ito, H., Aoki, W., Beers, T. C., et al. 2013, ApJ, 773, 33
Iwamoto, N., Umeda, H., Tominaga, N., Nomoto, K., & Maeda, K. 2005, Science, 309, 451
Jacobson, H. R., Keller, S., Frebel, A., et al. 2015, ApJ, 807, 171
Karakas, A. I., & Lattanzio, J. C. 2014, PASA, 31, e030
Katz, D., Soubiran, C., Cayrel, R., Adda, M., & Cautain, R. 1998, A&A, 338, 151
Katz, D., Sartoretti, P., Cropper, M., et al. 2018, ArXiv e-prints, arXiv:1804.09372
Keller, S. C., Bessell, M. S., Frebel, A., et al. 2014, Nature, 506, 463
Kielty, C. L., Venn, K. A., Loewen, N. B., et al. 2017, MNRAS, 471, 404
Koch, A., McWilliam, A., Preston, G. W., & Thompson, I. B. 2016, A&A, 587, A124
Koesterke, L., Allende Prieto, C., & Lambert, D. L. 2008, ApJ, 680, 764
Koleva, M., Prugniel, P., Bouchard, A., & Wu, Y. 2009, A&A, 501, 1269
Koleva, M., Prugniel, P., Ocvirk, P., et al. 2007, in IAU Symposium, Vol. 241, Stellar Populations as Building Blocks of Galaxies, ed. A. Vazdekis & R. Peletier, 183–184
Koleva, M., & Vazdekis, A. 2012, A&A, 538, A143
Kollmeier, J. A., Zasowski, G., Rix, H.-W., et al. 2017, arXiv e-prints, arXiv:1711.03234
Kordopatis, G., Gilmore, G., Wyse, R. F. G., et al. 2013a, MNRAS, 436, 3231
Kordopatis, G., Gilmore, G., Steinmetz, M., et al. 2013b, AJ, 146, 134
Kovalev, M., Bergemann, M., Ting, Y.-S., & Rix, H.-W. 2019, A&A, 628, A54
Kunder, A., Koch, A., Rich, R. M., et al. 2012, AJ, 143, 57
Kunder, A., Rich, R. M., Koch, A., et al. 2016, ApJ, 821, L25
Kurucz, R. L. 2017, ATLAS9: Model atmosphere program with opacity distribution functions, Astrophysics Source Code Library, ascl:1710.017
Lai, D. K., Lee, Y. S., Bolte, M., et al. 2011, ApJ, 738, 51
Latham, D. W., Stefanik, R. P., Torres, G., et al. 2002, AJ, 124, 1144
Lau, H. H. B., Stancliffe, R. J., & Tout, C. A. 2007, MNRAS, 378, 563
Lee, Y. S., Beers, T. C., Kim, Y. K., et al. 2017, ApJ, 836, 91
Lee, Y. S., Beers, T. C., Masseron, T., et al. 2013, AJ, 146, 132
Lee, Y.-W., Hong, S., Lim, D., et al. 2018, ApJ, 862, L8
Lee, Y.-W., Joo, S.-J., & Chung, C. 2015, MNRAS, 453, 3906
Leung, H. W., & Bovy, J. 2019, MNRAS, 483, 3255
Lewis, I. J., Cannon, R. D., Taylor, K., et al. 2002, MNRAS, 333, 279

Li, H., Tan, K., & Zhao, G. 2018, ApJS, 238, 16
Li, T. S., Koposov, S. E., Zucker, D. B., et al. 2019, arXiv e-prints, arXiv:1907.09481
Limongi, M., Chieffi, A., & Bonifacio, P. 2003, ApJ, 594, L123
Longeard, N., Martin, N., Starkenburg, E., et al. 2018, MNRAS, 480, 2609
—. 2020, MNRAS, 491, 356
Lucatello, S., Tsangarides, S., Beers, T. C., et al. 2005, ApJ, 625, 825
Lucey, M., Hawkins, K., Ness, M., et al. 2019, MNRAS, 488, 2283
Luck, R. E., & Bond, H. E. 1989, ApJS, 71, 559
Luck, R. E., & Lambert, D. L. 1992, ApJS, 79, 303
Lugaro, M., Karakas, A. I., Stancliffe, R. J., & Rijs, C. 2012, ApJ, 747, 2
Mackereth, J. T., Schiavon, R. P., Pfeffer, J., et al. 2019, MNRAS, 482, 3426
Magg, M., Klessen, R. S., Glover, S. C. O., & Li, H. 2019, MNRAS, 487, 486
Magnier, E. A., & Cuillandre, J. C. 2004, PASP, 116, 449
Magnier, E. A., Lewin, W. H. G., van Paradijs, J., et al. 1992, AAPS, 96, 379
Makarov, D., Prugniel, P., Terekhova, N., Courtois, H., & Vauglin, I. 2014, A&A, 570, A13
Manset, N., & Donati, J.-F. 2003, in SPIE Proceedings, Vol. 4843, Polarimetry in Astronomy, ed. S. Fineschi, 425–436
Martins, L. P., & Coelho, P. 2007, MNRAS, 381, 1329
Matsuno, T., Aoki, W., & Suda, T. 2019, ApJ, 874, L35
Matsuno, T., Aoki, W., Suda, T., & Li, H. 2017, PASJ, 69, 24
McClure, R. D., & Woodsworth, A. W. 1990, ApJ, 352, 709
McConnachie, A., Babusiaux, C., Balogh, M., et al. 2016, arXiv e-prints, arXiv:1606.00043
McKinney, W. 2010a, in Proceedings of the 9th Python in Science Conference, ed. S. van der Walt & J. Millman, 51 – 56
McKinney, W. 2010b, in Proceedings of the 9th Python in Science Conference, ed. S. van der Walt & J. Millman, 51 – 56
McWilliam, A., Preston, G. W., Sneden, C., & Shectman, S. 1995, AJ, 109, 2736
McWilliam, A., & Zoccali, M. 2010, ApJ, 724, 1491
Mészáros, S., Allende Prieto, C., Edvardsson, B., et al. 2012, AJ, 144, 120
Meynet, G., Ekström, S., & Maeder, A. 2006, A&A, 447, 623
Meynet, G., Hirschi, R., Ekstrom, S., et al. 2010, A&A, 521, A30
Moe, M., Kratter, K. M., & Badenes, C. 2018, ArXiv e-prints, arXiv:1808.02116
Myeong, G. C., Vasiliev, E., Iorio, G., Evans, N. W., & Belokurov, V. 2019, MNRAS, 488, 1235
Nagasawa, D. Q., Marshall, J. L., Li, T. S., et al. 2018, ApJ, 852, 99
Nataf, D. M., Udalski, A., Gould, A., Fouqué, P., & Stanek, K. Z. 2010, ApJ, 721, L28
Ness, M., Hogg, D. W., Rix, H. W., Ho, A. Y. Q., & Zasowski, G. 2015, ApJ, 808, 16
Ness, M., & Lang, D. 2016, AJ, 152, 14
Ness, M., Freeman, K., Athanassoula, E., et al. 2012, ApJ, 756, 22
—. 2013a, MNRAS, 430, 836
—. 2013b, MNRAS, 432, 2092
Nomoto, K., Kobayashi, C., & Tominaga, N. 2013, ARA&A, 51, 457
Nordlander, T., Amarsi, A. M., Lind, K., et al. 2017, A&A, 597, A6
Nordlander, T., Bessell, M. S., Da Costa, G. S., et al. 2019, MNRAS, 488, L109
Norris, J. E., Christlieb, N., Korn, A. J., et al. 2007, ApJ, 670, 774
Norris, J. E., Gilmore, G., Wyse, R. F. G., Yong, D., & Frebel, A. 2010, ApJ, 722, L104
Norris, J. E., Ryan, S. G., & Beers, T. C. 1997, ApJ, 488, 350
Norris, J. E., & Yong, D. 2019, ApJ, 879, 37
Norris, J. E., Bessell, M. S., Yong, D., et al. 2013a, ApJ, 762, 25
Norris, J. E., Yong, D., Bessell, M. S., et al. 2013b, ApJ, 762, 28

Oort, J. H. 1926, PhD thesis, -
Ortolani, S., Renzini, A., Gilmozzi, R., et al. 1995, Nature, 377, 701
Payne, C. H. 1925, PhD thesis, RADCLIFFE COLLEGE.
Percival, S. M., & Salaris, M. 2009, ApJ, 703, 1123
Pérez-Villegas, A., Portail, M., & Gerhard, O. 2017, MNRAS, 464, L80
Pietrukowicz, P., Kozłowski, S., Skowron, J., et al. 2015, ApJ, 811, 113
Placco, V. M., Beers, T. C., Reggiani, H., & Meléndez, J. 2016a, ApJ, 829, L24
Placco, V. M., Frebel, A., Beers, T. C., & Stancliffe, R. J. 2014, ApJ, 797, 21
Placco, V. M., Kennedy, C. R., Beers, T. C., et al. 2011, AJ, 142, 188
Placco, V. M., Frebel, A., Beers, T. C., et al. 2016b, ApJ, 833, 21
Plez, B. 2008, Physica Scripta Volume T, 133, 014003
Plez, B., & Cohen, J. G. 2005, A&A, 434, 1117
Portail, M., Wegg, C., Gerhard, O., & Ness, M. 2017, MNRAS, 470, 1233
Preston, G. W., & Sneden, C. 2001, AJ, 122, 1545
Price-Whelan, A., & Hogg, D. W. 2017, adrn/thejoker: Release v0.1, doi:10.5281/zenodo.264481
Price-Whelan, A. M., Hogg, D. W., Foreman-Mackey, D., & Rix, H.-W. 2017, ApJ, 837, 20
Price-Whelan, A. M., Sipőcz, B. M., Günther, H. M., et al. 2018, AJ, 156, 123
Price-Whelan, A. M., Hogg, D. W., Rix, H.-W., et al. 2020, arXiv e-prints, arXiv:2002.00014
Prugniel, P., & Soubiran, C. 2001, A&A, 369, 1048
Prugniel, P., Vauglin, I., & Koleva, M. 2011, A&A, 531, A165
Queiroz, A. B. A., Anders, F., Santiago, B. X., et al. 2018, MNRAS, 476, 2556
Recio-Blanco, A., Bijaoui, A., & de Laverny, P. 2006, MNRAS, 370, 141
Robin, A. C., Marshall, D. J., Schultheis, M., & Reylé, C. 2012, A&A, 538, A106
Robin, A. C., Reylé, C., Fliri, J., et al. 2014, A&A, 569, A13
Roederer, I. U., Preston, G. W., Thompson, I. B., et al. 2014, AJ, 147, 136
Roederer, I. U., Frebel, A., Shetrone, M. D., et al. 2008, ApJ, 679, 1549
Saha, K. 2015, ApJ, 806, L29
Saha, K., Martinez-Valpuesta, I., & Gerhard, O. 2012, MNRAS, 421, 333
Sahlholdt, C. L., Casagrande, L., & Feltzing, S. 2019, ApJ, 881, L10
Salvadori, S., Skúladóttir, Á., & Tolstoy, E. 2015, MNRAS, 454, 1320
Sánchez-Blázquez, P., Peletier, R. F., Jiménez-Vicente, J., et al. 2006a, MNRAS, 371, 703
—. 2006b, MNRAS, 371, 703
Sanders, J. L., Smith, L., Evans, N. W., & Lucas, P. 2019, MNRAS, 487, 5188
Santiago, B. X., Brauer, D. E., Anders, F., et al. 2016, A&A, 585, A42
Saunders, W., Bridges, T., Gillingham, P., et al. 2004, Society of Photo-Optical Instrumentation Engineers (SPIE) Conference Series, Vol. 5492, AAOmega: a scientific and optical overview, ed. A. F. M. Moorwood & M. Iye, 389–400
Schiavon, R. P., Zamora, O., Carrera, R., et al. 2017, MNRAS, 465, 501
Schlafly, E. F., & Finkbeiner, D. P. 2011, ApJ, 737, 103
Schlafly, E. F., Meisner, A. M., Stutz, A. M., et al. 2016, ApJ, 821, 78
Schlaufman, K. C., Thompson, I. B., & Casey, A. R. 2018, ApJ, 867, 98
Schlegel, D. J., Finkbeiner, D. P., & Davis, M. 1998, ApJ, 500, 525
Schönrich, R., Binney, J., & Dehnen, W. 2010, MNRAS, 403, 1829
Schörck, T., Christlieb, N., Cohen, J. G., et al. 2009, A&A, 507, 817
Schultheis, M., Rojas-Arriagada, A., García Pérez, A. E., et al. 2017, A&A, 600, A14
Sestito, F., Longeard, N., Martin, N. F., et al. 2019, MNRAS, 484, 2166
Sestito, F., Martin, N. F., Starkenburg, E., et al. 2020, MNRAS, arXiv:1911.08491
Sharma, K., Prugniel, P., & Singh, H. P. 2016, A&A, 585, A64

Sharp, R., Saunders, W., Smith, G., et al. 2006, Society of Photo-Optical Instrumentation Engineers (SPIE) Conference Series, Vol. 6269, Performance of AAOmega: the AAT multi-purpose fiber-fed spectrograph, 62690G
Shen, J., Rich, R. M., Kormendy, J., et al. 2010, ApJ, 720, L72
Shetrone, M., Tayar, J., Johnson, J. A., et al. 2019, ApJ, 872, 137
Simmerer, J., Sneden, C., Cowan, J. J., et al. 2004, ApJ, 617, 1091
Skrutskie, M. F., Cutri, R. M., Stiening, R., et al. 2006, AJ, 131, 1163
Skúladóttir, Á., Tolstoy, E., Salvadori, S., et al. 2015, A&A, 574, A129
Smiljanic, R., Korn, A. J., Bergemann, M., et al. 2014, A&A, 570, A122
Soubiran, C., Bienaymé, O., & Siebert, A. 2003, A&A, 398, 141
Soubiran, C., Le Campion, J.-F., Brouillet, N., & Chemin, L. 2016, A&A, 591, A118
Spite, M., Caffau, E., Bonifacio, P., et al. 2013, A&A, 552, A107
Stanek, K. Z., Mateo, M., Udalski, A., et al. 1994, ApJ, 429, L73
Starkenburg, E., Oman, K. A., Navarro, J. F., et al. 2017a, MNRAS, 465, 2212
Starkenburg, E., Shetrone, M. D., McConnachie, A. W., & Venn, K. A. 2014, MNRAS, 441, 1217
Starkenburg, E., Martin, N., Youakim, K., et al. 2017b, MNRAS, 471, 2587
Starkenburg, E., Aguado, D. S., Bonifacio, P., et al. 2018, MNRAS, 481, 3838
Steinmetz, M., Matijevic, G., Enke, H., et al. 2020a, arXiv e-prints, arXiv:2002.04377
Steinmetz, M., Guiglion, G., McMillan, P. J., et al. 2020b, arXiv e-prints, arXiv:2002.04512
Suda, T., Aikawa, M., Machida, M. N., Fujimoto, M. Y., & Iben, Jr., I. 2004, ApJ, 611, 476
Takada, M., Ellis, R. S., Chiba, M., et al. 2014, PASJ, 66, R1
Takahashi, K., Umeda, H., & Yoshida, T. 2014, ApJ, 794, 40
Taylor, M. B. 2005, in Astronomical Society of the Pacific Conference Series, Vol. 347, Astronomical Data Analysis Software and Systems XIV, ed. P. Shopbell, M. Britton, & R. Ebert, 29
Ting, Y.-S., Rix, H.-W., Conroy, C., Ho, A. Y. Q., & Lin, J. 2017, ApJ, 849, L9
Tolstoy, E., Hill, V., & Tosi, M. 2009, ARA&A, 47, 371
Tominaga, N., Iwamoto, N., & Nomoto, K. 2014, ApJ, 785, 98
Tonry, J., & Davis, M. 1979, AJ, 84, 1511
Tonry, J. L., Stubbs, C. W., Lykke, K. R., et al. 2012, ApJ, 750, 99
Tumlinson, J. 2010, ApJ, 708, 1398
Umeda, H., & Nomoto, K. 2002, ApJ, 565, 385
—. 2003, Nature, 422, 871
—. 2005, ApJ, 619, 427
Vandenberg, D. A., & Smith, G. H. 1988, PASP, 100, 314
Vazdekis, A., Koleva, M., Ricciardelli, E., Röck, B., & Falcón-Barroso, J. 2016, MNRAS, 463, 3409
Venn, K. A., Puzia, T. H., Divell, M., et al. 2014, ApJ, 791, 98
Venn, K. A., Kielty, C. L., Sestito, F., et al. 2020, MNRAS, 492, 3241
Vernet, J., Dekker, H., D'Odorico, S., et al. 2011, A&A, 536, A105
Villaume, A., Conroy, C., Johnson, B., et al. 2017, ApJS, 230, 23
Weiland, J. L., Arendt, R. G., Berriman, G. B., et al. 1994, ApJ, 425, L81
Wenger, M., Ochsenbein, F., Egret, D., et al. 2000, AAPS, 143, 9
Wolf, C., Onken, C. A., Luvaul, L. C., et al. 2018, PASA, 35, e010
Woosley, S. E., & Weaver, T. A. 1995, ApJS, 101, 181
Wu, Y., Singh, H. P., Prugniel, P., Gupta, R., & Koleva, M. 2011a, A&A, 525, A71
Wu, Y., Luo, A.-L., Li, H.-N., et al. 2011b, Research in Astronomy and Astrophysics, 11, 924
Xiang, M. S., Liu, X. W., Yuan, H. B., et al. 2015, MNRAS, 448, 822
Yanny, B., Rockosi, C., Newberg, H. J., et al. 2009, AJ, 137, 4377
Yong, D., Norris, J. E., Bessell, M. S., et al. 2013a, ApJ, 762, 26

—. 2013b, ApJ, 762, 27
Yoon, J., Beers, T. C., Placco, V. M., et al. 2016, ApJ, 833, 20
Yoon, J., Beers, T. C., Dietz, S., et al. 2018, ApJ, 861, 146
York, D. G., Adelman, J., Anderson, John E., J., et al. 2000, AJ, 120, 1579
Youakim, K., Starkenburg, E., Aguado, D. S., et al. 2017, MNRAS, 472, 2963
Youakim, K., Starkenburg, E., Martin, N. F., et al. 2020, MNRAS, 492, 4986
Yuan, Z., Myeong, G. C., Beers, T. C., et al. 2020, ApJ, 891, 39
Zasowski, G., Schultheis, M., Hasselquist, S., et al. 2019, ApJ, 870, 138
Zoccali, M., Hill, V., Lecureur, A., et al. 2008, A&A, 486, 177
Zoccali, M., Gonzalez, O. A., Vasquez, S., et al. 2014, A&A, 562, A66
Zoccali, M., Vasquez, S., Gonzalez, O. A., et al. 2017, A&A, 599, A12